Universitat Politècnica de València
Departamento de Máquinas y Motores Térmicos

Doctoral Thesis

Experimental study of the behavior of gasoline direct injection GDI sprays during wall impingement under realistic engine conditions.

Presented by:
César Carvallo García

Supervised by:
Dr. Jaime Gimeno García

in fulfillment of the requirements for the degree of
Doctor of Philosophy

Valencia, May 2023

Ph.D. Thesis

Experimental study of the behavior gasoline direct injection GDI sprays during wall impingement under realistic engine conditions.

Written by: Mr. César Carvallo García
Supervised by: Dr. Jaime Gimeno García

Examination committee:

Chairman: Dr. XXXX
Secretary: Dr. XXXX
Member: Dr. Michele Bardi

Reviewing board:

Dr. Michele Bardi
Dr. Walter Martín Vera Tudela Fajardo
Dr. Francisco Javier Martos Ramos

Valencia, May 2023

Abstract

Fuel injection is one of the most important factor that must be considered to achieve cleaner and more efficient internal combustion engines. Its role is more evident when direct injection strategies are used. The injector internal geometry and the needle movement define the internal flow behavior affecting the spray external development and combustion performance inside the cylinder. As awareness of climate change and global emission reduction policies increase, efforts are being made to develop new technologies that enable cleaner and more environmentally friendly engines. The gasoline direct injection systems can fulfill strict emission standards and improve fuel consumption.

Because of the space constraints inside the combustion chamber for spray penetration, collision and interaction with the wall are common events in direct injection engines, considerably influencing spray formation and air-spray interaction inside the chamber. By this, the spray-wall interaction is a crucial factor during the combustion process and a complex phenomenon nowadays. In cold-start engine conditions, the lower injection pressures and temperatures in the combustion chamber enhance the fuel deposition over the piston surface, incrementing the soot and the unburned hydrocarbon formation. The novelty designs characterized by high injection pressures and reduced piston movement inside the cylinder favor the spray-wall interaction.

Even the evident importance of the spray-wall interaction phenomenon and the efforts made by researchers to understand it, the transitory nature and the complex physical events that occur in the surroundings of the wall make the direct monitoring and evaluation of this phenomenon challenging. Although computational tools are invaluable in this sector, the necessity of experimental findings to develop robust models is still a reality and a need.

The present work highlights the fundamental aspects of the spray-wall interaction for the gasoline direct injection (GDI) system under cold-start and other evaporative conditions. For that, a flat wall is located several distances and at different wall angles to the injector tip. Also, this thesis involves using a solenoid injector produced by Continental and the well-known “Spray G” injector using iso-octane as injected fuel covering several techniques and experimental facilities.

Three optical techniques were used for the external spray characterization: lateral visualization using Diffuse-Back Illumination (DBI) and Schlieren and frontal visualization using MIE-scattering. Also, the infrared thermography technique was used to study the spray-wall heat transfer.

To analyze the spray-wall interaction, three experimental approaches were used: The first used three high-speed cameras and a quartz wall inside the test rig vessel to study the macroscopic characteristics of the spray, which was observed lateral and frontal by using the optical accesses of the vessel. The second approach used a stainless steel wall to catch the effect of the operating and ambient conditions over the heat flux between the wall and the spray during the fuel injection event and determine how the spray development is affected by the cold-start realistic engine conditions and other evaporative conditions that were included in the test matrix. This wall was coupled with sensors to control the initial surface temperature and to compute the temperature variation in time and the surface heat flux using high-speed thermocouples. The spray under free-jet conditions was also analyzed as a comparison point with the spray-wall interaction conditions.

Time-resolved measures were made for the spray width at two different locations from the spray impact point with the wall to analyze in time and space that metric. The spray vapor phase was visualized using Schlieren, and the liquid phase was observed using Diffuse-Back Illumination.

The spray spreading along the wall, the effect of wall-to-tip distance, and the effect of the wall angle over the spray development were analyzed. The semi-circle area of impact was calculated by using the frontal MIE-scattering images of the spray-wall impingement phenomenon. Lastly, two heat flux analyses were conducted, the first using the thermal signal of the fast-response thermocouples coupled to the steel wall and the second using the infrared thermography technique applied to a heated thin foil.

The free spray penetration and the spray spreading over the wall were influenced mainly by the injection pressure and the wall angle. The spray thickness measured after the SWI was affected primarily by the wall-to-tip distance and the wall angle but even more by the distance from the impact point in which it is measured. The semi-circle impact area was susceptible to wall angles and wall-to-tip distance variations, essential in the spray-air entrainment. No remarkable differences were found between the liquid and vapor phases for the free jet or the isothermal wall configuration. In contrast, some differences were obtained for the instrumented and thermoregulated wall, remarking the contribution of fuel evaporation caused by the wall temperature increase.

Regarding the thermoregulated wall, the fuel and wall temperatures produced the most important peaks in terms of surface heat flux. A similar order of magnitude regarding the surface heat flux was found between the thermoregulated wall and infrared thermography experimental campaigns. The

flash boiling appearance for the lower ambient back pressure and higher fuel temperature condition changed the spray morphology in terms of the width (spray angle), having significant repercussions over the *R-parameter* (which depends on the spray penetration) and in the number of liquid droplets present in the spray affecting both the light extinction profiles and the surface heat flux profiles.

Resumen

A medida que aumenta la conciencia climática y se buscan reducir las emisiones globales, se están realizando esfuerzos para producir tecnologías que permitan desarrollar motores más limpios y amigables con el medio ambiente. Los sistemas GDI (inyección directa de gasolina) tienen el potencial de cumplir con los cada vez más estrictos estándares de emisiones y, al mismo tiempo, mejorar el consumo de combustible. La inyección de combustible es un proceso crítico que debe tenerse en cuenta para producir motores de combustión interna eficientes y limpios, especialmente cuando se emplean estrategias de inyección directa.

El espacio limitado dentro de la cámara de combustión hace que el impacto del chorro con la pared sea un fenómeno común en los motores de inyección directa de gasolina. Este fenómeno tiene un efecto significativo en el desarrollo del chorro y su interacción con el aire en la cámara. La interacción chorro-pared es un fenómeno interesante y difícil de comprender que ocurre durante el proceso de combustión. En condiciones de arranque en frío, las bajas presiones y temperaturas en la cámara facilitan la deposición del combustible en la superficie del pistón, lo que conduce a un aumento considerable en la formación de hollín y en los hidrocarburos sin quemar. Además, en los nuevos diseños de inyectores, que alcanzan presiones de inyección más altas y con desplazamientos del pistón en el cilindro cada vez más cortos, el fenómeno de choque pared ocurre con mayor frecuencia.

Aunque se están llevando a cabo múltiples esfuerzos para la comprensión del fenómeno de choque-pared, es complejo observar la interacción chorro-pared debido a su naturaleza transitoria y complejidad física. En este campo, las herramientas computacionales han sido de gran ayuda. Sin embargo, para desarrollar modelos más robustos, es necesario contar con datos experimentales.

Esta tesis busca proporcionar información sobre las características más relevantes de la interacción chorro-pared en sistemas de inyección directa de gasolina en condiciones de arranque en frío y otras condiciones evaporativas. Para ello, se utilizó una pared plana ubicada a diferentes distancias de impacto y ángulos con respecto a la punta del inyector. Se empleó un inyector solenoide fabricado por Continental y el inyector “Spray G”, utilizando iso-octano como combustible inyectado. El estudio se llevó a cabo en diversas instalaciones experimentales cubriendo varias técnicas ópticas.

Para la caracterización externa del chorro, se utilizaron tres técnicas ópticas: visualización lateral mediante DBI y Schlieren y visualización frontal

mediante MIE-scattering. También se utilizó termografía infrarroja para estudiar la transferencia de calor entre el chorro y una lámina delgada.

El estudio de la interacción chorro-pared se llevó a cabo utilizando tres campañas experimentales. En la primera, se utilizó una pared de cuarzo transparente para analizar las características macroscópicas del chorro al impactar la pared, observándola lateral y frontalmente con el uso de tres cámaras de alta velocidad gracias a los accesos ópticos de la instalación experimental. En la segunda, se empleó una pared termorregulada de acero inoxidable para medir el efecto que tienen las condiciones de operación y ambientales sobre la transferencia de calor entre la pared y el chorro durante el evento de inyección de combustible. A esta pared se le añadieron distintos sensores para controlar su temperatura superficial inicial y para medir la variación de la temperatura en el tiempo utilizando termopares de alta velocidad.

Se realizaron ensayos en condiciones de chorro libre y se tomaron como punto de comparación para los experimentos de interacción entre chorro y pared.

Se hicieron medidas resueltas en el tiempo para la altura o espesor del chorro a dos distancias distintas respecto al punto de impacto con la pared para analizar tanto temporal como espacialmente esa métrica. Al mismo tiempo que se visualizó la fase de vapor del chorro utilizando Schlieren y la fase líquida mediante "Diffuse-Back Illumination".

El desarrollo del chorro sobre la pared, el efecto de la distancia entre el inyector y la pared, así como el efecto del ángulo de inclinación de la pared fueron analizados. La semi-area de impacto fue calculada usando las imágenes frontales obtenidas con la técnica MIE-scattering. Por último, dos análisis de la transferencia de calor entre el chorro y la pared fueron llevados a cabo, el primero utilizando la señal de temperatura obtenida a través de los termopares de respuesta rápida acoplados a la pared de acero y el segundo análisis utilizando la termografía infrarroja para estudiar la transferencia de calor sobre una lámina calentada.

Se observó que la penetración del chorro libre y el desarrollo del chorro sobre la pared son influenciados por la presión de inyección y el ángulo de inclinación de la pared. El ancho del chorro medido después del impacto fue afectado principalmente por la distancia entre el inyector y la pared y por el ángulo de la pared pero más aún por la distancia respecto al punto de impacto sobre la cual fue medida. La semi área de impacto es susceptible a cambios en el ángulo de la pared y la distancia inyector-pared teniendo un papel fundamental en el arrastre de aire entre el chorro y el ambiente. No se encontraron

diferencias significativas entre las fases líquida y vapor tanto para la penetración de chorro libre como para el desarrollo del chorro sobre la pared a temperatura ambiente. Por el contrario, con la pared instrumentada, se obtuvieron diferencias entre la fase líquida y vapor, destacando la contribución de la evaporación de combustible causada por el incremento en la temperatura de la pared. Respecto a la pared instrumentada, tanto la temperatura del combustible como de la pared produjeron los picos más significativos en términos del flujo de calor superficial. Órdenes de magnitud similares respecto al flujo de calor superficial fueron encontrados entre las campañas experimentales de la pared instrumentada y la termografía infrarroja. La aparición del flash boiling en condiciones de menor contrapresión ambiental y mayor temperatura del combustible modificó la morfología del chorro en términos de anchura (ángulo del chorro), lo que tuvo repercusiones significativas en el parámetro R (que depende de la penetración del chorro) y en el número de gotas de líquido presentes en el chorro, afectando tanto a los perfiles de extinción de la luz como a los perfiles del flujo de calor superficial.

Resum

A mesura que augmenta la consciència climàtica i es busquen reduir les emissions globals, s'estan fent esforços per a produir tecnologies que permeten desenvolupar motors més nets i amigables amb el medi ambient. Els sistemes GDI (injecció directa de gasolina) tenen el potencial de complir amb els estrictes estàndards d'emissions i, al mateix temps, millorar el consum de combustible. La injecció de combustible és un procés crític que ha de tindre's en compte per a produir motors de combustió interna eficients i nets, especialment quan s'empren estratègies d'injecció directa.

L'espai limitat dins de la cambra de combustió fa que l'impacte del doll amb la paret siga un fenomen comú en els motors d'injecció directa de gasolina. Aquest fenomen té un efecte significatiu en el desenvolupament del doll i la seua interacció amb l'aire en la cambra. La interacció doll-paret és un fenomen interessant i difícil de comprendre que ocorre durant el procés de combustió. En condicions d'arrancada en fred, les baixes pressions i temperatures en la cambra faciliten la deposició del combustible en la superfície del pistó, la qual cosa condueix a un augment considerable en la formació de sutge i en els hidrocarburs sense cremar. A més, en els nous dissenys d'injectors, que aconsegueixen pressions d'injecció més altes i amb desplaçaments del pistó en el cilindre cada vegada més curts, el fenomen de xoc paret ocorre amb major freqüència.

Encara que s'estan duent a terme múltiples esforços per a la comprensió del fenomen de xoc-paret, és complex observar la interacció doll-paret a causa de la seua naturalesa transitòria i complexitat física. En aquest camp, les eines computacionals han sigut de gran ajuda. No obstant això, per a desenvolupar models més robustos, és necessari comptar amb dades experimentals.

Aquesta tesi busca proporcionar informació sobre les característiques més rellevants de la interacció doll-paret en sistemes d'injecció directa de gasolina en condicions d'arrancada en fred i altres condicions evaporatives. Per a això, es va utilitzar una paret plana situada a diferents distàncies d'impacte i angles respecte a la punta de l'injector. Es va emprar un injector solenoide fabricat per Continental i l'injector "Spray G", utilitzant iso-octà com a combustible injectat. L'estudi es va dur a terme en diverses instal · lacions experimentals cobrint diverses tècniques òptiques.

Per a la caracterització externa del doll, es van utilitzar tres tècniques òptiques: visualització lateral mitjançant DBI i Schlieren i visualització frontal mitjançant MIE-scattering. També es va utilitzar termografia infraroja per a estudiar la transferència de calor entre el doll i una làmina prima.

L'estudi de la interacció doll-paret es va dur a terme utilitzant tres campanyes experimentals. En la primera, es va utilitzar una paret de quars transparent per a analitzar les característiques macroscòpiques del doll en impactar la paret, observant-la lateral i frontalment amb l'ús de tres càmeres d'alta velocitat gràcies als accessos òptics de la instal · lació experimental. En la segona, es va emprar una paret termorregulada d'acer inoxidable per a mesurar l'efecte que tenen les condicions d'operació i ambientals sobre la transferència de calor entre la paret i el doll durant l'esdeveniment d'injecció de combustible. A aquesta paret se li van afegir diferents sensors per a controlar la seua temperatura superficial inicial i per a mesurar la variació de la temperatura en el temps utilitzant termoparells d'alta velocitat.

Es van realitzar assajos en condicions de doll lliure i es van prendre com a punt de comparació per als experiments d'interacció entre doll i paret.

Es van fer mesures resoltes en el temps per a l'altura o grossària del doll a dues distàncies diferents respecte al punt d'impacte amb la paret per a analitzar tant temporal com espacialment aqueixa mètrica. Al mateix temps que es va visualitzar la fase de vapor del doll utilitzant Schlieren i la fase líquida mitjançant "Diffuse-Back Illumination".

El desenvolupament del doll sobre la paret, l'efecte de la distància entre l'injector i la paret, així com l'efecte de l'angle d'inclinació de la paret van ser analitzats. La semi-area d'impacte va ser calculada usant les imatges frontals obtingudes amb la tècnica MIE-scattering. Finalment, dues anàlisis de la transferència de calor entre el doll i la paret van ser duts a terme, el primer utilitzant el senyal de temperatura obtinguda a través dels termoparells de resposta ràpida acoblats a la paret d'acer i la segona anàlisi utilitzant la termografia infraroja per a estudiar la transferència de calor sobre una làmina calfada.

Es va observar que la penetració del doll lliure i el desenvolupament del doll sobre la paret són influenciats per la pressió d'injecció i l'angle d'inclinació de la paret. L'ample del doll mesurat després de l'impacte va ser afectat principalment per la distància entre l'injector i la paret i per l'angle de la paret però més encara per la distància respecte al punt d'impacte sobre la qual va ser mesurada. La semi àrea d'impacte és susceptible a canvis en l'angle de la paret i la distancia injector-paret tenint un paper fonamental en l'arrossegament d'aire entre el doll i l'ambient. No es van trobar diferències significatives entre les fases líquida i vapor tant per a la penetració de doll lliure com per al desenvolupament del doll sobre la paret a temperatura ambient. Per contra, amb la paret calfada, es van obtindre diferències entre la fase líquida i vapor, destacant la contribució de l'evaporació de combustible causada per l'increment en

la temperatura de la paret. Respecte a la paret instrumentada, tant la temperatura del combustible com de la paret van produir els pics més significatius en termes del flux de calor superficial. Ordres de magnitud similars respecte al flux de calor superficial van ser trobats entre les campanyes experimentals de la paret instrumentada i la termografia infraroja. L'aparició del flaix boiling en condicions de menor contrapressió ambiental i major temperatura del combustible va modificar la morfologia del doll en termes d'amplària (angle del doll), la qual cosa va tindre repercussions significatives en el paràmetre R (que depén de la penetració del doll) i en el nombre de gotes de líquid presents en el doll, afectant tant els perfils d'extinció de la llum com als perfils del flux de calor superficial.

"The only thing greater than the power of the mind is the courage of the heart"
- John Nash

A mi familia, amigos y pareja
Especialmente a mi hermano Daniel y mi padre César que ya no están presentes pero que llevo día a día en el corazón

Agradecimientos

Siempre me ha parecido que esta es la sección más importante y difícil de escribir de todo el documento de tesis, hay tantas cosas para escribir y personas a las que mencionar. Es necesario destacar el enorme esfuerzo que han realizado para permitirme completar esta etapa de mi vida por lo que muchas veces no se encuentran las palabras correctas o la forma de plasmarlas en el papel.

Para empezar me gustaría mencionar el apoyo incondicional de mis padres, que desde chico se preocuparon por darme la mejor educación, el afecto, y la inspiración necesaria para nunca rendirme y seguir adelante, completando poco a poco hitos académicos y profesionales. Al hablar de mi familia, se me hace un nudo en la garganta puesto que un logro como este habría conmovido tanto a mi padre que hubiese sido imposible para él contener la emoción y el orgullo. Sin embargo, al no estar presente, se que desde allá arriba apoya y guía mis pasos y me acompaña siempre. En segundo lugar, a mi hermano Daniel, que hasta su último respiro me tuvo en un pedestal y siempre estuvo orgulloso de mi. Este logro no es solo mío, es de ustedes también.

Siguiendo el orden, quisiera agradecer a mi director de tesis Jaime Gimeno García, porque sin él, este trabajo no hubiese llegado a término. Jaime siempre será una de las personas a las que más admiraré y respetaré no solo por su intelecto, sino por sus buenos sentimientos, su forma de ser y el cariño y la vocación con la que resolvió cada una de mis inquietudes durante el desarrollo del doctorado. Bajo mi criterio es un gran ejemplo como educador y profesional.

También me gustaría agradecer a Raúl Payri por su papel como team leader del grupo de inyección, siempre orientando y marcando la dirección adecuada en la que enfocar nuevos proyectos dentro de la institución. Así mismo quiero resaltar al Centro de Motores Térmicos (CMT) por dejarme formar parte de su acreditado grupo de investigación, y de brindarme los medios y recursos para llevar a cabo esta tesis. Además, agradezco el trato personal de Amparo Cutillas en secretaría y del personal de informática por ayudarme en diversos procesos administrativos y burocráticos.

Esta tesis se ha desarrollado en el marco de una ayuda para la Formación de Personal Investigador (FPI) Subprograma 1 (PAID-01-19) financiada por la Universitat Politècnica de València. Agradezco, a la Universitat Politècnica de València, por abrirme las puertas de esta ciudad y financiar económicamente estos años de formación y dedicación a mi tesis de doctorado, y de brindarme la oportunidad de conseguir una meta académica de alto prestigio. Del mismo modo, agradezco a la Universitat Politècnica de València por haber

financiado mi estancia doctoral a Nápoles en donde pude llevar a cabo parte de los experimentos presentados en esta tesis. Debo agradecer al STEMS y a la Universidad de Napoli: Federico "II" por haberme abierto las puertas durante tres meses y haberme dado las herramientas para llevar a cabo algunos experimentos.

De igual forma, agradezco al equipo de doctorandos de inyección del CMT. Armando Moreno, Alberto Viera, Tomás Montiel, Jesús Peraza, Santiago Cardona, María Martinez, Abian Bautista, Vincenzo Pagano y Victor Mendoza, por dedicarme su tiempo y ayuda resolviendo mis preguntas y por haberse convertido en algo más que simples compañeros de trabajo. A mis amigos Sebastian Aceros e Ibrahim Barbery, por su apoyo durante todo este proceso.

De igual forma agradezco a Jose Enrique del Rey y Omar Huerta por toda su ayuda, sin ellos no hubiese sido posible realizar las campañas experimentales de esta tesis. Considero a Jose Enrique como un gran amigo, que aguantó mis novatadas y mis fallos durante todos los años del doctorado. Compartimos grandes momentos, bromas y muchas risas que hicieron todo el proceso doctoral mucho más agradable. Tampoco puede faltar agradecer a Jose Torner, porque sin sus grandes habilidades como tornero, muchas de las piezas utilizadas en los experimentos no hubiesen funcionado como estaban inicialmente previstas. El ingenio y la capacidad de adaptarse ante situaciones imprevistas, caracteriza a cada uno de los miembros del equipo de técnicos.

Gracias a todos por estar para mi y formar parte de este camino.

Contents

List of Figures

List of Tables

Chapter 1

Introduction

This chapter presents the grounds for studying the Gasoline Direct Injection (GDI) process and the effect of the spray-wall interaction under cold-start and other evaporative conditions that were included in the test matrix that are interesting for GDI engines. Initially, the framework of the study in the research community is described. Then, the objectives to be achieved and the methodology applied in this work. Finally, a summary of the upcoming chapters is discussed.

1.1 Overview

The Internal Combustion Engine (ICE) is one of the most notable inventions of the twentieth century, and it has had a significant impact on society. They sparked numerous technological advances that, without a doubt, revolutionized transportation and mobility. For example, this type of engine has been used in a variety of fields other than automotive, such as agriculture, service propulsion, and power generation. It generates mechanical power from fuel energyby a monitored combustion reaction. Its undeniable efficiency in providing power to transportation systems is backed up by a high power-to-weight ratio, the energy density of available fuels, and its low cost. The extensive use of ICE has proved that the detrimental toxins and emissions produced by fuel combustion should not be ignored. The principal pollutants that, if present in high numbers, could damage nature and human life are nitrogen oxides (NOx), greenhouse gases such as CO2, soot, and unburned fuels. As a result,

governments in the European Union, North America, and Asia have adopted directives to limit them in order to ensure clean air in cities and counteract the consequences of global warming. Emission restrictions have strengthened over time, prompting the automotive sector to continue looking for brand new technologies that allow for reduced emissions and better fuel economy. The worldwide car industry has recently undergone a significant transition from the usage of normal combustion engines to electrified powertrains, either hybridized or wholly electrical. Nonetheless, combustion engines continue to dominate, with a projected share of the market of 85% by 2030, according to [1].

Electric powertrains do not emit any emissions and help to expand the use of renewable energy in the transportation sector. However, if the energy source is not green, the usage of this sort of propulsion may affect the environment. Unless electric power is generated primarily from green sources, the entire well-to-wheels analysis would not be more promising than ICEs. Furthermore, the life cycle of the metallic element in batteries used in current electric vehicles could be a major disadvantage because waste treatment is harmful to the environment. There are works like García et al. [2] where the electric vehicle well-to-wheel and life-cycle emissions analysis was carried out, unveiling higher environmental impact regarding the CO_2 than expected.

Diesel engines were the dominant type for light-duty transportation systems and an integral part of personal automobiles in Europe for the past fifty years. Higher efficiency compared to gasoline engines and higher energy density for diesel fuel have been the two main reasons. Due to the Dieselgate scandal (in which some OEMs cheated the emission inspection for diesel engines), the perception of diesel engines as extremely polluting vehicles has shifted in recent years, prompting manufacturers to sell more gasoline engines. Furthermore, the issue of meeting NOx emission regulations has forced the design of valuable after-treatment systems, which raises the vehicle final cost. Given the circumstances, manufacturers are turning to lean gasoline engines, which are less complicated and less expensive. Downsizing and turbocharging advancements in gasoline engines improve fuel economy. It is also the most popular engine for hybrid vehicles due to its simplicity.

Fuel injection technology and spray development inside the cylinder are two of the most critical factors for engine improvement that have received attention in the last twenty years [3]. Understanding the phenomena of injection, evaporation, mixing, and combustion allows for the development of a new injector generation to reduce emissions. The fuel direct injection systems are cutting-edge for ICEs. Though direct injection of fuel into the combus-

tion chamber has been used in diesel systems since 1894, the first usage of this technology for gasoline engines was in aeronautics during World War I in Junkers planes. Later, in the 1950s, GDI was mandated in German automobiles, but it failed due to several difficulties and inflexibility. It was not until 1996 that GDI was widely used in automobiles, when Mitsubishi introduced an electronic GDI system. Since then, the GDI system has seen rapid adoption among OEMs, with adoption in the United States increasing from 2.3 percent in 2008 models to 50 percent in 2016 models [4].

The main benefit of GDI over earlier PFI systems is that the injection event happens directly in the cylinder, avoiding wall wetting of the intake port and valves. Furthermore, as the fuel evaporates in the cylinder, it cools the air, allowing for a larger compression ratio. As a result, it encourages the use of turbo chargers and the engine downsizing without the chance of the knock phenomena [5–7]. According to Johnson [8], it also favors particular engine situations such as part loads or cold starts. Also, encourage the development of sophisticated combustion techniques like gasoline compression ignition.

The diesel injectors were the primary research area due to their direct involvement in mixture formation and combustion, which is ultimately related to fuel economy and pollutant formation. Nonetheless, the injectors were not the most important component in PFI gasoline engines. After the introduction of the GDI system attempts were made to fully comprehend these injectors. The fuel delivery system in GDI engines is not fully understood, and it faces fuel consumption and emissions issues. As a result, companies and academic organizations are working hard to achieve their full potential. The GDI injectors are in charge of delivering the correct amount of fuel at the specified location within the cylinder, as well as providing the proper atomization, evaporation, and combination with the air at the appropriate time. Earlier GDI engines used the injections flexibility to work at stratified charge at partial loads and homogenized at high loads. However, that strategy is no longer used because it allows for a slightly higher compression ratio without the knock phenomenon and a leaner air-fuel ratio, but it increases NOx formation due to the presence of lean zones, necessitating the use of NOx after-treatment systems to meet strict emission regulations.

After impingement, a fuel film can build on the walls, promoting unburned hydrocarbons and soot generation. Additionally, heat transfer between the fuel deposits and the cylinder walls reduces engine performance. Also, secondary atomization produced by spray-wall interaction is widely recognized to improve droplet breakdown, reduce droplet size, and accelerate evaporation. This phenomena is essential, especially for direct injection during cold-start,

because low densities and temperatures favor a substantial liquid spray penetration that might reach the piston and combustion chamber boundaries.

Two injectors were used in this thesis and were studied with two different experimental campaigns carried out in different research institutes (using the hardware available at the CMT-Motores Térmicos and an experimental facility available at the STEMS and University of Naples "Federico II"). The injectors are the Continental solenoid six orifice GDI injector and the Engine Combustion Network (ECN) Spray G injector. The experimental data obtained from both injectors were compared regarding the heat flux magnitude, which was analyzed through infrared thermography (IR) (for the case of Spray G), and the thermal signal registered with fast-response thermocouples coupled to a wall for the Continental injector campaign, allowing comparison between research organizations via reliable experimental data used to design computational fluid dynamics (CFD) models. The experimental campaign carried out in Naples, Italy was done under the doctoral exchange with the mobility economic help provided by the Universitat Politècnica de València.

This work was created at the CMT-Motores Térmicos research institute, which is affiliated with the Universitat Politècnica de València (Spain). Since its inception 40 years ago, the institute has established a well-known global reputation in the field of combustion engines. Its primary focus in the past years has been on diesel engines. Still, nowadays, the institute is driven to other technologies, even covering the analysis of batteries and electric vehicles, and also working on combustion, air management, noise, after-treatments, fuel/urea/water injection, and simulations. Over the years, the institution has published over 180 books, 500 journal articles and completed over 165 doctoral theses.

Given the community increasing interest in GDI technology, the organization decided to invest in and specialize in it in recent years. This work is the third in the injection department focused on GDI spray atomization research [9, 10], and the third on the spray-wall interaction phenomenon [11, 12].

1.2 Aims and procedure

This thesis arose from a desire to gain a better understanding of the spray-wall interaction phenomenon in GDI engines, as well as to identify the parameters that enhance SWI and influence atomization, evaporation, and the formation of air-fuel mixtures. The CMT-Motores Térmicos injection research group, which typically worked with diesel injectors, has done little research on GDI only in the last years, and this is the third thesis in a gasoline injection related

topic [9, 10]. However, the group existing knowledge of diesel injectors and some techniques was transferred to the GDI systems. To conduct the necessary experiments, an instrumented wall (coupled with fast-response thermocouples) and a quartz wall support were designed and developed to analyze the spray-wall phenomenon inside the experimental vessel. Thus, the two primary goals of the current work can be encapsulated as follows:

1. Help to improve understanding of the impact of ambient, injection, and wall conditions on the macroscopic development of the spray and the spray-wall heat transfer once it interacts with a wall, by employing various optical techniques for spray-wall diagnostics and analysis.

2. Acquisition of spray-wall interaction experimental data at realistic cold-start and other evaporative engine conditions in order to obtain valuable information for CFD model development and validation.

The experimental campaign was carried out by using the hardware available at the CMT-Motores Térmicos and an experimental facility available at the STEMS and University of Naples "Federico II". In order to analyze the SWI phenomenon, two different wall setups were used in the campaign: a transparent quartz wall with initial isothermal condition ($T_w = T_{amb}$) and an instrumented and heated stainless steel wall provided with fast-response thermocouples. Iso-octane was used as the injected fuel and only inert spray data was obtained through the use of high speed cameras, getting simultaneously lateral vapor and liquid phases images and frontal images using MIE-scattering technique for the quartz wall. Also a squared target plate made of Invar foil of 50 µm in thickness was used to investigate the wall heat transfer with infrared thermography allowing comparisons with the stainless steel wall.

The experimental facility used by [10] was modified in order to study the SWI for the first time, which was accomplished through the design and implementation of suitable wall systems, as discussed in this manuscript.

The Continental injector with six holes has been thoroughly characterized. The experimental campaign was divided into two parts: hydraulic characterization and external visualization. The hydraulic characterization for this injector was reported in [13] for similar conditions to the one used in this work and also can be depicted in Appendix A. The experimental facilities available in the CMT laboratories are classified as follows:

- Hydraulic Continental injector characterization

  - Rate of injection measurements
  - Momentum flux measurements
- Spray Visualization
  - GDI visualization vessel coupled with the wall systems

The GDI test rig available in the CMT-Motores Térmicos was used. In a first instance the conditions used were the ones in the guidelines of the ECN [14] for the Spray G injector under real cold-start engine conditions and variations around it.

1.3 Thesis framework

The text is organized into eight chapters. It begins with a general introduction (**chapter 1**) that provides the reader with a general framework as well as the thesis incentives.

The evolution and fundamental concepts of combustion engines are presented in **chapter 2**. The concepts of more specific GDI theory and spray-wall phenomenon are then introduced. Finally, a review of the most recent SWI-related findings in the literature are presented.

A detailed description of the experimental facilities and all of the equipment used to obtain the data for the current work can be found in **chapter 3**. The injection hardware and selected operating conditions, as well as the hydraulic characterization facilities, are discussed. In addition, the two different wall systems used to simulate spray-wall interaction under cold-start conditions are described in detail.

The data processing methodologies are described in **chapter 4**, which includes information on the optical techniques principles and data treatment for both images and signals.

The fifth chapter **chapter 5** is the first one to include results, the visualization results obtained from the free-jet campaign and from the transparent quartz wall using the optical techniques Schlieren, DBI, and MIE-scattering are shown. In addition, the spray semi-circle area of impact calculation is examined for all conditions tested during the experimental campaign. The results obtained for the thermoregulated steel wall and the heat flux results are shown in **chapter 6**.

Spray visualization for vapor and liquid phases is shown in both chapters, and the information related to the spray penetration, spray spreading, and wall thickness are used to discuss the observed trends.

chapter 7 present the heat transfer results after wall impingement obtained through the infrared thermography technique applied to the Spray G injector, this work was entirely carried out at the experimental facilities provided by the Istituto di Scienze e Tecnologie per l'Energia e la Mobilità Sostenibili (STEMS) and the University of Naples "Federico II".

The **chapter 8** concludes the thesis outline by providing a summary of the main findings of this work, emphasizing the most important points from each chapter presented. Finally, future works and directions for furthering research on this topic are suggested.

Finally, **Appendix A** represents an appendix related to the hydraulic characterization of the Continental injector, results that were obtained in the CMT-Motores Térmicos and already published. This aims to provide more information that will help to describe some spray behaviors present in the result chapters of this thesis.

References

[1] Gomot, Dipl Baudouin and Hülser, Holger. "Delphi Technologies Next Generation GDi-System, improved Emissions and Efficiency with higher Pressure". In: *Internationales Wiener Motorensymposium* (2019), pp. 1–21.

[2] García, Antonio, Serrano, Javier Monsalve, Boggio, Santiago Martinez, and Soria Alcaide, Rafael. "Carbon footprint of battery electric vehicles considering average and marginal electricity mix". In: *Energy* 268 (2023), p. 126691. DOI: `https://doi.org/10.1016/j.energy.2023.126691`.

[3] Kuo, Kenneth K and Zarchan, Paul. *Recent Advances in Spray Combustion: Spray Atomization and Drop Burning Phenomena*. 1996. DOI: `10.2514/4.866418`.

[4] EPA. "Light-Duty Automotive Technology, Carbon Dioxide Emissions, and Fuel Economy Trends: 1975 Through 2016 - Executive Summary (EPA-420-S-16-001, November 2016)". In: November (2016), pp. 1–11.

[5] Zimmerman, Naomi, Wang, Jonathan M, Jeong, Cheol Heon, Wallace, James S, and Evans, Greg J. "Assessing the Climate Trade-Offs of Gasoline Direct Injection Engines". In: *Environmental Science and Technology* (2016). DOI: `10.1021/acs.est.6b01800`.

[6] Fontanesi, Stefano, D'Adamo, Alessandro, and Rutland, Christopher J. "Large-Eddy simulation analysis of spark configuration effect on cycle-to-cycle variability of combustion and knock". In: *International Journal of Engine Research* (2015). DOI: 10.1177/1468087414566253.

[7] Saliba, Georges et al. "Comparison of Gasoline Direct-Injection (GDI) and Port Fuel Injection (PFI) Vehicle Emissions: Emission Certification Standards, Cold-Start, Secondary Organic Aerosol Formation Potential, and Potential Climate Impacts". In: *Environmental Science and Technology* (2017). DOI: 10.1021/acs.est.6b06509.

[8] Johnson, Timothy. "Vehicular Emissions in Review". In: *SAE International Journal of Engines* 7.3 (2014), pp. 1491–2014. DOI: 10.4271/2014-01-1491.

[9] Vaquerizo, Daniel. "Study on Advanced Spray-Guided Gasoline Direct Injection Systems". PhD thesis. Universitat Politècnica de València, 2017.

[10] Bautista Rodriguez, Abian. "Study of the Gasoline direct injection process under novel operating conditions". PhD thesis. Universitat Politècnica de València, 2021.

[11] González, Uriel. "Efecto del choque de pared en las características del chorro Diesel de inyección directa". PhD thesis. Valencia: E.T.S. Ingenieros Industriales. Universidad Politécnica de Valencia, 1998.

[12] Peraza Avila, Jesus Enrique. "Experimental study of the diesel spray behavior during the jet-wall interaction at high pressure and high temperature conditions". PhD thesis. Universitat Politècnica de València, 2020.

[13] Payri, Raul, Gimeno, Jaime, Marti-Aldaravi, Pedro, and Mendoza Alvarez, Victor. "Study of the hydraulic characteristics of two injectors fed with different fuels in a GDI system". In: *Fuel* 317 (2022), p. 123196. DOI: https://doi.org/10.1016/j.fuel.2022.123196.

[14] ECN. "Engine Combustion Network". In: *https://ecn.sandia.gov/gasoline-spray-combustion/* (2020).

Chapter 2

Gasoline injection fundamentals and spray-wall interaction

The objective of this section is to deliver the fundamentals of gasoline spray injection and the wall interaction phenomenom, giving an overview of the literature underpinning this work. The mechanisms and principles of operation used in gasoline engines for fuel injection are briefly described.

First, a brief explanation of the actual status of the internal combustion engines worldwide, locating the GDI engine in the actual global picture. Then, a classification of the different internal combustion engine technologies and characteristics. After that, an explanation of how the gasoline fuel injection system works and the types of injectors present in the market. Finally, the SWI phenomenon is introduced with its physical characteristics and complexities

2.1 ICEs worldwide status

The first vehicle driven by an internal combustion engine (ICE) in 1860 marked the beginning of an era of constant changes. The technologies and systems involved have been in continual evolution and development.

The evolution of machines has had to adapt to the needs demanded by society and nowadays by pursuing the goal to obtain cleaner and more efficient

devices to mitigate climatic change. Starting with the Kyoto protocol, the car industry has constantly been changing, driven by emission restrictions, and all the new designs and technologies have been oriented to fight that goal.

To reduce the pollutants produced by the ICEs, strategies regarding limiting the NOx present in the exhaust gases, the unburned hydrocarbons, and the soot emissions. At the same time, the continual search for alternatives to the existent propulsion model for those using fossil fuels has characterized the path to sustainability and the future.

The automobile industry must continue with the same adaptation process since its creation, guaranteeing the maximum emissions of 95 g CO_2/km proposed by the European Commission until 2024. After that, these emissions should gradually decrease until they disappear in 2050.

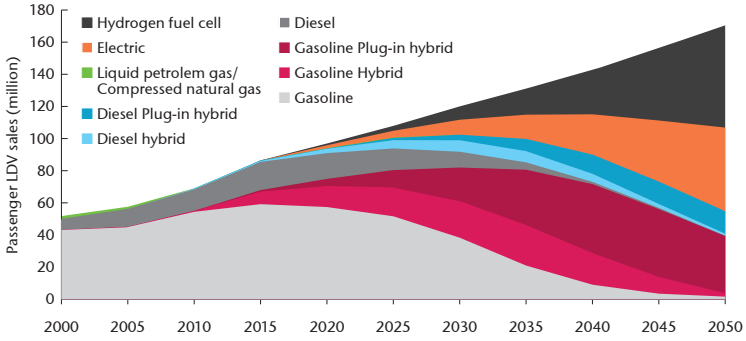

Figure 2.1: Extrapolation of annual light vehicle sales by technology type [1].

Figure 2.1 shows the annual sales projections for light vehicles up to 2050. It is possible to notice that the sustainability path translates into the development of various propulsion models, as fully electrified cars or hydrogen fuel. However, due to the nonexistent technologies or the lack of energy supply production and distribution, gasoline and diesel engines will continue in the market for the upcoming years. The main goal right now is to reduce emissions to extend the life of the internal combustion engine technologies and gradually shift into mixed strategies. To meet the aforementioned goal, GDI engines should focus on fuel consumption reduction, advanced injection strategies, and a complete understanding of the wall-impingement phenomenon to avoid pollutant emissions per kilometer.

Figure 2.2 shows the global CO_2 emissions from transport by sub-sector based on the data available in [2], being the light-duty vehicle sector the more affected one in terms of the million metric tonnes of carbon dioxide reduction

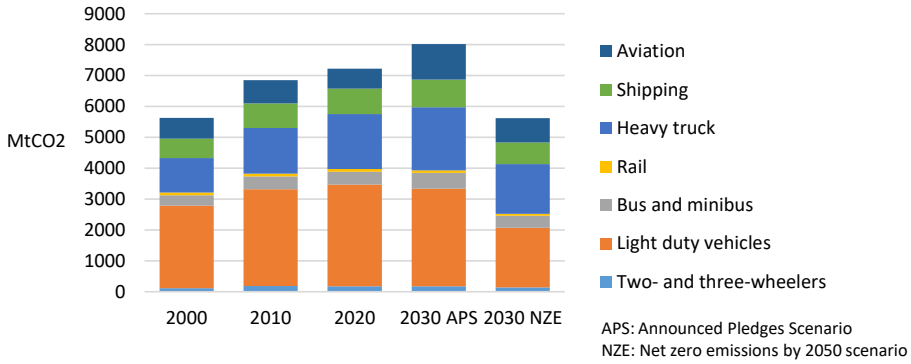

Figure 2.2: Global CO2 emissions by transport subsector (2000-2030)[2].

compared to the other sectors under the net zero emission projection expected by 2050. This scenario indicates a global commitment focused on improving the internal combustion engines and the need for a meeting point between the electrification and combustion approaches due to the actual conditions of both isolated scenarios.

2.2 ICE classification and description

A thermal machine that converts the majority of the energy released by chemical combustion reactions of fuels into useful mechanical work is known as an internal combustion engine (ICE). They are called internal because the reaction takes place within the machine.

Exists several general ICE classifications according to the thermodynamic cycle and the number of steps, 2-stroke or 4-stroke, required to carry it out. In a two-stroke engine, two-piston revolutions make one crankshaft revolution in one cycle. In a 4-stroke engine, the piston moves four times inside the cylinder, and the crankshaft rotates two times per cycle. The former is more straightforward and cheaper, so they are typically used to propel light-duty vehicles or motorcycles or when the activity requires a smaller engine. Four-stroke engines are more fuel efficient and more popular in passenger cars.

Various classifications can be made based on different thermodynamic cycles. The Otto and Diesel cycles, named after their creators, are the most well-known internal combustion engine cycles. Each has a unique method of igniting the fuel. In diesel engines, fuel is ignited by establishing the appropriate temperature and pressure conditions in the cylinder; hence the reason they are referred to as compression ignition (CI) engines.

The CI engine cylinder is only filled with air and fuel is injected to control combustion when the piston is approaching the top dead center (TDC). When fuel is injected at this point, ignition conditions are reached, and vaporization and mixing occur. As a result, a diffuse flame forms at the spray edge. Because it only occurs in areas where the air/fuel mixture is sufficiently rich, it is inherently heterogeneous combustion. Fuel injectors are important in combustion control because fuel atomization characteristics and air movement in the cylinder control combustion.

The Otto cycle, uses constant volume combustion, which is started by a spark, which provides the energy required to start the combustion. They are also referred to as spark ignition (SI) engines. Recent studies have attempted to further control ignition using plasma or laser rather than spark ignition [3–6]

In a spark ignition engine, as previously discussed, the supply of energy towards an electric arc generated by the spark plug ignites combustion. The Otto cycle case for a homogeneous charge with a stoichiometric air/fuel ratio is applicable to classic gasoline engines that employ carburetors or port injectors (indirect injection), with the percentage of mixture governed by a throttle placed upstream of the admission valves. GDI engines, on the other hand, have direct injection into the cylinder, as we will see later. It is possible to use both homogeneous and stratified charges. The operation mode is determined by the timing of the injection events.

As previously stated, the primary distinction between the two cycles involves the way the mixture is created, followed by how combustion begins and progresses. This essentially determines the characteristics and operating conditions of each engine [7].

2.3 Fuel injection mechanism

2.3.1 Gasoline injection systems

To ensure the engine cycle to function properly, the mixture inside the cylinder must have to be capable to ignite when the spark plug is activated. The air-fuel ratio must be determined based on the engine conditions and is typically discussed using two main definitions. First, lambda (λ), or the air-fuel equivalent ratio, expresses the actual mixture stoichiometry. The ratio is expressed as Equation 2.1, and the value indicates the composition of the mixture: $\lambda =$

1.0 denotes stoichiometric conditions, while λ <1 denotes rich mixtures and λ >1 denotes lean mixtures.

$$\lambda = \frac{\text{Mass of air}}{\text{Stoichiometric mass of air}} \tag{2.1}$$

Another common definition is the fuel-air equivalence ratio (ϕ), which is calculated as the ratio of fuel-to-oxidizer to stoichiometric fuel-to-oxidizer, as shown in Equation 2.2. This is the inverse of the value of λ.

$$\phi = \frac{m_{fuel}/m_{ox}}{(m_{fuel}/m_{ox})_{st}} = \frac{1}{\lambda} \tag{2.2}$$

These ratios are critical because they represent the mixture ignition limit, i.e., the possible operating point. SI engines have tighter limits than CI engines due to the nature of combustion. The limit for stable combustion in SI is ϕ values ranging from 0.6 to 1.6. If the engine goal is to maximize fuel efficiency, it will aim for a slightly leaner mixture ($\phi < 1$), but the value at full power will be $\phi \approx 1.15$. Finally, the exact value is determined by the throttle valve angle, cylinder temperature, and pressure [7].

In contrast to CI engines, where the injector controls the air-fuel mixture, the SI injects the fuel directly into the intake valve, allowing for more mixing time and operating in a homogeneous mode. In gasoline engines, the typical fuel injection system is a carburetor first, followed by port fuel injection. Control the amount of air and fuel precisely for optimal mixing. Throttle valves, on the other hand, limit the amount of air passing through the intake by creating a pressure drop, which reduces volumetric efficiency. To avoid this unnecessary loss and the wall wetting phenomenon, the direct injection systems described in section 2.4 are chosen as the solution [8, 9].

Gasoline indirect injection

In gasoline indirect injection, fuel is delivered upstream of the inlet valves in a single or multi-point configuration via one or more injectors.

The following are the common indirect injection strategies:

- Single-point injection: A single injector is located on the throttle body in the same location as the carburetor. In the 1940s, it was used in large aircraft engines, and in the automotive industry in the 1980s. The reason for single-point injection was that it was a less expensive and more efficient alternative to the carburetor.

- Continuous injection: Unlike most fuel injection systems, which deliver fuel in short bursts, fuel flows continuously from the injectors but at varying rates. It was primarily used in high-performance luxury vehicles..

- Fuel injection at multiple locations MPI or port fuel injection (PFI): The fuel for each engine cylinder is injected just before the intake valve in this case. A range of 2-5 bar is a typical fuel pressure for these injectors. They are usually programmed to inject during the intake stroke. The schematic of MPI in the engine is shown in Figure 2.3.

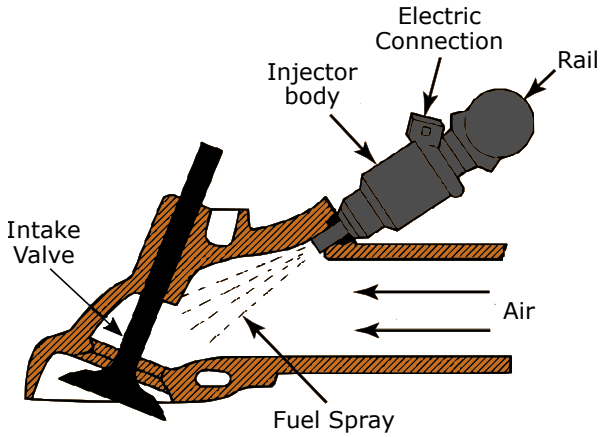

Figure 2.3: A port fuel-injection system injecting fuel into the intake manifold. [10].

A mist of fuel is injected into the intake port with port fuel injection (PFI), cooling the intake valve and causing it to vaporize. Fuel demand is so high at certain engine loads and speeds that the injectors continue to inject even when the valve is closed. When the spark plugs are activated, the heat in the manifold promotes vaporization and better mixing with the air. Fuel must travel a greater distance to enter the cylinder in comparison to single-point injection, where wall wetting is greater. Because PFI is more volumetric efficient, it generally results in lower emissions due to less wall wetting. [7, 11, 12]. This system intake manifold is also designed to increase airflow as it enters the cylinder. PFI, on the other hand, must overcome short injection times when the engine is idle with controlled and precise fuel delivery into the cylinder. Because of the short air mixing distance and time, PFI also runs the risk of producing a rich mixture.

Leon Levavasseur invented the first mechanically actuated indirect injector, which he used in gasoline-powered aircraft in 1902. This technology was not introduced to luxury cars equipped with carburetors until the 1950s. Mechanical fuel injectors were limited in their ability to provide the correct quantity of fuel for each engine condition, such as various speeds and loads, starting regime, ambient temperature and pressure caused by climatic conditions, and so on. To avoid a lack of fuel management, electronic fuel injection (EFI) employs a plethora of sensors and controls. Sensors collaborate to provide input to the system, which uses a "engine map" to calculate the optimal amount of fuel for each engine condition in order to improve engine performance for specific requirements.

Bendix Corporation introduced the first electronic fuel injection system in 1957 [13]. This was the first step toward better fuel control and timing, but the first version had many flaws, so only a few cars used it. Bosch later purchased the patent and developed "D-Jetronic", the first mass-produced electronic injection system controlled by intake air pressure. "L-Jetronic" and "K-Jetronic" have supplanted it. The most recent innovation was the implementation of closed-loop regulation using a lambda oxygen sensor. The "L-Jetronic" was then integrated with engine control technology to enable for programmable ignition map control. These technologies were designed with multi-port fuel injection in mind. The "Mono-Jetronic", on the other hand, was invented in 1987 and it was a low-cost approach that aided the fuel injection become more widely adopted and accessible to the general public. It was ideal for medium to small vehicles and consisted of a single port injector located in the main throttle body (SPI). Carburetors were no longer used after this point. Fuel injection was required for the three-way catalytic converter to function properly and for the lambda sensor to regulate it. Furthermore, fuel injection resulted in lower fuel consumption and emissions, higher power output, higher torque, higher volumetric efficiency, better drivability and response, and ultimately less noise than a carburetor-based engine [11]. To meet fuel economy and emissions requirements, the most common architectures used in cars today use a combination of Motronic and multipoint injection [14]. PFIs must meet performance criteria such as rapid opening and closing, sediment resistance, a small deviation between pulses, a wide mass flow rate, and precise atomization. As a result, it is a complex part of the engine that is still being researched and developed for future engines such as hybrid types [12, 14–22].

2.4 Gasoline direct injection strategy

2.4.1 An Overview of GDI

Because of their simpler construction, low cost, excellent maneuverability, and high specific power, gasoline engines dominated the market. Diesel engines are more expensive due to increasing emission regulations because they need a complex fuel injection and after-treatment technologies and require a robust engine block. Current developments are aiming to create gasoline engines competitive with diesel engines regarding pollution and fuel efficiency. In order to achive that, new strategies such as gasoline direct injection (GDI) are being improved as a possible solution.

GDI engines are solving current problems in gasoline systems, such as improving fuel economy by preventing knocking at high loads [23, 24], lowering HC and NOx pollutants, and lowering pumping losses under part-load conditions [25]. Because the injection occurs directly in the cylinder, the vaporization of the fuel cools and helps reduce the temperature of the air-fuel mixture. This directly affects NOx reduction and knock reduction during combustion. The use of stratified combustion results in a reduction in pumping losses because a rich mixture is obtained around the spark plug in stratified combustion, but the overall mix inside the cylinder stays lean.

Although the stratified mode saves fuel, it is not obvious to use it directly because significant constraints have also prevented its expansion. GDI implementations also allow for the use of novel approaches to lowering emissions, such as downsizing, increasing compression ratios, turbocharging, or a combination of these. GDI systems also enabled the development and research of previously impossible-to-implement combustion models, such as GDCI (Gasoline Direct Compression Ignition), HCCI (Homogeneous Charge Compression Ignition), RCCI (Reactivity Controlled Compression-Ignition), homogeneous lean spark ignition, and water injection for knocking resistance [11, 25, 26].

The first GDI engine design was created in 1916 for Junkers aircraft powered by gasoline and diesel engines in Germany. To avoid misfires, direct injection was used. But it was not until 1952 that Bosch developed a mechanical GDI system to power his two-stroke engines in the Goliath GP700 and Gutbrod Superior. The Mercedes-Benz 300SL, the first with a four-stroke engine with GDI technology, was introduced in 1955 [7]. This early-stage technology is depicted in Figure 2.4. Apart from fuel savings, the primary reason for using GDI in these early vehicle applications was to improve powertrain performance. Companies such as American Motor Company (AMC) and Ford attempted to implement mechanical prototypes of GDI in the 1970s, but none

were successful. The standardization of electronic fuel injection in the 1990s, as well as the development of common rails for diesel engines, brought together the technology required for the successful implementation of GDI engines. In fact, the Mitsubishi Galant was the first production car with a GDI engine to enter the Japanese market in 1996. Then, a year later, it debuted in Europe under the "Charisma" model [27]. Toyota introduced its GDI engine model in the European and Japanese markets around the same time [28]. Automakers began releasing variants of direct-injection gasoline engines while maintaining and improving PFI technology from that point forward.

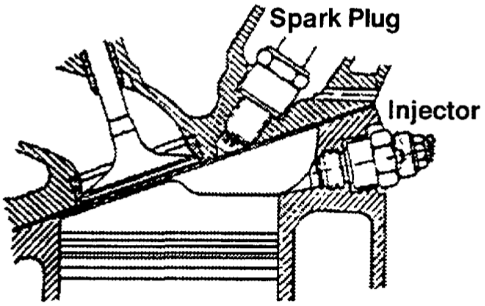

Figure 2.4: Schematic of a Benz 300SL GDI system (1954) [27].

The Figure 2.5 sketch depicts the main components of a gasoline direct injection engine, in which the injector is mounted inside the cylinder and fed by high-pressure fuel. The fuel is injected into the combustion chamber, where it mixes with the air that enters through the throttle valve and inlet valve. In this case, two lambda sensors at each end of the after-treatment device operate in a closed-loop controlled by the ECU, regulating the appropriate quantity of fuel for each operation condition [29, 30].

Nonetheless, the actual fuel efficiency of DI engines under real-world driving conditions was not as high as claimed at the time. This is due to the possibility that stricter emissions regulations will force three-way catalyst systems to operate only at stoichiometric conditions, necessitating the use of costly and inefficient lean-burn NOx after-treatment for stratified lean-burn operation, as cited by [29]. Furthermore, stratified combustion in gasoline engines increased soot formation due to the liquid fuel film on the piston surface, increased HC emissions due to incomplete combustion, and flame extinction [31]. Following that, GDI engines built after 2001 were designed to operate in homogeneous charge mode. They are designed and marketed to be more powerful. Indeed, at high RPM, the GDI system may not have enough time

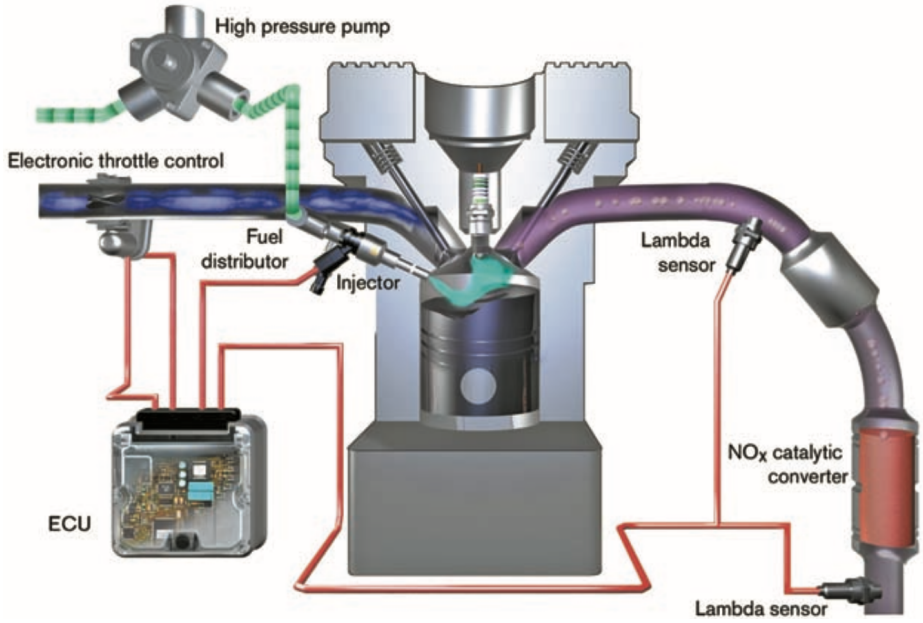

Figure 2.5: Schematic of a GDI system. [30].

to supply all of the fuel required. For maximum performance and smooth operation in part-load conditions, some automakers have combined the system with their PFI structure.

Despite the challenges of producing efficient and emission-free GDI engines, these engines were further developed and researched due to their potential for improvement [18–21, 32–37].

2.4.2 Stratified charge combustion

Historically, gasoline engines used stoichiometric mixtures, with the throttle controlling the load. When the engine is running at partial load, this valve reduces volumetric efficiency. Reducing this intake loss may help to improve fuel efficiency. By eliminating or limiting the use of throttle valves to control engine load, stratified charge mode aims to mitigate this loss. In order to get an overall stoichiometry, a rich, ignitable (within flammability restrictions) mixture is delivered near the spark plug, while a lean mixture is maintained throughout the combustion chamber. As a result, when compared to the throttle configuration, this strategy achieves lower pumping losses at partial load, lower in-cylinder gas temperatures, and thus lower heat losses and NOx

production, ultimately increasing the work taken out by increasing the specific heat ratio [31].

The timing of injection events is the fundamental distinction between stratified and homogenous charging regimes. Fuel is injected in the compression stroke at around 60-70 degrees crank angle (CAD) before top dead center (BTDC) in stratified charge mode, while on the contrary, fuel is injected in the inlet stroke (much earlier) at 270-300 degrees CAD BTDC in homogenous charge mode. [12]. Figure 2.6 denotes two distinct combustion modes. When the spark plug is activated in stratified operation (right), the fuel does not have time to fully mix with the air in the chamber. In contrast, in homogeneous operation, injection occurs much earlier during intake. The airflow turbulence and the longer time allowed for sufficiently uniform mixing. To avoid volumetric efficiency loss (half closed throttle), the ideal operation is to operate in stratified mode at partial load while operating in homogeneous mode with fully open throttle at full load. [9, 29]

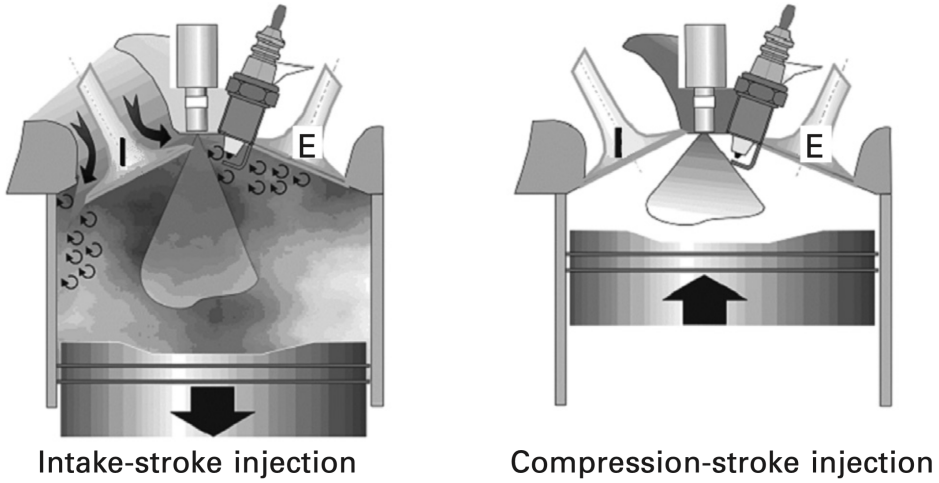

Figure 2.6: GDI combustion modes: Homogeneous charge (left) and Stratified charge (right). [29].

Fuel injection is challenging in stratified mode because there is little time to get the right mixture around the spark plugs. Good fuel convection and successful mixing are dependent on a variety of factors, including the approach used. There are three methods for obtaining an ignitable mixture near the spark plug: air-guided, wall-guided, and spray-guided, as shown in Figure 2.7

Costa et al. [39], the first DI engines used a wall guide system that used a specific shape on the piston surface to channel fuel to the spark plug. However,

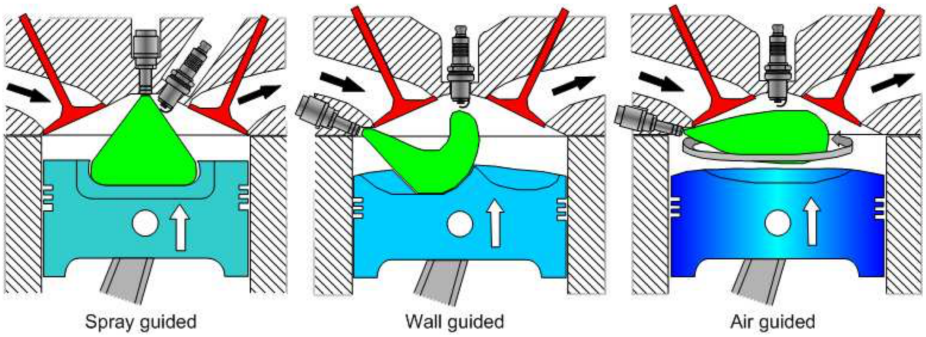

Figure 2.7: Fuel injection approaches for DI engines. [38].

this system is inefficient on its own. Fuel is not completely vaporized when injected onto the piston surface, resulting in high HC and CO emissions and poor fuel economy. The air-guided approach, on the other hand, injects fuel into an airstream that carries it close to the spark plug; a specially designed intake duct achieves the required airflow.This strategy does not use wet pistons or cylinders, instead employs a mixture of swirl and tumble air motion, typically together with specifically surfaced pistons, to deliver a dense cloud of fuel to the required spot. In either situation, the injector is positioned distant from the spark plug.

In the early 2000s, Volkswagen was one of the first companies to introduce a DI combustion system that combined wall-guided and air-guided approaches, demonstrating advantages in both stratified and homogeneous charging modes. In Figure 2.8 a system schematic shows the injector placed near to the inlet port and the piston head with two bowls. One on each side of the inlet valves, one on each side of the exhaust valves. The bowl near the injector deviates the fuel to the spark plug, while the other create a movement of air that carried the rest of the fuel to the ignition zone [40]. The proper functioning of these strategies is highly dependent on the cylinder air movement and the shape of the piston head. Each of these factors contribute to a loss in engine and thermal efficiency as a result of heat loss. Furthermore, by design, these strategies tend to wet the walls of the piston head, resulting in excessive HC and soot emissions.

The final engine concept is the most recent Spray Direct Injection configuration (SGDI). This system was first introduced by Mercedes and BMW in 2006. It can be considered a 2nd generation DI gasoline engine with a wide operating range [12]. Injectors are primarily responsible for bringing fuel closer to the spark plug, where it vaporizes. Under each flow and pressure circum-

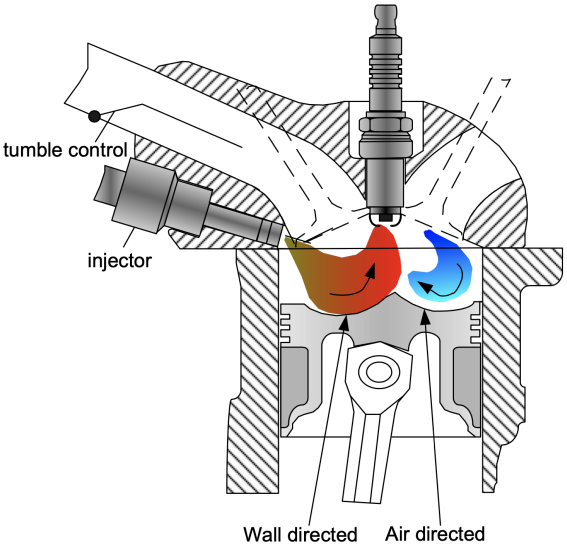

Figure 2.8: Air-wall guided Volkswagen engine design. [11].

stances within the chamber, it must generate an uniform spray pattern. This approach offers the best theoretical efficiency and is being explored for new combustion concepts at the moment. [39, 41–46]. Its advantages over previous systems are numerous. Greater stratified operating range, less prone to cylinder flow fluctuations, less wall wetting, and lower HC emissions. However, there are some issues or new challenges that the SGDI system must address. Coking can occur in SG injectors, owing to the low combustion temperature at the tip of the injector nozzle, but carefully designed holes or counterbores can alleviate this [43, 47]. Contamination also has an impact on spark plug reliability. Finally, the system is vulnerable to injection and ignition timing errors, resulting in a low level of robustness. The limited time for the mixture to form when operating in stratified mode can result in excessive rich zones that cause misfires, HC emissions, and unsteady combustion. Euro VI, which intended to control maximum PM emissions from gasoline engines, was Europe response to the development of stratified gasoline engines. New combustion approaches are being investigated, like homogeneous stratified combustion, that employs a split injection during the air inlet to produce a first lean homogeneous charge and a subsequent injection during compression to produce a rich mixture near the spark plug [39]. This notion, along with several others, has the potential to overcome stratified charging shortcomings, and significant efforts have been made in this regard, but stratified charging GDI operation is still under investigation. [48–53].

2.4.3 Novel combustion notions and GDI technology

In addition to the stratified charge, the DI gasoline engine is very versatile because it allows the use of other technologies and combustion processes. Turbocharging is traditionally used to improve performance while maintaining the same engine architecture. More recently, however, combined with engine downsizing, there has been an opportunity to increase knock resistance. Thanks to the variable camshaft phasing technology, it can increase the manifold pressure and operate at a much greater BMEP [29]. A downsizing initiative to reduce pump loss by installing an engine with a smaller displacement than usual for its output. At full load power, a pressure charging system is used to compensate for losses. As a result, the throttle valve opens wider for a given load, reducing irreversible losses in incoming airflow. As the industry continues to trend toward four-stroke engines, the main advantage of this approach to minimizing losses is that it is not subject to fuel specification or emissions compliance requirements. Modifying the compressor map is possible due to the improved scavenging gained by delaying fuel injection until the output valve is closed. This approach enhances system performance (by reducing turbo lag) and addresses one of the customer more critical characteristics: engine responsiveness, which is more pronounced on larger displacement engines.

The compression ratio can be increased through piston stroke design or supercharging to increase the engine thermal efficiency. However, it is severely constrained by the knocking phenomenon. Excess air and cooled engine gas recirculation (EGR) are both promising approaches for reducing knock, but DI provides greater control over fuel auto-ignition. Alcohol can also increase the heat of vaporization of the fuel, which is an approach to reducing knock.

There are other combustion principles, like gasoline direct compression ignition (GDCI). To decrease fuel consumption, PM and NOx emissions, GDCI adopts a stratified mixture formed from several late injections. This unique idea has the potential to address the drawbacks of stratified combustion as mentioned in subsection 2.4.2. This system has the potential to usher in a new generation of engines that employ both SI and CI approaches. Using lower cetane fuel results in a longer ignition delay, giving you more time to achieve better mixing, which reduces soot and HC [12].

The concept of lean boost combustion exemplifies the combination of downsizing, direct injection, and pressurization in a lean operation. The octane rating of a fuel is critical to the proper operation of engine supercharging. To accommodate the boost pressure and avoid knocking, the engine geometric compression ratio is usually reduced (which adversely affects thermal effi-

ciency). The use of homogeneous dilute operation and DI, on the other hand, relaxes the octane number requirement and assumes a higher compression ratio. The operational limit lies between the risk of knocking on the rich side and generating sparks and flame propagation on the lean side. Adding a boost to the equation shifts the operating range to higher λ values. Shifting to the lean side reduces engine power, so boost pressure must eventually be raised to levels higher than naturally aspirated to allow downsizing in lean conditions. The richest mixture is used to ensure stable operation to minimize the need for air. Therefore, octane reduction is achieved due to the knock suppression effect of DI and excess air [52–56].

When summarizing the charging and combustion strategies, it should be recognized that the injector is the central element of the direct injection system. This is due to the fact that it is in charge to provide the appropriate spray for each situation or engine demand. Because of that, a lot of efforts are located on the development and improvement of injector technology. The same is true for both GDI and PFI injectors as the requirements of new combustion strategies become more and more stringent. Not only because they need to provide the proper amount of fuel, but the degree and position of fuel atomization required for each engine operating scenario must also be achieved. The following section will introduce the different types of GDI injectors that have been developed so far, focusing on the SG system, which is the leading player in this work.

2.5 GDI fuel injectors description

2.5.1 The advancement of gasoline injectors

The diesel injector design and manufacturing technology has been transferred to the gasoline DI. Both injectors have similarities that are mutually beneficial. As mentioned in previous sections, fuel injection is a critical process in DI engines. In order to do so, injectors must be able to deliver fuel at high and low pressures depending on operating conditions, as well as follow precise and consistent strategies. In addition, to work under uniform load conditions, they must provide a well-atomized mixture along the cylinder and around the spark plug in the case of stratified mode operation. In order to achieve proper atomization and the required amount of fuel in such a short period of time, the injectors are typically operated at high pressures of 50-250 bar [14, 23, 29, 57–60].

However, because of new materials and design advances, it has been discovered that using higher pressures has some advantages. Johansson et al. [61]

reduced particulate emissions but discovered that high pressure had a direct impact on soot formation. Hoffmann et al. [62] from Delphi Technologies investigated the performance of injectors as well as the feasibility of increasing the pressure of fuel pumps and other components. Delphi claimed to have introduced the first commercial GDI injector capable of operating at 350 bar in 2016 [63]. Furthermore, Granqvist [64], the president of Denso Sweden, stated at 2017 that mass production of durable GDI injectors and pumps above 35 MPa has never occurred. Husted et al. [65] investigated the effect of rail pressure on fuel consumption using a 400-bar injector. Despite the higher energy demand from the fuel pump, they conclude that increased fuel pressure results in a modest increase in fuel economy. Numerous injector manufacturers, like Bosch, Delphi, Magneti Marelli, and Continental, are currently developing new GDI approaches with injection pressures that vary from 400 bar to 800 bar in order to reduce fuel consumption and emissions [62, 66, 67]. Magneti Marelli 800 bar prototype injector and fuel pump are shown in Figure 2.9.

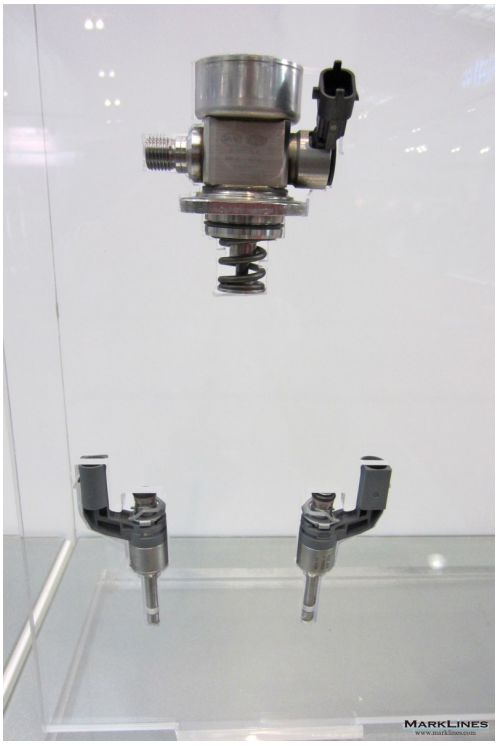

Figure 2.9: Magneti Marelli GDI high-pressure pump and injectors prototypes. Exhibit in SAE China 2015 [66].

The first GDI generation was installed in wall guidance systems operating between 50 and 100 bars. These first injector designs were swirl-type with a single hole and a pin that moved inward to allow fuel to pass through. The working principle of these injectors was to set the fuel into a rotational motion at the exit nozzle through tangential holes or slots that impart a swirling motion to the liquid. The main feature of this type of injection is that the swirl motion creates a hollow conical jet [9]. This design had several drawbacks. Most importantly, the cone angles produced by different engine operating points and environmental conditions varied significantly, making calibration and correct design determination very difficult. Furthermore, using a camera to generate a swirl produces a lost volumetric efficiency, leading to the development of the slit injector [68]. The SG type of next-generation GDI injectors were required to improve the stratified charging system under full load conditions and increase the operating range. To fulfill the demands of these systems, piezoelectrically and electromagnetically operated multi-hole injectors have been designed and employed [29]. Piezoelectric injectors use the mechanical deformation of some ceramics under an electrical charge. Because the geometrical variation of piezoelectric materials is small, the injector is outfitted with a crystal stack, also known as a piezo stack [69] to achieve sufficient displacement. The description scheme for the piezoelectric GDI injector is shown in Figure 2.10

Because the needle comes out of the injector and allows the fuel to pass through, piezoelectric injectors open outwards. They form thin hollow conical jets with small radial openings. The outward aperture of these nozzles is helpful because it inhibits the creation of deposits that can disturb the flow, preventing the unwanted cocking phenomena that is typically related with other types of nozzles, such as multi-orifice nozzles. One of the most defining features of this type of injector is its great response and ability to provide exact little and consistent volumes of fuel, which makes it the perfect injector for multi-injection methods. Multi-hole solenoid injectors are more common than piezoelectric injectors. This is due to the sacrifice of reproducibility and precision, and thus economic [31, 70]. The injection rates of piezoelectric and magnetically driven injectors were studied and compared by Dahlander et al. [71]. For short excitation times, they concluded that piezoelectric injectors delivered fuel more consistently than solenoid injectors. At 15 bar, the piezo could accurately deliver small doses of less than 1 mg, whereas the electromagnet could only deliver robust amounts beginning at 1.8 mg. These disadvantages, however, can be addressed for the latest generation of GDI solenoids by adopting the ballistic regime, which requires a balance of accu-

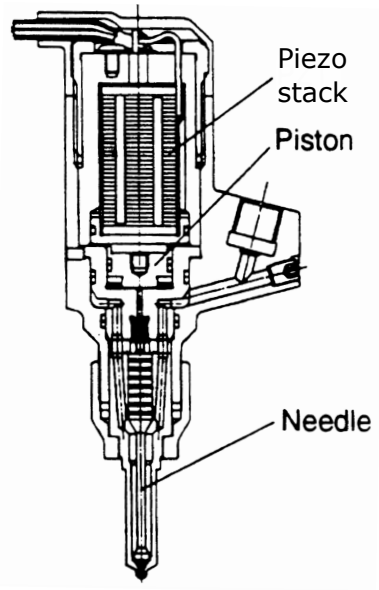

Figure 2.10: Piezoelectric GDI injector scheme. Adapted from [9].

rate fuel measuring at the injector side and an electronic control system to modify the injection signal and timing. [31, 67].

The penetration rate, a key variable that defines the mixing process, is a critical parameter of GDI injectors. Higher spray penetration speeds may improve the mixture, but they may also wet the cylinder walls, resulting in more soot and unburned HC. Mercedes [72] proposed the use of piezoelectric injectors to increase atomization (improve mixing) and reduce penetration in its BlueDirect technology. Nonetheless, the application was aimed at luxury car engines. The fuel spray for a standard piezo-driven outward opening nozzle, multi-hole, and pressure swirl injector is shown in Figure 2.11

Piezoelectric injectors are well suited for operating GDI engines in stratified charging and uniform modes due to their fast response, precise fuel metering, sediment resistance, and preferential penetration [39, 74, 75]. However, despite its obvious benefits, it is not always appropriate for real-world engine testing. Furthermore, injector temperature has a significant impact on performance, and different voltages are required to operate the piezo stack [76]. Under steady-state warm-up conditions, Smith et al. [77] investigated and compared the performance of an SG multi-hole solenoid driven and an outward-opening piezoelectric injector. In a simulated Federal Test Procedure (FTP) cycle, the multi-hole system emits 18% less carbon monoxide,

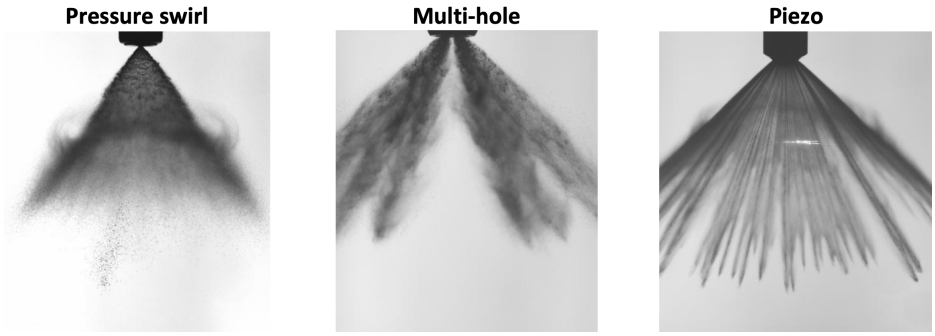

Figure 2.11: Spray patterns for various GDI injector types [69, 73].

15% less hydrocarbon, and, most importantly, 3% more fuel. Due to their lower cost, solenoid-driven multi-hole injectors are more commonly used than piezoelectric injectors. Nonetheless, they have another significant advantage: they offer better options for distributing fuel into the desired location, avoiding wall wetting and reaching the best location near the spark plug, as stated by [78]. Because of the versatility and cost-effectiveness of this type of injector in GDI engines, the amount of research and scientific efforts on these injectors has increased significantly [29, 31, 79, 80].

2.5.2 Multi-hole solenoid driven GDI injectors

As an existing evolution of the older PFI injector, the GDI injector was developed by taking over diesel injector technology to operate at significantly higher pressures [31]. The normal operating range for these injectors is 50-200 bar [14, 58, 59], but in the market, there are several designs capable of operating at 350 bar [61, 67], 400 bar [81], and 500-800 bar of injection pressure [62, 66, 82].

The cross-section of a commonly used Bosh GDI solenoid multi-hole injector is depicted in Figure 2.12. Other manufacturers, however, employ similar structures and techniques. Fuel enters the system through the inlet (1), which is linked to the valve seat (fuel pressure is the same). At rest, the nozzle orifices are covered by a ball at the needle tip. The coil is energized by current provided by an electrical connection, creating a magnetic field that forces the needle up. Eventually, the needle is brought back to its initial position by a spring, thus sealing the valve.

The injectors used in this work are a six-hole solenoid injector manufactured by Continental and the well-known Spray G of the ECN group. Figure 2.13 depicts a close-up of the injector nozzle in comparison to the ECN

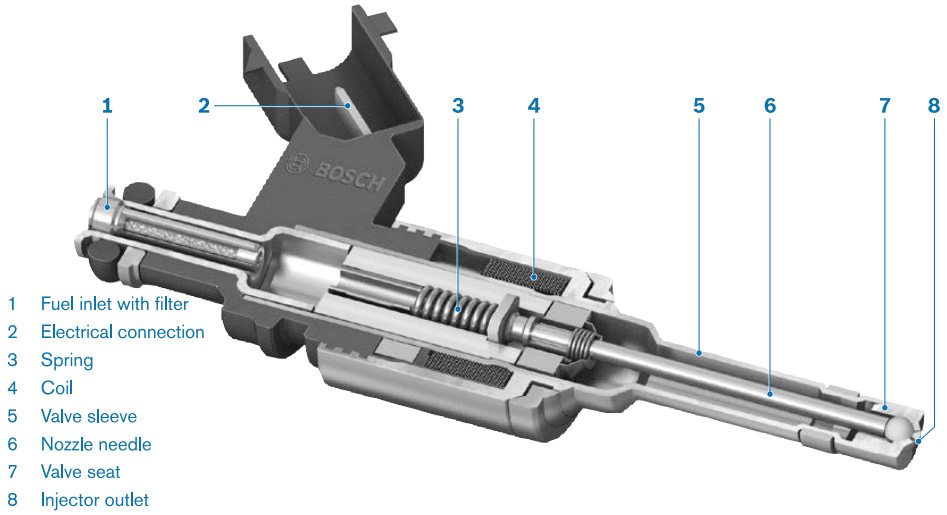

Figure 2.12: Cross-section of a Bosch HDEV5 high-pressure injector. Adapted from [14].

group GDI injector, the Spray G. On the left the Spray G nozzle with eight straight orifices constructed in a stepped shape, commonly known as a "counterbore" can be depicted. The holes are bored and spaced evenly around the injector axis into hemispherical ridges that provide the proper hole angle and spacing. The Continental nozzle has six straight orifices on the right. One of the most noticeable differences between these and standard diesel injectors is the close spacing of the holes. This is because of the large diameter of the hole and the small angle between the hole and the axis of the injector.

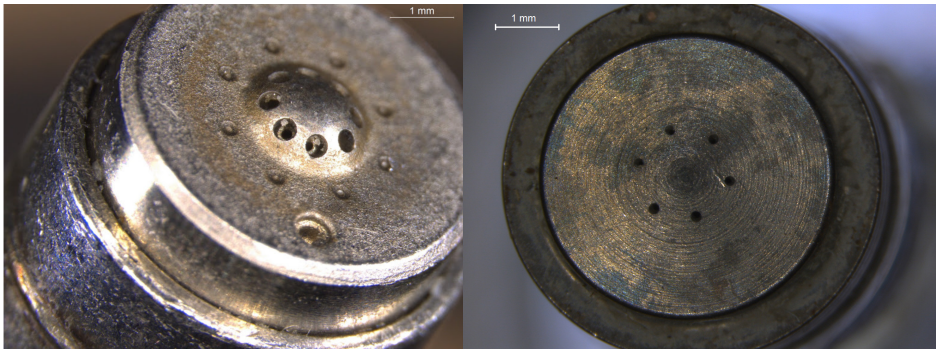

Figure 2.13: Close-up of two kinds of injector nozzles. The Spray G from ECN (left) [23], and the manufactured by Continental (right).

These two injectors are examples of the combinations and versatility of multi-orifice solenoid-controlled injectors. Due to the free placement of the orifice, the nozzle can be configured to avoid collisions with walls or valves and optimize the mixture when the injector is positioned in the combustion chamber. The SG injector can be mounted centrally or on the side of the top of the cylinder (usually on the intake port side). The injectors investigated are examples of centrally mounted injectors. Another possible variable that controls fuel atomization is the diameter of each orifice, as shown in Figure 2.14. Individual spray hole size optimization improves fuel distribution and lowers soot emissions (prevents wall wetting). This does not, however, apply to the injector in this work, which has the same orifice diameter.

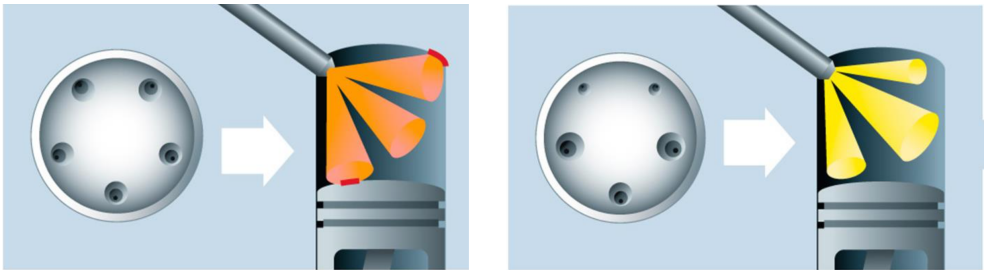

Figure 2.14: Schematic of the diameter and drill angle effect over the wall wetting. Source Bosch [14]

CFD simulation and optimization tools are used in works such as Rivera et al. [79] and Yi et al. [80] to select the best hole placement and spray pattern to improve mixing and prevent wall wetting. Injectors with a limited number of holes are commonly used in research. This is due to the ease with which the effects of pressure, fuel, or geometry can be isolated and studied (experimentally or computationally) [81, 83, 84]. Nevertheless, in real-world applications, injectors typically have six or more holes to provide the required fuel quantity in a limited amount of time and disperse the fuel within the combustion chamber.

Moon et al. [85] describes a study that used ultra-fast X-rays to investigate the effects of nozzle hole number and length on spray formation for multi-hole GDI injectors with 2-hole and 10-hole configurations. They came to the conclusion that increasing the number of holes reduces radial and axial flow velocities, resulting in less flow breakup and atomization. Because the needle lift in these injectors is a tenth of a micron, it is much smaller than the orifice size. A minor needle lift both accelerates and restricts fuel flow upstream of the sac. This interferes with the release of fuel from the holes, resulting in

instability and turbulence in the fuel spray. On the one hand, the turbulence caused by the needle lift can benefit in atomization, but the pressure drop in the bag caused by multiple holes slows the spray and brake speed. As a result, there is a trade-off between the number of holes required in the nozzle and the displacement of the needle, and optimizing it is difficult given the complexity of the internal flow.

The length (L) and diameter (D), which are usually dictated by the L/D ratio, are important parameters to consider when designing an orifice. A small L/D is usually preferred because it increases the spray angle and jet velocity, atomizes into smaller droplets, and shortens the braking length [86]. Befrui et al. [87] calculated Volume of Fluid Large Eddy Simulation (VOF-LES) volumes using a single-hole nozzle geometry and discovered that the flow characteristics of the GDI holes differed from diesel injectors, owing to the short L/D ratio. Furthermore, nozzles with L/D ratios ranging from 0.8 to 1.5 exhibited hydraulic flip, a cavitation-related phenomenon that occurs when cavitation bubbles propagate beyond the nozzle area and mix with the surrounding environment. Ambient conditions, which are typically higher than the fuel vapor saturation pressure, draw ambient air into the nozzle region between the liquid core and the orifice wall. This significantly reduces liquid-wall interaction and increases the instability of the liquid-air interface [88]. The flow of two nozzles with L/D ratios of 0.5 and 1.1 was simulated by Shost et al. [89], who discovered that the shorter the hole, the larger the plume cone angle. The effect of the L/D ratio between L/D=3 and L/D=1.1 nozzles was also studied by Shost [90]. LES simulations were used to make the comparison, which revealed a significant difference in the runoff coefficient, which was 0.8 for the long nozzle and 0.6 for the short nozzle. Moon et al. [85] investigated the effect of orifice length in various multi-hole GDI nozzles and discovered that shorter holes increased the axial and radial flow velocities at the nozzle exit as well as the void fraction. These speed increases resulted in shorter breakup lengths, more turbulence, and decreased jet penetration in the plume axis direction. The results corroborate the conclusions of the LES simulation comparing nozzle lengths from Befrui et al. [87].

Injector designers have used various methods to create injector holes. Some of them, such as Spray G Delphi, have counterbore or stepped holes. This is the increase in orifice diameter in the nozzle outer portion. The outer diameter is part of the counterbore, and the geometry is barely visible in the Figure 2.13 (left). Counterbores are the result of the design process attempting to reduce the L/D ratio. Because GDI nozzles must withstand high working pressures during injection, using an L/D=1 geometry while keeping the number and size of holes the same will not tolerate the nozzle mechanical loads. A stepped

hole offers the required L/D ratio while preserving injector integrity. In addition to keeping thickness for structural stability, the counterbore protects the inner hole exit from the elevate temperatures of the combustion chamber. The tendency for deposits to build up at the nozzle exit is a disadvantage of this type of geometry. As a result, this must be considered in hole design. Otherwise, it may affect spray morphology as well as combustion and emission performance [90].

Shost [90] investigated the effect of counterbore using VOF-LES simulations. In this study, two identical single-hole nozzles were used. Both nozzles internal nozzle flow and plume angle were found to be identical. In the counterbore region, however, fuel spray turbulence was observed to propagate into the adjacent air. This is most likely due to a combination of pressure perturbations and air movement caused by atomization. Additional visualization experiments using another of the 3-hole nozzles and VOF-LES simulations revealed that the spray cone angle was reduced due to the effect of the counterbore [81]. Payri et al. [91] investigated the stepped hole effect in diesel injectors experimentally and reported that the counterbore increased the cone angle and decreased the jet penetration velocity, which was consistent with the GDI results. As previously stated, careful counterbore design is required to avoid deposits, but it can also cause droplets to form at the nozzle tip, affecting emissions performance [67]. The current stepped holes on the Spray G injector are relatively small in order to accommodate all of the holes. Internal nozzle flow simulations revealed a strong interaction between the flow and the stepped hole walls [92]. Another geometrical variable is nozzle conicity, which is determined by whether the nozzle orifices are straight (cylindrical) or tapered (conical). Straight nozzles are prone to cavitation due to flow separation at the inner edge, resulting in lower discharge coefficients, according to the extensive research in diesel injectors. Nonetheless, cavitation aids in the removal of deposits from orifices and facilitates atomization [93]. GDI nozzle holes, on the other hand, are generally straight and help to break up the jet. Befrui et al. [87] and Shost [90] by comparing straight and conical orifices, the effect of conicity on GDI nozzle performance was investigated. Previously observed trends in diesel nozzles (tapered holes reduce cavitation and flow separation) were confirmed. Also, they discovered that, for GDI nozzles, the conical nozzles have significantly higher discharge coefficients than straight nozzles ($C_d \approx 0.9$ vs $C_d \approx 0.6$). Despite this, almost no flow separation resulted in less instability and unacceptably long break-up lengths.

As reported previously, nozzle geometry has a significant impact on the development and behavior of fuel flow in and out of the injector. As a result, reliable information about the final nozzle geometry is required to properly

investigate nozzle performance, particularly for CFD analysis. There are several methods for determining nozzle geometry. To register the counterbore and inner hole diameters, aperture measurements can be taken from the outside using an optical microscope. However, determining the diameter rather than the projection is more difficult. Another method presented by Macian et al. [94] is to create a negative of the aperture using a silicon mold, which is then coated with gold and viewed with a scanning electron microscope (SEM). This methodology was applied to the Spray G nozzle and yielded detailed geometries [57]. Nonetheless, evaluating this procedure for injectors where the nozzle cannot be removed is difficult. The only way to proceed is to remove the injector nozzle. Furthermore, finished silicone molds are frequently difficult to coat evenly, resulting in defects and errors in his later SEM images.

X-ray tomography is a third method for determining the shape of the nozzle. Manin et al. [95] obtained the nozzle geometry from the same Spray G injector using a commercial X-ray source. Acceptable resolution was reported in areas where the counterbore metal was not thick (low amount of metal passed through by X-rays). Nonetheless, there was little contrast between the nozzle seat and the inner hole (a high amount of metal passed through). Matusik et al. [96] used X-rays with a more intense and continuous beam at Argonne National Laboratory Advance photon source facility. These high-energy X-rays enabled high-resolution tomography of the same injector, resulting in increased image contrast and pixel resolution, even in internal nozzle areas like the needle seat.

The nozzle model is simpler to obtain because it has a greater metal-to-air distinction and a pixel resolution of 1.17 μm, as well as the surface imperfections shown in Figure 2.15. The same beam source was used by Strek et al. [97] to measure nearby nozzle flow density predictions and compare them to Euler internal simulations. Matusik et al. [98] used the same methodology to evaluate the effect of small geometric variations in the main nozzle dimensions on the time-resolved predicted injector density of an 8-hole Spray G nozzle.

2.6 Spray-wall interaction phenomenon

Free-jet injection and combustion analysis have been extremely helpful in comprehending how fuel injection systems perform in engine applications and developing accurate empirical and CFD models. It is, however, a simplified model of the injection process. Nowadays, it is even more critical because downsizing is popular, with the goal of producing smaller engines. Spray-wall interaction (SWI) is critical in the atomization, mixing, and combustion be-

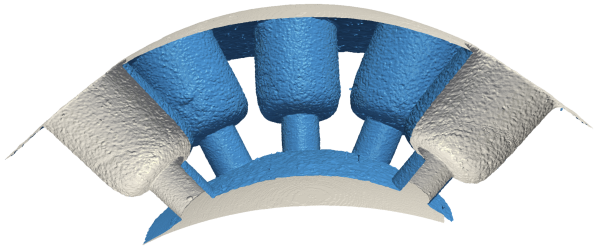

Figure 2.15: Internal geometry of the Spray G nozzle as an isosurface. [96].

havior of fuels, as well as the formation of pollutant emissions. In first place, fuel impingement and buildup on the cylinder wall lead to the creation of a fuel film, that worsens combustion and increases the production of carbon monoxide and unburned hydrocarbons, as well as an increase in energy loss due to heat transfer with the surroundings. The impingement of the spray on the surface. In second place, results in secondary atomization caused by the impingement, this also exposes the spray surface to the chamber gases, enhancing the air-fuel mixture and, ultimately, combustion. These elusive effects have an impact on internal combustion engine performance as well as other engineering applications such as spray-induced cooling, painting, and solid deposit control. As a result, spray wall interactions are an active area of research.

The dimensionless Weber number $We = \rho u^2 D \sigma^{-1}$ is an important way to understand the probability of a spray forming a fuel film on the piston chamber walls or facilitating droplet breakup to enhance evaporation. Where ρ is the density of the droplet, u is the impact velocity, D is the characteristic diameter, and σ is the surface tension. Several authors have proposed models of possible impact behavior regimes based on the study of impingement drops [99, 100]. Figure 2.16 shows maps of various droplet wall impingement regimes, based on the map used by Bai and Gosman [101]. Wall temperature influences the occurrence of specific regimes in addition to the effect of *We*. The boiling point of the liquid is represented by T_b, and the temperature that defines the adhesion phenomenon at low impact energy is represented by T_{PA}. The Nakayama temperature at which the droplet reaches its maximum evaporation rate is denoted by T_N. T_{PR} is the temperature above which the bounces phenomenon occurs under low-energy impact conditions, and T_{leid} is the temperature at which a vapor layer appears between the drop and the wall.

Even schemes like Figure 2.16 provide a qualitative explanation of *We* and heat-induced mechanisms a profound definition of the different regimes

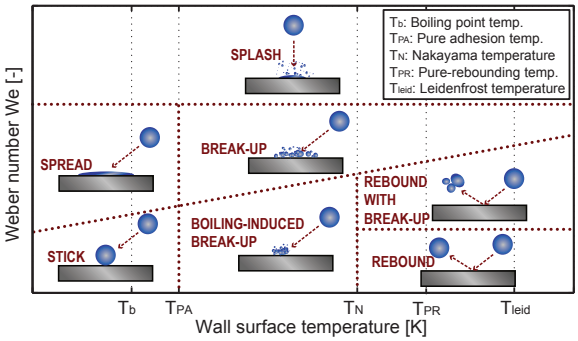

Figure 2.16: Diagram of the different drop-wall impact regimes proposed by Bai and Gosman [101].

is difficult because each one has to deal with the phenomena observed in different schemes due to the complexity of adding a surface temperature. Although these spray droplet collision heat transfer mechanisms are universal (e.g., Panão and Moreira [102] and Toda [103]), collision conditions affect the critical points of the boiling curves. Extensive research on boundary temperatures has been conducted over the last decade, highlighting their influencing parameters and yielding valuable and interesting but not always conclusive results. Because of variations in convection behavior, when the impact velocity increases, the Leidenfrost temperature can either increase, as carried out by various authors as Chaves et al. [104] and Yao and Cai [105], or drop, as conducted by [106]. Likewise, several studies [107, 108] describes that droplet diameter has no effect on boundary temperatures, whilst Shi et al. [109] observed an increase in T_{leid} with droplet size, which is explained by the force balance between the dynamic pressure of droplets and the vapor pressure of the vapor layer. It is not possible to use similarity laws between the heat transfer over the entire impacted area and a single model because of the uneven distribution of liquid mass above the impacted area [102].

There are currently few studies reported in the literature [110–112], and they are still in their early stages, indicating that multi-droplet interaction phenomena are one of the most critical open research topics. However, a precise integration of the interaction phenomena of droplets impinging on walls and spray impingement with a wall is far from successful, allowing for more realistic approaches such as impinging spray characterization to move forward.

To meet the growing demand for cleaner engines, we must expand our understanding of the free jet and consider its interaction with the combustion

chamber boundaries. Similarly, spray-wall interactions are used to generate approximate approaches for droplet-wall impact analysis. Spray-wall contact in particular has a significant impact on powertrain exhaust emissions and engine performance [113–118]. In a PFI gasoline engine (port fuel injection), full vaporization within the port is not achieved, and droplets are deposited on the chamber walls. This phenomenon also occurs during a cold start of a direct injection gasoline engine. Several studies have attempted to define the macroscopic properties of the colliding spray and its various regions, with varying degrees of success. In Figure 2.17, some conceptual model adaptations of [113, 119–121] are shown.

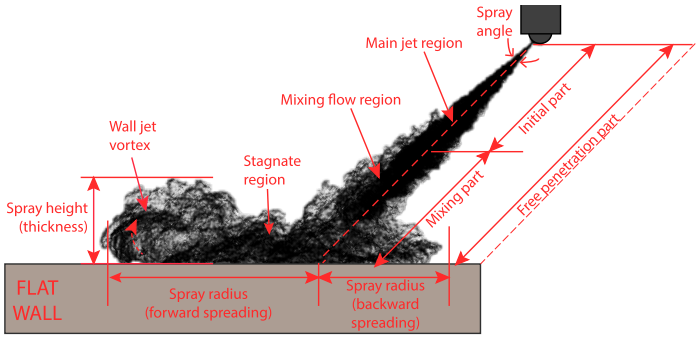

Figure 2.17: Scheme of an impinging spray with flat wall.

Montanaro et al. [122] investigated the effects of injection pressure and wall temperature in a GDI under non-reactive conditions, they perform a single-hole injector visualization of liquid and vapor phases using optical techniques. The authors discovered that at the same pressure, the wall temperature affected the radial spread, but they could not find a direct correlation between the maximum thickness of the spray along the wall. When the wall temperature is fixed, however, the rates of linear spread growth with injection pressure and spray spread are comparable. Yu et al. [123, 124] examined several fuels and injection procedures and discovered that gas entrainment and spray momentum had a substantial effect over the wall film appearance, and spray spreading. On the other hand, the viscosity and surface tension had a direct effect on spray width along the wall. Montorsi et al. [125] employed PDA (Phase Doppler Anemometry) and high-speed imaging methods to set the chamber to environment comparable to those seen during the compression stroke of heavy-duty diesel engines. The heat flux through the wall was computed in his work using a 1-D transient heat model, as well as simulations on

STAR-CD and KIVA-3V, leading to the conclusion that SWI is susceptible to ambient pressure and wall temperature, changing both heat-release rate and emission production.

Meingast et al. [115] used a similar experimental approach for a heated wall, improving overall gas-liquid mixing and lowering the wall heat flux when conditions like higher injection pressures and wall temperatures as well as larger distances between the injector tip and the wall are employed; these factors promote lesser droplet sizes when impingement occurs. Zhu et al. [126], carried out an investigation on non-vaporizing sprays at high-density and high-injection pressures with only an impingement angle of 60°, in which the wall-impinged spreading spray evolution is divided into four sections: the rapidly decelerated stage, the slowly decreasing rate stage, the nearly steady rate stage, and the growing termination stage. Bruneaux [127] used LIEF (Laser Induced Exciplex Fluorescence) to analyze the gas-fuel mixing process, contrasting both perpendicular spray-wall collision and free-jet scenarios. The aforementioned study demonstrates that mixing is reduced when compared to the free-spray conditions at the center of the impingement region close to the spray axis, whereas mixing is enhanced again in the region in which the spray moves over the wall. The contribution of both effects fluctuates with the injection pressure due to impingement momentum and turbulence alteration. Zhao et al. [128] investigated the spray-wall interaction with the use of a constant volume combustor as well as a RANS-based simulation approach to obtain an increase in spray momentum at the impingement wall when the ambient density was low or the injection pressure was high.

Several works as the one of Tang et al. [129] and Shi et al. [130] studied the spray-wall interaction in an optical engine using the Planar laser-induced fluorescence (PLIF) technique. Maliha et al. [131] characterize secondary droplets in size, velocity, and composition using the PLIF technique. Steinberg et al. [132] analyzed the macroscopic and microscopic spray behavior when impacting step geometries through experimental and numerical approaches. Wu et al. [133] performed a numerical study on fuel film emissions formations during cold-start in a diesel engine using an improved spray-wall impingement model. Roque et al. [134] found that the vaporization is not considerably affected by the injection pressure inside the impingement region at a wall temperature of 80 °C. Roque et al. [135] studied the characteristics of the liquid film generated using a multicomponent fuel, measuring the impact of the wall temperature changes over the soot generation. Shway et al. [136] used an absortion of UV and visible light diagnostic technique to analyze the thickness of combusting fuel films.

As mentioned in the first paragraph of this section, spray cooling is also an interesting field where the heat transfer between a spray and a heated surface is analyzed. This opens an opportunity to mix both research fields to explain the considerable surface heat flux and convective coefficients magnitudes that can be achieved in spray cooling systems. Works as Freund et al. [137], Cebo-Rudnicka et al. [138], and Cheng et al. [139] present a wide range of magnitudes of the heat flux that can be obtained in those systems and that are comparable with the magnitudes obtained in the present thesis. In those works the infrared thermography technique was applied to measure the heat transfer and heat convective coefficient.

All the previously mentioned works provide fundamental knowledge to understand some aspects of the spray-wall interaction phenomenon using different optical techniques and computational models. This thesis aims to combine macroscopic spray characteristics and surface heat flux computation of SWI when impacting both isothermal and heated walls to understand its effect on the spray characteristics and heat flux magnitudes.

References

[1] IEA. *A technology roadmap: Electric and plug-in hybrid electric vehicles*. Tech. rep. June. International Energy Agency, 2011, pp. 3471–3473.

[2] "Global CO2 emissions from transport by subsector, 2000-2030". In: *IEA* (2021).

[3] Starikovskiy, Andrey and Aleksandrov, Nickolay. "Plasma-assisted ignition and combustion". In: *Progress in Energy and Combustion Science* 39.1 (2013), pp. 61–110. DOI: 10.1016/j.pecs.2012.05.003.

[4] Wang, Zhongli et al. "Experimental Study of Influence on Microwave Plasma Ignition Combustion Performance of Pulse Microwave Signals". In: *IEEE Access* 7 (2019), pp. 23951–23958. DOI: 10.1109/ACCESS.2019.2899911.

[5] Pavel, Nicolaie et al. "Laser ignition - Spark plug development and application in reciprocating engines". In: *Progress in Quantum Electronics* 58.April (2018), pp. 1–32. DOI: 10.1016/j.pquantelec.2018.04.001.

[6] Chehroudi, Bruce. "Laser Ignition For Combustion Engines". In: *Engineering* October (2004), pp. 1–5. DOI: 10.13140/2.1.1845.1206.

[7] Payri, Francisco and Desantes, Jose Maria. *Motores de combustion interna alternativos*. Editorial Universitat Politecnica de Valencia, 2011.

[8] Spicher, U, Reissing, J, Kech, J M, and Gindele, J. "Gasoline Direct Injection (GDI) Engines - Development Potentialities". In: *SAE Technical Papers*. 724. 1999. DOI: 10.4271/1999-01-2938.

[9] Zhao, F, Lai, M.-C, and Harrington, D L. "Automotive spark-ignited direct-injection gasoline engines". In: *Progress in Energy and Combustion Science* 25.5 (1999), pp. 437–562. DOI: 10.1016/S0360-1285(99)00004-0.

[10] Halderman, James D. *Automotive Fuel and Emissions control systems*. 2012.

[11] Bahattin, Mustafa and Ozdaly, Bulent. "Gasoline Direct Injection". In: *Fuel Injection*. Sciyo, 2010. DOI: 10.5772/9693.

[12] Pham, P X, Vo, D Q, and Jazar, R N. "Development of fuel metering techniques for spark ignition engines". In: *Fuel* 206 (2017), pp. 701–715. DOI: 10.1016/j.fuel.2017.06.043.

[13] Ingraham, Joseph C. *Automobiles: Races; Everybody Manages to Win Something At the Daytona Beach Contests*. 1957.

[14] Konrad Reif, ed. *Gasoline Engine Management*. Wiesbaden: Springer Fachmedien Wiesbaden, 2015. DOI: 10.1007/978-3-658-03964-6.

[15] Saliba, Georges et al. "Comparison of Gasoline Direct-Injection (GDI) and Port Fuel Injection (PFI) Vehicle Emissions: Emission Certification Standards, Cold-Start, Secondary Organic Aerosol Formation Potential, and Potential Climate Impacts". In: *Environmental Science and Technology* (2017). DOI: 10.1021/acs.est.6b06509.

[16] He, Lv, Jingyuan, Li, Xiumin, Yu, Mengliang, Li, and Tian, Yang. "Numerical study on combustion and emission characteristics of a PFI gasoline engine with hydrogen direct-injection". In: *Energy Procedia* 158 (2019), pp. 1449–1454. DOI: 10.1016/j.egypro.2019.01.348.

[17] Ma, Dong Shuo and Sun, Z Y. "Progress on the studies about NOx emission in PFI-H2ICE". In: *International Journal of Hydrogen Energy* 45.17 (2020), pp. 10580–10591. DOI: 10.1016/j.ijhydene.2019.11.065.

[18] McCaffery, Cavan, Durbin, Thomas D, Johnson, Kent C, and Karavalakis, Georgios. "The effect of ethanol and iso-butanol blends on polycyclic aromatic hydrocarbon (PAH) emissions from PFI and GDI vehicles". In: *Atmospheric Pollution Research* August (2020), p. 1. DOI: 10.1016/j.apr.2020.08.024.

[19] Chen, Longfei, Liang, Zhirong, Zhang, Xin, and Shuai, Shijin. "Characterizing particulate matter emissions from GDI and PFI vehicles under transient and cold start conditions". In: *Fuel* 189 (2017), pp. 131–140. DOI: 10.1016/j.fuel.2016.10.055.

[20] Zhu, Rencheng et al. "Tailpipe emissions from gasoline direct injection (GDI) and port fuel injection (PFI) vehicles at both low and high ambient temperatures". In: *Environmental Pollution* 216 (2016), pp. 223–234. DOI: 10.1016/j.envpol.2016.05.066.

[21] Yang, Zhengjun et al. "Real driving particle number (PN) emissions from China-6 compliant PFI and GDI hybrid electrical vehicles". In: *Atmospheric Environment* 199.September 2018 (2019), pp. 70–79. DOI: 10.1016/j.atmosenv.2018.11.037.

[22] Li, Yaoting et al. "A comprehensive experimental investigation on the PFI spray impingement: Effect of impingement geometry, cross-flow and wall temperature". In: *Applied Thermal Engineering* 159.May (2019), p. 113848. DOI: 10.1016/j.applthermaleng.2019.113848.

[23] Vaquerizo, Daniel. "Study on Advanced Spray-Guided Gasoline Direct Injection Systems". PhD thesis. Universitat Politècnica de València, 2017.

[24] Chincholkar, S P and Suryawanshi, J G. "Gasoline Direct Injection: An Efficient Technology". In: *Energy Procedia* 90.December 2015 (2016), pp. 666–672. DOI: 10.1016/j.egypro.2016.11.235.

[25] Shuai, Shijin, Ma, Xiao, Li, Yanfei, Qi, Yunliang, and Xu, Hongming. "Recent Progress in Automotive Gasoline Direct Injection Engine Technology". In: *Automotive Innovation* 1.2 (2018), pp. 95–113. DOI: 10.1007/s42154-018-0020-1.

[26] Van Basshuysen, Richard and Spicher, Ulrich. *Gasoline engine with direct injection : processes, systems, development, potential*. Ed. by Richard Van Basshuysen and Ulrich Spicher. Wiesbaden, 2009.

[27] Iwamoto, Y, Noma, K, Nakayama, O, Yamauchi, T, and Ando, H. "Development of Gasoline Direct Injection Engine". In: *SAE Technical Papers*. 412. 1997. DOI: 10.4271/970541.

[28] Harada, Jun, Tomita, Tsutomu, Mizuno, Hiroyuki, Mashiki, Zenichiro, and Ito, Yasushi. "Development of direct injection gasoline engine". In: *SAE Technical Papers* 412 (1997). DOI: 10.4271/970540.

[29] Zhao, Hua. *Advanced direct injection combustion engine technologies and development*. Woodhead Publishing Limited, 2010. DOI: 10.1533/9781845697327.

[30] Erjavec, Jack. *Automotive Technology : A systems approach*. 5th. Cengage Learning, Inc, 2009, p. 1665.

[31] Fansler, Todd D and Parrish, Scott E. "Spray measurement technology: a review". In: *Measurement Science and Technology* 26.1 (2015), p. 12002. DOI: 10.1088/0957-0233/26/1/012002.

[32] Zhuang, Yuan et al. "Investigation of water injection benefits on downsized boosted direct injection spark ignition engine". In: *Fuel* 264.October 2019 (2020). DOI: 10.1016/j.fuel.2019.116765.

[33] Berni, Fabio, Breda, Sebastiano, Lugli, Mattia, and Cantore, Giuseppe. "A numerical investigation on the potentials of water injection to increase knock resistance and reduce fuel consumption in highly downsized GDI engines". In: *Energy Procedia* 81 (2015), pp. 826–835. DOI: 10.1016/j.egypro.2015.12.091.

[34] Cho, Jaeho, Kim, Kangjin, Baek, Sungha, Myung, Cha Lee, and Park, Simsoo. "Abatement potential analysis on CO2 and size-resolved particle emissions from a downsized LPG direct injection engine for passenger car". In: *Atmospheric Pollution Research* 10.6 (2019), pp. 1711–1722. DOI: 10.1016/j.apr.2019.07.002.

[35] Cavicchi, Andrea, Postrioti, Lucio, and Scarponi, Edoardo. "Hydraulic analysis of a GDI injector operation with close multi-injection strategies". In: *Fuel* 235.July 2017 (2019), pp. 1114–1122. DOI: 10.1016/j.fuel.2018.08.089.

[36] Cavicchi, Andrea and Postrioti, Lucio. "Simultaneous needle lift and injection rate measurement for GDI fuel injectors by laser Doppler vibrometry and Zeuch method". In: *Fuel* 285.August 2020 (2021), p. 119021. DOI: 10.1016/j.fuel.2020.119021.

[37] Cavicchi, Andrea, Postrioti, Lucio, Berni, Fabio, Fontanesi, Stefano, and Di Gioia, Rita. "Evaluation of hole-specific injection rate based on momentum flux measurement in GDI systems". In: *Fuel* 263.June 2019 (2020). DOI: 10.1016/j.fuel.2019.116657.

[38] Hentschel, Werner. "Optical Diagnostics Combustion Process Development DI Gasoline Engines". In: 28 (2000), pp. 1119–1135.

[39] Costa, M et al. "Split injection in a homogeneous stratified gasoline direct injection engine for high combustion efficiency and low pollutants emission". In: *Energy* 117.2016 (2016), pp. 405–415. DOI: 10.1016/j.energy.2016.03.065.

[40] Hentschel, W et al. “Optical Diagnostics and CFD-Simulations to Support the Combustion Process Development of the Volkswagen FSI®Direct-Injection Gasoline Engine”. In: *SAE Technical Papers*. 724. 2001. DOI: 10.4271/2001-01-3648.

[41] Zeng, Wei, Sjöberg, Magnus, Reuss, David L, and Hu, Zongjie. “The role of spray-enhanced swirl flow for combustion stabilization in a stratified-charge DISI engine”. In: *Combustion and Flame* 168.x (2016), pp. 166–185. DOI: 10.1016/j.combustflame.2016.03.015.

[42] Zeng, Wei and Sjöberg, Magnus. “Utilizing boost and double injections for enhanced stratified-charge direct-injection spark-ignition engine operation with gasoline and E30 fuels”. In: *International Journal of Engine Research* 18.1-2 (2017), pp. 131–142. DOI: 10.1177/1468087416685512.

[43] Moon, Seoksu, Huang, Weidi, and Wang, Jin. “Spray formation mechanism of diverging-tapered-hole GDI injector and its potentials for GDI engine applications”. In: *Fuel* 270.March (2020), p. 117519. DOI: 10.1016/j.fuel.2020.117519.

[44] Lee, Ziyoung, Kim, Taehoon, Park, Sungwook, and Park, Suhan. “Review on spray, combustion, and emission characteristics of recent developed direct-injection spark ignition (DISI) engine system with multihole type injector”. In: *Fuel* 259.July 2019 (2020), p. 116209. DOI: 10.1016/j.fuel.2019.116209.

[45] Duan, Xiongbo et al. “Quantitative investigation the influences of the injection timing under single and double injection strategies on performance, combustion and emissions characteristics of a GDI SI engine fueled with gasoline/ethanol blend”. In: *Fuel* 260.August 2019 (2020), p. 116363. DOI: 10.1016/j.fuel.2019.116363.

[46] Cho, Jungkeun and Song, Soonho. “Prediction of hydrogen-added combustion process in T-GDI engine using artificial neural network”. In: *Applied Thermal Engineering* 181.May (2020), p. 115974. DOI: 10.1016/j.applthermaleng.2020.115974.

[47] Zhou, Jianwei et al. “Characteristics of near-nozzle spray development from a fouled GDI injector”. In: *Fuel* 219.92 (2018), pp. 17–29. DOI: 10.1016/j.fuel.2018.01.070.

[48] Banerjee, R and Kumar, Santhosh. “Numerical investigation of stratified air/fuel preparation in a GDI engine”. In: *Applied Thermal Engineering* 104 (2016), pp. 414–428. DOI: 10.1016/j.applthermaleng.2016.05.050.

[49] Su, Yu Hsuan and Kuo, Ting Fu. "CFD-assisted analysis of the characteristics of stratified-charge combustion inside a wall-guided gasoline direct injection engine". In: *Energy* 175.x (2019), pp. 151–164. DOI: 10.1016/j.energy.2019.03.031.

[50] Zheng, Zhaolei, Tian, Xuefeng, and Zhang, Xiaoyu. "Effects of split injection proportion and the second injection time on the mixture formation in a GDI engine under catalyst heating mode using stratified charge strategy". In: *Applied Thermal Engineering* 84 (2015), pp. 237–245. DOI: 10.1016/j.applthermaleng.2015.03.041.

[51] Feng, Shuang et al. "Influence of stratified charge organized by double injection strategy on combustion and emissions on an EGR diluted GDI engine". In: *Applied Thermal Engineering* 158.May (2019), p. 113803. DOI: 10.1016/j.applthermaleng.2019.113803.

[52] Gong, Changming, Yi, Lin, Zhang, Zilei, Sun, Jingzhen, and Liu, Fenghua. "Assessment of ultra-lean burn characteristics for a stratified-charge direct-injection spark-ignition methanol engine under different high compression ratios". In: *Applied Energy* 261.January (2020), p. 114478. DOI: 10.1016/j.apenergy.2019.114478.

[53] Jeon, J, Bock, N, and Northrop, W F. "In-cylinder flame luminosity measured from a stratified lean gasoline direct injection engine". In: *Results in Engineering* 1.January (2019), p. 100005. DOI: 10.1016/j.rineng.2019.100005.

[54] Costa, M, Catapano, F, Sementa, P, Sorge, U, and Vaglieco, B M. "Mixture preparation and combustion in a GDI engine under stoichiometric or lean charge: an experimental and numerical study on an optically accessible engine". In: *Applied Energy* 180 (2016), pp. 86–103. DOI: 10.1016/j.apenergy.2016.07.089.

[55] Jeon, Joonho. "Spatiotemporal flame propagations, combustion and solid particle emissions from lean and stoichiometric gasoline direct injection engine operation". In: *Energy* 210 (2020), p. 118652. DOI: 10.1016/j.energy.2020.118652.

[56] Yu, Xiumin et al. "Investigation of combustion and emissions of an SI engine with ethanol port injection and gasoline direct injection under lean burn conditions". In: *Energy* 189 (2019), p. 116231. DOI: 10.1016/j.energy.2019.116231.

[57] Payri, Raul, Gimeno, Jaime, Marti-Aldaravi, Pedro, and Vaquerizo, Daniel. "Momentum Flux Measurements on an ECN GDi Injector". In: *SAE Technical Paper 2015-01-1893*. 2015. DOI: 10.4271/2015-01-1893.

[58] Payri, Raul, Gimeno, Jaime, Martí-Aldaraví, Pedro, and Vaquerizo, Daniel. "Internal flow characterization on an ECN GDi injector". In: *Atomization and Sprays* 26.9 (2016), pp. 889–919. DOI: 10.1615/AtomizSpr.2015013930.

[59] Payri, Raul, Bracho, Gabriela, Gimeno, Jaime, and Bautista, Abian. "Rate of injection modelling for gasoline direct injectors". In: *Energy Conversion and Management* 166 (2018), pp. 424–432. DOI: 10.1016/j.enconman.2018.04.041.

[60] Parotto, Marco, Sgatti, Stefano, and Sensi, Fabio. "Advanced GDI Injector Control with Extended Dynamic Range". In: *SAE Technical Papers*. Vol. 2. 2013. DOI: 10.4271/2013-01-0258.

[61] Johansson, Anders N, Hemdal, Stina, and Dahlander, Petter. "Reduction of Soot Formation in an Optical Single-Cylinder Gasoline Direct-Injected Engine Operated in Stratified Mode Using 350 Bar Fuel Injection Pressure, Dual-Coil and High-Frequency Ignition Systems". In: *SAE International Journal of Engines* 10.3 (2017), pp. 2017–9278. DOI: 10.4271/2017-01-9278.

[62] Hoffmann, Guy, Befrui, Bizhan, Berndorfer, Axel, Piock, Walter F, and Varble, Daniel L. "Fuel System Pressure Increase for Enhanced Performance of GDi Multi-Hole Injection Systems". In: *SAE International Journal of Engines* 7.1 (2014), pp. 1209–2014. DOI: 10.4271/2014-01-1209.

[63] Gomot, Dipl Baudouin and Hülser, Holger. "Delphi Technologies Next Generation GDi-System, improved Emissions and Efficiency with higher Pressure". In: *Internationales Wiener Motorensymposium* (2019), pp. 1–21.

[64] Granqvist, Peter. "High efficient SI-engine with ultra high injection pressure [Research @ Chalmers University]". In: October. Gothenburg, Sweden: Energirelaterad forskning 2017, 2017.

[65] Husted, Harry, Spegar, Timothy D, and Spakowski, Joseph. "The Effects of GDi Fuel Pressure on Fuel Economy". In: *SAE Technical Papers*. Vol. 1. 2014. DOI: 10.4271/2014-01-1438.

[66] Magneti Marelli. "Gasoline Direct Injection Technology advancements". In: *2015 SAE-China Congress & Exhibition*. Shanghai, China: Society of Automotive Engineers, 2015.

[67] Pauer, Thomas, Yilmaz, Hakan, Zumbrägel, Joachim, and Schünemann, Erik. "New Generation Bosch Gasoline Direct-injection Systems". In: *MTZ worldwide* 78.7-8 (2017), pp. 16–23. DOI: 10.1007/s38313-017-0053-6.

[68] Kanda, Mutsumi et al. "Application of a New Combustion Concept to Direct Injection Gasoline Engine". In: *SAE Technical Papers*. Vol. 2000. 724. 2000. DOI: 10.4271/2000-01-0531.

[69] Wood, Andrew. "Optical investigations of the sprays generated by gasoline multi-hole injectors under novel operating conditions". PhD thesis. Loughborough University, 2014.

[70] Wu, Zengyang, Wang, Libing, Badra, Jihad A, Roberts, William L, and Fang, Tiegang. "GDI fuel sprays of light naphtha, PRF95 and gasoline using a piezoelectric injector under different ambient pressures". In: *Fuel* 223.December 2017 (2018), pp. 294–311. DOI: 10.1016/j.fuel.2018.03.009.

[71] Dahlander, Petter, Iemmolo, Daniele, and Tong, Yifei. "Measurements of Time-Resolved Mass Injection Rates for a Multi-Hole and an Outward Opening Piezo GDI Injector". In: *SAE Technical Papers*. Vol. 2015-April. April. 2015. DOI: 10.4271/2015-01-0929.

[72] Vent, Guido and Enderle, Christian. "The new 2.0 l turbo engine from the Mercedes-Benz 4-cylinder engine family". In: *2nd Aachen Colloquium China* (2012).

[73] Wigley, G, Pitcher, G, Nuglisch, H, Helie, J, and Ladommatos, N. "Fuel Spray Formation and Gasoline Direct Injection". In: *8th AVL international symposium on combustion diagnostics*. 2008.

[74] Marchi, A, Nouri, J, Yan, Y, and Arcoumanis, C. "Spray stability of outwards opening pintle injectors for stratified direct injection spark ignition engine operation". In: *International Journal of Engine Research* 11.6 (2010). Ed. by Dinos Arcoumanis, pp. 413–437. DOI: 10.1243/14680874JER605.

[75] Zigan, L, Schmitz, I, Flügel, A, Wensing, M, and Leipertz, A. "Structure of evaporating single- and multicomponent fuel sprays for 2nd generation gasoline direct injection". In: *Fuel* 90.1 (2011), pp. 348–363. DOI: 10.1016/j.fuel.2010.08.001.

[76] Payri, Raul, Gimeno, Jaime, Mata, Carmen, and Viera, Alberto. "Rate of injection measurements of a direct-acting piezoelectric injector for different operating temperatures". In: *Energy Conversion and Management* 154.October (2017), pp. 387–393. DOI: 10.1016/j.enconman.2017.11.029.

[77] Smith, James, Szekely Jr, Gerald, Solomon, Arun, and Parrish, Scott. "A Comparison of Spray-Guided Stratified-Charge Combustion Performance with Outwardly-Opening Piezo and Multi-Hole Solenoid Injectors". In: *SAE International Journal of Engines* 4.1 (2011), pp. 1217–2011. DOI: 10.4271/2011-01-1217.

[78] Kwak, H C et al. "The New V6 3.5L Turbo GDI Engine from Hyundai-Kia". In: *27th Aachen Colloquium Automobile and Engine Technology*. Aachen, 2018.

[79] Rivera, Edwin A, Mastro, Noreen, Zizelman, James, Kirwan, John, and Ooyama, Robert. "Development of Injector for the Direct Injection Homogeneous Market using Design for Six Sigma". In: *SAE Technical Papers*. 2010. DOI: 10.4271/2010-01-0594.

[80] Yi, Jianwen et al. "Development and Optimization of the Ford 3.5L V6 EcoBoost Combustion System". In: *SAE International Journal of Engines* 2.1 (2009), pp. 1494–2009. DOI: 10.4271/2009-01-1494.

[81] Befrui, Bizhan, Hoffmann, Guy, Kirwan, John, Piock, Walter, and Schilling, Sebastian. "Analytical Optimization of Delphi GDi Fuel Injection Systems". In: *15th Conference "The Working Process of the Internal Combustion Engine"* September 2015 (2015).

[82] Delphi Technologies. "New 500+ bar GDi system cuts particulates by up to 50% without engine changes". In: *News release* (2019).

[83] Postrioti, Lucio et al. "Momentum Flux Measurement on Single-Hole GDI Injector under Flash-Boiling Condition". In: *SAE Technical Papers*. Vol. 24. 2480. 2015. DOI: 10.4271/2015-24-2480.

[84] Cavicchi, Andrea et al. "Numerical and experimental analysis of the spray momentum flux measuring on a GDI injector". In: *Fuel* 206 (2017), pp. 614–627. DOI: 10.1016/j.fuel.2017.06.054.

[85] Moon, Seoksu et al. "Ultrafast X-ray study of multi-hole GDI injector sprays: Effects of nozzle hole length and number on initial spray formation". In: *Experimental Thermal and Fluid Science* 68 (2015), pp. 68–81. DOI: 10.1016/j.expthermflusci.2015.03.027.

[86] Tu, Po-Wen et al. "Numerical Investigation of GDI Injector Nozzle Geometry on Spray Characteristics". In: *SAE Technical Papers*. Vol. 2015-Septe. September. 2015. DOI: 10.4271/2015-01-1906.

[87] Befrui, Bizhan, Corbinelli, Giovanni, Spiekermann, Peter, Shost, Mark, and Lai, Ming-Chia. "Large Eddy Simulation of GDI Single-Hole Flow and Near-Field Spray". In: *SAE International Journal of Fuels and Lubricants* 5.2 (2012), pp. 392–2012. DOI: 10.4271/2012-01-0392.

[88] Befrui, B, Corbinelli, G, Hoffmann, G, Andrews, R J, and Sankhalpara, S R. "Cavitation and Hydraulic Flip in the Outward-Opening GDi Injector Valve-Group". In: *SAE Technical Papers*. 2009. DOI: 10.4271/2009-01-1483.

[89] Shost, Mark A, Lai, Ming-Chia, Befrui, Bizhan, Spiekermann, Peter, and Varble, Daniel L. "GDi Nozzle Parameter Studies Using LES and Spray Imaging Methods". In: *SAE Technical Papers*. Vol. 1. 2014. DOI: 10.4271/2014-01-1434.

[90] Shost, Mark Anthony. "Evaluation of nozzle geometry on high pressure Gasoline Direct Injection spray atomization". PhD thesis. Wayne State University, 2014, p. 295.

[91] Payri, Raul, Hardy, Gilles, Gimeno, Jaime, and Bautista, Abian. "Analysis of counterbore effect in five diesel common rail injectors". In: *Experimental Thermal and Fluid Science* 107 (2019), pp. 69–78. DOI: 10.1016/j.expthermflusci.2019.05.008.

[92] Befrui, Bizhan et al. "ECN GDi Spray G : Coupled LES Jet Primary Breakup - Lagrangian Spray Simulation and Comparison with Data". In: *ILASS Americas 28th* June (2016).

[93] Payri, F, Payri, Raul, Salvador, F J, and Martínez-López, Jorge. "A contribution to the understanding of cavitation effects in Diesel injector nozzles through a combined experimental and computational investigation". In: *Computers & Fluids* 58 (2012), pp. 88–101. DOI: 10.1016/j.compfluid.2012.01.005.

[94] Macian, Vicente, Bermudez, V, Payri, Raul, and Gimeno, Jaime. "New technique for determination of internal geometry of a diesel nozzle with the use of silicone methodology". In: *Experimental Techniques* 27.2 (2003), pp. 39–43. DOI: 10.1111/j.1747-1567.2003.tb00107.x.

[95] Manin, Julien et al. "Experimental Characterization of DI Gasoline Injection Processes". In: *SAE Technical Paper Series*. SAE International, 2015. DOI: 10.4271/2015-01-1894.

[96] Matusik, Katarzyna E, Duke, Daniel J, Swantek, Andrew B, Powell, Christopher F, and Kastengren, Alan L. "High Resolution X-Ray Tomography of Injection Nozzles". In: *ILASS Americas 28th Annual Conference on Liquid Atomization and Spray Systems, Dearborn, MI, May 2016*. May. 2016.

[97] Strek, Piotr et al. "X-Ray Radiography and CFD Studies of the Spray G Injector". In: *SAE Technical Papers* 2016-April.April (2016). DOI: 10.4271/2016-01-0858.

[98] Matusik, Katarzyna E et al. "A study on the relationship between internal nozzle geometry and injected mass distribution of eight ECN Spray G nozzles." In: *Proceedings ILASS–Europe 2017. 28th Conference on Liquid Atomization and Spray Systems*. September. Valencia: Universitat Politècnica València, 2017, pp. 6–8. DOI: 10.4995/ILASS2017.2017.4766.

[99] Akhtar, S W and Yule, A J. "Droplet impaction on a heated surface at high Weber numbers". In: *ILASS-Europe, Zurich* September 2001 (2001).

[100] Lee, Sang Yong and Ryu, Sung Uk. "Recent progress of spray-wall interaction research". In: *Journal of Mechanical Science and Technology* 20.8 (2006), pp. 1101–1117. DOI: 10.1007/BF02916010.

[101] Bai, Chengxin and Gosman, A. D. "Development of Methodology for Spray Impingement Simulation". In: *SAE Technical Paper 950283* 412 (1995). DOI: 10.4271/950283.

[102] Panão, M R O and Moreira, A L N. "Thermo- and fluid dynamics characterization of spray cooling with pulsed sprays". In: *Experimental Thermal and Fluid Science* 30 (2005), pp. 79–96. DOI: 10.1016/j.expthermflusci.2005.03.020.

[103] Toda, Saburo. "A Study of Mist Cooling : 1st Report, Experimental Investigations on Mist Cooling by Mist Flow Sprayed Vertically on Small and Flat Plates Heated at High Temperatures". In: *Transactions of the Japan Society of Mechanical Engineers* 38.307 (1972), pp. 581–588. DOI: 10.1299/kikai1938.38.581.

[104] Chaves, Humberto, Kubitzek, Artur Michael, and Obermeier, Frank. "Dynamic processes occurring during the spreading of thin liquid films produced by drop impact on hot walls". In: *International Journal of Heat and Fluid Flow* 20.5 (1999), pp. 470–476. DOI: https://doi.org/10.1016/S0142-727X(99)00034-X.

[105] Yao, Shi-Chune and Cai, Kang Yuan. "The dynamics and leidenfrost temperature of drops impacting on a hot surface at small angles". In: *Experimental Thermal and Fluid Science* 1.4 (1988), pp. 363–371. DOI: 10.1016/0894-1777(88)90016-7.

[106] Celata, G P, Cumo, M, Mariani, A, and Zummo, Giuseppe. "Visualization of the impact of water drops on a hot surface: Effect of drop velocity and surface inclination". In: *Heat and Mass Transfer* 42 (2006), pp. 885–890. DOI: 10.1007/s00231-006-0139-1.

[107] Labeish, V.G. "Thermohydrodynamic study of a drop impact against a heated surface". In: *Experimental Thermal and Fluid Science* 8.3 (1994), pp. 181–194. DOI: 10.1016/0894-1777(94)90047-7.

[108] Bernardin, J D and Mudawar, I. "The Leidenfrost Point: Experimental Study and Assessment of Existing Models". In: *Journal of Heat Transfer* 121.4 (1999), pp. 894–903. DOI: 10.1115/1.2826080.

[109] Shi, M H, Bai, T C, and Yu, J. "Dynamic behavior and heat transfer of a liquid droplet impinging on a solid surface". In: *Experimental Thermal and Fluid Science* 6.2 (1993), pp. 202–207. DOI: https://doi.org/10.1016/0894-1777(93)90030-M.

[110] Moreira, A L N and Moita, A.s. "Droplet-Wall Interactions". In: 2011, pp. 183–197.

[111] Zhang, Fan, Ma, T Y, Zhang, F, Liu, H F, and Yao, M F. "Modeling of droplet / wall interaction based on SPH method". In: *International Journal of Heat and Mass Transfer* 105.February (2017), pp. 296–304. DOI: 10.1016/j.ijheatmasstransfer.2016.09.103.

[112] Li, Chao, Wu, Guanjie, Li, Mengzhe, Hu, Chunbo, and Wei, Jinjia. "A heat transfer model for aluminum droplet/wall impact". In: *Aerospace Science and Technology* 97 (2020), p. 105639. DOI: https://doi.org/10.1016/j.ast.2019.105639.

[113] Stanton, Donald W. and Rutland, Christopher J. "Multi-dimensional modeling of thin liquid films and spray-wall interactions resulting from impinging sprays". In: *International Journal of Heat and Mass Transfer* 41.20 (1998), pp. 3037–3054. DOI: 10.1016/S0017-9310(98)00054-4.

[114] Bruneaux, Gilles. "Combustion structure of free and wall-impinging diesel jets by simultaneous laser-induced fluorescence of formaldehyde, poly-aromatic hydrocarbons, and hydroxides". In: *International Journal of Engine Research* 9.3 (2008), pp. 249–265. DOI: 10.1243/14680874JER00108.

[115] Meingast, Ulrich, Staudt, Michael, Reichelt, Lars, and Renz, Ulrich. "Analysis of Spray / Wall Interaction Under Diesel Engine Conditions". In: *SAE Technical Paper 2000-01-0272* 724 (2000), pp. 1–15.

[116] Cossali, G E, Coghe, A, and Marengo, M. "The impact of a single drop on a wetted solid surface". In: *Experiments in Fluids* 22 (1997), pp. 463–472.

[117] Payri, Raul, Gimeno, Jaime, Peraza, Jesús E, and Bazyn, Tim. "Spray / wall interaction analysis on an ECN single-hole injector at diesel-like conditions through Schlieren visualization". In: *Proc. 28th ILASS-Europe, Valencia* September (2017).

[118] Dempsey, Adam B, Seiler, Patrick, Svensson, Kenth, and Qi, Yongli. "A Comprehensive Evaluation of Diesel Engine CFD Modeling Predictions Using a Semi-Empirical Soot Model over a Broad Range of Combustion Systems". In: *SAE Int. J. Engines* 11 (2018), pp. 1399–1420. DOI: 10.4271/2018-01-0242.

[119] Zhang, Yanzhi et al. *Development of anew spray/wall interaction model for diesel spray under PCCI-engine relevant conditions*. Vol. 24. 1. 2014, pp. 41–80. DOI: 10.1615/AtomizSpr.2013008287.

[120] Arai, Masataka, Amagai, Kenji, Nagataki, Tsubasa, and Okita, Hideki. "Ignition Positions of a Diesel Spray Impinging on an Inclined Wall". In: (2005).

[121] Akop, Mohd Zaid, Zama, Yoshio, Furuhata, Tomohiko, and Arai, Masataka. "Characteristics Of Adhesion Diesel Fuel On An Impingement Disk Wall Part 1: Effect Of Impingement Area And Inclination Angle Of Disk". In: *Atomization and Sprays* 23.8 (2013), pp. 724–725.

[122] Montanaro, Alessandro, Allocca, Luigi, Meccariello, Giovanni, and Lazzaro, Maurizio. "Schlieren and Mie Scattering Imaging System to Evaluate Liquid and Vapor Contours of a Gasoline Spray Impacting on a Heated Wall". In: *SAE Technical Papers* 2015 (2015). DOI: 10.4271/2015-24-2473.

[123] Yu, Hanzhengnan, Liang, Xingyu, Shu, Gequn, Wang, Yuesen, and Zhang, Hongsheng. "Experimental investigation on spray-wall impingement characteristics of n-butanol/diesel blended fuels". In: *Fuel* 182 (2016), pp. 248–258. DOI: https://doi.org/10.1016/j.fuel.2016.05.115.

[124] Yu, Hanzhengnan, Liang, Xingyu, Shu, Gequn, Sun, Xiuxiu, and Zhang, Hongsheng. "Experimental investigation on wall film ratio of diesel, butanol/diesel, DME/diesel and gasoline/diesel blended fuels during the spray wall impingement process". In: *Fuel Processing Technology* 156 (2017), pp. 9–18. DOI: https://doi.org/10.1016/j.fuproc.2016.09.029.

[125] Montorsi, Luca, Magnusson, Alf, and Andersson, Sven. "A Numerical and Experimental Study of Diesel Fuel Sprays Impinging on a Temperature Controlled Wall". In: *SAE Technical Paper 2006-01-3333* 724 (2006), pp. 776–790. DOI: 10.4271/2006-01-3333.

[126] Zhu, Xiucheng et al. "An Experimental Study of Diesel Spray Impingement on a Flat Plate: Effects of Injection Conditions". In: September (2017). DOI: 10.4995/ilass2017.2017.4733.

[127] Bruneaux, Gilles. "Mixing Process in High Pressure Diesel Jets by Normalized Laser Induced Exciplex Fluorescence Part II: Wall Impinging Versus Free Jet". In: *SAE Technical Paper 2005-01-2100* c (2005). DOI: 10.4271/2005-01-2097.

[128] Zhao, Le et al. "Evaluation of Diesel Spray-Wall Interaction and Morphology around Impingement Location". In: 2018. DOI: 10.4271/2018-01-0276.

[129] Tang, Qinglong et al. "Experimental Study on the Effects of Spray Wall Interaction on Partially Premixed Combustion and Engine Emissions". In: *Energy & Fuels* 33.6 (2019), pp. 5673–5681. DOI: 10.1021/acs.energyfuels.9b00602.

[130] Shi, Hao et al. "Study of spray/wall interaction in transition zones from HCCI via PPC to CI combustion modes". In: *Fuel* 268 (2020), p. 117341. DOI: https://doi.org/10.1016/j.fuel.2020.117341.

[131] Maliha, Malki et al. "Optical investigation on the interaction between a fuel-spray and an oil wetted wall with the focus on secondary droplets". In: *International Journal of Engine Research* 0.0 (0000), p. 14680874221095235. DOI: 10.1177/14680874221095235.

[132] Steinberg, Christoph, Liu, Menqgi, and Hung, David L.S. "A combined experimental numerical study towards the elucidation of spray wall interaction on step geometries". In: *Engineering Applications of Computational Fluid Mechanics* 16.1 (2022), pp. 1866–1882. DOI: 10.1080/19942060.2022.2098828.

[133] Wu, Zhenkuo, Deng, Peng, and Han, Zhiyu. "A numerical study on fuel film and emissions formations during cold start in a diesel engine using an improved spray-wall impingement model". In: *Fuel* 320 (2022), p. 123898. DOI: https://doi.org/10.1016/j.fuel.2022.123898.

[134] Roque, Anthony, Foucher, F., and Helie, Jerome. "Spray wall interaction: study of preferential vaporization of fuel film as function of injection pressure and wall temperature". In: 2019.

[135] Roque, Anthony et al. "Impact of gasoline direct injection fuel films on exhaust soot production in a model experiment". In: *International Journal of Engine Research* 21.2 (2020), pp. 367–390. DOI: 10.1177/1468087419879851.

[136] Shway, Kamal, Jüngst, Niklas, Bardi, Michele, Bruneaux, Gilles, and Kaiser, Sebastian A. "A multispectral UV–vis absorption technique for quantitative high-speed field-sequential imaging of fuel films and soot in combustion". In: *Proceedings of the Combustion Institute* (2022). DOI: https://doi.org/10.1016/j.proci.2022.08.099.

[137] Freund, S., Pautsch, A.G., Shedd, T.A., and Kabelac, S. "Local heat transfer coefficients in spray cooling systems measured with temperature oscillation IR thermography". In: *International Journal of Heat and Mass Transfer* 50.9 (2007), pp. 1953–1962. DOI: https://doi.org/10.1016/j.ijheatmasstransfer.2006.09.028.

[138] Cebo-Rudnicka, Agnieszka, Malinowski, Zbigniew, and Buczek, Andrzej. "The influence of selected parameters of spray cooling and thermal conductivity on heat transfer coefficient". In: *International Journal of Thermal Sciences* 110 (2016), pp. 52–64. DOI: https://doi.org/10.1016/j.ijthermalsci.2016.06.031.

[139] Cheng, Wen-Long, Liu, Qi-Nie, and Fan, Han-lin. "Experimental investigation of parameters effect on heat transfer of spray cooling". In: *Heat and Mass Transfer* 46 (2010). DOI: https://doi.org/10.1007/s00231-010-0631-5.

Chapter 3

Experimental resources and tools

The experimental tools and methods used in the current thesis are described in this chapter. It depicts the experimental setup and methodology used during the measurements. The first section discusses the injector and injection system, while the subsequent sections go over the experimental setup. The experimental setup and raw data processing steps for each setup are also described. The experimental campaign measurements were all carried out at the CMT-Motores Térmicos in Universitat Politècnica de València and at the Istituto di Scienze e Tecnologie per l'Energia e la Mobilità Sostenibili (STEMS) and the University of Naples "Federico II" facilities.

3.1 Injection system description

Injectors require high-pressure systems to deliver fuel correctly into the test chamber. The conditions should be monitored and steady over the wide operating range required for the study. The injection system is formed by an injector, a common rail, a high-pressure unit, and a fuel supply, all of which are commercially available and suitable for research and experimentation.

3.1.1 Continental and Spray G injectors

The two injectors employed in the present thesis corresponds to a commercial injector manufactured by Continental and the well-known "Spray G" injector.

A picture of both injectors is depicted in Figure 2.13.

Both injectors are a multi-hole solenoid-driven injector intended for direct injection spark ignition. They are destined to be located near the spark plug at the top of the chamber. The injectors design characteristics are shown in Table 3.1.

The Continental injector was used to carry out the spray-wall impingement measurements of the quartz and heated walls at the CMT-Motores Térmicos experimental facilities. On the other hand, the Spray G was used to perform the IR measurements at the Istituto di Scienze e Tecnologie per l'Energia e la Mobilità Sostenibili (STEMS) and the University of Naples "Federico II" facilities.

Table 3.1: Injectors geometrical characteristics.

Parameter	Continental	Spray G
Cone bend angle	0°	0°
# Holes	6	8
Orifice	circular	circular
Hole	straight	straight
Nozzle	conical hole	step hole
L/D ratio	2.6	1.4
Orifice diameter	170 μm	165 μm
Orifice length	444 μm	160-180 μm*
Orifice drill angle	0°	0°
Spray umbrella angle	70°	80°

* Lengths for inner and outer diameters.

The electrical signal that controls the injectors has several variations. Each manufacturer specifies the current required to actuate the solenoid in order for the injector hardware to function properly.

The Continental injector driver is made up of a simplified engine control unit (ECU), as shown in Figure 3.1. The current required to actuate the injector solenoid can be generated after the trigger signal is received and used to determine the start and duration of the injection signal.

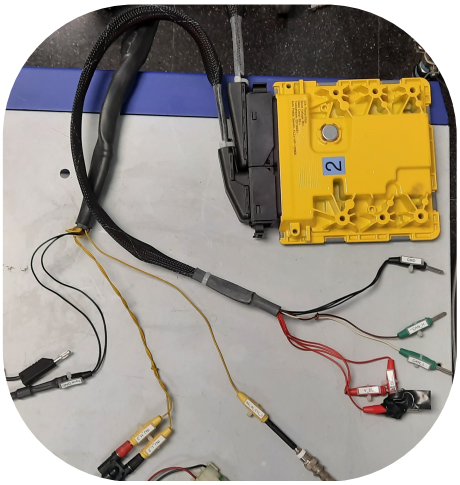

Figure 3.1: Commercial Continental injector driver.

3.1.2 High-pressure common-rail system

The system for consistently delivering fuel has previously been described in a number of publications, including [1–5], and is equivalent to the system used for diesel injectors. A high-pressure pump draws fuel from the deposit and compresses it into a first rail, which is used to control the injection pressure. The pressurized fuel is then delivered to his second rail, which is primarily used to dampen pressure surges from the pump. To precisely measure injection pressure, the Kistler pressure sensor is mounted on the second rail. Because the pump has a pressure rating of more than 20 MPa, a safety valve is installed on the second rail. This maintains the fuel pressure below 30 MPa and the injectors in good working condition. The fuel is then returned to the pump and tank and is cooled by heat exchange with glycol at 5°C. Figure 3.2 depicts a figure as well as an image of the high-pressure system.

3.2 GDI test rig vessel

The GDI vessel design of the CMT-Motores Térmicos was one of the PhD thesis objectives of Bautista [6] and allows the research and experiments on external fuel atomization under gasoline engine conditions. Stable chamber settings can be simulated covering early injection strategies that may lead to sub-atmospheric conditions. Therefore, it is suitable for studying flash boiling and spray collapse. Additionally, a wide optical access was positioned to provide a wide field of view of the examination volume. The core of the tank

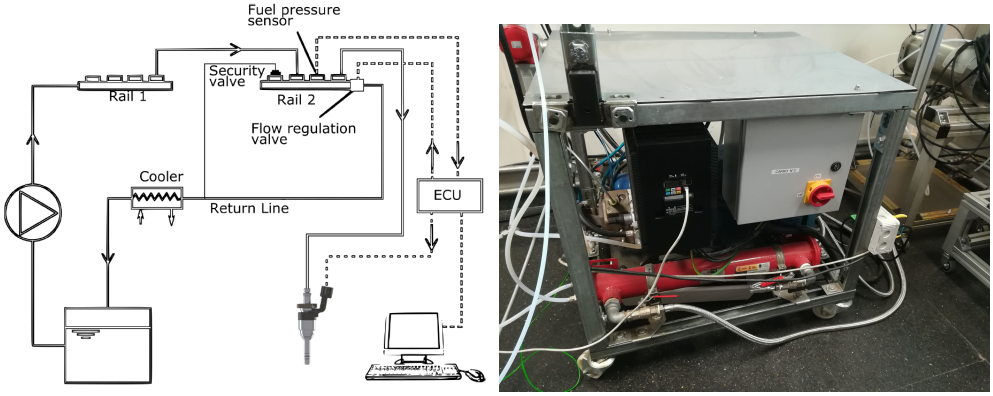

(a) Schematic figure of the high-pressure system circuit. Adapted from [1].

(b) Image of the high pressure system.

Figure 3.2: Scheme and image of the high-pressure circuit.

is derived from extruded steel beams to reduce cost and is made of AISI 1042 carbon steel like the rest of the components. Additionally, a continuous flow heater module was constructed to regulate the internal temperature, consisting of a resistor, an air diffuser and its housing. The integrity and safe performance of the system under high-pressure, as well as proper heat transmission from the heater module, were verified using FEA. According to the simulation, a 2 kW resistor is enough to produce the desired flow temperature. Finally, prior to measurements, some tests were carried out to guarantee that the facility could safely tolerate the required conditions.

The GDI experimental test rig is depicted in Figure 3.3 and Figure 3.4. The design involves four 180 mm optical accesses constructed of fused quartz with a unique polish that improves transparency and allows for the employment of laser optical techniques. The vessel can also withstand pressures ranging from 0.01 to 15 bar absolute, as well as temperatures ranging from room temperature to 150°C.

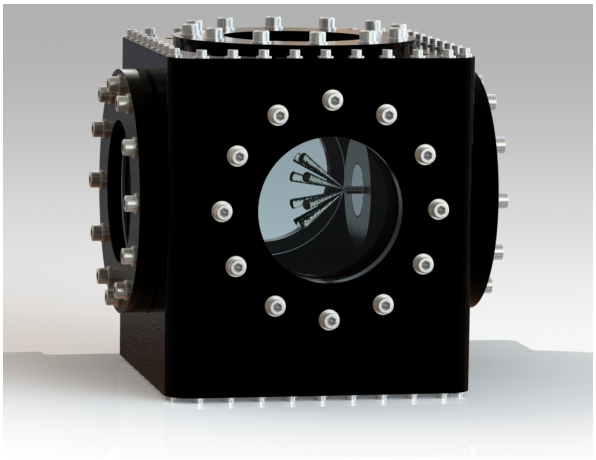

Figure 3.3: Model of the GDI vessel

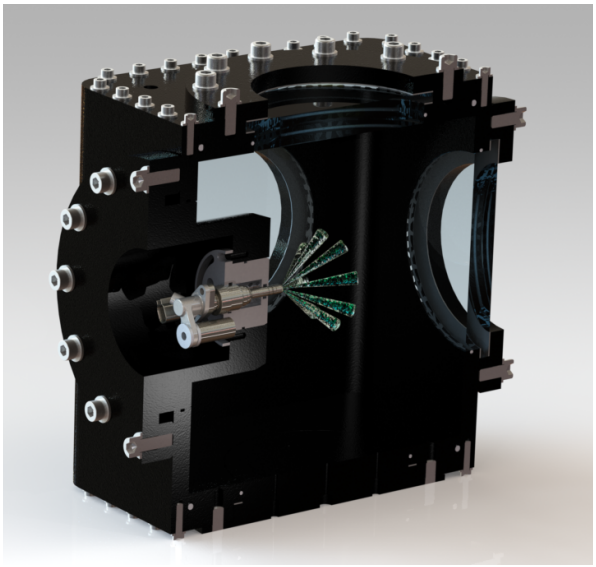

Figure 3.4: Middle section of the GDI vessel.

3.3 Transparent wall system

The GDI vessel is suitable for characterizing free spray. Nonetheless, additional hardware was required to adapt the facility to spray-wall impingement

experiments. A transparent quartz wall was used inside the chamber to visualize spray impingement at temperatures comparable to the hot ambient gases. This means that the wall is heavily exposed to the hot gases of the vessel on all of its surfaces. The entire support assembly was mounted on a specially designed injector holder. The entire system has been meticulously sized to maximize the vessel internal volume. It is adaptable enough to change the position of the wall in terms of distance from the injector tip and angle of impact.

3.3.1 Supporting system description

The system used to hold the quartz wall within the vessel in the desired configuration is shown in Figure 3.5-left. The injector holder is what holds the rest of the wall system together. Two folded seats bolted to the injector holder carry two fixed U-shaped structures. A specific removable pair of frames is used to support the wall holder depending on the target position of the wall. Figure 3.5-right depicts various shapes of these frames used to achieve different distances (d_w) and angles (θ_w) between the injector tip and the wall. These laterals pieces are used to hold a rectangular frame to which the quartz wall is attached via four screwed hooks. With the exception of the quartz wall, all components of this system are made of stainless steel for ease of manufacture, durability, and high temperature stability.

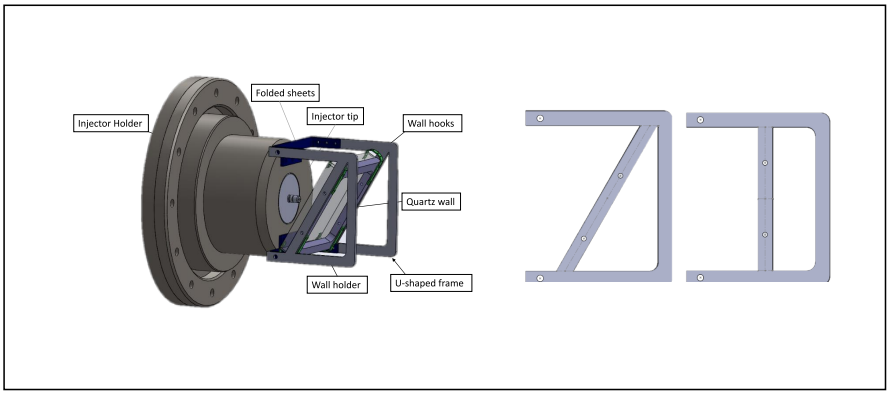

Figure 3.5: Transparent quartz wall assembly. Left: System identifyed with part labels. Right: Lateral frame variations for different wall angle.

The reference system for the measurements is depicted in Figure 3.6. The spray spread is measured parallel to the wall, and the spray thickness is mea-

sured perpendicular to the wall surface. Figure 3.6 also displays different views of the reference system (x axis and y projected according to the viewpoint of $sin(\theta_{wall})$. To avoid light reflections that interfere with image recording, the injector holder was painted matte black.

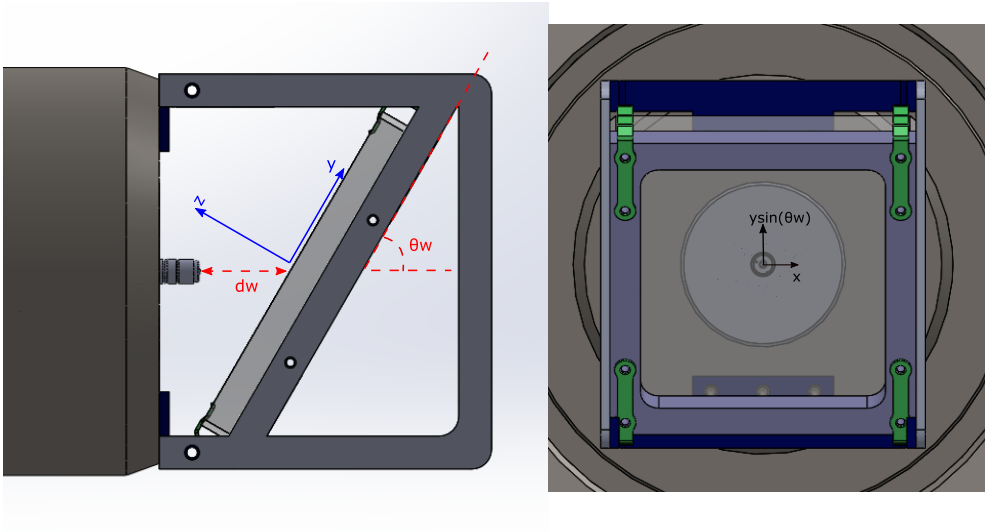

Figure 3.6: Orthogonal views of the transparent quartz wall assembly (d_w = 30 mm; θ_w = 60°). Left: Lateral view. Right: Frontal view.

3.4 Thermoregulated wall system

The quartz wall previously described permits optical access to the phenomenon through the wall allowing visualization to investigate the macroscopic properties of the spray during the SWI. Nonetheless, the heat transfer which occurs during the spray wall interaction is a very interesting process given its impact on overall engine performance [7–9]. To study the heat transfer through the wall, a thermoregulated steel wall was designed, sacrificing the frontal view possibility, and provided with one conventional thermocouple and two fast-response thermocouples[1] to register the instantaneous wall temperature drop during the injection event. The wall was designed with a cavity to allow a hot fluid circulation to regulate the wall surface temperature

[1] Unfortunately, one of the thermocouples was broken during the wall system mounting, so only one thermocouple was used to record the surface temperature variations and compute the heat flux.

by forced flow convection. A controlled hot oil flow was employed to heat the inner part of the plate.

In this case, the wall system is not connected to the injector holder. Still, it replaces the frontal window and, like the quartz wall assembly, can operate varying wall distances from the injector tip. There are three sections in this system: the wall structure, the heating oil circuit, and the temperature measuring system.

3.4.1 Wall structure

Figure 3.7 shows the thermoregulated wall system designed to allow an oil flow circulation to set the surface wall temperature. It was designed to withstand the experimental conditions of pressure and temperature and to remain properly sealed during the measurements. Figure 3.7-right shows the system from the inside. As can be seen, the wall structure is formed by a set of separate parts. This design has several advantages, such as easier manufacturing of each section, greater freedom of orientation, and the ability to change configuration. For this system, a wall configuration of 90° was used, and two different steel spacers were used to set the two wall distances used in the measurements.

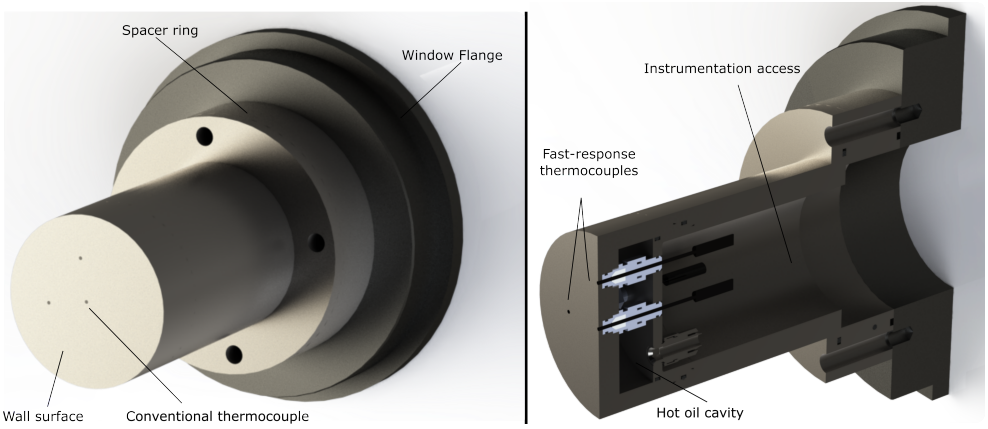

Figure 3.7: Wall structure assembly. Left: Isometric view. Right: View with a section cut.

The thermoregulated wall is more detailed in Figure 3.8, where a section cut is shown. The wall is threaded to the main body of the assembly, sealed with one O-ring. Between the wall and the main body, there is a piece that creates an internal cavity where the hot oil flow through two quick fittings (inlet and outlet). Also, this middle piece has three orifices to allocate the

thermocouple grommets. The distance between the injector tip and the wall surface is regulated using a spacer ring between the window flange and the main body of the assembly. Internally, the system is hollow, allowing instrumentation access (the electric thermocouple connectors and the flexible tube in which the hot oil circulates).

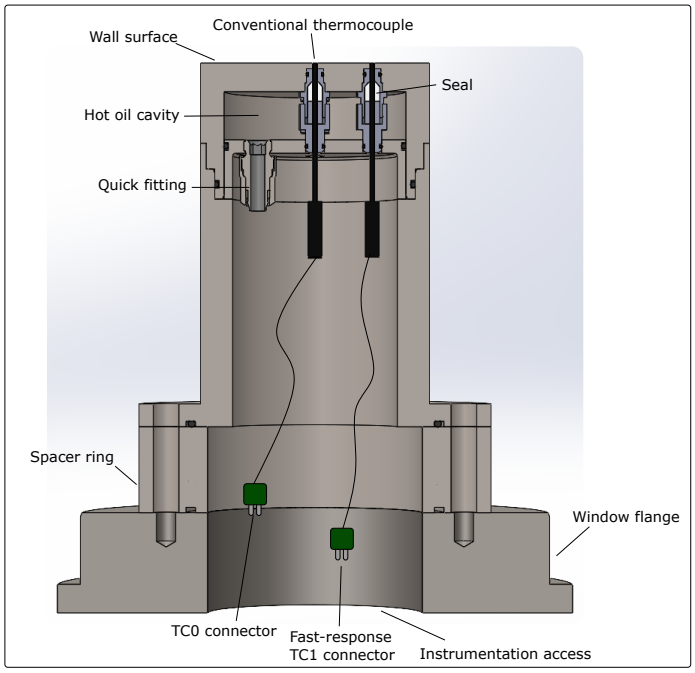

Figure 3.8: Lateral view with transversal cut of the entire wall system (d_w = 20 mm; θ_w = 90°).

The middle piece that creates the internal cavity (from now on called Divider) has one oil inlet and one oil outlet with brass fittings for the flexible tubes of hot oil. This piece is drilled in the center and at the two locations of 20 mm, with respect to the center of the piece to place the conventional and the fast-response thermocouple. With this, in the internal cavity, the flow is in complete contact with the wall, heating it via convection. The conventional thermocouple is used to have a wall temperature reference for each test of the experimental campaign. The heat transfer during the spray wall interaction is computed using this reference temperature and the temperature drop signal obtained from the fast-response thermocouples.

The temperature measuring thermocouples, which are explained in greater detail in the following section, are embedded through 1.6 mm diameter holes

in the wall and fastened to it with their corresponding fittings. These thermocouples are placed 20mm from the geometric wall center. These dimensions are described in Figure 3.9, which depicts the wall in both normal-to-wall and sectioned lateral perspectives. The diameter and width of the wall are 80 mm and 10 mm, respectively. To have a reliable temperature reference sensor, TC0 always refers to the ordinary K-type thermocouple with a standard acquisition rate (non-fast), whereas TC1 and TC2 are the labels for the two fast-response thermocouples. The standard probe TC0 was designed to be the same size and composition as the fast-response probe.

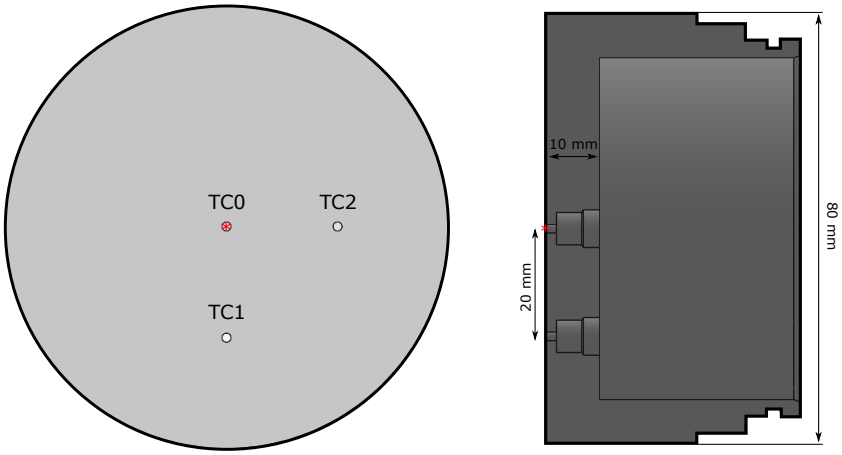

Figure 3.9: Wall pieces with a frontal and lateral view

3.4.2 Heating oil circuit

The oil circuit primary function is to maintain the wall at a fixed temperature, which could be between 293 and 363 K, while the air inside the vessel (in the wall surroundings) could be between 298 and 373 K. The oil is heated in a heat exchanger to the desired temperature and delivered to the internal cavity of the wall assembly by using flexible tubes (monitoring also the line oil pressure). Two thermocouples are used to fix the temperature of the oil in order to reach the desired temperature in the TC0 thermocouple attached to the wall surface. Figure 3.10 shows a scheme of the oil circuit used in the experimental campaign.

3.4.3 Temperature measuring system

This final subsystem function is to collect data on changes in wall temperature during the spray wall interaction events. Traditional data acquisition systems

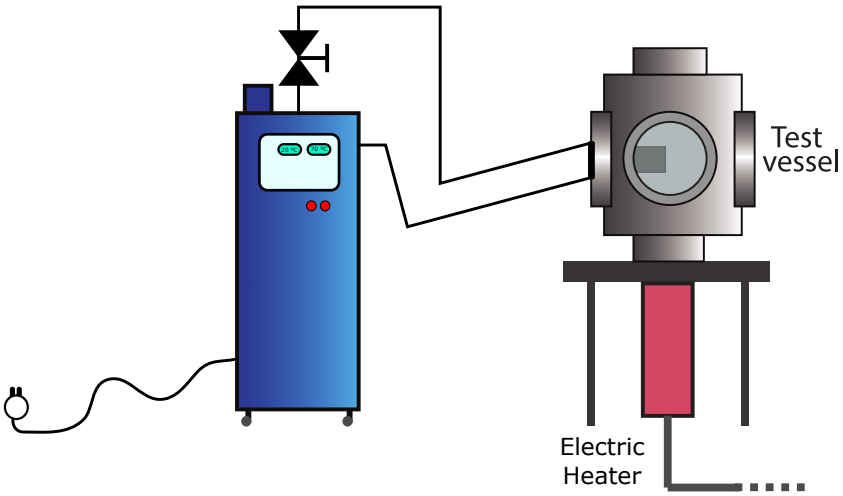

Figure 3.10: Schematic diagram of the hot oil heating system of the thermoregulated wall system.

were abandoned due to the event small temporal range and the desire for high resolution. Instead, the used configuration can be found in Figure 3.11, which only shows one thermocouple (TC1) connection. The thermoelectric voltage is measured at the circuit hot junction (where the probe is connected to the wall) and cold junction (both copper terminals and the thermocouple material are immersed into the hot oil used to heat the wall, which also acts as an isothermal block). The cold junction is covered to prevent any wire damage. Then the copper cables are connected to the high-sensitivity channel of a Yokogawa DL750 ScopeCorder oscilloscope. This wall-to-scope circuit is equivalent for all three thermocouples. The oscilloscope allowed a resolution of 0.000 305 2 mV and by using the calibration slope of the thermocouple (0.0407 mV/K) a temperature resolution of 0.007 498 K was obtained.

The two fast response thermocouples (TC1 and TC2) used to sense the wall temperature in the microsecond range are the critical components of this section. The image on the left of Figure 3.12 shows one of the MedTherm TCS-061-K thermocouples being used. In addition, TC0 is a conventional thermocouple placed alongside a fast thermocouple to check the target surface temperature using a more robust sensor. The thermocouples are attached to the wall through screwed fittings. Inside the fittings, a Teflon gland tightens the probe in its axial position.

The TC1 and TC2 fast-response thermocouples have a diameter of 1/16 ” (1.6 mm) and possess a unique junction design that allows for high response

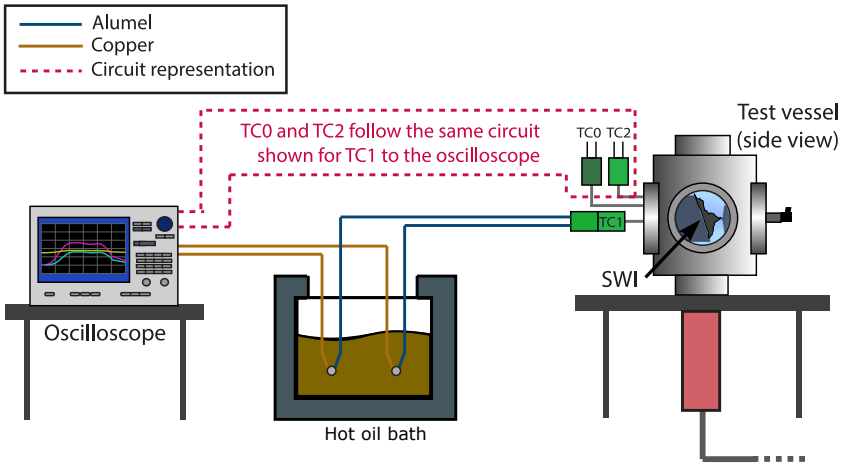

Figure 3.11: Temperature measuring circuit. The circuit is shown for one fast-response thermocouple TC1 but is equivalent for the rest.

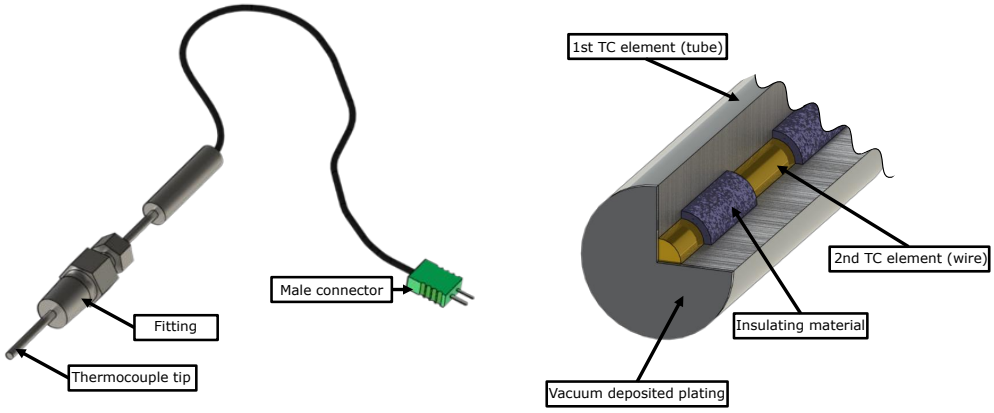

Figure 3.12: Scheme of the MedTherm TCS-061-K fast-response thermocouple (TC1 and TC2). Left: Image of the thermocouple. Right: Detail of the junction.

and acquisition rates. This is shown in greater detail in Figure 3.12-right. These coaxial thermocouples are made up of a small wire made of one junction

material that is covered with a unique ceramic insulator with a thickness of 0.0127 mm and a high dielectric strength that is compressed in a tube made of the second junction material. The junction between both materials is formed by vacuum depositing 1-2 µm of metallic coating on the sensor face, as described in Lefeuvre et al. [10].

The wall-mounted thermocouples were calibrated by using the Fluke temperature bath system before using them. The thermocouple was immersed in a dry bath of alumina sand fluidized by low-pressure air. The bath temperature is controlled by a PID-controlled heater. Alumina is non-corrosive, non-flammable, and has excellent heat transfer properties, allowing for safe and accurate calibration and temperature stability at ±0.01 °C. Five calibration campaigns on three probes were carried out in order to register voltage profiles corresponding to temperature sweeps and to verify linearity over a reasonable test temperature range. Each thermocouple averaged raw signal is calculated for each calibration, along with a standard K-type thermocouple curve obtained from NIST [11] (U.S. National Institute of Standards and Technology) identified as NIST-K. The four curves match very well in this image, demonstrating how the fast-response probe is tuned to the conventional TC0 and the theoretical Type-K curve. The thermocouple voltage signal has a high linearity with probe temperature (worst case R^2=0.9998). This is depicted in the figure corner by the linear fit equation. For each probe, these linear relationships were inverted to obtain the transformation from mV to °C.

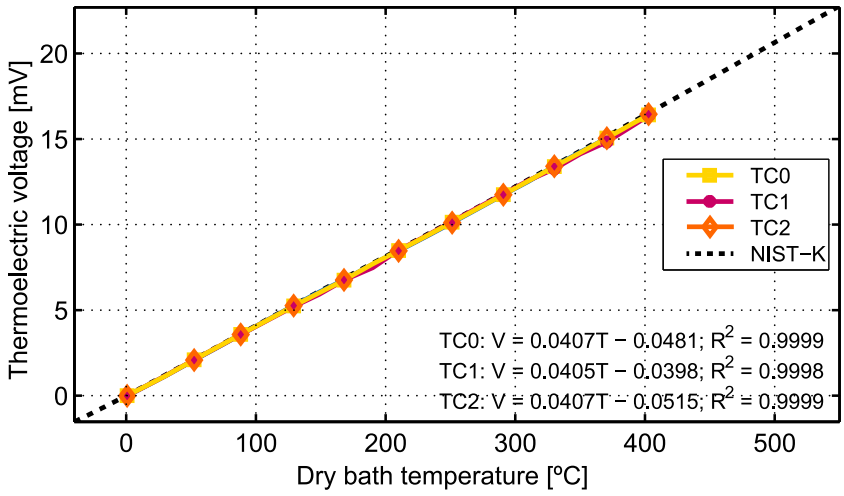

Figure 3.13: Calibration curves for the thermocouples compared to the standard type-K.

3.5 Infrared thermography

This section describes the experimental setup used for the infrared thermography measurements carried out with the Spray G injector, using the facilities provided by the Istituto di Scienze e Tecnologie per l'Energia e la Mobilità Sostenibili (STEMS) and the University of Naples "Federico II".

A render of the experimental setup used to evaluate the time history of the wall temperature and the heat transfer of a spray impacting on an electrically heated thin foil is shown in Figure 3.14 [12]. As it can be noticed in Figure 3.15 the apparatus can be divided in two different sub-systems: the spray injection/impinging wall and the acquisition system.

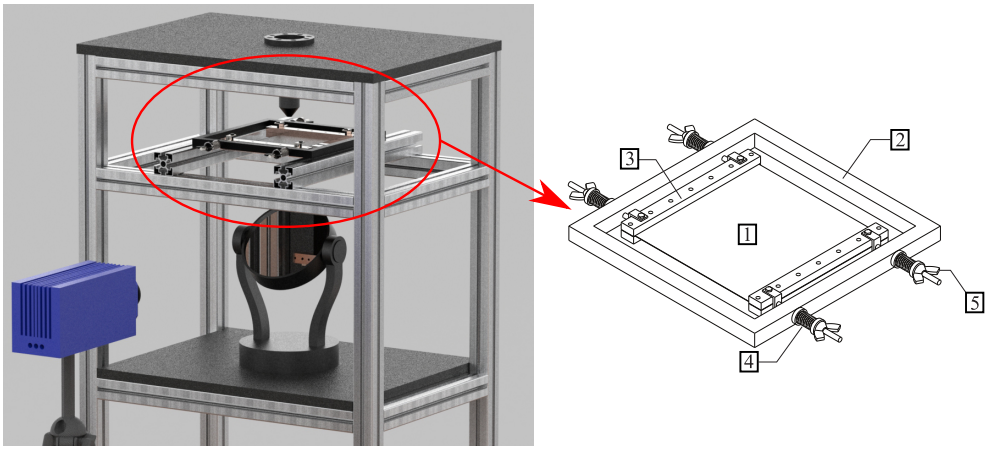

Figure 3.14: Rendering of the experimental apparatus with the detailed drawing of the clamped thin foil that includes the following components: 1. Invar thin foil 2. Square rigid frame 3. Copper clamp 4. Spring 5. Holding nut.

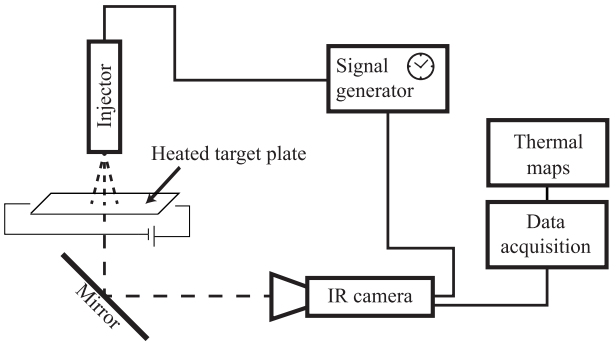

Figure 3.15: Schematic of the experimental setup.

The ECN injector eight-hole nozzle ($d_0 = 165\,\mu m$) are equally spaced on a circumference. As commonly seen in GDI applications, the nozzle holes are stepped and thus a 388 µm counterbore was machined coaxially with each of the eight inner holes. The complete technical description of the adopted injector is reported in [13–15]. The details of the spray geometry are described in Figure 3.16. Due to the nozzle tip counterbore, the Coanda effect produces a deviation of the spray from the drill hole design axis.

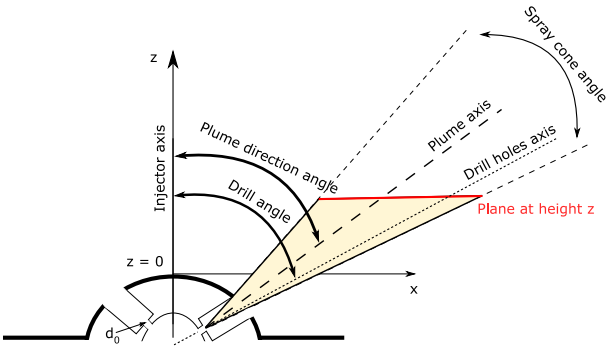

Figure 3.16: Spray G single plume geometry.

The spray impingement characterization is carried out by using a target plate reported in Figure 3.14. It is a squared, 100 mm in side, Invar foil (Goodfellow FE02-FL-000140) of 50 µm in thickness included within an aluminum rigid frame electrically insulated and clamped between two copper clamps. A current controlled DC power supply allows to set a specific amperage between the two sides of the target plate which, in turn, is uniformly and steadily heated by Joule effect. For the present work, the tests are performed with two wall temperatures of 373 and 473 K, which are obtained with the current application of 31.2 and 53.2 A through the foil respectively, resulting in a voltage drop of 1.17 and 1.92 V (36.5 and 102.1 W*respectively*).

A continuous tension stress is applied through four springs and holding nuts to keep the foil straight during heating and to absorb the thermal expansion effects. The target plate is located at $z = 11\,mm$, corresponding to $z/d_0 = 66.66$, downstream of the injector tip and facing the injector's axis perpendicularly to minimize the natural convection effects on the foil.

The IR thermal camera and the digital signal generator represent the whole data acquisition and control system. The IR camera employed in the present

work is the Cedip JADE III, a focal plane array (FPA) camera with spectral response in the 3-5 µm infrared band, noise equivalent temperature difference (NETD) of 25 mK at 298 K, InSb sensor dimensions equal to 320×240 pixel, and a maximum acquisition frame rate of 170 Hz. A cropped sensor (160×120 pixel) has been employed during acquisition for data bandwidth issues resulting in a spatial resolution of 3.05 pixel/mm. Two IR camera integration times (IT) are employed for the two investigated wall temperatures: 150 µs ($T_w = 373$ K), 30 µs ($T_w = 473$ K). It is worth noting that the ITs have been chosen to maximize the IR camera thermal sensitivity in the selected temperature range. As it can be noted in Figure 3.14 and Figure 3.15, the IR camera acquires the radiations deviated by a first surface mirror which has been interposed for safety reasons. Since the latter absorbs part of the radiations, an in situ camera calibrations by using a blackbody [16] has been conducted by respecting the optical path employed during the experimental tests. Further details on the camera calibration procedure are reported in Contino et al. [12]. In order to improve the accuracy of the thermal measurements, the dry side of the foil is painted with a high emissivity black paint ($\epsilon = 0.95$).

Isooctane has been employed as a single-component fuel surrogate for gasoline. For the present work, the injection duration has been set to 1 ms and two different injection pressures of 10 and 20 MPa have been investigated. Furthermore, both the injector and the fuel temperature operate at room temperature (298 K) and all the tests are carried out in an open environment at room temperature (298 K) and atmospheric pressure (0.1 MPa). Under direct injection strategies, the wall wetting phenomenon is quite common, followed by poor evaporation of the fuel film adhered to the piston surface. This phenomenon is more pronounced under engine cold-start conditions because of the low cylinder temperature. Also, when the wall surface is at a lower temperature than the saturation temperature of the fuel results in significant film formation. For the IR case study, the 373K temperature was selected to define a surface temperature close to the cold-start engine condition, and the 473K temperature was selected to use a higher temperature than the Nukyama and Leidenfrost temperature of the isooctane.

Since the studied phenomenon is faster than the maximum acquisition rate of the IR camera, the time-history of the wall spray cooling is reconstructed by a single-image acquisition delayed with respect to the start of the injection and repeating the spray shots. In particular, the injector frequency is fixed to 0.0625 Hz which corresponds to 16 s of time interval between one shot and the next one in order to recover the initial wall temperature between them. A BNC-575 digital delay/pulse generator has been employed to synchronize the injection start ($t = 0$ s) and the IR camera acquisition delay steps every 50 µs

from 0 to 1.2 ms, and every 100 µs up to 1.8 ms. To improve the accuracy of the measured data, 125 repetitions of the spray impact were carried out for each time delay step. Some of the camera settings can be found in Table 3.2.

Table 3.2: IR camera settings.

IR camera settings		
Detector format	[pixel]	half cropped: 160×120
Spatial resolution	$[\frac{pixel}{mm}]$	3.05
Integration time (IT) @$T_w = 373$ K	[µs]	150
Integration time (IT) @$T_w = 473$ K	[µs]	30

References

[1] Vaquerizo, Daniel. "Study on Advanced Spray-Guided Gasoline Direct Injection Systems". PhD thesis. Universitat Politècnica de València, 2017.

[2] Viera, Alberto. "Effect of multiple injection strategies on the diesel spray formation and combustion using optical diagnostics". PhD thesis. Universitat Politècnica de València, 2019.

[3] Viera, Juan Pablo. "Experimental Study of the Effect of Nozzle Geometry on the Performance of Direct-Injection Diesel Sprays for Three Different Fuels". PhD thesis. Universitat Politècnica de València, 2017.

[4] Payri, Raul, Bracho, Gabriela, Gimeno, Jaime, and Bautista, Abian. "Rate of injection modelling for gasoline direct injectors". In: *Energy Conversion and Management* 166 (2018), pp. 424–432. DOI: 10.1016/j.enconman.2018.04.041.

[5] Bardi, Michele. "Partial needle lift and injection rate shape effect on the formation and combustion of the Diesel spray". PhD thesis. Valencia (Spain): Universitat Politècnica de València, 2014. DOI: 10.4995/Thesis/10251/37374.

[6] Bautista Rodriguez, Abian. "Study of the Gasoline direct injection process under novel operating conditions". PhD thesis. Universitat Politècnica de València, 2021.

[7] González, Uriel. "Efecto del choque de pared en las características del chorro Diesel de inyección directa". PhD thesis. Valencia: E.T.S. Ingenieros Industriales. Universidad Politécnica de Valencia, 1998.

[8] Meingast, Ulrich, Staudt, Michael, Reichelt, Lars, and Renz, Ulrich. "Analysis of Spray / Wall Interaction Under Diesel Engine Conditions". In: *SAE Technical Paper 2000-01-0272* 724 (2000), pp. 1–15.

[9] Köpple, Fabian et al. "Experimental Investigation of Fuel Impingement and Spray-Cooling on the Piston of a GDI Engine via Instantaneous Surface Temperature Measurements". In: *SAE International Journal of Enginesngines* 7.3 (2014), pp. 2014–01–1447. DOI: 10.4271/2014-01-1447.

[10] Lefeuvre, T., Myers, P. S., and Uyehara, O. A. "Experimental Instantaneous Heat Fluxes in a Diesel Engine and Their Correlation". In: (1969). DOI: 10.4271/690464.

[11] NIST. *National Institute of Standards and Technology standard reference data*. Online.

[12] Contino, Mattia, Zaccara, Mirko, Montanaro, Alessandro, Allocca, Luigi, and Cardone, Gennaro. "Dynamic Thermal Behavior of a GDI Spray Impacting on a Heated Thin Foil by Phase-Averaged Infrared Thermography". In: 2020. DOI: https://doi.org/10.4271/2019-24-0036.

[13] Manin, Julien et al. "Experimental Characterization of DI Gasoline Injection Processes". In: *SAE Technical Paper Series*. SAE International, 2015. DOI: 10.4271/2015-01-1894.

[14] Moulai, Maryam, Grover, Ronald, Parrish, Scott, and Schmidt, David. "Internal and Near-Nozzle Flow in a Multi-Hole Gasoline Injector Under Flashing and Non-Flashing Conditions". In: *SAE Technical Paper Series*. SAE International, 2015. DOI: 10.4271/2015-01-0944.

[15] Duke, Daniel J. et al. "Internal and near nozzle measurements of Engine Combustion Network "Spray G" gasoline direct injectors". In: *Experimental Thermal and Fluid Science* 88 (2017), pp. 608–621. DOI: https://doi.org/10.1016/j.expthermflusci.2017.07.015.

[16] Carlomagno, Giovanni Maria and Cardone, Gennaro. "Infrared thermography for convective heat transfer measurements". In: *Experiments in Fluids* 49.6 (2010), pp. 1187–1218. DOI: 10.1007/s00348-010-0912-2.

Chapter 4

Data processing strategies

4.1 Introduction

The preceding chapter covered the majority of the hardware used for collecting data. This section of the work describes both laboratory work and data processing methodologies. The optical techniques used to record spray information during the experimental campaign are presented and the image processing routines that were used to extract metrics from high-speed imaging. The thermoelectric signal obtained from the fast-response thermocouples was processed to obtain the surface temperature variation used to calculate the wall surface heat flux. Also, the data post-processing of the infrared thermal images is also explained.

4.2 Optical techniques and setups

Depending on the equipment set chosen, some diagnostics can be performed using optical techniques. Despite the fact that making a phenomenon optically accessible frequently necessitates the use of specialized facilities, requiring a setup that is farther from the currently available commercial hardware, optical techniques are a potent, non-intrusive approach for obtaining pertinent information not just in the engine research field. For gasoline spray research, there are studies of the vapor and liquid macroscopic characteristics with high temporal resolution [1–5], droplet diameter, projected fuel mass, soot concentration, and temperature distribution. All of the variables mentioned

above are examples of variables of interest derived via imaging techniques. Internal flow parameters such as cavitation regime [6–8] and needle lift [6, 9] may also be measured through optical approaches.

Three different optical techniques for visualizing the spray were used in this work. Single-pass schlieren was used to obtain the spray gas-phase contours and macroscopic properties in inert conditions. The liquid penetration was determined using a diffused back-illumination (DBI) setup, and MIE-scattering was the selected technique to visualize the frontal development of the spray (used to obtain the spray semi-area of impact with the wall). This section explains the basic theory behind these techniques and then describes the optical setups used. These setups are designed to simultaneously obtain different types of information from the injection event using three cameras simultaneously, thus improving data consistency and reducing the time expended in the measurement campaign.

4.2.1 Single-pass Schlieren technique

The macroscopic vapor spray properties have been widely studied by engine researchers using Schlieren [10–15]. The technique is employed in other applications, such as photography of atmospheric disturbances produced by high-velocity projectiles, estimation of the speed of sound, and detection of heated gases and pressure waves [16], and is based on relation between the density and refractive index [17]. The light beams are deflected proportionally to the refractive index gradient n_r of the medium when passing through it. Equation 4.1 describes the behavior of this deflection ε of a ray traversing a path of length L on generic axis u through a medium with a refractive index of n_r. This formula takes into account the density gradients in the environment.

$$\varepsilon_u = \frac{L}{n_{r0}} \cdot \frac{\partial n_r}{\partial u} \tag{4.1}$$

In sprays research, the Schlieren technique is used to view the spray vapor phase boundaries caused by the deflection of light beams by the change in density gradients between the injected fuel and the ambient gas in the surrounds Equation 4.1 [18]. The two most common Schlieren setups are single-pass and double-pass Schlieren. The latter is mostly employed for multi-hole injectors or facilities with just one optical access. Because of its low interference with other optical techniques, the single-pass Schlieren arrangement was chosen for this work to analyze the vapor phase of the injected sprays. Figure 4.1 shows the principle of a standard single-pass Schlieren configuration. The image is

split vertically, showing different types of light sources. We can observe how the lens collimates the rays, starting with a single point source (below). After that, the undeflected light beams, represented by thin dashed lines in the figure, converge to the focal distance after the second lens, going through the slit and arriving at the screen, which contains the observer (camera or sensor). The rays influenced by the density gradient in the test chamber (red dashed line), are deviated by the angle ε and obstructed by the slit, resulting in a black-and-white image. Still, the actual light source is finite rather than a point. This case is shown in the upper half of Equation 4.1, which can be viewed as a set of point light sources that produce a grayscale composition of the image on the screen.

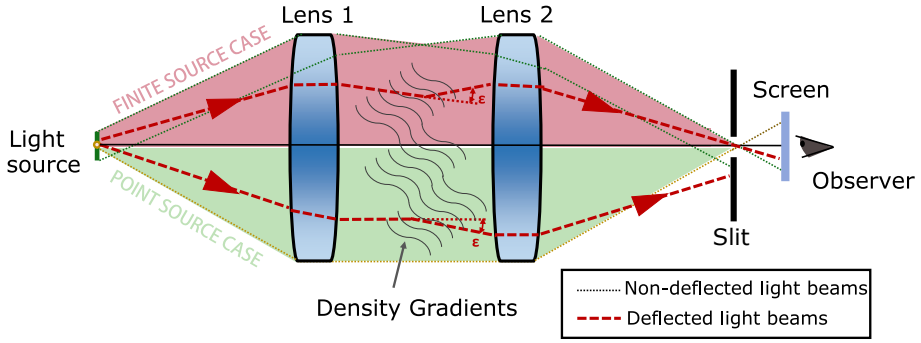

Figure 4.1: Diagram of the Schlieren optical technique. Top: Finite source case. Bottom: Point source case.

4.2.2 Diffused back-illumination (DBI)

Diffused back-illumination, or DBI, is frequently employed in spray diagnostics to offer information on the air-fuel mixture by measuring spray liquid penetration, [19]. The background is lighted in this technique by a diffuse light blocked by the spray optical thickness τ. The Beer-Lambert law represents the relationship between the optical thickness and the image intensity, and its written as:

$$\frac{I}{I_0} = e^{-\tau} \tag{4.2}$$

where I is the intensity matrix of the image at a particular time, accounting for the absorbance created by the spray, and I_0 is the intensity of the reference image from a diffuse source with no block or attenuation. Similarly, another

way to define τ is to consider the length of light traveled through the spray L_s and the attenuation coefficient K_{ext}, which varies based on the spray or attenuating source composition:

$$\tau = K_{ext} \cdot L_s \tag{4.3}$$

Numerous studies cited in the literature use rapid light-emitting diode (LED) devices to enhance light throughput by using short pulses rather than continuous light sources [10, 20–23]. This method, which was employed in the experiments conducted for this thesis, permits managing the light entering the camera sensor by setting the light pulse to a short duration.

Various optical setups can be utilized to create a diffused background. The approach applied in this thesis is based on notions presented by Ghandhi and Heim [24] and shown in Figure 4.2. The designed diffuser generates an irradiance distribution from the collimated input in this case. The light is then collected and sent to the observer via a Fresnel lens. At the expense of the needed diffuser size and array dimensions, this arrangement ensures spatial uniformity of the intensity distribution.

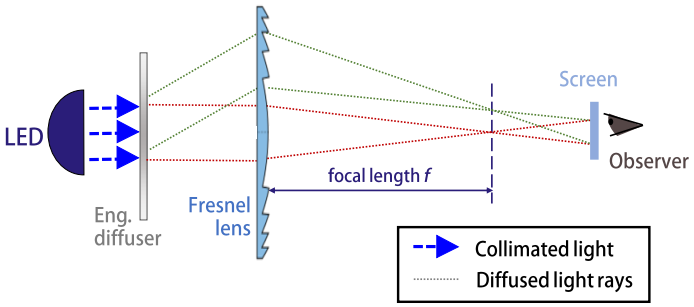

Figure 4.2: DBI setup diagram presented in [24].

4.2.3 Mie-scattering technique

Gustav Mie inspired the optical phenomenon known as Mie-scattering (MIE). It corresponds to the elastic scattering of light from particles with diameters higher than the incident light wavelength. This suggests that MIE phenomena can be applied to liquid spray research since the spray liquid droplets reflect light. Figure 4.3 depicts the MIE configuration used in the experimental campaign. Two Mercury-Xenon arc lamp light sources are used. The light is

transferred by optical fiber to a 7 mm collimating lens, which can focus the light on the area of interest.

Setting up the MIE is more complex than the DBI, as the orientation of the light source can significantly affect the visible spray. Hamzah et al. [25] compared an optical DBI and MIE technique for measuring liquid length in intense flashing sprays. They concluded that qualitative assessments were similar for both scenarios, although maximum liquid penetration can be highly dependent on setup and imaging method. In some cases, there is a difference between the two optical approaches of up to 20%.

In general, DBI results are more independent of the source and the setup than MIE, but in some cases, only the MIE setup can study the spray. For this work, a frontal view of the spray was required to investigate the spreading along the transparent wall and to study the semi-area of impact against the wall.

4.2.4 Quartz wall optical setup

The optical setup was set based on the understanding of each optical technique physical principles. A relevant criterion to define the final configuration was related to the need to perform several experimental campaigns simultaneously using the three techniques to ensure that all the cameras recorded the same events under the same conditions, reducing the total recording duration. In addition, interference between techniques were avoided.

Figure 4.3 shows the optical setup arrangement used for the quartz wall and for the free jet inert conditions. The light beams used for the Schlieren are achieved by using a white light 150 W halogen lamp pointing to a parabolic mirror which parallelizes the beams and directs the beams through the test rig vessel (the zone where the injection event occurs and where the light is affected by the density gradient) and finally, to the Photron SA-X2 camera sensor. In the middle, a biconvex lens (150 mm focal length) is placed to converge the light beams into a point where a slit or digraph is placed just before the camera. The aquamarine color indicates the path followed by the Schlieren technique in Figure 4.3, and represents the vapor spray visualization technique used for the whole work.

The main trajectory of the DBI rays used for the liquid spray visualization is shown in Figure 4.3 identified with the purple path color. A green LED beam is directed into a diffuser that homogenizes the background before passing through a Fresnel lens which increases the light intensity. Then there are two 50/50 beam splitters (one before the vessel, used to redirect the beams to the

test area, and one after the vessel to direct the light to the green filter and the camera sensor) to direct the beam into the chamber without interfering with the Schlieren imaging path. The camera used for this technique is the Photron SA5. The LED pulse duration was reduced, as specified in the DBI section to improve image quality.

Lastly, the MIE-scattering path, used for the frontal imaging is shown in Figure 4.3, identified with the pink color. A frontal illumination of the spray and a Phantom V12 camera is used for this technique. In this way all the cameras are set to start recording at the same time when the injector is energized.

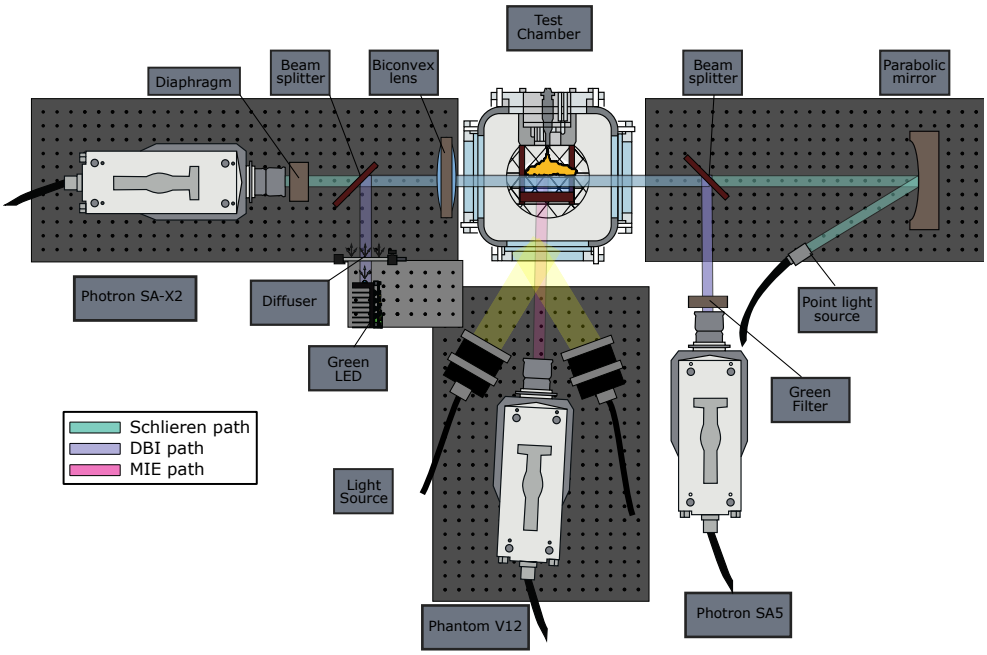

Figure 4.3: Setup used in the spray visualization for the Quartz-Wall and free-jet campaign.

4.2.5 Thermoregulated wall optical setup

The thermoregulated wall was used in the same inert conditions as the quartz wall. Due to the different hardware used to mount the wall system inside the vessel, one vessel optical access was sacrificed, and two optical techniques were used. Figure 4.4 shows the optical arrangement employed where two high-speed cameras were employed to record both the vapor and liquid phase

of the SWI event at the same time. The heat flow between the spray and the wall was evaluated using the temperature data obtained by the standard and fast-response thermocouples fitted to the wall surface.

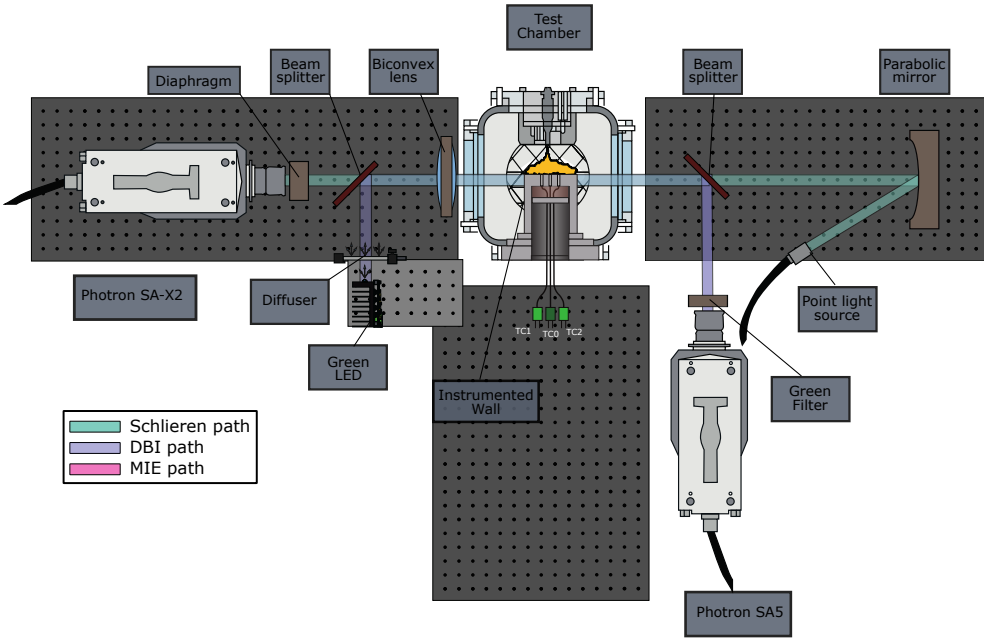

Figure 4.4: Optical setup diagram used in the tests with the Insrumented Wall.

4.3 Image processing strategies

All images were treated with specifically built MATLAB® routines. According to their desired properties, the image processing algorithms used in this work fall into two broad categories: Spray geometry aspects such as spray penetration and propagation over the walls, and temporal variables such as the start of injection (SOI) or the start of interaction between the spray and the wall (τ_w). The principal method is to binarize the image and then compute certain metrics using its contours or intensity levels.

Each frame of every high-speed spray video is processed in four phases. To save computing time, the picture is first masked. The image is then removed of its background. The picture is then binarized and filtered for improved processing before the contours are recognized and processed to obtain the related variables.

4.3.1 Image masking

MATLAB® recognizes the picture as a height-pixel × width-pixel matrix whose element values are provided by the grayscale intensity of each pixel. The zero represents black, and values increase with the image bit depth (white value = 2^{bits}-1). Pixels of no interest are omitted to reduce processing time. To do this, two masks are created. These masks are essentially matrices of ones and zeros depending on whether the region is of interest. An element-to-element conjunctive mask masks the raw image. The first mask is created from the pixels where the injector tip is located and defines the region of interest at an angle.The second mask removes all pixels from behind the wall. To guarantee that the spray is not masked at any time throughout the injection event, the target angle specified by the first mask is adjusted by d_w and θ_w. The result of the masking procedure, as demonstrated in the Figure 4.5 example, is simply the definition of three zones where the region of interest remains constant.

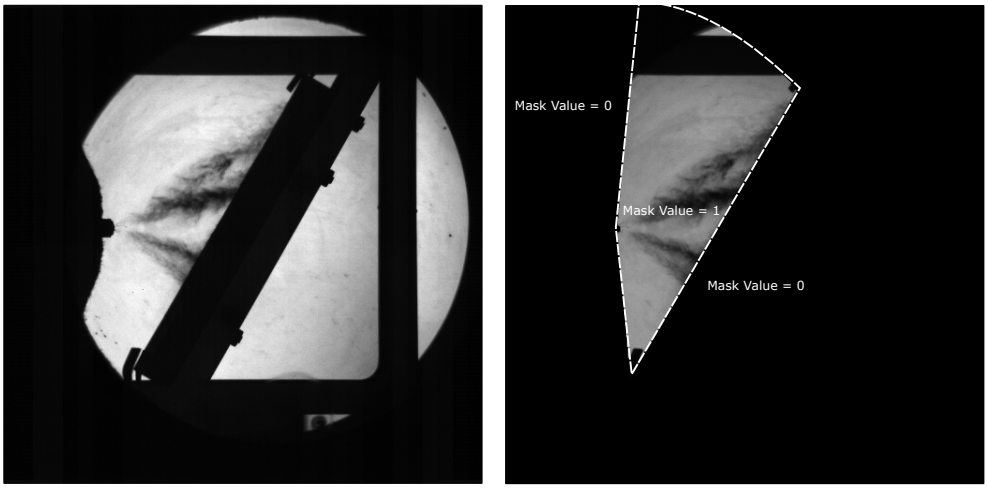

Figure 4.5: Masking process example (Isothermal Wall; T_{amb} = 373 K; p_{rail} = 250 MPa; d_w = 35 mm; θ_w = 60°; Fuel = Iso-octane. Left: Raw image. Right: Masked image

4.3.2 Image binarization and background subtraction.

After masking the frame, the spray must be separated from the background. This is done using Equation 4.2 for the DBI images case. The optical thickness is determined by comparing the background image before the I_0 injection event to the image with the I spray.

For Schlieren data, the process is similar but requires additional considerations. Background density gradients can deflect light rays and appear in the final image. These gradients are induced by the test chamber uneven temperature distribution and heated convection from the chamber walls. A set of images from an injection event may contain a variety of background patterns that change throughout the event.

As described in Payri et al. [26], the countour of the spray is obtained. Its principle is based on dynamic background synthesis subtraction [22, 26, 27] but improved with time derivative evaluation of images [26, 28–30]. A dynamic background continuously updates the background information that is subtracted. As a result, it is computed in two steps. First, set anything that did not correspond to the spray in the previous image as the background, and second, fill the spots where there was spray in the previous image with the average of the first five images (static background).

4.3.3 Image filtering and other criteria combination

After the above steps, two binary images are collected from both the variable background method and the time derivative method. However, just using an intensity threshold only partially removes the background. To improve the detection, image filtering is applied, using pixel erosion-dilation operations and connectivity criteria. This is a two-stage pixel erosion procedure that removes background noise and tiny white structures. The next step is to remove any white regions below a certain pixel count. A two-stage dilation is applied to the white areas to compensate for the erosion strategy. Finally, any remaining white islands not part of the spray are removed. The criteria are to take the area closest to the tip of the injector as a spray during the first stages of the injection and the largest area for the rest of the images recorded at each test point.

The filtered images from both processing methods are merged with a weighted average [31] to generate a binary image representing the spray area, whose borders determine the spray contour. The whole spray contour detection procedure is detailed in Figure 4.6.

4.3.4 Image contour analysis

Following the calculation of the spray contour, post-processing procedures are used to acquire the needed variables. As stated in the start of this section, the variables can be classified into two categories: The first one, represented by the variables that are identified and characterized by the spray boundaries since

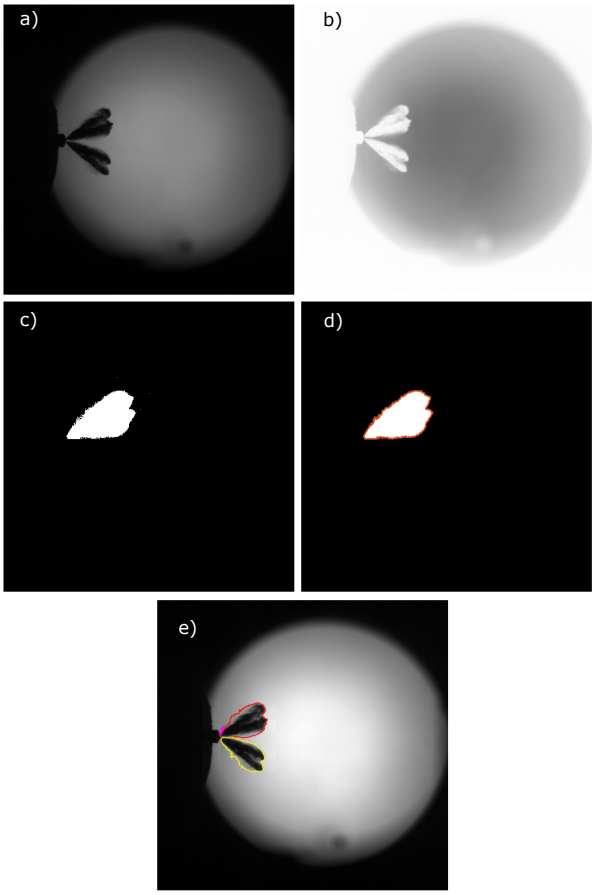

Figure 4.6: DBI image processing steps: a) Original raw image b)Image normalization c)Erode-dilate image filtering d) Contour detection e) Original image with the found contour overlapped.

they represents properties linked to the spray pattern and to the geometric progression during the injection event. The variables represented in Figure 4.7 and Figure 4.8 are examples of this kind of variables and may be extracted from both the side and frontal images. The second category is formed by the temporal variables that represents critical aspects such as the start of injection and spray-wall interaction. In this work, all the time variables are presented in ASOI (after start of injection) reference.

In the following lines, there are the various macroscopic parameters and the criteria used to calculate them:

- **Spray penetration (S):** is obtained by choosing the farthest point of the jet profile simply by taking the axial distance to the nozzle tip. This metric is calculated only under free-jet conditions.

- **Plume spray angle(ϕ):** The plume angle is the angle formed between the difference of two linear fits of the spray contour data, as shown in the Figure 4.7. These linear fits are made by using a data range between 10% and 50% of the free jet penetration.

- **Spray width for free-jet penetration at 20 mm:** The spray width was obtained at 20mm from the injector tip to have an additional reference value to compare the effects of the different variables over the opening of the spray.

- **Spray spreading along the wall (Y_+):** The spread of spray along the wall is the distance between the "impingement point" and the furthest contour point toward the top of the wall. In Figure 4.7-right is possible to see the "collision point", indicated by the small white circle, defined as the intersection between a spray direction of 35° respect to the injector tip and the wall surface. This spray direction was obtained from the spray angle measurements explained in section A.2.

- **Thickness of the spray along the wall (Z_{th}):** The Thickness of the spray along the wall varies with time and space. Two different and consecutive points from the "collision point" (Figure 4.7) at 0 mm and 5 mm were used to measure the thickness of the spray contour calculated as the normal distance between the wall and the farthest point of the spray contour.

- **Semi-area of impact (A_i):** By using the MIE-scattering frontal images, the semi-area of impact is defined as the area of the semi-circle formed by the intersection of the spray direction with a perpendicular line that passes through the impact point (calculated as the point with maximum intensity in the spray direction). Also, the penetration is calculated as the furthest point in the spray direction passing through the impact point with the wall, as can be seen in Figure 4.8.

- ***R-parameter*** **(R_{par}):** The steady vapor penetration for inert sprays is proportional to time to the 0.5th power as described by [32–34]. By using this proportionality, a method to express the penetration and the spray development in a time-independent way through a constant parameter derived from the conservation of the spray momentum flux is applied.

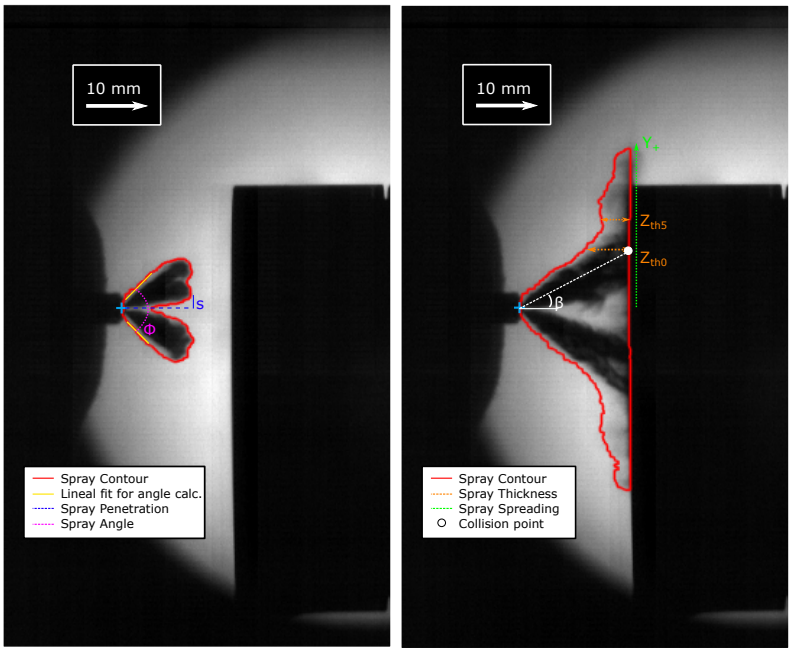

Figure 4.7: Macroscopic spray parameters for the side spray images. (Left: Jet before impingement. Right: Spray-wall interaction.

This constant variable, called *R-parameter*, is defined as the the square root time derivative of the spray penetration with respect to the square root of time as shown in Equation 4.4.

$$R_{parS} = \frac{\partial S_v(t)}{\partial \sqrt{t}} \propto \dot{M}^{\frac{1}{4}} \cdot \rho_{amb}^{-\frac{1}{4}} \cdot \tan^{-\frac{1}{2}}\left(\frac{\phi_v}{2}\right) \tag{4.4}$$

The proportional relationship with the right-hand part of the equation corresponds to several models of spray-free penetration [32, 35]. *R-parameter* is a helpful tool applied in previous studies to investigate the spray penetration [21, 36, 37] and the spray propagation along walls [26]. The free vapor penetration behavior and its derivative with respect to time increased to 0.5 for another ECN diesel injector analyzed in [21] is shown in Figure 4.9. The *R-parameter* of the penetration ($RparS$) has a stable temporal trend in the steady phase with slight deviations, as seen in the right figure. Also, in most of the result figures presented in this work, the standard deviation is represented using a lighter shade behind all the curves.

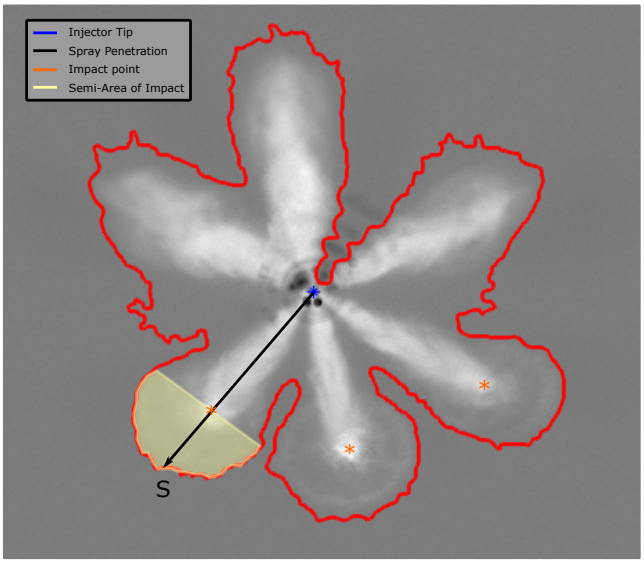

Figure 4.8: Frontal spray spreading

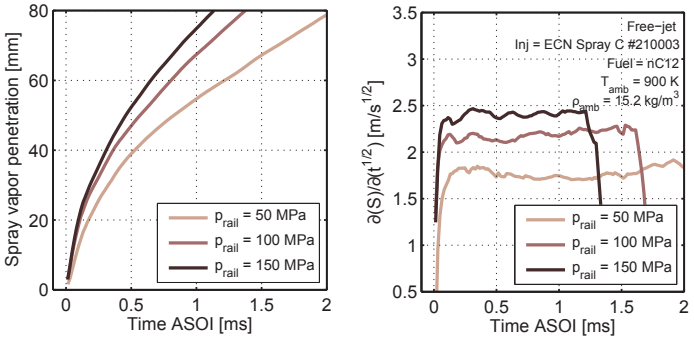

Figure 4.9: Spray penetration sample and its R-parameter at free-jet non-reactive conditions for a diesel ECN "Spray C" injector. (adapted from [21]).

The geometric variables mentioned above are calculated for all the repetitions of each test point condition of the experimental campaign. All the data is then collected and averaged using a polynomial averaging algorithm [21, 38, 39] to get both the shot-to-shot variance and the signal average for each time step. Samples of the averaged signals from 10 repetitions for the spray penetration and the *R-parameter* are presented in Figure 4.9. As seen in Figure 4.9, this method is frequently used to obtain shot-by-shot averages from time-resolved metrics along this work.

Regarding the calculation of the temporal variables, the following methodologies were employed:

- **Start of Injection (*SOI*)**: Start of Injection is used to phase the results and to establish a proper comparison between the different experimental points. Since the optical setups allow the simultaneous image acquisition of the same injection event applying various techniques, all the images recorded refer to the energizing time of the injector, which represents the moment when the injection signal is sent to the injector and the cameras. The methodology used to obtain the SOI was to take the penetration data and apply a numerical fit (Figure 4.10 dashed line) to extrapolate the data and compute SOI as the ASOE time when $S_{fitted} = 0\,\text{mm}$ is achieved [29, 31, 39].

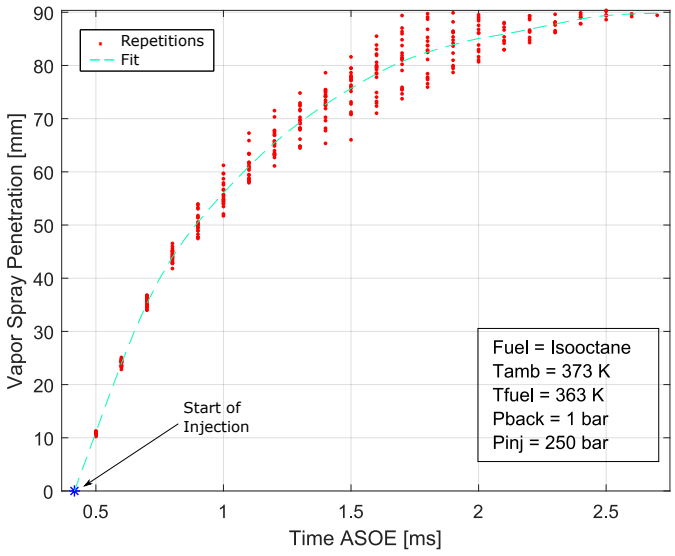

Figure 4.10: Methodology for the SOI calculation for a random penetration curve.

- **Start of spray-wall interaction (τ_w):** From the definition of spray penetration, we can assume that the start of spray-wall interaction starts at $S = d_w$. First, the actual distance from the tip of the injector to the wall was measured from each image. Then a numerical grid fitting was performed using the penetration data from $0.2 \cdot d_w$ to $0.8 \cdot d_w$ to avoid the transient close to the start of injection and the spray part near the wall. This fit is extrapolated to d_w, and the time they coincide is taken as τ_w.

4.4 Wall heat flux and temperature calculation

The signals from the fast thermocouple were used to generate surface temperature profiles at different probe sites. Using the correlation from Figure 3.13, the local surface temperature signal (maximum about 20 mV) was accurately transformed to temperature units, obtaining a time and temperature resolution of 10 µs and approximately 0.0075 K, which are reasonable for the duration of the entire spray-wall interaction phenomenon (1-2 ms).

The data was employed to calculate the heat flux with a MATLAB® routine. The heat equation may be simplified using a one-dimensional heat conduction model with the wall:

$$\frac{\partial T_w}{\partial t} = \alpha_w \cdot \left(\cancelto{0}{\frac{\partial^2 T_w}{\partial x^2}} + \cancelto{0}{\frac{\partial^2 T_w}{\partial y^2}} + \frac{\partial^2 T_w}{\partial z^2} \right) \tag{4.5}$$

$$\frac{\partial T_w}{\partial t} = \alpha_w \cdot \left(\frac{\partial^2 T_w}{\partial z^2} \right) \tag{4.6}$$

where z is the normal coordinate to the surface, T_w is the wall temperature at each point along z, α_w is the thermal diffusivity of the wall material which is 316 stainless steel ($3.476 \times 10^{-6}\,\mathrm{m^2 s^{-1}}$). The 1-D heat flux conduction was justified because the injection time is too short to generate a large radial heat flux and because the temperature change of a solid wall due to SWI occurs just a few millimeters behind the wall surface. This makes the geometry of the wall holes made for thermocouple fittings have a negligible effect on heat flux calculations.

Several numerical and analytical methods to calculate heat flux under this one-dimensional assumption have been explored. There are different analytical formulas for heat flux calculation in the literature, like the one shown in Equation 4.7 [40, 41], where $\sqrt{k_w \rho_w c_{pw}}$ represent the thermal effusivity of the thermocouple junction ($8430\,\mathrm{Ws^{0.5} m^{-2} K^{-1}}$ in this case). Even this solution applies to our case, the final approach to calculate the heat flux for both approaches used in this work (infrared thermography and through the temperature signal of the fast-response thermocouples) was the finite difference method (FDM) because this method allows fixing an initial wall temperature

condition and gives more information regarding the heat transfer through the wall as presented in Figure 4.11.

$$\dot{q}_w(t) = \sqrt{\frac{k_w \rho_w c_{pw}}{\pi}} \cdot \int_{t'=-\infty}^{t} \frac{\partial T_w}{\partial t} \cdot \frac{dt'}{\sqrt{t - t'}} \tag{4.7}$$

The FDM method was applied to solve the parabolic partial derivative Equation 4.6 [42, 43] to obtain the numerical solution of the model shown in Figure 4.11. From this approach, not only $\dot{q}_w(t)$ is obtained, but also the temperature at any wall depth and time, opening the possibility to assess the depth of the wall affected by the SWI. From the known Δt of the data and to the have a computational stability criterion [43], the Fourier number (Fo) was kept below 0.5, accordingly to:

$$Fo = \left(\frac{\alpha_w \cdot \Delta t}{\Delta z^2} \right) < 0.5 \tag{4.8}$$

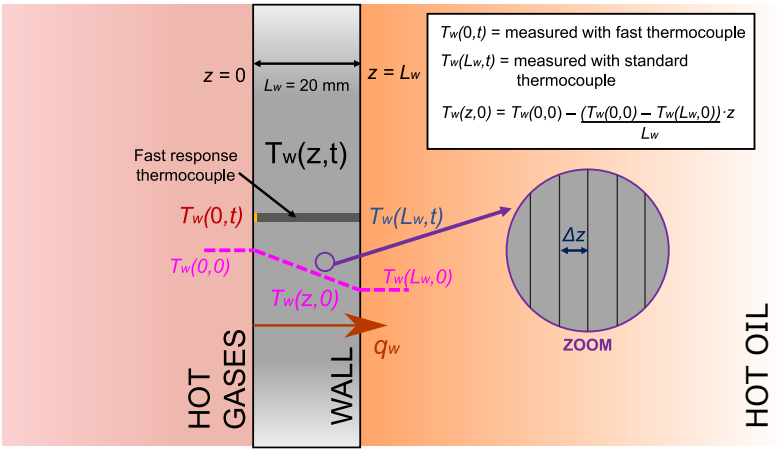

Figure 4.11: Wall heat transfer scheme used for heat flux computation.

By forcing Fo to be 0.3, a spatial resolution of $\Delta z = 11\,\mu m$ was defined. $T_w(z,t)$ was defined as a function of the dimension z and time t, the boundary conditions $T_w(0,t)$ and $T_w(L_w,t)$ are measured with the thermocouples in both sides of the wall by keeping in mind that the inner face of the wall which is in contact with the oil and is not affected by the injection process. Knowing the initial conditions $T_w(0,0)$ and $T_w(L_w,0)$, the initial wall temperature profile $T_w(z,0)$ is estimated as the gradient between these temperatures, and with that, all the assumptions for the FDM implementation are considered.

As an example of this calculation, Figure 4.12 shows a map of the wall temperature change (ΔT_w) for the initial condition ($T_w(z,0)$), showing the solid wall temperature variation with depth through the SWI over time. As can be seen, as is the case for all cases and probes, there is no temperature change beyond the wall depth of 1.5 mm.

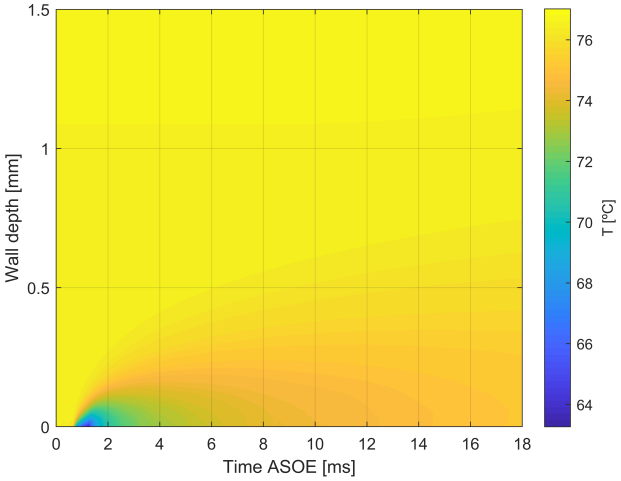

Figure 4.12: Wall temperature fluctuation respect to the initial condition (T_{amb} = 25°C; p_{back} =0.05 MPa; p_{inj} = 25 MPa; T_w = 70°C).

Lastly, the heat transfer per area unit or heat flux calculation is obtained by using the temperature acquired in the hot surface $T_w(0,t)$ and the temperature profile along the whole width of the wall z, as illustrated in Equation 4.9, where k_w is the wall heat conduction coefficient:

$$\dot{q}_w(t) = k_w \cdot \left(\frac{T_w(0,t) - T_w(\Delta z, t)}{\Delta z} \right) \tag{4.9}$$

In Figure 4.13, it is possible to see the curves obtained with the method mentioned above. The top plot (a) shows the raw surface temperature signal obtained from TC1 of the thermoregulated wall for one repetition. The signal noise was eliminated with a Savitzky-Golay filter [44] to get the black line. This filtering is required since the heat flow computation is extremely sensitive to temperature signal fluctuations, even if some information is lost due to this filter, such as a miscalculation of the severity of the initial temperature rise. The filtered wall temperature signals for each repetition are shown in

Figure 4.13-b, where an average is applied to obtain a single curve for each test point. This is also done for the wall temperature variation (Figure 4.13-c) and the surface heat flux curve (Figure 4.13-d).

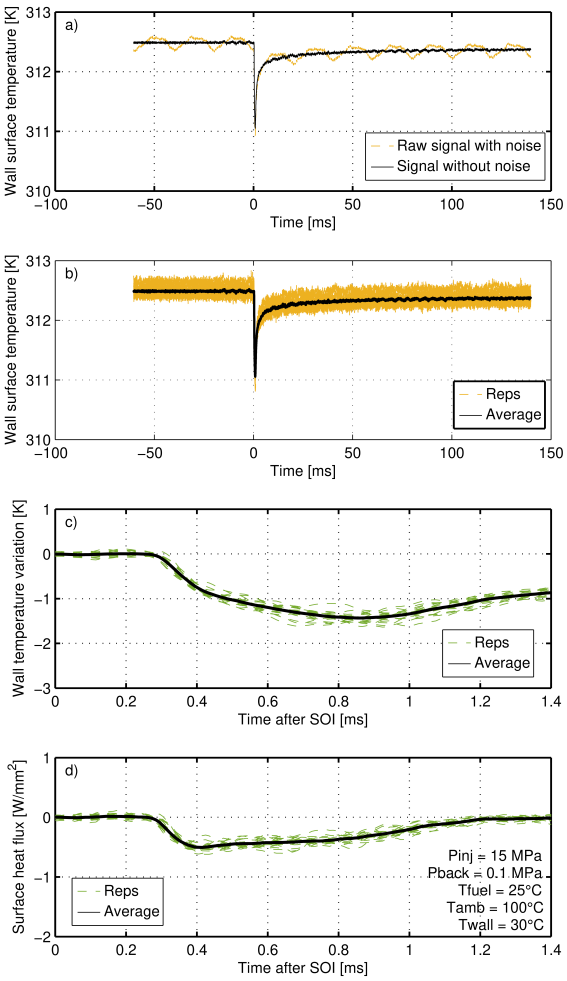

Figure 4.13: Temperature variation and heat flux per repetition and averaged. a) Wall temperature raw signal. b) Wall temperature average. c) Wall temperature variation. d) Surface heat flux.

4.5 Infrared thermography data post-processing

In this section, the methodologies adopted to extract the information from the thermal images acquired in the IR experimental campaign are presented. The section is divided into five subsections: the temperature measurements, the heat flux calculations, the area of impact evaluation, the spray cooling efficiency and the plume jet axis and the spray cone angle.

The foil and paint properties are outlined in Table 4.1.

	Invar		Paint		Units
Thickness	δ_{invar}	50 ± 5	δ_{paint}	10.2 ± 1.6	µm
Density	ρ_{invar}	8000 ± 80	ρ_{paint}	1303 ± 39	$kg{\cdot}m^{-3}$
Thermal conductivity	k_{invar}	21.7 ± 0.22 @373K 42.1 ± 0.42 @473K	k_{paint}	0.74 ± 0.02	$\frac{W}{mK}$
Specific Heat	Cp_{invar}	515 ± 10	Cp_{paint}	2557 ± 230	$\frac{J}{kgK}$
Emissivity	ϵ_{invar}	0.15 ±0.01	ϵ_{paint}	0.95 ± 0.01	-

Table 4.1: Foil and paint properties.

4.5.1 Temperature measurements

A typical delay step temperature drop of the dry side ΔT map obtained by averaging the 125 acquired temperature images after subtracting the one at $t = 0\,s$ is reported in Figure 4.14.

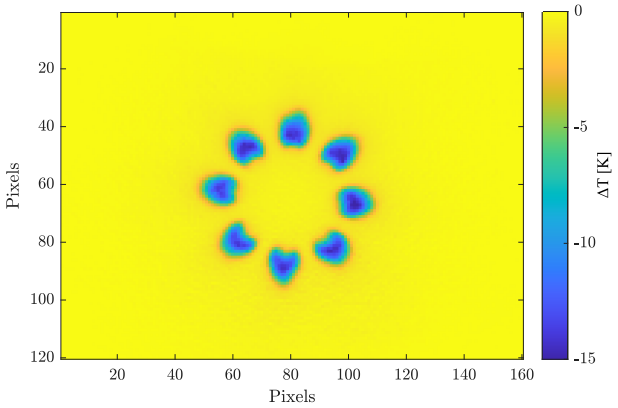

Figure 4.14: Average temperature drop map for $p_{inj} = 20\,MPa$, $T_w = 473\,K$ and $t = 0.9\,ms$.

As it can be noted, the plume shapes present a slight non-uniformity which can be ascribed to a difference in the holes diameters and discharge coefficients [45]. As a result, a post-process has been applied to the temperature drop maps consisting in a rotation around the injector axis and a 45-degree sector symmetrization to reduce the plume to plume temperature variation. The rotation center has been identified as the center of a least square circumference which fits the barycentre of each plume after applying a threshold close to the maximum. An example of a post-processed temperature map is shown in Figure 4.15. The injector nozzle diameter d_0 has been used for the axes normalization.

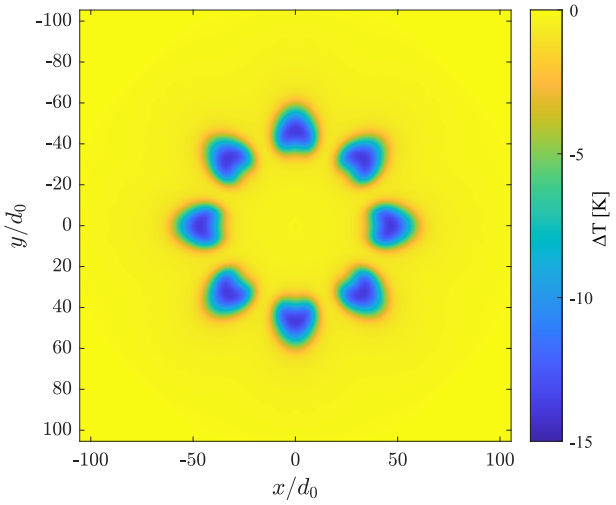

Figure 4.15: Post-processed temperature drop map for $p_{inj} = 20\,MPa$, $T_w = 473\,K$ and $t = 0.9\,ms$.

The time history of the temperature drop of the stagnation spray impact point, which coincides with the maximum temperature drop point, is reported in Figure 4.16 for each investigated condition. Since the IR camera measures the back temperature of the target plate, the first significant temperature drop is obtained only after 0.4 ms from the injection start. This delay is due to the time needed from the spray to reach the plate and to the thermal inertia of the foil which does not allow the thermal wave to instantaneously propagate from the front to the back surface [46].

As it can be seen, the higher the wall temperature of the foil, the higher the temperature drop obtained after the impingement. This behavior is related to the strong influence of the wall temperature on the vaporization of the fuel.

On the other hand, by fixing the wall temperature, the injection pressure contribution has fewer effects on the temperature drop. It is worth noting that the condition at $p_{inj} = 20\,\text{MPa}$ and $T_w = 473\,\text{K}$ exhibits a change in the temperature drop trend for the time interval from 1 ms to 1.3 ms. Such a behavior could be ascribed to small changes in the ambient temperature and the IR camera temperature during the data acquisition. However, these measurement points are not taken into account for the heat flux calculation described later in section 4.5.2.

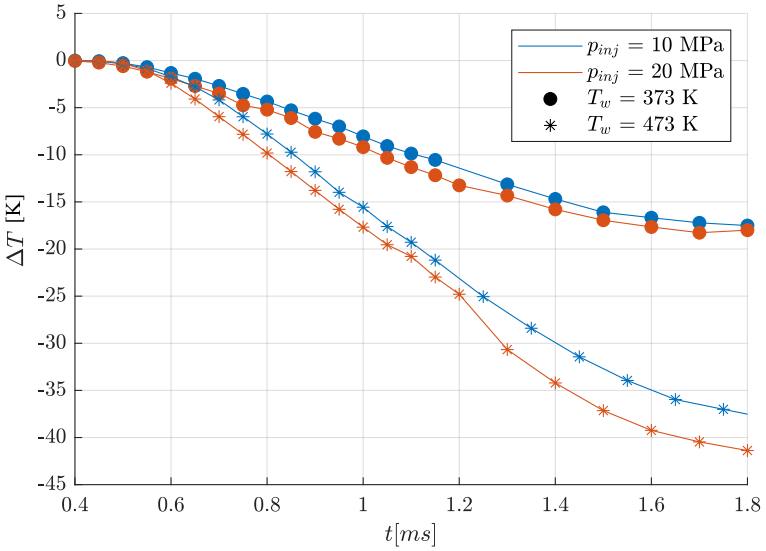

Figure 4.16: Temperature drop curves of the stagnation points over time.

4.5.2 Heat flux

To increase the heat transfer evaluation accuracy and robustness an Inverse Heat Transfer Problem (IHTP) was implemented [47]. For each pixel (x, y coordinate) of the recorded thermal image the spray wall heat flux q_{spray} is computed assuming one dimensional temperature distribution across target plate (slab). Due to the short measuring time (Fourier number <1), also if the Biot number ($Bi = h \cdot s/k$) is < 1, the slab cannot be assumed thermally thin [46]. A sketch of the slab model with all acting heat fluxes, is presented in Figure 4.17. The slab is composed of two materials (Invar and black paint with thickness δ_{invar} and δ_{paint} respectively). The thermal conductivity of Invar was assumed temperature dependent according to [48] while the thickness and the remaining thermal physical properties were defined using the supplier data

sheet. The paint thermal physical properties were determined from the data of Raghu and Philip [49], while the paint thickness was measured using Fisher Dualscope MPOR-FP.

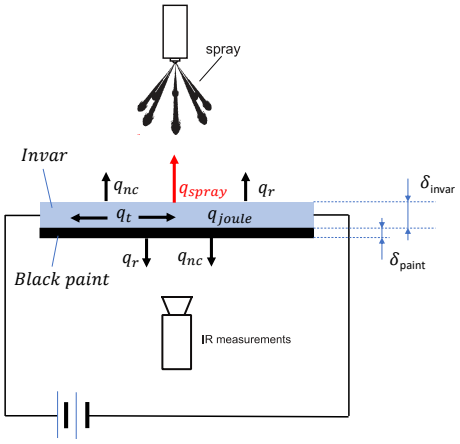

Figure 4.17: A sketch of the slab model with all acting heat fluxes.

In the following T_w, is the temperature of the upper wall and T_1 is the temperature of the lower wall. The test run time [0, t_f] can be divided in two phases: the spray start-up (the time required from the spray to reach the wall plus the time required to the spray jet to be completely developed) and the quasi-steady phase where the spray wall heat flux is steady. These two phases are indicated hereinafter as [0,t_i] and [t_i,t_f]. Different heat fluxes are present on the upper wall: the spray wall heat flux q_{spray} (assumed equal zero in [0,t_i] and constant in [t_i,t_f]), natural convection heat flux q_{nc} and radiative heat flux q_r. On the lower wall only the natural convection and radiative heat flux are present. The Invar slab part is also heated by Joule effect q_{joule} as described in the experimental apparatus. The radiative flux for the upper wall is computed as $q_r = \sigma \cdot \epsilon_{invar} \cdot (T_w^4 - T_{amb}^4)$, while at lower wall $q_r = \sigma \cdot \epsilon_{paint} \cdot (T_1^4 - T_{amb}^4)$ where σ is the Stefan-Boltzmann constant. The natural convection heat flux at the upper wall is $q_{nc} = h_{up} \cdot (T_w - T_{amb})$ while at lower wall $q_{nc} = h_{down} \cdot (T_1 - T_{amb})$. For an horizontal plate, the Nusselt number for the natural convection with exchange on the upper side is $Nu = 0.54 \cdot (Gr \cdot Pr)^{1/4}$ while with exchange on the lower side is $Nu = 0.27 \cdot (Gr \cdot Pr)^{1/4}$ [50]. As such, it can be assumed $h_{up} = 2 \cdot h_{down}$. Up to time t_i, the temperature across the slab was assumed

constant in time and equal to the temperature $T_{1_{exp}}$ measured by the infrared camera. Then, by making an energy balance in the phase [0, t_i] between the measured q_{joule} , q_{nc} and q_r on upper and lower wall, it is possible to compute the natural convection heat transfer coefficient h_{up} and h_{down}. Due to the small temperature variation, the h_{down} will be assumed constant during the next phase.

In the phase [t_i, t_f] the transient one-dimensional Fourier heat equation in the slab is solved with a finite difference method that guarantees a second order accuracy in both space and time without high computational burden. An initial guess of the heat conduction solution is formulated by an arbitrary spray heat flux. Then, the calculated back surface temperature solution ($T_{1_{num}}$) is compared to the measured one ($T_{1_{exp}}$) in a least-square sense.

$$R(q_{spray}, t_i) = \int_{t_i}^{t_f} \cdot \left[T_{1_{num}}(t - t_i) - T_{1_{exp}}(t)\right]^2 dt \tag{4.10}$$

The function is used as an objective functional to be minimized through a proper optimization scheme by updating the heat flux guess until convergence is reached. The optimization procedure is based on the trust-region-reflective algorithm [51]. In the present data reduction *tf* was limited to 1.05 ms, that is less of spray duration (1 ms) plus time required from spray to reach the wall (0.113-0.126 ms), when the spray was still active. It should be noted also that the terms q_{joule} , q_{nc} and q_r are very small respect q_{spray} at the stagnation point (typically 0.1%). These latter terms influence the data reduction essentially in the region of low q_{spray}.

In Figure 4.18, the typical experimental and optimized numerical temperature drop obtained by the Fourier equation hereinafter have been compared in four different point of coordinates. As it can be noted the experimental and numerical data are in good agreement, as illustrated by the coefficient of determination. Most importantly, in the presence of strong spatial temperature gradients, 1D techniques may underestimate the heat flux by neglecting the effects of lateral conduction q_t [52–54]. To prove that q_t is negligible in the present tests, thanks to the computed temperature distribution along the slab, first order tangential conduction heat flux is estimated by the following relationship

$$q_t = -k_{invar} \cdot \delta_{invar} \cdot \left(\frac{\partial^2 \overline{T_{invar}}}{\partial^2 x} + \frac{\partial^2 \overline{T_{invar}}}{\partial^2 y} \right) - k_{paint} \cdot \delta_{paint} \cdot \left(\frac{\partial^2 \overline{T_{paint}}}{\partial^2 x} + \frac{\partial^2 \overline{T_{paint}}}{\partial^2 y} \right) \tag{4.11}$$

where $\overline{T_{invar}}$ and $\overline{T_{paint}}$ are the spatial average temperature along the slab in the Invar and paint parts respectively at final time t_f when q_t is maximum.

In Figure 4.19, the tangential conduction heat flux distribution limited to the spray impact area (see subsection 4.5.3) is presented for the test condition p_{inj}=20 MPa and T_w=473 K, in which the maximum values of q_t are detected. As it can be noted, the absolute maximum values are measured on the borders of the impact area and on the two sides of the stagnation points where the temperature gradient is maximum. In Figure 4.19 is also presented the percentage tangential conduction error $\tau = \frac{|q_t|}{q_{spray}} \cdot 100$ map which is at worst equal to 2.7%, with an average value of 0.66% and 0.45% in the stagnation point confirming the negligibility of the tangential conduction.

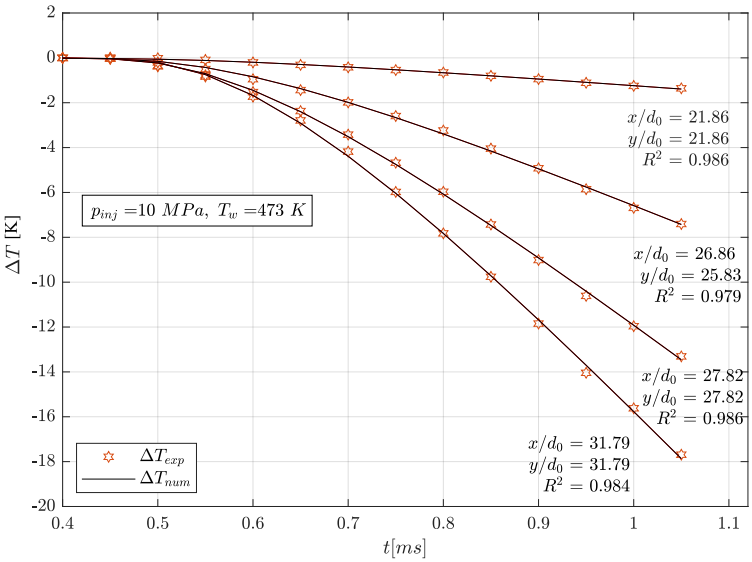

Figure 4.18: Comparison between the measured and the numerically computed temperature (from the inverse heat transfer model) for $p_{inj} = 10$ MPa and $T_w = 473$ K.

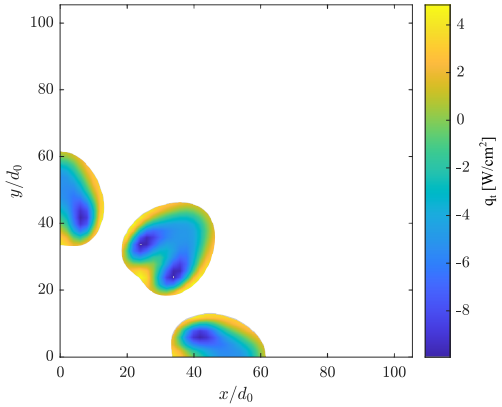

(a) Tangential conduction heat flux q_t

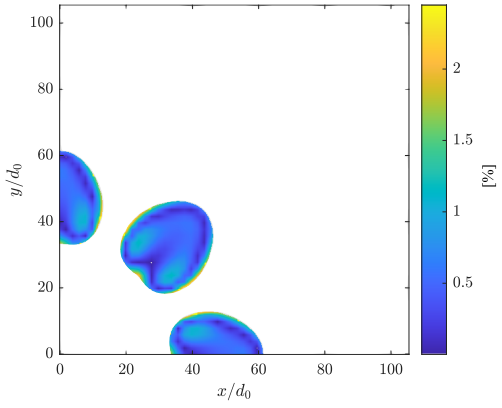

(b) Tangential conduction error

Figure 4.19: Tangential conduction heat flux distribution limited to the spray impact area for $p_{inj} = 20\,\mathrm{MPa}, T_w = 473\,\mathrm{K}$.

4.5.3 Area of impact

Different solutions to correctly identify the spray area of impact from the heat flux maps were analyzed. The approach that has shown the better agreement with flow visualizations (not shown herein) was the Otsu method [55, 56], which is based on an automatic threshold analysis by maximizing the inter-class variance of the image Black to obtain the best separation of its interest regions. In Figure 4.20, the methodology is applied and the results shown are related to the test configuration at $p_{inj} = 10\,\mathrm{MPa}$ and $T_w = 473\,\mathrm{K}$. Figure 4.20 reports the heat flux map before the segmentation, the area of impact

region calculated using the Otsu method and its accuracy can be checked by overlapping the two previous images.

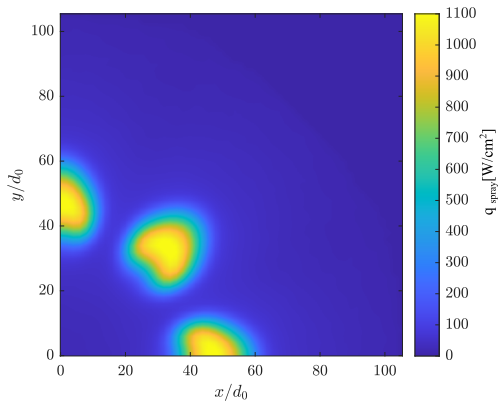

(a) Spray heat flux map (W/cm^2)

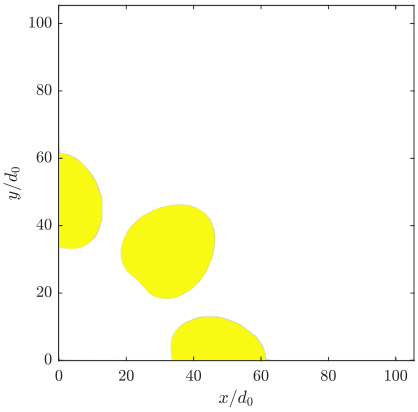

(b) Area of impact

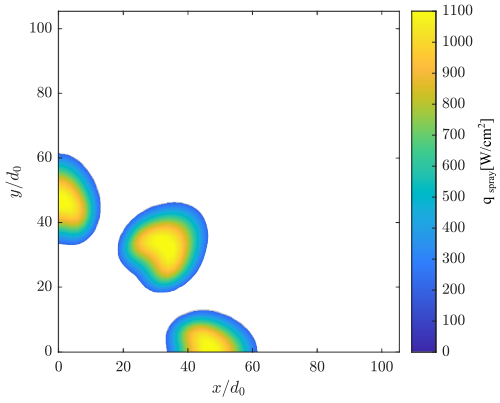

(c) Methodology examination

Figure 4.20: Area of impact determination methodology for $p_{inj} = 20\,\text{MPa}, T_w = 473\,\text{K}$.

4.5.4 Plume jet axis and spray cone angle evaluation.

The plume direction angle β and the spray cone angle θ are obtained with a geometrical reconstruction approach, by making use 3D geometry of the "Spray G" injector (available in ECN website [57]) and the wall heat flux distribution. The position of the maximum heat flux in the impinging area and the origin of jet are used to estimate the angle β assuming that plume jet axis is the line joining these two points. To increase the accuracy identification

of the maximum position (with subpixel resolution) the heat transfer data near maximum was fitted with a gaussian function. The spray cone angle θ was estimated by using a similar geometrical approach assuming that it is equal to the angle between the two lines starting from the origin of jet and that end at the extremity of the minor axis of the elliptical like shape spray area of impact.

References

[1] Du, Jianguo, Mohan, Balaji, Sim, Jaeheon, Fang, Tiegang, and Roberts, William L. "Experimental and analytical study on liquid and vapor penetration of high-reactivity gasoline using a high-pressure gasoline multi-hole injector". In: *Applied Thermal Engineering* 163.July (2019), p. 114187. DOI: 10.1016/j.applthermaleng.2019.114187.

[2] Cavicchi, Andrea et al. "Numerical and experimental analysis of the spray momentum flux measuring on a GDI injector". In: *Fuel* 206 (2017), pp. 614–627. DOI: 10.1016/j.fuel.2017.06.054.

[3] Guo, Hengjie, Li, Yanfei, Wang, Bo, Zhang, Huiqiang, and Xu, Hongming. "Numerical investigation on flashing jet behaviors of single-hole GDI injector". In: *International Journal of Heat and Mass Transfer* 130 (2019), pp. 50–59. DOI: 10.1016/j.ijheatmasstransfer.2018.10.088.

[4] Cavicchi, Andrea, Postrioti, Lucio, and Scarponi, Edoardo. "Hydraulic analysis of a GDI injector operation with close multi-injection strategies". In: *Fuel* 235.July 2017 (2019), pp. 1114–1122. DOI: 10.1016/j.fuel.2018.08.089.

[5] Vaquerizo, Daniel. "Study on Advanced Spray-Guided Gasoline Direct Injection Systems". PhD thesis. Universitat Politècnica de València, 2017.

[6] Moon, Seoksu et al. "Ultrafast X-ray study of multi-hole GDI injector sprays: Effects of nozzle hole length and number on initial spray formation". In: *Experimental Thermal and Fluid Science* 68 (2015), pp. 68–81. DOI: 10.1016/j.expthermflusci.2015.03.027.

[7] Papoulias, D, Giannadakis, E, Mitroglou, N, Gavaises, M, and Theodorakakos, A. "Cavitation in fuel injection systems for spray-guided direct injection gasoline engines". In: *SAE Technical Papers* 724 (2007), pp. 776–790. DOI: 10.4271/2007-01-1418.

[8] Mitroglou, N, Nouri, J M, Yan, Y, Gavaises, M, and Arcoumanis, C. "Spray structure generated by multi-hole injectors for gasoline direct-injection engines". In: *SAE Technical Papers* 724 (2007), pp. 776–790. DOI: 10.4271/2007-01-1417.

[9] Shost, Mark A, Lai, Ming-Chia, Befrui, Bizhan, Spiekermann, Peter, and Varble, Daniel L. "GDi Nozzle Parameter Studies Using LES and Spray Imaging Methods". In: *SAE Technical Papers*. Vol. 1. 2014. DOI: 10.4271/2014-01-1434.

[10] Jung, Yongjin, Manin, Julien, Skeen, Scott A, and Pickett, Lyle M. "Measurement of Liquid and Vapor Penetration of Diesel Sprays with a Variation in Spreading Angle". In: *SAE Technical Paper 2015-01-0946* (2015). DOI: 10.4271/2015-01-0946.

[11] Payri, Raul, Salvador, Francisco Javier, Manin, Julien, and Viera, Alberto. "Diesel ignition delay and lift-off length through different methodologies using a multi-hole injector". In: *Applied Energy* 162 (2016), pp. 541–550. DOI: 10.1016/j.apenergy.2015.10.118.

[12] Pastor, Jose Vicente, Payri, Raul, Garcia-Oliver, Jose Maria, and Briceño, Francisco Javier. "Schlieren Methodology for the Analysis of Transient Diesel Flame Evolution". In: *SAE International Journal of Engines* 6.3 (2013), pp. 1661–1676. DOI: 10.4271/2013-24-0041.

[13] Montanaro, Alessandro et al. "Schlieren and Mie Scattering Visualization for Single- Hole Diesel Injector under Vaporizing Conditions with Numerical Validation". In: *SAE Technical Paper* (2014). DOI: 10.4271/2014-01-1406.

[14] Lillo, Peter M, Pickett, Lyle M, Persson, Helena, Andersson, Öivind, and Kook, Sanghoon. "Diesel Spray Ignition Detection and Spatial/Temporal Correction". In: *SAE Technical Paper 2012-01-1239* (2012). DOI: 10.4271/2012-01-1239.

[15] Allocca, Luigi, Lazzaro, Maurizio, Meccariello, G, and Montanaro, Alessandro. "Schlieren visualization of a GDI spray impacting on a heated wall: Non-vaporizing and vaporizing evolutions". In: *Energy* 108 (2016), pp. 93–98. DOI: 10.1016/j.energy.2015.09.107.

[16] Gawthrop, D. B. "Applications of the Schlieren method of photography". In: *Review of Scientific Instruments* 2.9 (1931), pp. 522–531. DOI: 10.1063/1.1748821.

[17] Gladstone, J H and Dale, T P. "Researches on the Refraction, Dispersion, and Sensitiveness of Liquids". In: *Philosophical Transactions of the Royal Society of London* 153 (1863), pp. 317–343. DOI: 10.2307/108799.

[18] Settles, G. S. *Schlieren and Shadowgraph Techniques*. 2001. DOI: 10.1007/978-3-642-56640-0.

[19] Manin, Julien, Bardi, Michele, and Pickett, Lyle M. "Evaluation of the liquid length via diffused back-illumination imaging in vaporizing diesel sprays". In: *Comodia*. Fukuoka, 2012.

[20] Westlye, Fredrik R et al. "Diffuse back-illumination setup for high temporally resolved extinction imaging". In: *Applied Optics* 56.17 (2017). DOI: 10.1364/AO.56.005028.

[21] Gimeno, Jaime, Bracho, Gabriela, Martí-Aldaraví, Pedro, and Peraza, Jesús E. "Experimental study of the injection conditions influence over n-dodecane and diesel sprays with two ECN single-hole nozzles. Part I: Inert atmosphere". In: *Energy Conversion and Management* 126 (2016), pp. 1146–1156. DOI: 10.1016/j.enconman.2016.07.077.

[22] Payri, Raul, Salvador, Francisco Javier, Marti-Aldaravi, Pedro, and Vaquerizo, Daniel. "ECN Spray G external spray visualization and spray collapse description through penetration and morphology analysis". In: *Applied Thermal Engineering* 112 (2017), pp. 304–316. DOI: 10.1016/j.applthermaleng.2016.10.023.

[23] Pickett, Lyle M, Genzale, Caroline L, Manin, Julien, Malbec, Louis-Marie, and Hermant, Laurent. "Measurement Uncertainty of Liquid Penetration in Evaporating Diesel Sprays". In: *ILASS Americas 23rd Annual Conference on Liquid Atomization and Spray Systems*. Ventura, CA (USA): ILASS-Americas, 2011.

[24] Ghandhi, J B and Heim, D M. "An optimized optical system for backlit imaging". In: *Review of Scientific Instruments* 80 (2009). DOI: 10.1063/1.3128728.

[25] Hamzah, A et al. "A comparison of diffuse back-illumination (DBI) and Mie-scattering technique for measuring the liquid length of severely flashing spray". In: *20th Australasian Fluid Mechanics Conference*. December. Perth, Australia, 2016.

[26] Payri, Raul, Gimeno, Jaime, Peraza, Jesús E, and Bazyn, Tim. "Spray / wall interaction analysis on an ECN single-hole injector at diesel-like conditions through Schlieren visualization". In: *Proc. 28th ILASS-Europe, Valencia* September (2017).

[27] Payri, Raul, Hardy, Gilles, Gimeno, Jaime, and Bautista, Abian. "Analysis of counterbore effect in five diesel common rail injectors". In: *Experimental Thermal and Fluid Science* 107 (2019), pp. 69–78. DOI: 10.1016/j.expthermflusci.2019.05.008.

[28] Bardi, Michele. "Partial needle lift and injection rate shape effect on the formation and combustion of the Diesel spray". PhD thesis. Valencia (Spain): Universitat Politècnica de València, 2014. DOI: 10.4995/Thesis/10251/37374.

[29] Payri, Raul, Viera, Juan Pablo, Gopalakrishnan, Venkatesh, and Szymkowicz, Patrick G. "The effect of nozzle geometry over the evaporative spray formation for three different fuels". In: *Fuel* 188 (2017), pp. 645–660. DOI: 10.1016/j.fuel.2016.06.041.

[30] Pastor, Jose Vicente, Payri, Raul, Garcia-Oliver, Jose Maria, and Nerva, Jean-Guillaume. "Schlieren Measurements of the ECN-Spray A Penetration under Inert and Reacting Conditions". In: *SAE Technical Paper 2012-01-0456* (2012). DOI: 10.4271/2012-01-0456.

[31] Payri, Raul, Salvador, Francisco Javier, Bracho, Gabriela, and Viera, Alberto. "Differences between single and double-pass schlieren imaging on diesel vapor spray characteristics". In: *Applied Thermal Engineering* 125 (2017), pp. 220–231. DOI: 10.1016/j.applthermaleng.2017.06.140.

[32] Naber, Jeffrey D and Siebers, Dennis L. "Effects of Gas Density and Vaporization on Penetration and Dispersion of Diesel Sprays". In: *SAE Paper 960034* (1996). DOI: 10.4271/960034.

[33] Araneo, Lucio, Coghe, Aldo, Brunello, G, and Cossali, Gianpietro E. "Experimental Investigation of gas density effects on diesel spray penetration and entrainment". In: *SAE Paper 1999-01-0525* (1999).

[34] Desantes, Jose Maria, Payri, Raul, Salvador, Francisco Javier, and Gil, Antonio. "Development and validation of a theoretical model for diesel spray penetration". In: *Fuel* 85.7-8 (2006), pp. 910–917.

[35] Gimeno, Jaime. "Desarrollo y aplicación de la medida de flujo de cantidad de movimiento de un chorro Diesel". PhD thesis. E.T.S. Ingenieros Industriales, Universidad Politécnica de Valencia, 2008.

[36] Payri, Raul, Salvador, Francisco Javier, Gimeno, Jaime, and Peraza, Jesús E. "Experimental study of the injection conditions influence over n-dodecane and diesel sprays with two ECN single-hole nozzles. Part II: Reactive atmosphere". In: *Energy Conversion and Management* 126 (2016), pp. 1157–1167. DOI: 10.1016/j.enconman.2016.07.079.

[37] Martí-Aldaraví, Pedro. "Development of a computational model for a simultaneous simulation of internal flow and spray break-up of the Diesel injection process". PhD thesis. Valencia: Universitat Politècnica de València, 2014. DOI: 10.4995/Thesis/10251/43719.

[38] Benajes, Jesus, Payri, Raul, Bardi, Michele, and Martí-aldaraví, Pedro. "Experimental characterization of diesel ignition and lift-off length using a single-hole ECN injector". In: *Applied Thermal Engineering* 58.1-2 (2013), pp. 554–563. DOI: 10.1016/j.applthermaleng.2013.04.044.

[39] Payri, Raul, Salvador, Francisco Javier, Gimeno, Jaime, and Viera, Juan Pablo. "Experimental analysis on the influence of nozzle geometry over the dispersion of liquid n-dodecane sprays". In: *Frontiers in Mechanical Engineering* 1 (2015), pp. 1–10. DOI: 10.3389/fmech.2015.00013.

[40] Moussou, Julien, Pilla, Guillaume, Rabeau, Fabien, Sotton, Julien, and Bellenoue, Marc. "High-frequency wall heat flux measurement during wall impingement of a diffusion flame". In: *International Journal of Engine Research* (2019).

[41] Meingast, Ulrich, Staudt, Michael, Reichelt, Lars, and Renz, Ulrich. "Analysis of Spray / Wall Interaction Under Diesel Engine Conditions". In: *SAE Technical Paper 2000-01-0272* 724 (2000), pp. 1–15.

[42] Carnahan, Brice, Luther, H A, and Wilkes, James O. *Applied Numerical Methods*. Wiley, 1969.

[43] Nakamura, Joyce. *Applied Numerical Methods with Software*. 1st. Upper Saddle River, NJ, USA: Prentice Hall PTR, 1990.

[44] Savitzky, Abraham. and Golay, M J E. "Smoothing and Differentiation of Data by Simplified Least Squares Procedures." In: *Analytical Chemistry* 36.8 (1964), pp. 1627–1639. DOI: 10.1021/ac60214a047.

[45] Duke, Daniel J. et al. "Internal and near nozzle measurements of Engine Combustion Network "Spray G" gasoline direct injectors". In: *Experimental Thermal and Fluid Science* 88 (2017), pp. 608–621. DOI: https://doi.org/10.1016/j.expthermflusci.2017.07.015.

[46] Astarita, Tommaso and Carlomagno, Giovanni Maria. *Infrared Thermography for Thermo-Fluid-Dynamics*. Springer Berlin Heidelberg, 2013. DOI: 10.1007/978-3-642-29508-9.

[47] Walker, D. Greg and Scott, Elaine P. "Evaluation of Estimation Methods for High Unsteady Heat Fluxes from Surface Measurements". In: *Journal of Thermophysics and Heat Transfer* 12.4 (1998), pp. 543–551. DOI: 10.2514/2.6374.

[48] Watson, T. W. and Robinson, H. E. "Thermal Conductivity of Some Commercial Iron-Nickel Alloys". In: *Journal of Heat Transfer* 83.4 (1961), pp. 403–407. DOI: 10.1115/1.3683651.

[49] Raghu, O. and Philip, J. "Thermal properties of paint coatings on different backings using a scanning photo acoustic technique". In: *Measure. Sci. Technol* (2006).

[50] Khalifa, Abdul-Jabbar N. "Natural convective heat transfer coefficient a review: I. Isolated vertical and horizontal surfaces". In: *Energy Conversion and Management* 42.4 (2001), pp. 491–504. DOI: https://doi.org/10.1016/S0196-8904(00)00042-X.

[51] Coleman, T.F. and Li, Y. "An Interior trust region approach for nonlinear minimization subject to bounds". In: *SIAM* (1996), pp. 418–445. DOI: doi:10.1137/0806023.

[52] Gibbons, M.J. and Robinson, A.J. "Heat transfer characteristics of single cone-jet electrosprays". In: *International Journal of Heat and Mass Transfer* 113 (2017), pp. 70–83.

[53] Luca, L. de, Cardone, G., Aymer de la Chevalerie, D., and Fonteneau, A. "Goertler instability of a hypersonic boundary layer". In: *Experiments in Fluids* 16.1 (1993), pp. 10–16. DOI: 10.1007/BF00188500.

[54] Avallone, F., Greco, C. S., Schrijer, F. F. J., and Cardone, G. "A low-computational-cost inverse heat transfer technique for convective heat transfer measurements in hypersonic flows". In: *Experiments in Fluids* 56.4 (2015), p. 86. DOI: 10.1007/s00348-015-1951-5.

[55] Vende, Trinque, Lacour, Delahaye, and Fournaison. "Efficiency of water spraying on a heat exchanger: Local characterization with the impacted surface". In: *Applied Thermal Engineering* 128 (2017), pp. 684–695. DOI: http://dx.doi.org/10.1016/j.applthermaleng.2017.09.031.

[56] Otsu, Noboyuki. "A Threshold Selection Method from Gray-Level Histograms". In: *IEEE Transactions on system, Man, and Cybernetics* (1979). DOI: 0018-9472/79/0100-006200.75.

[57] ECN. "Engine Combustion Network". In: *https://ecn.sandia.gov/gasoline-spray-combustion/* (2020).

Chapter 5

Inert spray under free-jet and wall-impingement conditions against an ambient-temperature wall

5.1 Introduction

In this chapter, a characterization of the spray morphology and geometrical parameters such as spray penetration, area of the spray, spray spreading onto the quartz wall, and spray width after the impingement are analyzed. The analysis is made through external flow visualization and described along with the effects of variations in the measuring conditions (as the injection and ambient pressures, fuel, and ambient temperatures, and the injector tip-to-wall distance) over those magnitudes. The conditions measured were decided, taking into account the recommendations of the ECN [1].

This section presents two main sub-parts, the results obtained from the free-jet injection campaign and the results from the quartz wall-spray impingement interactions.

5.2 Test matrix and fuel properties

Gasoline is formed from different types of hydrocarbons, and their differences are a function of the various factors contributing to their formation. For this reason, it is difficult to reproduce the same gasoline composition in a research environment, and surrogates that mimic its behavior are sought. A typical gasoline substitute is an isooctane/n-heptane mixture intended to simulate octane rating to control the degree of auto-ignition.

Of the surrogates, single-component fuels are the easiest to reproduce. In this case, the isooctane has been chosen to approximate the distillation curve of commercial gasoline to simulate volatility. The following publication use isooctane as research fuel for GDI research [2]. Table 5.2 shows the most relevant properties of the isooctane, and Table 5.1 shows the test matrix used in the visualization campaign.

Table 5.1: Test matrix for the transparent isothermal wall.

Parameter	Value/Type	Units
Injector	Continental	-
Fuel	Isooctane	-
ET	0.8	ms
Rail pressure (P_r)	150/200/250	bar
Back pressure (P_b)	0.5**/1	bar
Fuel temperature (T_{fuel})	25/90**	°C
Ambient temperature (T_{amb})	25/50/100	°C
Wall distance (d_w)	25/35	mm
Wall angle	60/90	°
Repetitions per test	10	-

** The low ambient back pressure with the higher fuel temperature represent flash boiling conditions.

5.3 Free-jet visualization

This section examines liquid and vapor free spray penetration in regards of spray break-up and fuel evaporation, as well as how they are influenced by changing the operating conditions of the tests. This is made by visualizating the liquid phase of the spray with the use of the DBI technique, and the vapor phase of the spray using the Schlieren technique, to acquire the image contours such as those seen in the samples presented in Figure 5.1. Higher ambient temperatures increase the kinetic energy of the molecules at the spray surface,

Table 5.2: Isooctane properties obtained from National Institute of Standards and Technology (NIST) [3].

Properties (@300K)	iso-octane	Units
Liquid density	696.57	kg/m^3
Viscosity	0.456	$mN{\cdot}s/m^2$
Surface tension	20.96	mN/m
Vapor pressure	2.08	kPa
Latent heat	41.4	kJ/mol
Specific heat	2.04	kJ/Kg·K

shortening the distance covered by the liquid core and thus accelerating the liquid evaporation rate. As observed in the literature [4–6], a higher rail pressure increases the fuel injection rate while increasing the gas entrainment and maintaining the energy balance.

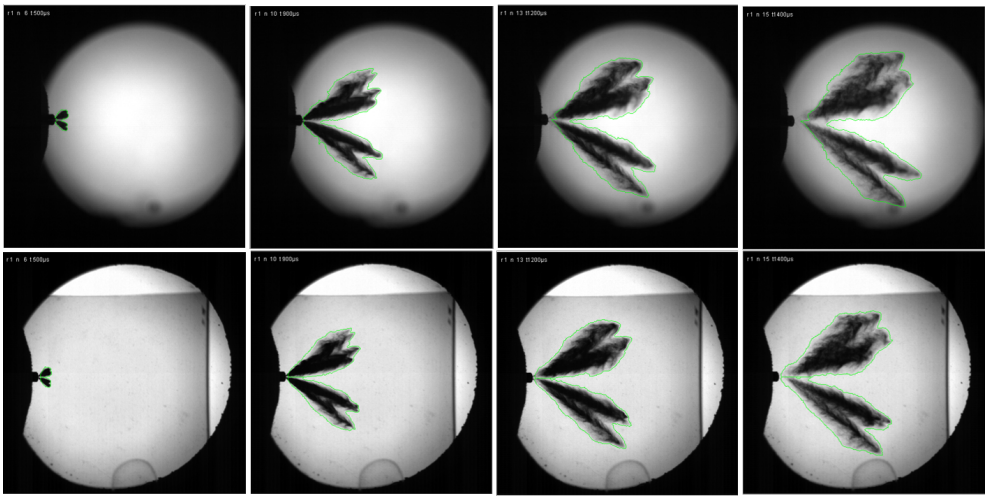

Figure 5.1: Example of images acquired by DBI (top) and Schlieren (bottom) techniques for free jet visualization conditions. All the images are presented with ASOE time reference. $p_{inj} = 25\,\mathrm{MPa}, p_{back} = 0.1\,\mathrm{MPa}, T_{amb} = 25\,^{\circ}\mathrm{C}, T_{fuel} = 25\,^{\circ}\mathrm{C}$

Various injection conditions are investigated in the following subsections, and their effects on the spray morphology and development are presented in terms of spray penetration and R-parameter (which is its derivative respect to the square root of time), this variable was explained in subsection 4.3.4. The standard deviation is represented by using a lighter shade behind all the

curves. For further analysis will be necessary to keep in mind that the spray penetration follows the correlation shown in Equation 5.1. This correlation was employed in several works and calculated using dimensional analysis [7, 8].

$$S \propto \rho_{amb}^{-1/4} \cdot \Delta p_{inj}^{1/4} \cdot tan(\phi/2)^{-1/2} \cdot D_o^{1/2} \cdot t^{1/2} \tag{5.1}$$

where D_o represents the nozzle outlet diameter, ρ_{amb} the chamber air density, p_{inj} the injection pressure, ϕ the spray angle and t the time. It is important to say that this expression can be written also, as a function of the spray momentum flux.

5.3.1 Injection pressure variation

Three injection pressures were used in the experimental campaign covering the typical operating range of the Continental Injector as described in Table 5.1. In Figure 5.2-top, it is possible to notice that a higher injection pressure corresponds with a higher spray penetration. For the conditions tested, the behavior of the vapor and liquid phase of the spray is nearly similar. The R-parameter is presented and follows the same trend in the Figure 5.2-bottom. With higher injection pressures, a higher R-parameter value is obtained. The trend obtained can be explained because as the injection pressure increases, more momentum is transmitted to the fluid when the injector needle rises, increasing the speed of fuel through the nozzle. It is important to add that the R-parameter value remains nearly constant, corroborating the theory in which $R \propto \dot{M}^{1/4}$ or $R \propto \Delta p_{inj}^{1/4}$ as shown in Equation 5.1.

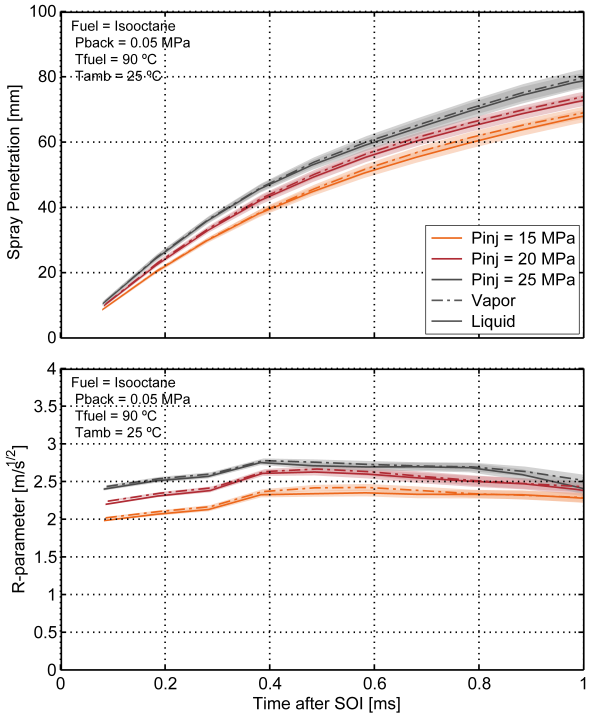

Figure 5.2: Pressure effect on liquid and vapor penetration along time.

Figure 5.3 shows the spray width variation with time measured at 20mm from the nozzle tip. The spray width is greater for the higher injection pressure in the first moments of the injection event. Then, a decreasing trend is noticeable at the end of the curves caused by the end of the injection and the fuel evaporation in the outer part of the spray plume.

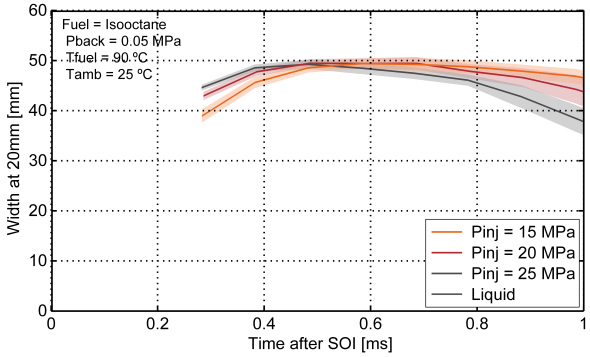

Figure 5.3: Pressure effect over the spray width at 20mm from the injector tip.

5.3.2 Ambient back-pressure variation

Two ambient back-pressures were used in the experimental campaign, obtaining as expected, a higher spray penetration value for the chamber pressure below the atmosfheric reference. And again, as in the previous case the behavior of the vapor and liquid phase of the spray is nearly similar. The back-pressure acts as a force that slows down the advance of the spray during its development, the greater the back-pressure, the greater the resistance exerted by the air on the advance of the spray inside the chamber.

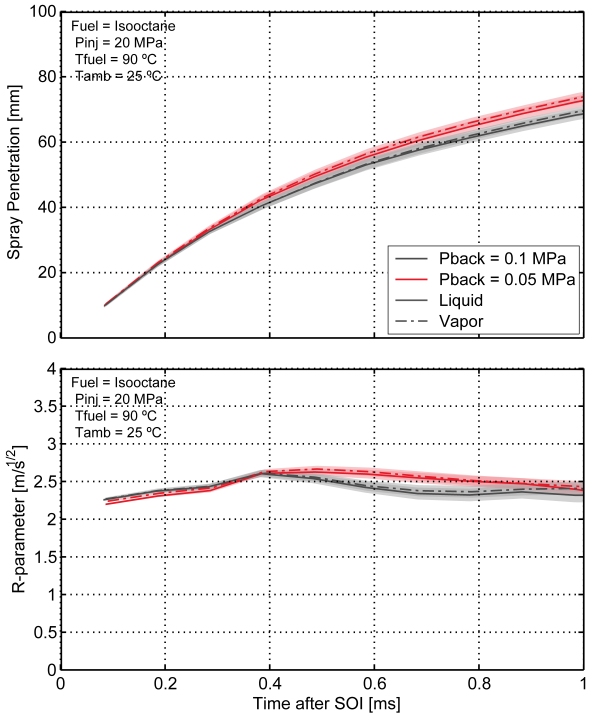

Figure 5.4: Ambient back-pressure effect over the liquid and vapor penetration.

Figure 5.5 shows the effect of the ambient back-pressure over the spray width. The trend is different than expected because the lower ambient back-pressure should produce lesser spray angles, translating into smaller spray widths. The possible explanation is the flash boiling that occurs when higher fuel temperatures and lower ambient back pressure conditions are defined. The flash boiling produces an expansion of the spray that can accelerate the spray and increase the spray angle [9].

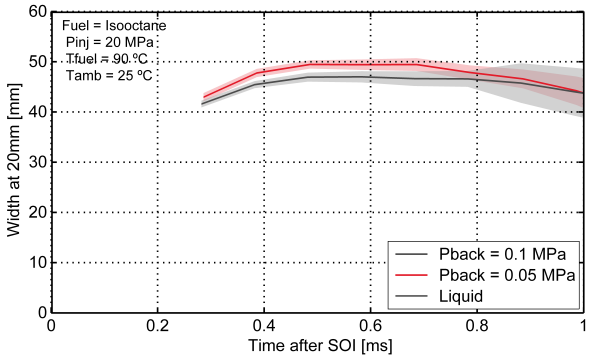

Figure 5.5: Ambient back-pressure effect over the spray width at 20mm from the injector tip.

5.3.3 Fuel temperature variation

A noticeable change in the penetration curve was found by varying the fuel temperature for the case of low ambient back pressure condition, as it can be seen in Figure 5.6, where a higher fuel temperature means a lower spray penetration over time. This is caused mainly by differences in the spray angle values. A higher spray angle for the higher fuel temperature produces a lesser spray penetration under low ambient back pressure conditions, as seen in Figure 5.6 and Figure 5.7. The changes in the spray angle are related to the flash-boiling and evaporation of the spray under the combination of low ambient back pressure and higher fuel temperatures.

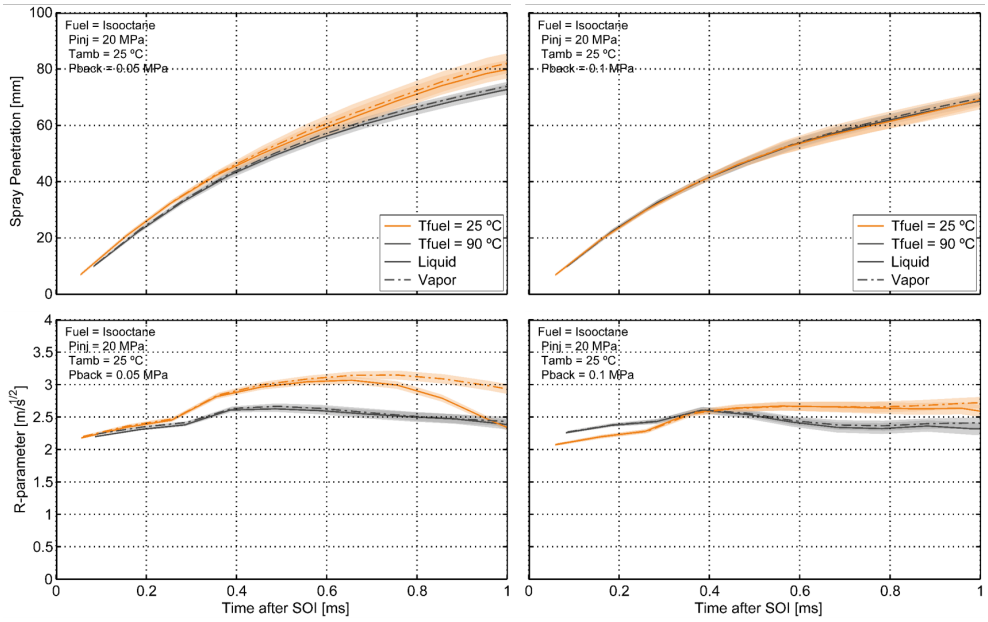

Figure 5.6: Fuel temperature effect over the liquid and vapor penetration and R-parameter with ambient back pressure variation from left to right.

In Figure 5.7, the lower fuel temperatures have lower width values under the lower ambient back pressure condition, which mean a decrease in the spray angle, explaining the differences observed in the penetration curves, which is in agreement with the proportionality between the spray penetration and the spray angle presented in Equation 5.1. For the lower ambient back pressure (left), the flash boiling occurrence at the higher fuel temperature expands the spray obtaining higher values in the liquid and vapor fuel widths.

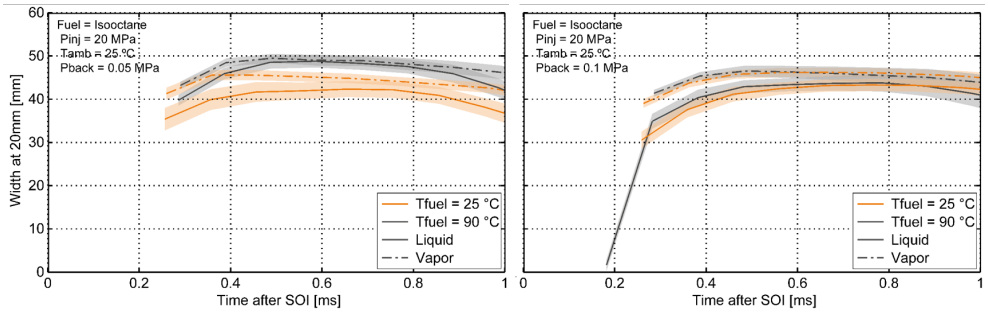

Figure 5.7: Fuel temperature effect over the spray width at 20mm from the injector tip with ambient back pressure variation from left to right.

5.3.4 Ambient temperature variation

The effect of the ambient temperature variation over the spray penetration was almost negligible for the temperature range employed in the present work, as it can be seen in Figure 5.8. Also, the R-parameter curves remain nearly equal during the entire injection event.

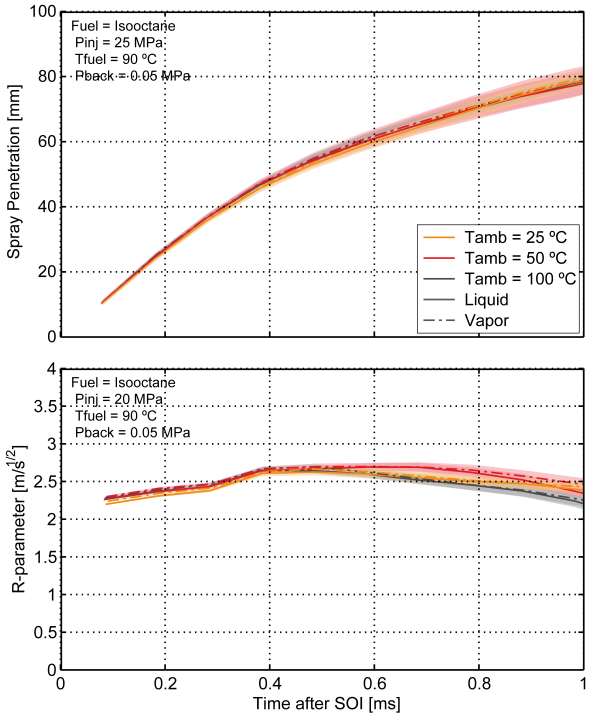

Figure 5.8: Ambient temperature effect over the liquid and vapor penetration.

In Figure 5.9, the effect of the ambient temperature variation over the spray width is depicted. As expected, the spray width behavior remains nearly equal between the curves until 0.4 ms (in ASOI reference), where the curves start a decreasing behavior caused by the end of the injection and the fuel evaporation in the outer part of the spray plume (this evaporation is higher for the higher ambient temperatures for the liquid phase of the spray while the vapor width remains almost the same).

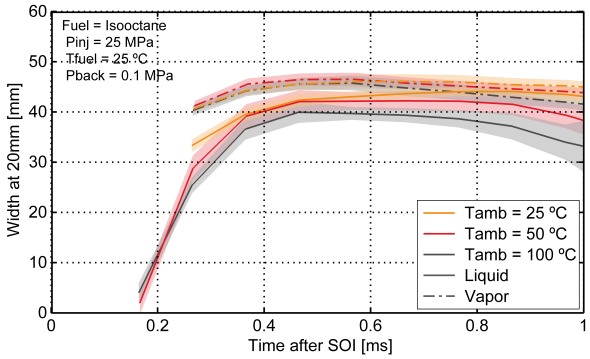

Figure 5.9: Ambient temperature effect over the spray width at 20mm from the injector tip.

5.3.5 R-parameter variation

A summary of the R-parameter behavior averaged in the steady zone of the curves (between 0.4 and 0.6 ms ASOI reference) is shown in Figure 5.10, as stated before, the R-parameter is proportional to the momentum flux, injection pressure, ambient density and spray angle, being a representative variable of the thrust of the spray. As can be seen in the figure, a higher ambient back-pressure produces a slowing effect over the spray, producing lesser values of the R-parameter for all the variables combinations. Also, it is noticeable that lower fuel temperatures produce higher R-parameter values being this difference more prominent for the lower ambient back pressure condition. As explained in subsection 5.3.2, this noticeable difference for the lower ambient back pressure, is caused by a change in the spray angle as a product of the flash boiling and fuel evaporation.

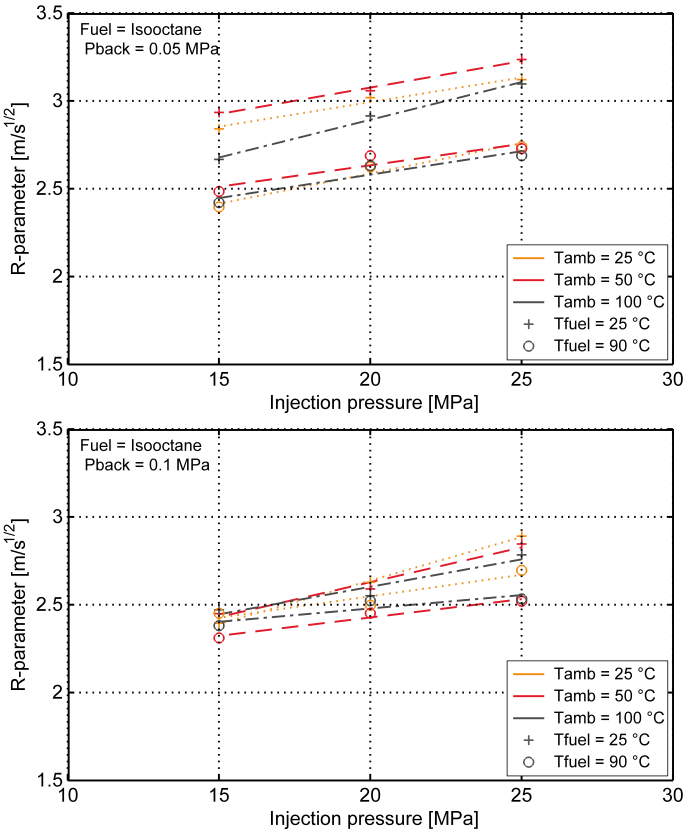

Figure 5.10: R-parameter variation with injection pressure and fuel and ambient temperature.

5.3.6 Light extinction analysis

Using the Beer-Lambert law Equation 4.2, the *KL* coefficient, which measures the light extinction of the images recorded with the DBI technique, was calculated. This parameter gave an idea of the concentration of liquid droplets in certain zones of the images since higher *KL* values mean higher concentration of liquid droplets. This analysis was made to have an idea of the injection condition effects over the spray liquid concentration to explain certain evaporation phenomena that will be presented in the rest of this work, even if it is not possible to know the number of droplets, droplet distribution, and droplet diameter which have a determinating effect over the extinction values obtained. As it is impossible to obtain information on the distribution of the droplets through the techniques used in this work and to asseverate the

assumption regarding the extinction profile, it is necessary to consider that higher evaporation entails a less amount of droplets in general and even less amount of the smaller diameter droplets [10].

Given the considerations mentioned above, a higher *KL* corresponds to a higher amount of liquid in the spray. In Figure 5.11, a description of the method used to obtain the *KL* and the *KA* of the free-jet DBI images is depicted. In this section, the results are reported in terms of the light attenuation in a vertical sheet-of-sight point of view (*KA*). This attenuation profile was obtained by taking all the *KL* at 25mm from the injector tip (where the wall will be located in the further analysis) and then integrating all these values over the selected point for the entire injection event.

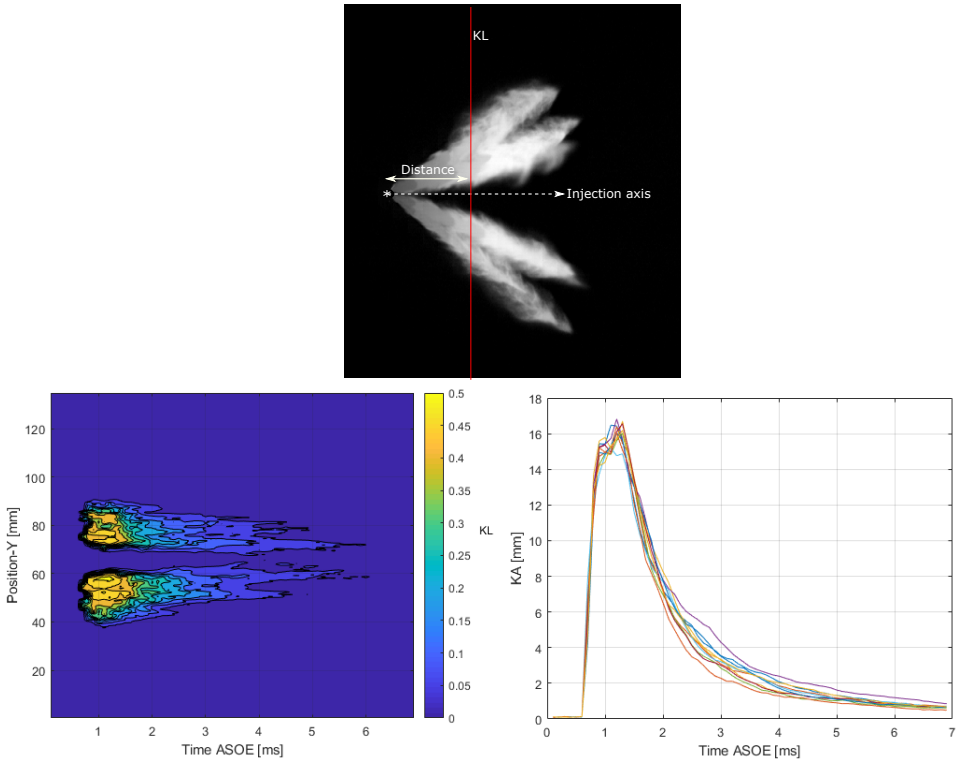

Figure 5.11: Description of the KA methodology.

In Figure 5.12, the effect of the injection pressure over the *KA* is depicted. Higher injection pressures produce higher extinction values, which means a higher fuel liquid amount in the studied region. This is caused because the injection pressure is directly related to the spray angle; higher injection pressures

mean less spray angles which means lesser air entrainment, lesser fuel evaporation, and, therefore, more fuel liquid droplets. In this point, it is important to highlight that from all the parametric variation, the injection pressure also represents another degree of complexity because it directly affects the Sauter mean diameter (SMD) of the droplets, meaning that higher injection pressures cause a decrease in the SMD and producing a higher amount of liquid droplets and higher light attenuation.

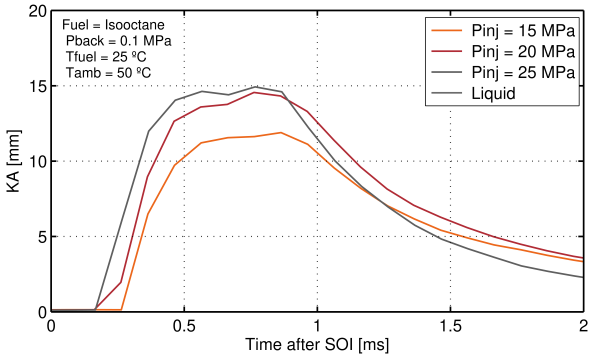

Figure 5.12: KA variation with the injection pressure.

In Figure 5.13, the ambient back-pressure variation over the extinction profile curves can be seen. Lower ambient back-pressure results in lower extinction curves and can be related to fuel evaporation at low ambient back-pressures meaning more vapor amount than liquid, which translates into a lesser light attenuation. Also, there is an important relation between the ambient back-pressure and the spray air-entrainment, where lower back pressure mean higher spray angles and more air-fuel mixing during the injection event. By seeing the Figure 5.4 and Figure 5.5, it is possible to state that at lower back pressure, the droplets have lower drag force; therefore, they move faster and further, meaning that the spray is more dispersed in the entire volume contributing to lowering the KL.

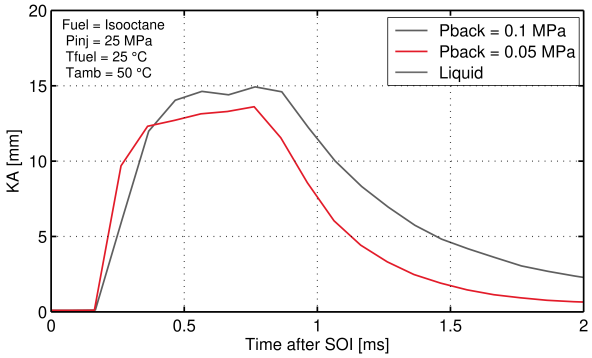

Figure 5.13: KA variation with the ambient back-pressure.

In Figure 5.14, the effect of the ambient temperature over the *KA* curves is shown. A lower ambient temperature produces a higher extinction profile. This is caused because the amount of liquid droplets is higher at lower ambient temperatures. This also can be corroborated by the fact that in Figure 5.8 and Figure 5.9, the penetration and width curves behave equally, meaning that the changes observed in the *KA* profiles are caused by the liquid light attenuation. Higher ambient temperatures means higher fuel evaporation meaning less light attenuation.

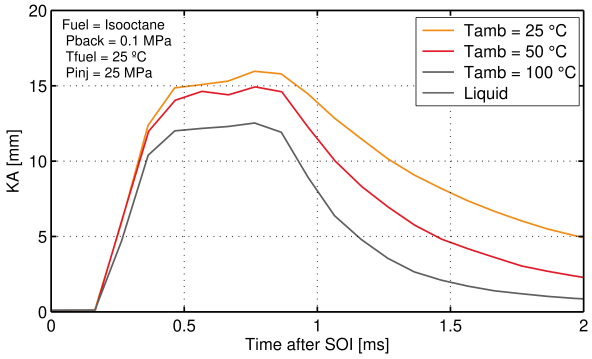

Figure 5.14: Ambient temperature effect over the KA.

In the same way, Figure 5.15 shows the fuel temperature effect over the extinction profiles. For the higher ambient back pressure (right), a higher fuel temperature produces a smaller extinction profile because the fuel temperature itself enhances fuel evaporation. Also, a higher spray angle is obtained, as shown in subsection 5.3.3, causing higher air entrainment and higher evaporation resulting in a lesser amount of liquid (Figure 5.7). On the contrary,

the higher fuel temperature increases the extinction profile for the lower ambient back pressure where the flash boiling effects appear, making both curves similar. This is because the flash boiling decreases the droplet diameter [11], affecting the amount of light attenuated (more droplets with less diameter produce a higher light attenuation).

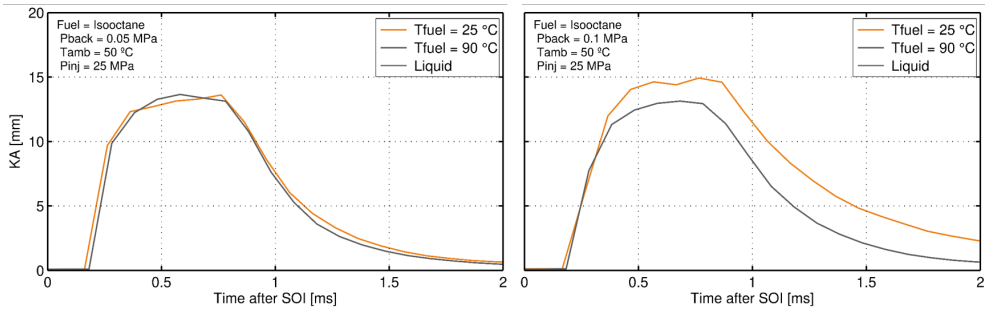

Figure 5.15: Fuel temperature effect over the KA.

5.4 Spray-wall interaction visualization

The preceding analysis took into account factors observed upstream of the wall. Even if some of them may be affected by SWI, the existence of walls does not define them. The parameters defined by the spray-wall interaction are detailed further below.

5.4.1 Spray spreading over the wall

In Figure 5.16, a comparison between different wall angles contour images using the Schlieren technique are shown for the same operating condition. Two different wall angles (60° and 90°) and two wall-to-tip distances ($d_w = 25mm$ and $d_w = 35mm$) were used in the experimental campaign as described in Table 5.1.

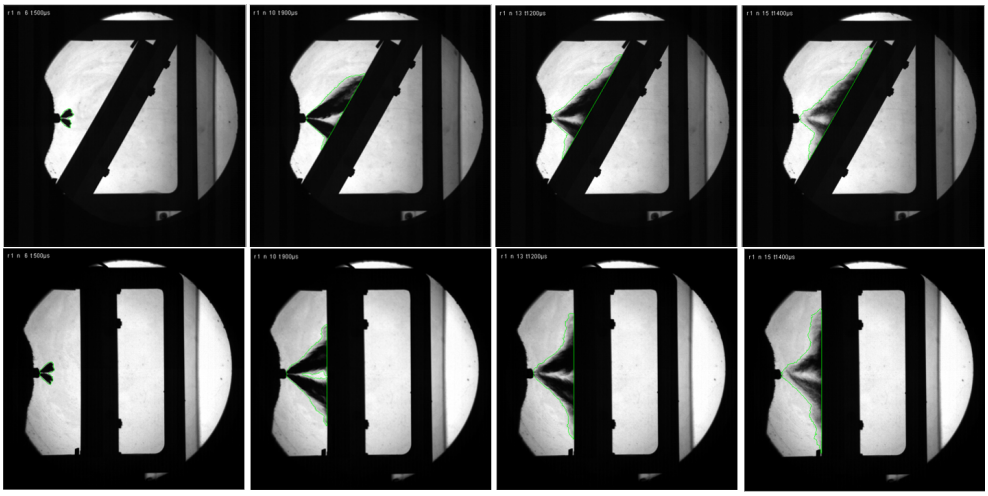

Figure 5.16: Samples of the images observed via Schlieren technique for different wall angle conditions. All the images are presented with ASOE time reference. $p_{inj} = 20\,\text{MPa}, p_{back} = 0.1\,\text{MPa}, T_{amb} = 25\,°\text{C}, T_{fuel} = 25\,°\text{C}, w_d = 25\,\text{mm}$

τ_w is the name used to identify the start of the spray-wall interaction phenomenon, and it was defined from the beginning of injection. Some of the τ_w values obtained for different injection pressures are shown in Figure 5.17 and Figure 5.18.

In Figure 5.17, the effect of the ambient temperature over τ_w is depicted. As expected, the τ_w relies entirely on the penetration behavior. At higher injection pressures, lower values of τ_w are found. It is possible to notice the effect of the ambient temperature and chamber back-pressure over τ_w, the ambient temperature does not produce significant variation, and this is in agreement with the results obtained in the previous section for the free spray penetration curves. Important differences are obtained when the ambient back-pressure is modified for the lower fuel temperature (top part of the figure). Obtaining lower τ_w values for the lower back-pressure is in agreement with the penetration results of the previous section, where the lower fuel temperature produces higher penetration curves due to a lesser spray angle.

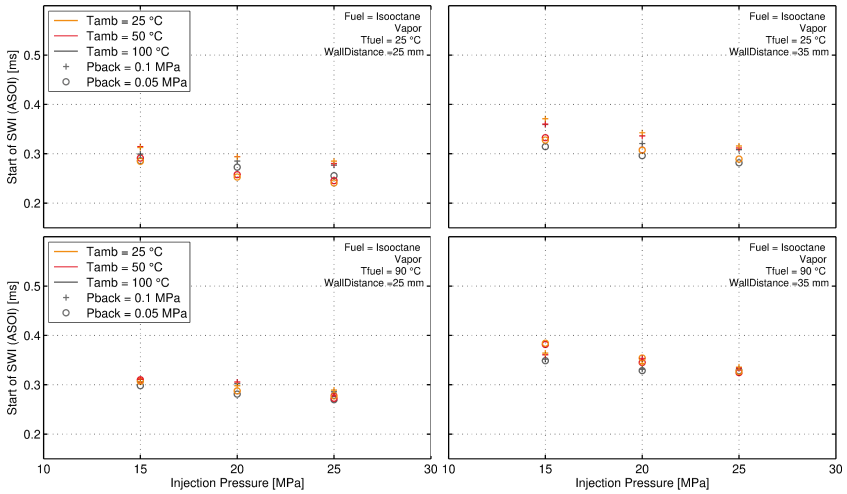

Figure 5.17: Start of spray-wall interaction computed for different injection pressures and ambient conditions. Left: Wall at $d_w = 25mm$. Right: Wall at $d_w = 35mm$. Top: Liquid phase. Bottom: Vapor phase.

In Figure 5.18, the τ_w values for the vapor phase of the spray and from left to right variations in the chamber back-pressure are shown. As expected, lower values of τ_w are obtained for the closest wall distance. The spray take more time to reach the wall when the wall-to-tip distance increases, remarking the importance of air entrainment over the development of the spray and the start of the spray-wall interaction. Also, lower ambient back-pressures produces higher spray penetration, obtaining lower τ_w values. There is a remarkable difference in the τ_w values by changing the wall angle, obtaining a significant delay for the 60° upper part wall configuration. This is caused by the geometric definition of the impact point respect with all the metrics measured Figure 5.24.

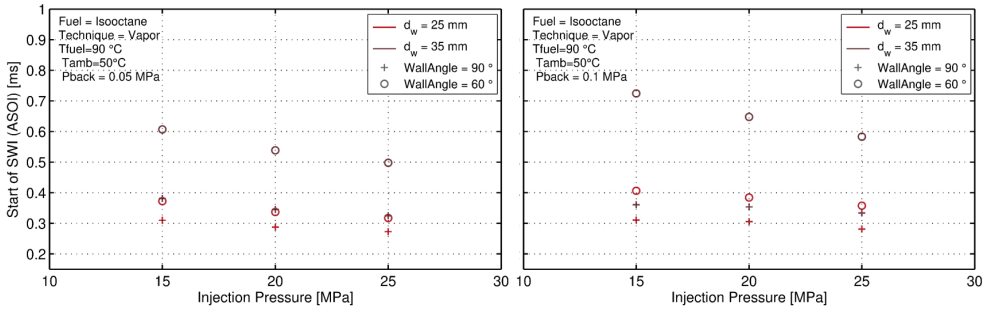

Figure 5.18: Start of spray-wall interaction calculated for different injection pressures and wall conditions. Left: Pback = 0.05MPa. Right: Pback = 0.1MPa. Top: Liquid phase. Bottom: Vapor phase.

In Figure 5.19 and Figure 5.20 a sample of images of the spray-wall interaction is shown for different wall distances respect to the injector tip. From the images, a qualitative difference can be easily identified in the shape of the fuel cloud located at the near nozzle region of the image and will be key to carry out the description of the results presented in the following figures.

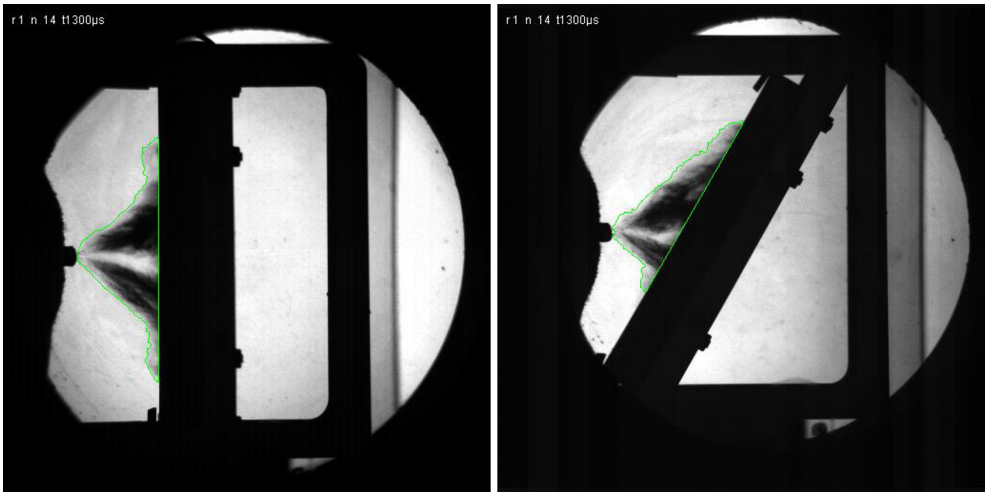

Figure 5.19: Samples of the SWI for different wall angles and Schlieren technique at $d_w = 25mm$. $p_{inj} = 15\,\mathrm{MPa}, p_{back} = 0.1\,\mathrm{MPa}, T_{amb} = 25\,^{\circ}\mathrm{C}, T_{fuel} = 25\,^{\circ}\mathrm{C}$.

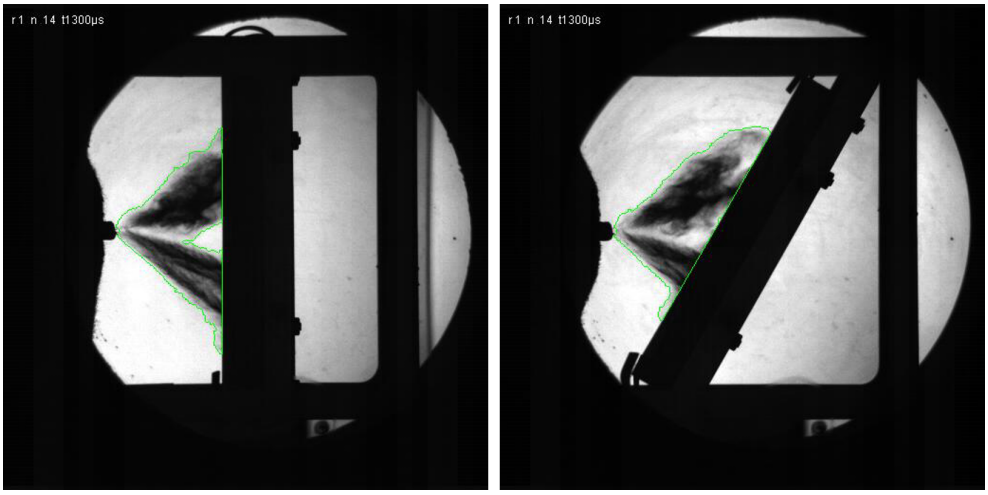

Figure 5.20: Samples of the SWI for different wall angles and Schlieren tecnique at $d_w = 35mm$. $p_{inj} = 15\,\text{MPa}, p_{back} = 0.1\,\text{MPa}, T_{amb} = 25\,°\text{C}, T_{fuel} = 25\,°\text{C}$.

For the following figures, the spray spreading along the wall is referenced to the time the spray hits the wall (τ_w). Also, its corresponding R-parameter is presented. For the analysis, all the jets are considered a hole under the same contour, meaning that when the spray hits the wall, the first point considered in the penetration curves corresponds to the distance between the farthest point of the spray contour in the wall direction and the collision point.

Figure 5.21 depicts the spray spreading, free-jet penetration, and R-parameter for one selected condition. The dotted line refers to the start of the spray-wall interaction phenomenon. As expected, a reduction in the R-parameter and penetration is obtained. After the spray collides with the wall, the spray thrust is significantly reduced.

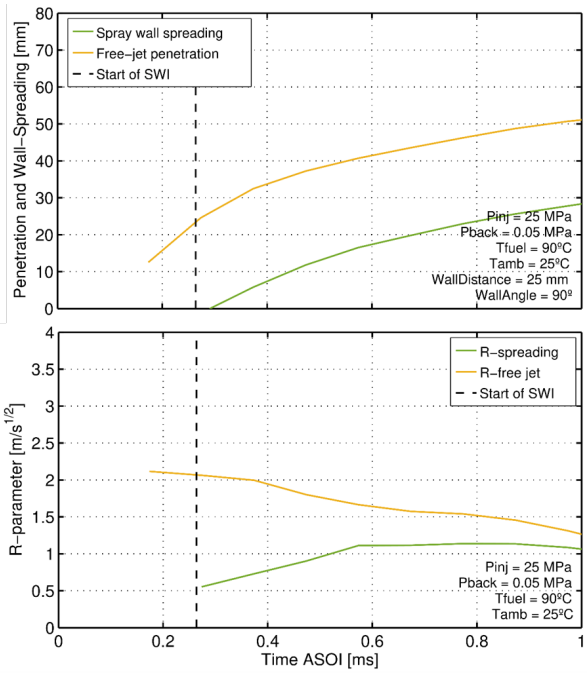

Figure 5.21: Comparison between the free jet penetration and the spray wall spreading and its R-parameter with time in ASOI reference.

As well as the case of the free-jet analysis, the liquid and vapor phases of the curves have similar behavior, which is why only the vapor curves are presented in the following analysis.

As obtained in the free-jet penetration curves, in Figure 5.22 the spray-wall spreading has the same behavior in terms of the injection pressure variations. The injection pressure increases the spray penetration curves due to the momentum transferred to the fuel flow. Different wall-to-tip distances are presented from left to right. A slowing effect over the spray advance over the wall is achieved when the wall distance is increased, and it can be attributed to the spray velocity losses due to the air interaction. Also, the same trend is observed for the R-parameter, where a higher value is obtained for the higher injection pressure. The slowing in the spray advance over the wall when the wall-to-tip distance is increased is reflected in the R-parameter magnitude, where lower values are observed when increasing the wall distance.

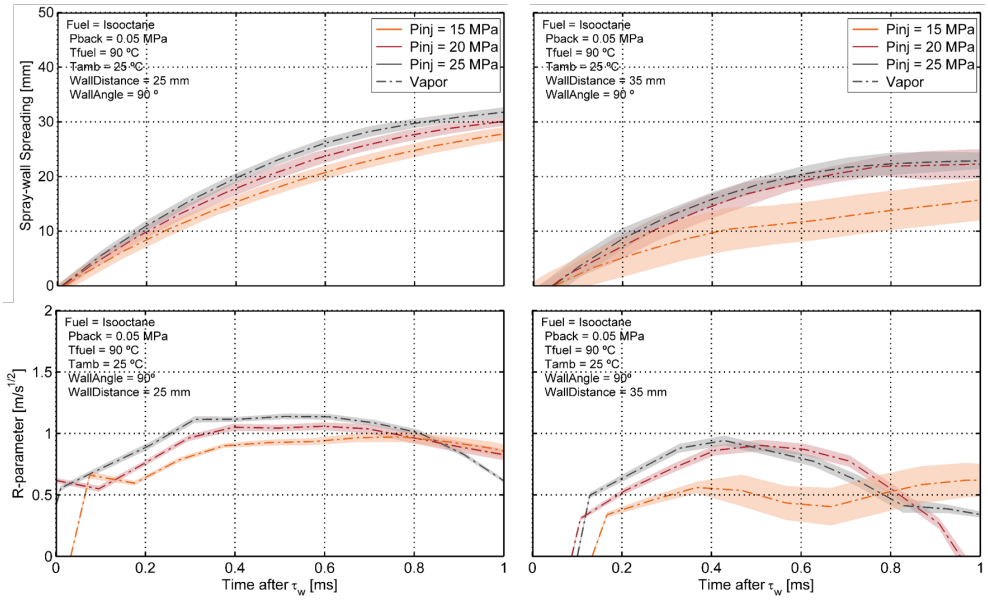

Figure 5.22: Spray spreading (top) and the R-parameter (bottom) for different injection pressures and wall distances. Left: Wall at $d_w = 25mm$. Right: Wall at $d_w = 35mm$.

The wall angle variation with time is presented in Figure 5.23 where as well as in the previous case, the increase of the wall distances has a slowing effect over the spray advance over the wall, even more, noticeable for the 60° wall angle configuration (in previous analysis more air entrainment was observed for this wall configuration). Also, it is possible to notice how the wall angle also impacts the speed of the spray movement over the wall. For the lower wall angle configuration, the start of spray-wall interaction occurs later than for the 90° case, and its development on the wall lasts less time because of the spray evaporation losing its forward force when interacting with the air. This is also noticeable when comparing the R-parameters, obtaining lesser values when increasing the wall distance (which, as described previously, is directly related to the spray thrust). When comparing the R-parameter curves, a slight preferent direction for the spray spreading over the wall after the impact with the 60° wall angle configuration (yellow lines) is noticed.

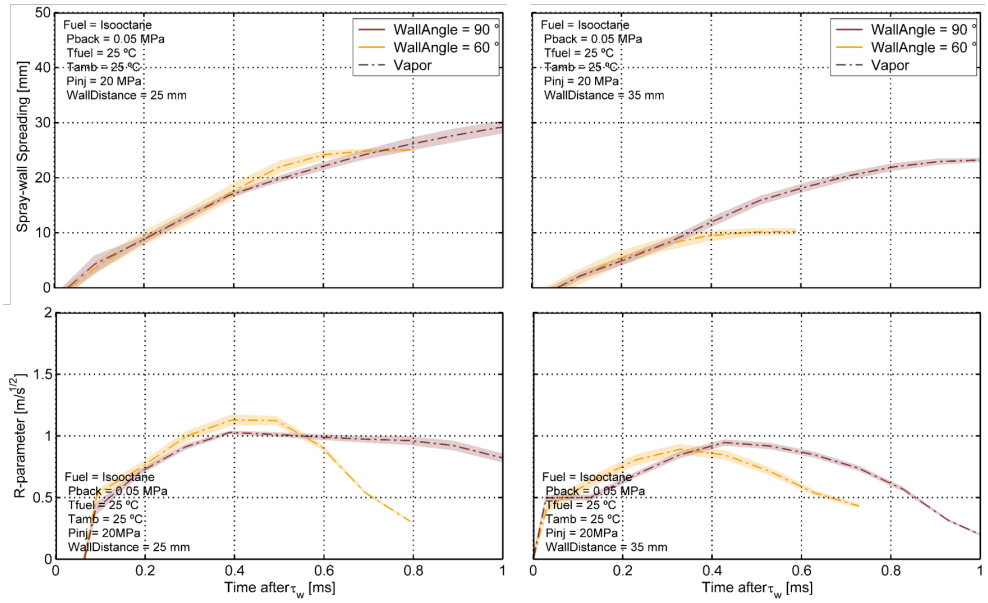

Figure 5.23: Spray spreading over the wall (top) and the R-parameter (bottom) for different wall positions. Left: Wall at $d_w = 25mm$. Right: Wall at $d_w = 35mm$.

5.4.2 Spray width over the wall

The following figures will present the effect of the injection conditions over the width of the spray measured at two different distances from the collision point, showing the variation from left to right with respect to the wall-to-tip distance. Figure 5.24 depicts a scheme of the selected reference system used for the spray width calculation for both wall angles configuration.

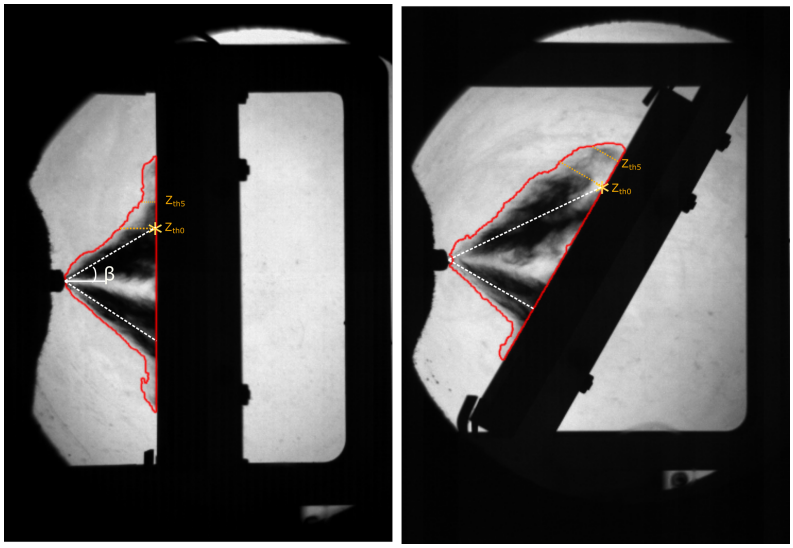

Figure 5.24: Scheme of the spray width measurement reference system used for the isothermal wall.

The increase in width observed by varying the wall distance, as seen in Figure 5.19 and Figure 5.20, means that the width of the spray increases in the closer region to the collision point near the injection axis. This phenomenon can be attributed to the air-mixing process in the area closer to the injector tip, which changes the morphology of the spray before hitting the wall.

In Figure 5.25, the effect of the injection pressure over the spray width measured after SWI is depicted. It is possible to observe two behaviors when comparing zth_0 and zth_5. In the first behavior, the width curves follow a decreasing trend, obtaining higher width values for the higher wall-to-tip distance and observing that higher injection pressures produce higher width values. This is caused because more energy is transferred to the fuel, increasing the spray velocity and finally transferring more energy to the spray after the collision. The second behavior, related to zth_5 curves, is characterized by an increase in the width curves as the spray spreads over the wall. Those values are affected by the injection pressure; higher injection pressures produce higher width values for the same time instant, being more evident for the higher wall distance.

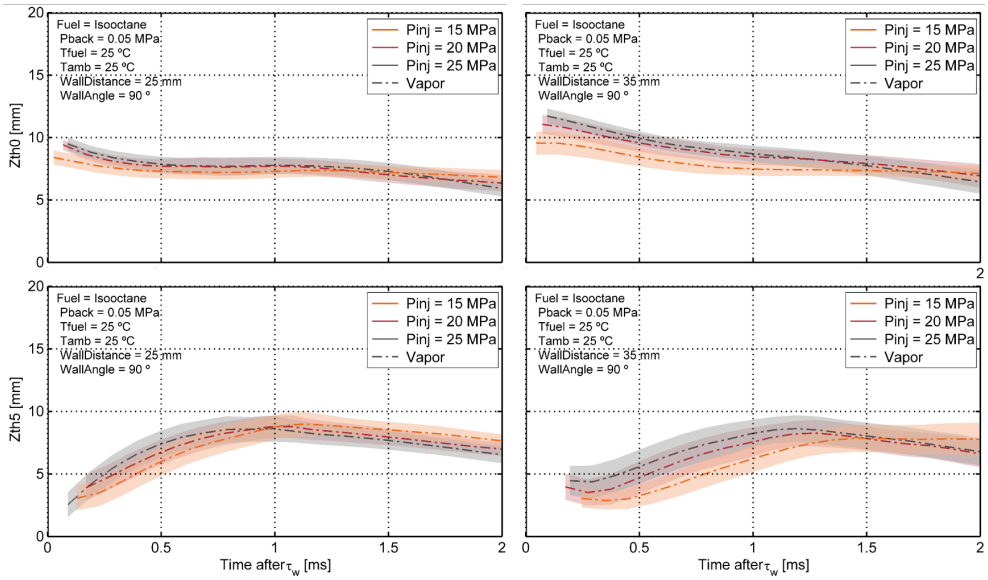

Figure 5.25: Spray thickness measured at two different positions for different injection pressures. Left: Wall at $d_w = 25mm$. Right: Wall at $d_w = 35mm$.

In Figure 5.26, a comparison of the effect of the wall angle over the spray width is shown for the same test condition. Increasing the wall-to-tip distance increases the 60° wall angle width curve, and this can be corroborated by seen Figure 5.19 and Figure 5.20. In the same way, increasing the wall distance produce a slight increase in the width value for the lower wall angle curve and a decrease for the higher wall angle value. This can be related to the loss in momentum caused by the impact with the wall compared to the slight interference caused by the inclined wall configuration plus the air-entrainment effect achieved with the farthest wall-to-tip distance.

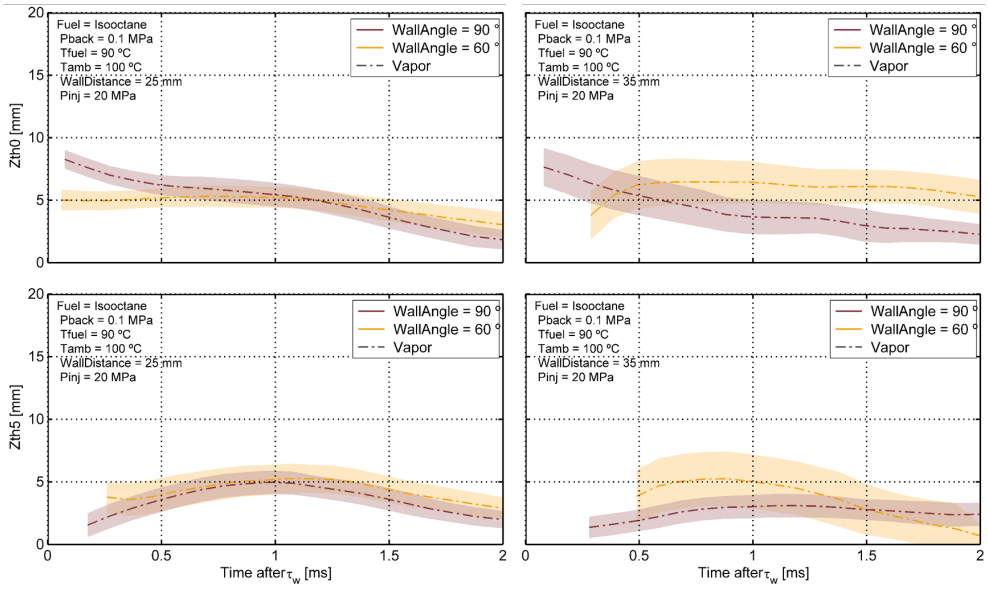

Figure 5.26: Spray thickness measured at two different positions varying the angle of the wall. Left: Wall at $d_w = 25mm$. Right: Wall at $d_w = 35mm$.

5.4.3 Light extinction after SWI

The following figures will show the effect of the injection parameters over the extinction profiles curve obtained through the DBI images using the methodology described in subsection 5.3.6. For the SWI images, the *KA* profiles were calculated by integrating all the *KL* values over a perpendicular direction defined at zth_5 and over the wall. The following curves provide information about the spray liquid amount variation for the different parameters used in the experimental campaign and finally serve as a measure of the amount of liquid present in the spray.

In Figure 5.27, the effect of the injection pressure over the extinction profiles is shown with wall distance variation from left to right. As in the free-jet case, higher injection pressures produce higher extinction profiles, which means higher liquid amount caused by the lesser spray angle. The *KA* curves behaves equally by varying the wall-to-tip distance.

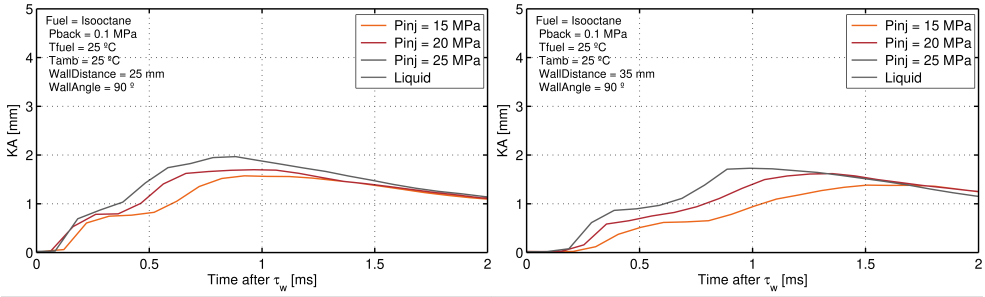

Figure 5.27: Extinction profile at zth_5 varying the injection pressure. Left: Wall at $d_w = 25mm$. Right: Wall at $d_w = 35mm$.

In Figure 5.28, the ambient temperature effect over the KA curves is depicted. As expected, and as obtained in the free-jet scenario, higher ambient temperature produces fewer extinction profiles due to higher spray evaporation which causes lesser light attenuation. As with the injection pressure, the magnitude of the extinction profile is not affected by the location.

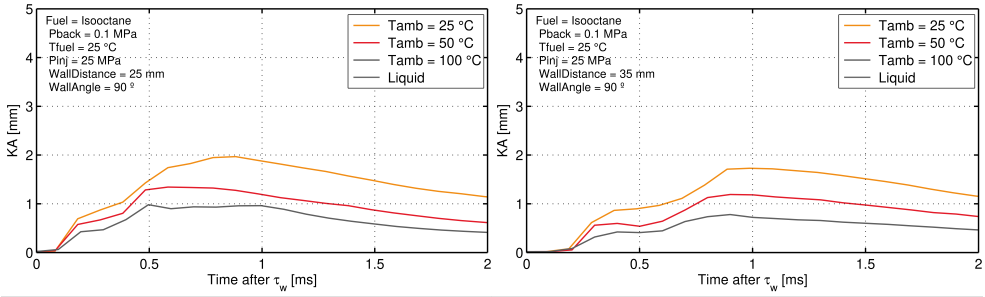

Figure 5.28: Extinction profile at zth_5 varying the ambient temperature. Left: Wall at $d_w = 25mm$. Right: Wall at $d_w = 35mm$.

In Figure 5.29, the fuel temperature effect over the KA curves is shown. From these curves, it is possible to notice that on the contrary, as was obtained for the free-jet, the flash boiling that appears at lower ambient back pressures does not produce any considerable changes to the extinction profiles, which can be understood as a possible uniformization of the distribution of the droplets after the interaction with the wall.

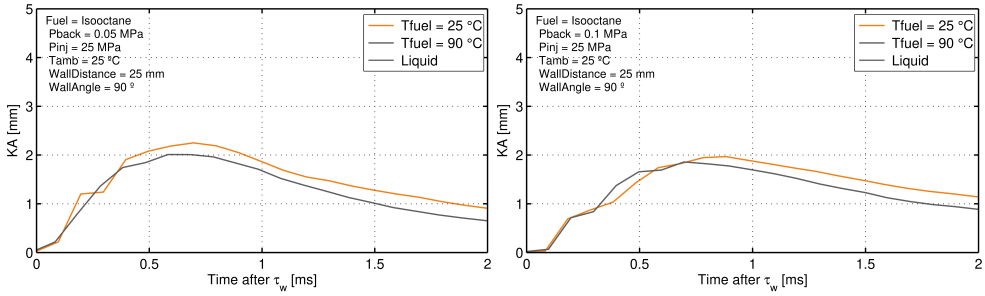

Figure 5.29: Extinction profile at zth_5 varying the fuel temperature. Left: Wall at $Pback = 0.05\,\text{MPa}$. Right: Wall at $Pback = 0.1\,\text{MPa}$.

In Figure 5.30, the ambient back pressure effect over the KA curves is depicted. As in Figure 5.29, the extinction profiles do not present any considerable changes with this variation; this reaffirms that the collision with the wall may provoke a uniformization of the spray droplet distribution obtaining similar light attenuation profiles.

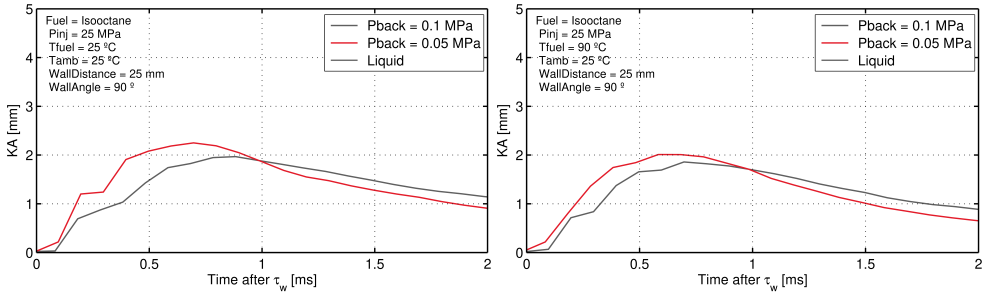

Figure 5.30: Extinction profile at zth_5 varying the ambient back pressure. Left: Wall at $Tfuel = 25\,°\text{C}$. Right: Wall at $Tfuel = 90\,°\text{C}$.

Lastly, Figure 5.31 shows the effect of the wall angle over the extinction profile curves. Here, an interesting trend is depicted, where for the higher wall distance, an important reduction over the KA magnitude is achieved for the lower wall angle. Higher air entrainment causes the spray to take more time to reach the upper impact point over the wall because it has less energy available to spread over the wall, meaning less liquid.

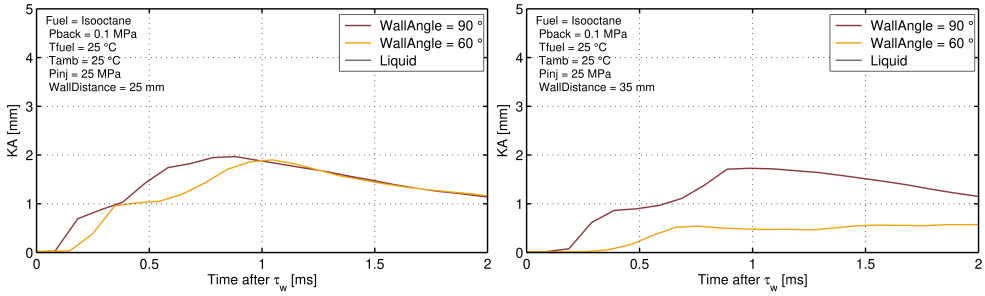

Figure 5.31: Extinction profile at zth_5 varying the wall angle. Left: Wall at $d_w = 25mm$. Right: Wall at $d_w = 35mm$.

The *KA* profiles also show an important magnitude reduction compared to the free-jet scenario (almost an eighth-time reduction). This is caused because light extinction is considered at different locations, and the liquid distribution differs in both scenarios.

5.5 Frontal area of impact after the spray-wall interaction

In this section, the semi-circle area of impact described in Figure 4.8 is presented for different injection conditions. All the figures refers to the semi-circle area of one of the six plumes of the spray. A sample of frontal images obtained in the experimental campaign for the quartz transparent wall is shown in Figure 5.32. It is essential to clarify that for the incline wall angle, the half-bottom plumes reach the wall faster than the upper plumes, and the semi-area of impact was analyzed for one of those plumes.

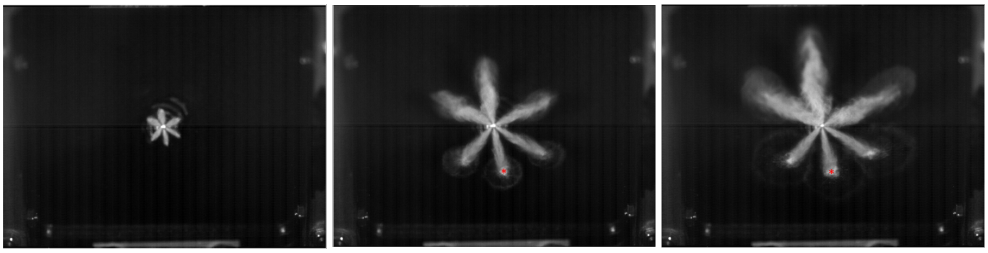

Figure 5.32: Sample of frontal images used to calculate the semi-circle area of impact. Wall at $d_w = 25mm$ and 60°

In Figure 5.33 from left to right is possible to see a variation in the wall-to-tip distance and, and from top to bottom, the ambient temperature variation for different injection pressures. It is essential to clarify that the quartz wall surface temperature is the same as the ambient temperature of the chamber for each test condition.

It is possible to notice that the area follows an increasing linear trend, and the higher the wall distance, the higher the area value. This can be explained through the spray air entrainment with the surroundings and the recirculation zones created as the spray spreads over the wall, promoting spray dispersion and increasing the area. Similar behavior was also present in Figure 5.26, where a wider spray is obtained by increasing the wall distance. Also, the distance of the wall and the wall angle could have a role in the fuel droplets splashing, spreading, or rebound regimes once they hit the wall.

As in the free-jet configuration, the injection pressure variation is the most relevant parameter that produces changes in the semi-circle impact area.

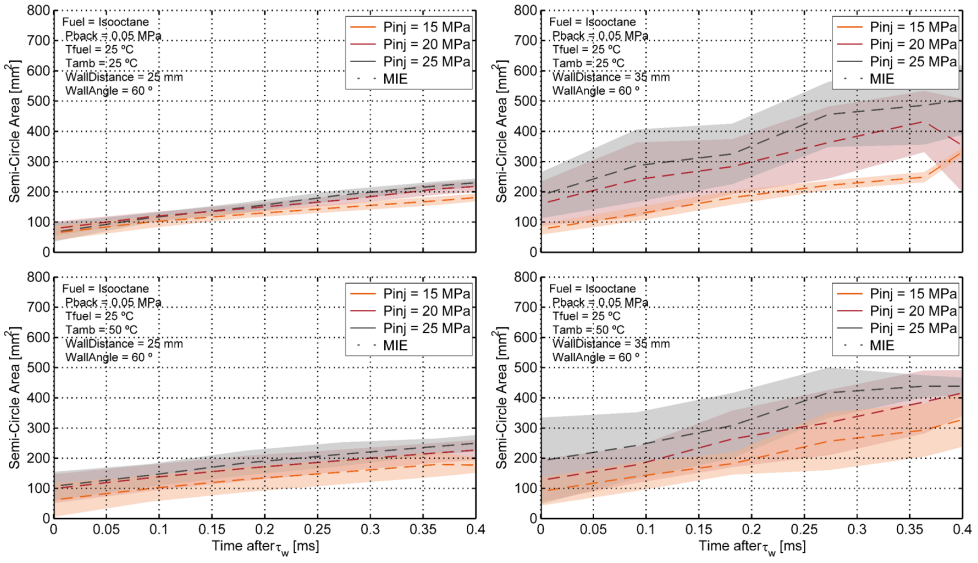

Figure 5.33: Semi-circle area of impact for different injection pressures and wall distances. Left: Wall at $d_w = 25mm$. Right: Wall at $d_w = 35mm$. Top: Ambient temperature at $Tamb = 25°C$. Bottom: Ambient temperature at $Tamb = 50°C$.

The effect of the wall angle over the area can be seen in Figure 5.35 with a left-to-right variation in wall angle and top to bottom variation in ambient temperature. In the previous sub-section, the spray wall spreading decreases

with the increase in the wall-to-tip distance and increases with lower wall angles. In Figure 5.35 is possible to notice that an increase in the wall angle produces an increase over the semi-circle area of impact. It is possible to state that the slowing in the lateral wall direction is explained through a spray expansion in the radial direction, meaning a higher area caused by the splashing effect of the spray colliding directly with the wall.

Also, for the 90° wall angle configuration, the spray impacts the wall with a certain angle, producing a preferent direction for the spray spreading onto the wall, causing the increase in the semi-area of impact when compared with the lower wall angle configuration. This effect agrees with the spray spreading along the wall results in the previous subsection. A scheme of this can be depicted in Figure 5.34

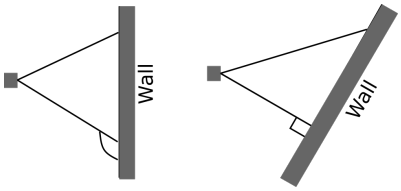

Figure 5.34: Scheme of the wall angle effect over the semi-area spray spreading.

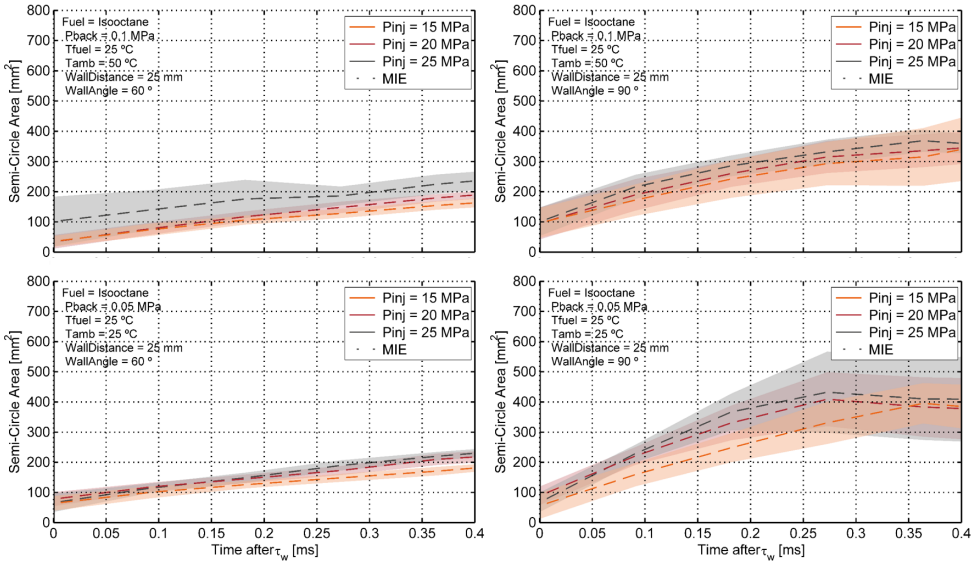

Figure 5.35: Semi-circle area of impact for different injection pressures and wall angles. Left: Wall at = 60°. Right: Wall at 90°. Top: Ambient temperature at Tamb = 50°C. Bottom: Ambient temperature at Tamb = 25°C.

5.6 Summary and conclusions

This chapter analyzed the spray free penetration and the spray spreading by a parametric variation of the conditions tested in the experimental campaign. Observing the impact of the cold-start-like engine and other evaporative conditions over the spray morphology through high-speed imaging visualization using DBI, MIE, and Schlieren optical techniques simultaneously. Regarding the free-jet conditions, the injection pressure and the fuel temperature were the variables that most affected the spray penetration with time. Even those variations were slight for the range of conditions tested. The R-parameter magnifies those differences and allows to compare the curves easily. Also, it was found that the small changes in back pressure and ambient temperatures are not enough to produce relevant changes in the spray penetration behavior. Also, by using the extinction profile curves was found that the ambient temperature and fuel temperature variation produce important changes in the spray fuel evaporation, being an indicator of the amount of liquid present in the spray that cause the light attenuation.

Regarding the spray-wall interaction visualization, the influence of the conditions tested over the start of the SWI was analyzed. In addition to

reducing the start of SWI for higher injection pressures, other variables, such as the increase of the wall-to-tip distance and the decrease of the ambient back-pressure, reduce the start of SWI. No remarkable trends were obtained for the ambient temperature variations.

The same trends of the free-jet campaign were observed for the spray spreading over the wall, even being proportional to the square root of time, where a higher injection pressure produces a higher spray spreading over the wall. Also, the wall-to-tip distance reduces the spray spreading and the R-parameter for all the parametric variations, which is more remarkable for the 60° wall angle configuration.

No remarkable differences were found between the liquid and vapor phases of the spray for neither of the two experimental campaigns (free jet and SWI).

Spray thickness was measured at two different distances from the "impact point" affected by changes in wall-to-tip distance and wall angle but, even more, by the distance from the "impact point" in which it is measured.

The extinction profiles were calculated for the SWI scenario, as in the case of the free-jet campaign. It was obtained that the injection pressure and the ambient temperature produce important changes in the spray liquid amount. Higher ambient temperature produces lesser liquid caused by more vapor in the spray.

The semi-circle impact area was susceptible to wall angles and wall-to-tip distance variations. As in the case of the spray thickness, it can be related to the spray air entrainment in the near nozzle region and the droplet breakup regime caused by differences in the collision energy.

References

[1] ECN. "Engine Combustion Network". In: *https://ecn.sandia.gov/gasoline-spray-combustion/* (2020).

[2] Moulai, Maryam, Grover, Ronald, Parrish, Scott, and Schmidt, David. "Internal and Near-Nozzle Flow in a Multi-Hole Gasoline Injector Under Flashing and Non-Flashing Conditions". In: *SAE Technical Paper Series*. SAE International, 2015. DOI: 10.4271/2015-01-0944.

[3] Lemmon, Eric W., McLinden, M. O., and Friend, D. G. "Thermophysical Properties of Fluid Systems". In: *NIST Chemistry WebBook, NIST Standard Reference Database Number 69*. Ed. by P. J. Linstrom and W. G. Mallard. 2011.

[4] Payri, Raul, Viera, Juan Pablo, Gopalakrishnan, Venkatesh, and Szymkowicz, Patrick G. "The effect of nozzle geometry over the evaporative spray formation for three different fuels". In: *Fuel* 188 (2017), pp. 645–660. DOI: 10.1016/j.fuel.2016.06.041.

[5] Xu, Min, Cui, Yi, and Deng, Kangyao. "One-dimensional model on liquid-phase fuel penetration in diesel sprays". In: *Journal of the Energy Institute* 89.1 (2016), pp. 138–149. DOI: 10.1016/j.joei.2015.01.002.

[6] Pickett, Lyle M, Genzale, Caroline L, and Manin, Julien. "Uncertainty quantification for liquid penetration of evaporating sprays at diesel-like conditions". In: *Atomization and Sprays* 25.5 (2015), pp. 425–452. DOI: 10.1615/AtomizSpr.2015010618.

[7] Gimeno, Jaime. "Desarrollo y aplicación de la medida de flujo de cantidad de movimiento de un chorro Diesel". PhD thesis. E.T.S. Ingenieros Industriales, Universidad Politécnica de Valencia, 2008.

[8] Giraldo Valderrama, Jhoan Sebastián. "Macroscopic and microscopic characterization of non-reacting diesel sprays at low and very high injection pressures". In: November (2018).

[9] Bornschlegel, Sebastian, Conrad, Chris, Eichhorn, Lisa, and Wensing, Michael. "Flashboiling atomization in nozzles for GDI engines". In: 2017. DOI: 10.4995/ILASS2017.2017.4750.

[10] Moreira, A, Moita, Cossali, E, Marengo, M, and Santini, M. "Secondary atomization of water and isooctane drops impinging on tilted heated surfaces". In: *Experiments in Fluids* 200 (2007), p. 117626. DOI: 10.1007/s00348-007-0330-2.

[11] Chang, Mengzhao, Yu, Young Soo, Park, Sungwook, and Park, Suhan. "Spray dynamics and atomization characteristics of multi-hole GDI injectors under flash boiling conditions". In: *Applied Thermal Engineering* 200 (2022), p. 117626. DOI: https://doi.org/10.1016/j.applthermaleng.2021.117626.

Chapter 6

Spray impingement against a heated and instrumented wall

6.1 Introduction

This chapter explains the observations obtained from the experimental campaign for the thermoregulated steel wall. As in the previous chapter, only inert conditions were performed, but the wall temperature was controlled to emulate conditions such cold-start and other evaporitve conditions present in a gasoline combustion engine. In chapter 5, both wall and ambient temperatures were approximately the same. The wall temperature changes allow to investigate spray-wall heat transfer and its influence on spray evolution. In addition to the optical diagnostics described in earlier chapters, the heat flux was measured with the high-speed thermocouples located in the wall surface and using a one-dimensional transient wall heat model. All the information regarding this model and its suitability has been explained and shown in section 4.4.

Iso-octane was used as the injected fuel. Four different wall temperatures have been set by regulating the oil flow temperature inside the wall system. The wall has been located at 20 mm from the injector tip to ensure the spray hits the thermocouple sensors. All the conditions tested can be seen in the Table 6.1. Two high-speed cameras were simultaneously used as shown in Figure 4.4.

Table 6.1: Test matrix for the thermoregulated wall.

Parameter	Value/Type	Units
Injector	Continental	-
Fuel	Isooctane	-
ET	0.8	ms
Rail pressure (P_r)	150/200/250	bar
Back pressure (P_b)	0.5**/1	bar
Fuel temperature (T_{fuel})	25/90**	°C
Ambient temperature (T_{amb})	25/50/100	°C
Wall distance (d_w)	20	mm
Wall angle	90	°
Wall temperature	30/50/70/90*	°C
Repetitions per test	10	-

* The 90°C wall temperature was used only for the $T_{amb} = 100°C$ condition.

** The low ambient back pressure with the higher fuel temperature represent flash boiling conditions.

6.2 Spray-wall interaction visualization

In this chapter, only the lateral visualization of the spray-wall interaction was recorded because, as stated in previous chapters, the wall system mounted in front of the injector tip requires the use of the frontal optical access of the vessel. In Figure 6.1 a sample of the images acquired during the experimental campaign is shown for Schlieren technique. The asterisk refers to the fast-response thermocouple location on the wall surface. The whole wall system was decentered respect to the injector tip to guarantee that the spray impacts the thermocouple location to register the temperature drop signal properly.

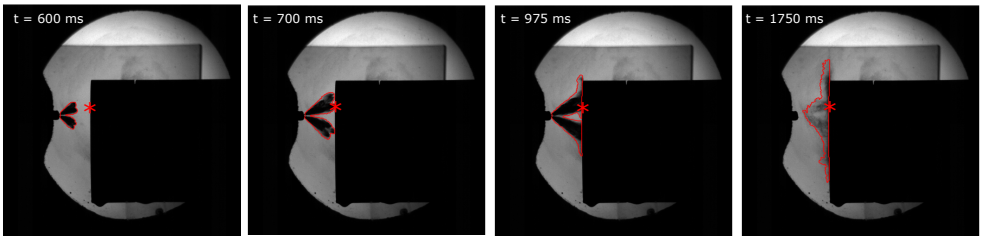

Figure 6.1: Samples of the spray-wall interaction Schlieren visualization for the thermoregulated steel wall.

6.2.1 Spray spreading over the wall

In Figure 6.2 is possible to see the liquid and vapor spray spreading along the wall with a pressure injection variation. As in the case of the quartz wall, there are small differences between the liquid and vapor phases of the spray. Nevertheless, greater vapor penetration can be observed and the expected trend is still observable where higher injection pressures produce higher penetration values. This is caused by the amount of momentum transferred to the fluid, increasing the velocity at the injector nozzle exit. In this figure, the importance of the R-parameter is remarkable because this variable increases the slight differences between the penetration curves, allowing to observe the changes in the slope of the penetration curves and highlighting the difference between them. In general, comparing the obtained spreading penetration curves of this campaign with the free-jet penetration, higher differences between the liquid and vapor phases were found, being more prominent when observing the differences in the R-parameter.

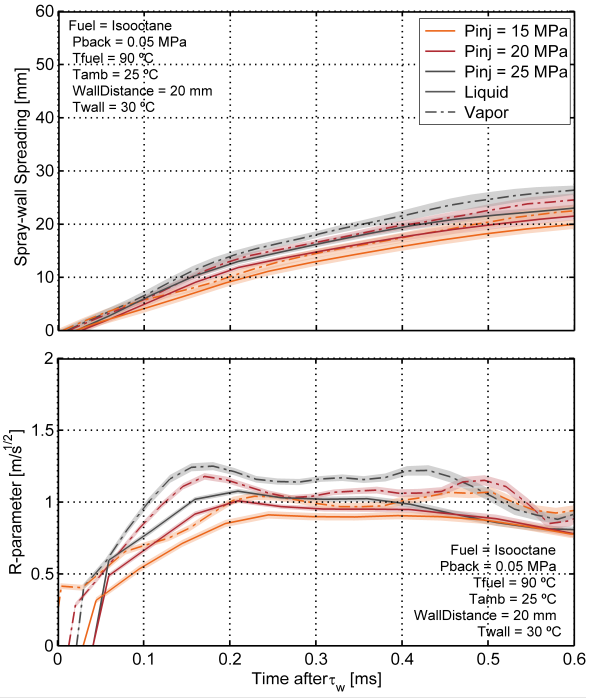

Figure 6.2: Spray-wall spreading and R-parameter for different injection pressures.

In Figure 6.3, the effect of the ambient back-pressure variation over the spray spreading for the thermoregulated wall can be depicted. Higher am-

bient back pressure produces lower spray penetration, as seen in the free-jet penetration chapter. It is important to highlight that for the thermoregulated wall, considerable differences were found between the vapor and liquid phases of the spray. Higher R-parameter values were obtained for the vapor phase of the spray.

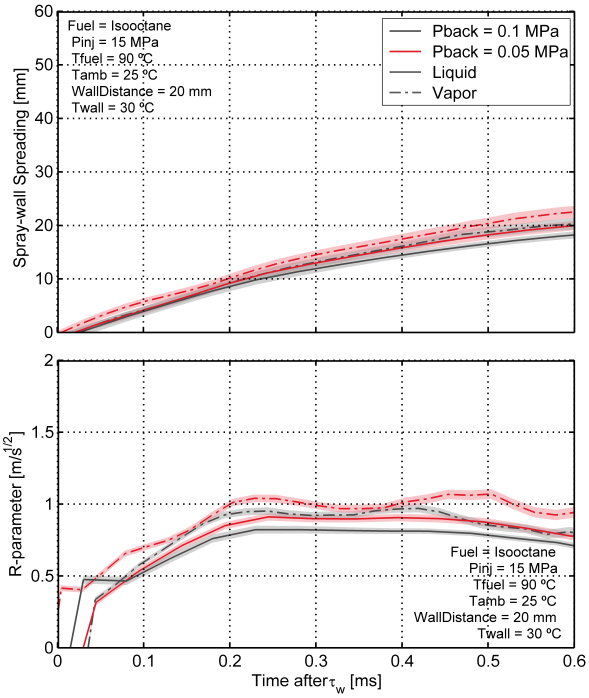

Figure 6.3: Spray-wall spreading and R-parameter for different ambient back-pressures.

In the same way, the effect of the wall temperature over the spray-wall spreading after the start of SWI is shown in Figure 6.4. The wall temperature changes do not produce any changes in the penetration curves for the conditions tested. It is possible to identify a difference between the vapor and liquid phases, meaning that the vapor develops faster than the liquid phase over the wall. The R-parameter allows to perceive the differences in the slope value between those curves.

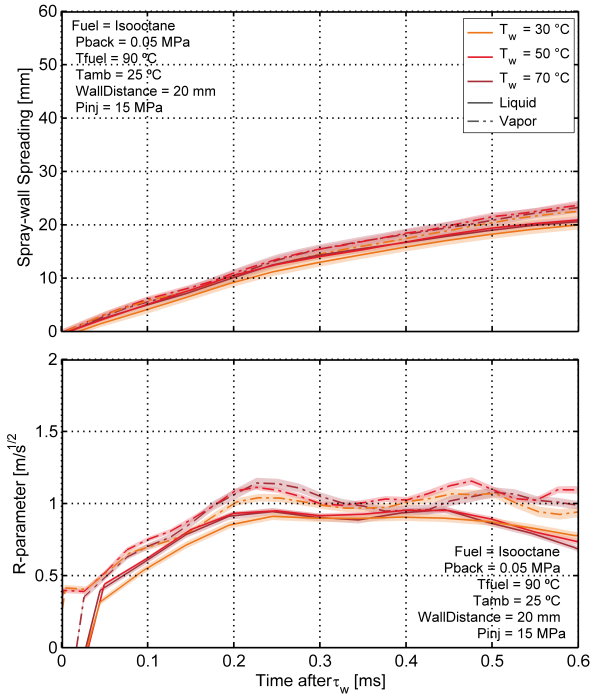

Figure 6.4: Spray-wall spreading and R-parameter for different wall temperatures.

6.2.2 Spray width after the SWI

The spray thickness was calculated at two different distances from the "impact point" in the same way as was calculated for the quartz wall. Figure 6.5 shows the obtained values for 0 mm and 5 mm from the collision point. As happened for the previous wall configuration, it is possible to notice two different behaviors when comparing the zth_0 and zth_5. In the first case, the thickness of the spray behaves almost constantly throughout the entire spray interaction event. When the fuel injection ends, the remaining fuel evaporation produces higher spray widths at the end of the injection event. The injection pressure changes did not produce any remarkable differences in the spray width for zth_0.

For the second case, when analyzing zth_5, the differences between the liquid and vapor phases of the spray are more evident, and the effect of the injection penetration is small but observable. The curves stop behaving constant as in the previously described case. After the spray hits the wall and begins the spreading, recirculation zones are created over the spray end, plus the air-fuel mixing and evaporation, increasing the vapor width in those zones,

explaining the differences obtained when higher distances from the impact point are analyzed.

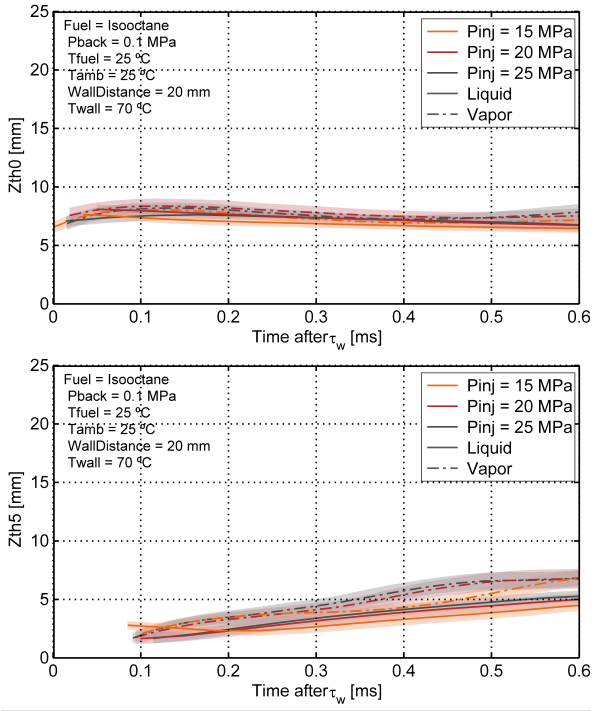

Figure 6.5: Spray thickness for liquid and vapor phases measured at two different positions for different injection pressures.

Figure 6.6 shows the spray thickness with wall temperature variation for the liquid and vapor phases of the spray spreading. As in Figure 6.5, the zth_0 curves are almost constant during the entire spray interaction event. The spray vapor thickness is slightly higher during the whole SWI event. For this point, the SWI is starting, and the spray evaporation due to the wall temperature is not evident. For zth_5, the spray width behaves differently, with a clear breach between the liquid and vapor phases that change with the wall temperature condition. Higher wall temperature produces lesser liquid spray width, explained by the spray evaporation and corroborated with the extinction profiles that will be presented in the following susbsection (the error of the curves is expressed through the shade and explains the differences observed).

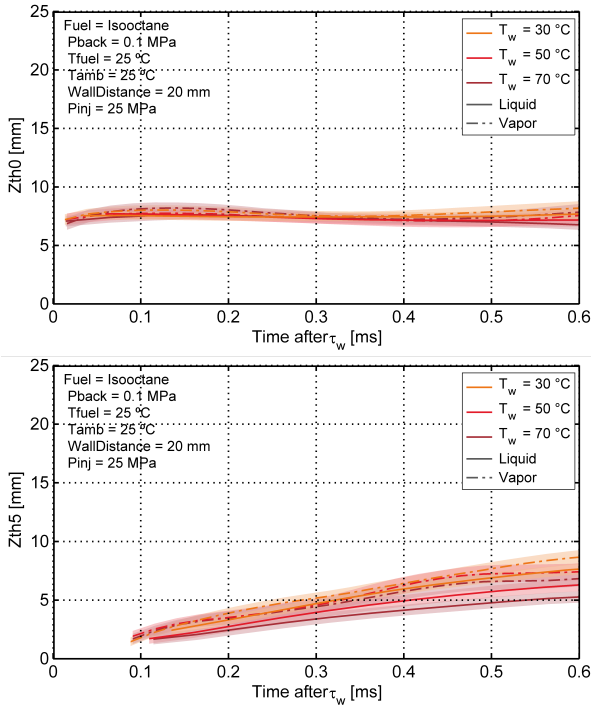

Figure 6.6: Spray thickness for liquid and vapor phases measured at two different positions for different wall temperatures.

6.2.3 Light extinction profiles

The following figures will present the extinction profiles with injection pressure and wall temperature variation. As in the case of the isothermal quartz wall (previous chapter), the KA profiles were measured by integrating all the KL values measured at zth_5.

In Figure 6.7, the extinction profiles varying the injection pressure with ambient temperature variation from left to right are depicted. It is possible to notice that as for the cases of free-jet and isothermal wall, higher injection pressures produce higher extinction curves caused by a higher amount of liquid due to smaller spray angles. Also, it is possible to notice that increasing the ambient temperature produces a significant reduction (almost 50%) over the KA magnitude, being a probe of a higher vapor amount in the spray.

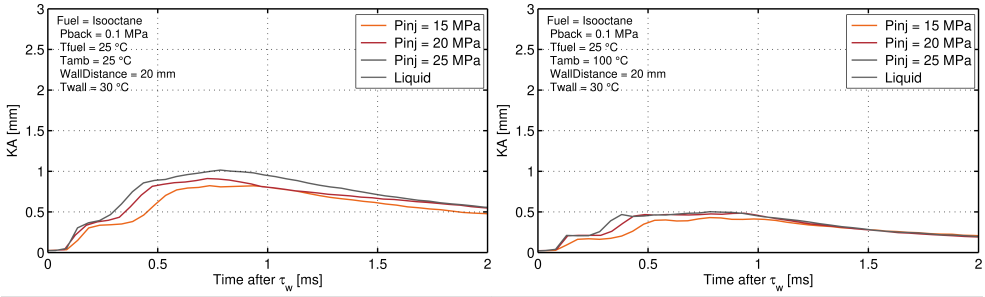

Figure 6.7: Extinction profile at zth_5 varying the injection pressure. Left: Wall at $T_{amb} = 25°C$. Right: Wall at $T_{amb} = 100°C$.

In Figure 6.8, the *KA* curves varying the wall temperature with ambient temperature variation from left to right are shown. As expected, higher wall temperatures produce lesser extinction values caused by less liquid in the spray. Also, the combined effect of ambient and wall temperature increase produces less liquid in the spray enhancing the spray evaporation.

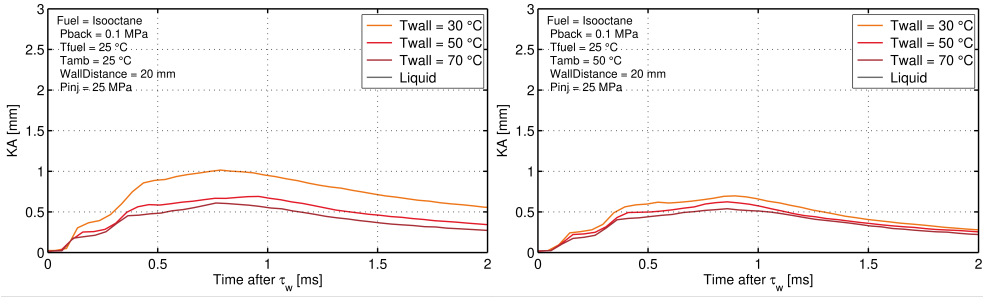

Figure 6.8: Extinction profile at zth_5 varying the wall temperature. Left: Wall at $T_{amb} = 25°C$. Right: Wall at $T_{amb} = 50°C$.

6.2.4 Comparison of both wall campaigns.

The following figures will present a comparison between the isothermal and the thermoregulated wall in terms of spray-wall spreading, spray thicknes and extinction profiles.

Figure 6.9 shows the vapor spray wall spreading for both walls. Both curves have different wall surface temperatures, and, for the case of the thermoregulated wall, it was fixed to 70°C. It is possible to see that a higher surface temperature produces a higher vapor penetration. The five millimeters difference in the wall-to-tip distance between both wall configurations

affect the remanent energy that the spray possesses after colliding with the wall and affect the τ_w (being smaller for the closer wall configuration).

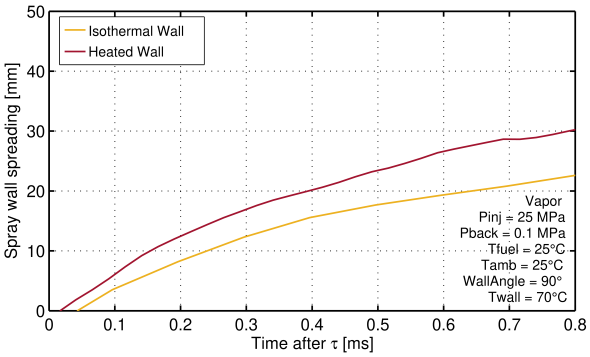

Figure 6.9: Spray spreading comparison for both the isothermal wall and the thermoregulated walls.

In Figure 6.10 and Figure 6.11, the spray thickness of both walls is compared at zth_0 and zth_5, respectively. It is noticeable that in the first case, both walls behave similarly during the first part of the injection event, and then after 0.5 ms, the heated wall begins to present a higher width value. Higher evaporation is achieved as a product of the higher surface wall temperature. For the second case, the heated spray thickness remains higher for the entire spray-wall interaction event, meaning that the higher evaporation as a result of higher wall surface temperature produces a higher width value in this zone.

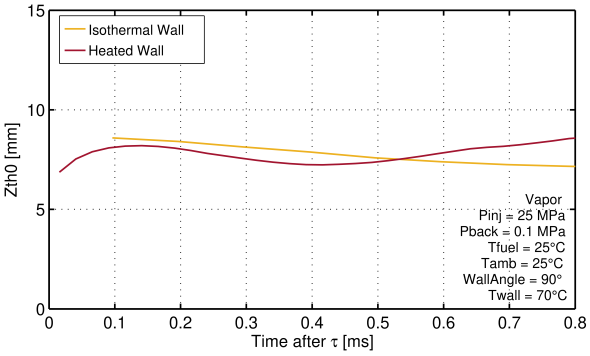

Figure 6.10: Spray thickness comparison at zth_0 for both wall used in the experimental campaign.

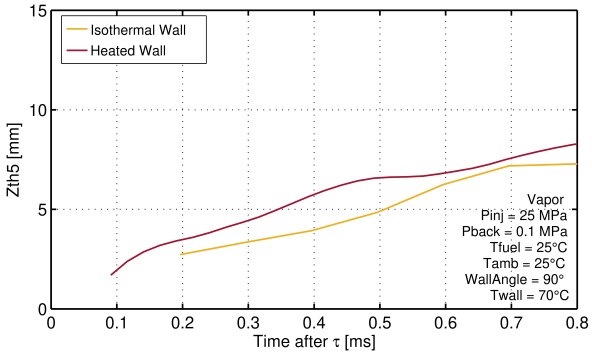

Figure 6.11: Spray thickness comparison at zth_5 for both the isothermal and the thermoregulated walls.

In Figure 6.12, it is possible to see a comparison between the heated and isothermal walls in terms of KA at zth_5. A higher extinction profile is obtained for the isothermal wall, meaning more liquid in the spray. The wall temperature increase enhances the spray evaporation causing lesser extinction profiles, as can be seen. There is a considerable difference between the isothermal wall ($Tw = Tamb = 25\,°C$) and the heated wall at 30 °C that could be attributed to the material of the wall, the stainless steel compared to the quartz have more thermal conductivity and less heat capacity which mean the heat transfer between the spray and the wall is faster affecting the fuel evaporation.

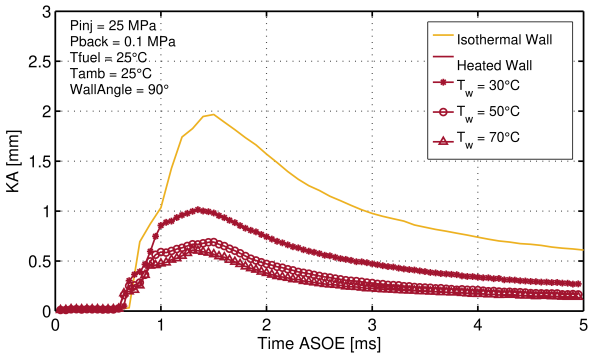

Figure 6.12: Extinction profile comparison at zth_5 for both walls used in the experimental campaign.

6.3 SWI heat flux results

The wall temperature variation presented in this section was obtained with the fast-response thermocouple directly impacted by the spray. The location of the thermocouples was explained in the scheme shown in Figure 3.9. Also, as described in the previous chapter, the whole wall support system was decentered with respect to the injector tip to ensure that the spray hit the thermocouple surface. The temperature signal acquired with the digital oscilloscope was used to obtain the heat flux transferred to the wall by the spray during the SWI. The wall temperature variation ΔT_w (which is obtained by subtracting the wall temperature before and after the SWI) and the wall heat flux $\dot{q}_w$ will be shown in the subsequent figures for different parametrical variations.

The profile of the wall temperature variation along all the parametrical analyses that will be presented remains the same, with an initial negative rise with a steep slope when the spray hits the sensor surface, reaching a peak. After this, the ΔT_w slowly decreases as the spray spreads over the wall and the fuel evaporation occurs. The temporal limit shown in the figures is set to 4 ms for the ΔT_w, and it is enough to show that the wall temperature recovers its initial target value before each injection event, being 2000 ms, the time between injections. On the other hand, the surface heat flux profiles present a steep rise (normally negative) followed by an almost steady value during the SWI which is in concordance with works found in literature [1–3]. All the figures presented have the same vertical limits to express visibly the effect of the parametrical variation over the magnitudes studied.

The wall temperature and surface heat flux comparisons usually describe a cooling behavior during the spray-wall interaction. Even though some combination of injection conditions produces a heating effect during the SWI, the results show a significant magnitude regarding the surface heat flux and ΔT_w comparable with the spray cooling research discussed in the literature [4–6]. An interesting phenomenon occurs when the fuel evaporation over the wall surface produces or enhances the cooling effect, producing considerable changes in the wall temperature profiles and over the surface heat flux curves. The evaporation by changing the wall temperature was corroborated in the previous section when the extinction profiles were analyzed.

In Figure 6.13, the injection pressure effect over the surface heat flux and ΔT_w is shown. It is possible to notice a delay in the temperature signals and surface heat flux curves that appears due to the known effect of the injection pressure over the spray velocity at the nozzle exit. For the lower injection

pressure, the spray took more time to reach the wall surface, causing a delay in the first rise of the curves. By increasing the injection pressure, the spray velocity and the number of droplets impacting the wall surface should also increase, expecting more heat flux with more injection pressure. However, this effect is appreciated with a smaller intensity than expected, as seen in the figure top part. Also, there are cases, such as the one presented in the bottom part of the figure, where the expected behavior is inverted.

What is appreciated in all cases is a direct correlation between the heat flux and the evaporation produced due to the impact against the wall. For example, in Figure 6.7, the KA after the spray impact is represented for the Figure 6.13-bottom conditions, and in which it is possible to see that higher injection pressures produce higher extinction profiles, meaning more liquid droplets in the spray. With the aforementioned in mind, a possible explanation for the behavior in the heat flux could be attributed to the appearance of the splashing droplet phenomena, causing the droplets to not evaporate onto the wall surface, reducing the total computed heat flux over the wall surface [7] and affecting the final amount of computed KA. Also, Roque et al. [8] found that the fuel vaporization is not considerably affected by the injection pressure inside the impingement region at a wall temperature of 80 °C, meaning that if the amount of liquid droplets remains the same for all the injection pressures, the differences in the heat flux can be explained with the fact that some liquid droplets are ejected far from the wall surface, obtaining less heat exchange with the wall surface.

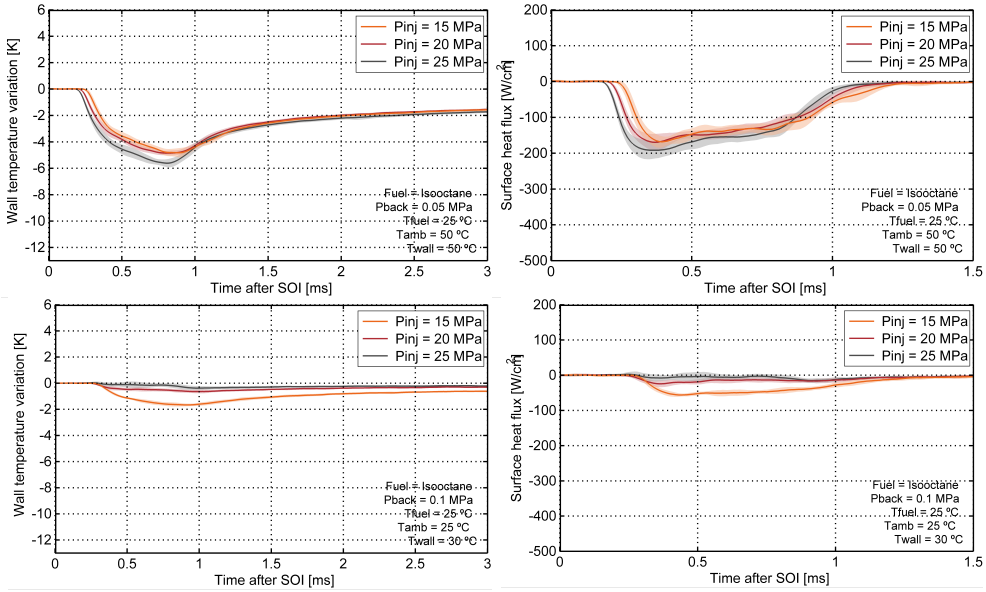

Figure 6.13: Wall temperature variation (left) and surface heat flux (right) for different injection pressures. Top: Direct effect of the injection pressure. Bottom: Inverse effect.

In Figure 6.14, the ambient back-pressure effect over the surface heat flux and ΔT_w is shown. The ambient back-pressure only influences the time the spray hits the surface sensor, which produces differences in the initial slope rise of the curves. Higher ambient back-pressures cause a higher restriction over the spray development, causing a delay in the spray impact time with the thermocouple sensor. By increasing the ambient back-pressure, the spray penetration decreases, along with the convective coefficient, which should cause a decrease in the surface heat flux. In the same way, in previous chapter of this work, was seeing how increasing the ambient back-pressure produced higher extinction profiles meaning more liquid in the spray, which can be seen as more liquid hitting the wall surface and increasing the surface heat flux magnitude. Both combined effect finally causes no remarkable differences to be observed by varying the back-pressure in the range tested.

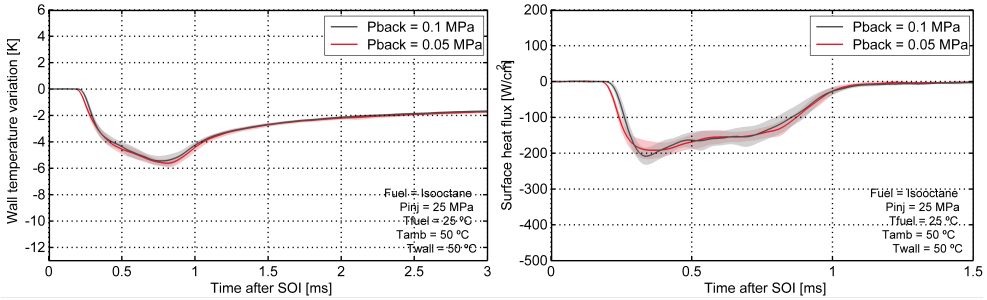

Figure 6.14: Wall temperature variation (left) and surface heat flux (right) for different ambient back-pressures.

Figure 6.15 shows the effect of the ambient temperature over the surface heat flux and the wall temperature variation. The comparison presented in this figure indicates that the fuel and ambient temperature play an essential role in the final spray temperature before the spray impacts the wall. In this case, higher ambient temperatures produce lower ΔT_w and surface heat flux because the test point illustrated in the figure presents a wall temperature set in 50°C meaning that the temperature difference is higher for the lower ambient temperature (25°C - yellow line). Unlike the previous comparison, the ambient temperature changes produce a visible difference in the magnitude of both variables studied.

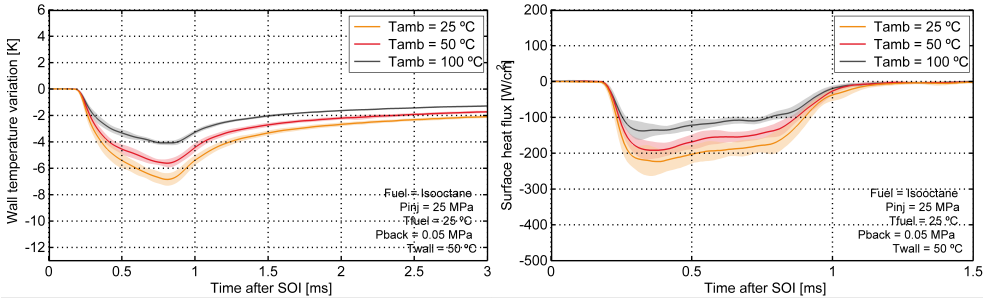

Figure 6.15: Wall temperature variation (left) and surface heat flux (right) for different ambient temperatures.

Figure 6.16 shows the fuel temperature variation effect over the heat flux and ΔT_w. The fuel temperature will be directly involved in the final spray temperature before the spray wall interaction occurs. After the fuel exit the injector nozzle, the fuel air-mixing and evaporation happens, changing the

mixture temperature and affecting the absolute temperature difference between the spray and the surface wall temperature. This plot reflects an interesting trend because if the spray hits the wall at the same nominal fuel temperature, the higher fuel temperature should produce a higher positive heat flux and surface temperature variation, which is not the case. It is important to consider that the boiling temperature of the isooctane is 99 °C at ambient pressure which is close to the fuel temperature value employed in the experimental campaign, meaning that a higher amount of fuel in vapor phase impacts the wall. For the lower fuel temperature, more liquid droplets hit the wall subtracting a higher amount of heat from the wall surface, producing the observed difference.

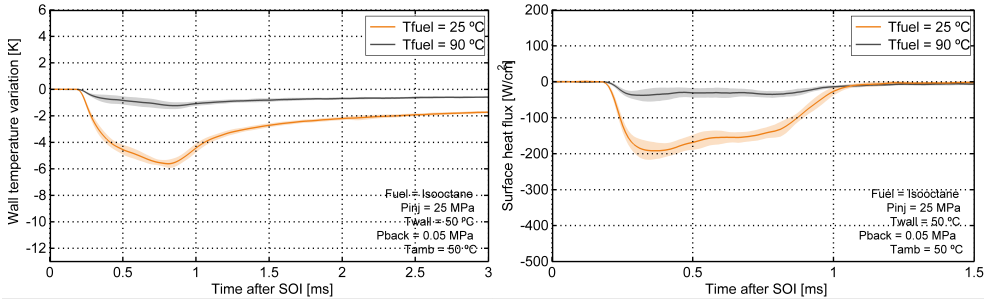

Figure 6.16: Wall temperature variation (left) and surface heat flux (right) for different fuel temperatures.

Figure 6.17 shows the combined effect of fuel temperature and ambient back pressure over the surface heat flux. As shown in previous sections of this work, the flash boiling occurrence modified the expected trend in some scenarios. In this case, it is possible to see that without flash boiling; there is less evaporation meaning more hot fuel reaches the wall and heats it. On the contrary, under flash boiling, the spray evaporates more, meaning more spray-air entrainment (which cools down the spray). At the same time, less liquid reaches the wall surface due to evaporation, producing a less significant wall cooling compared to the cold fuel scenario. Also, it is possible to notice that for the 25 °C fuel temperature, nothing change between both figures.

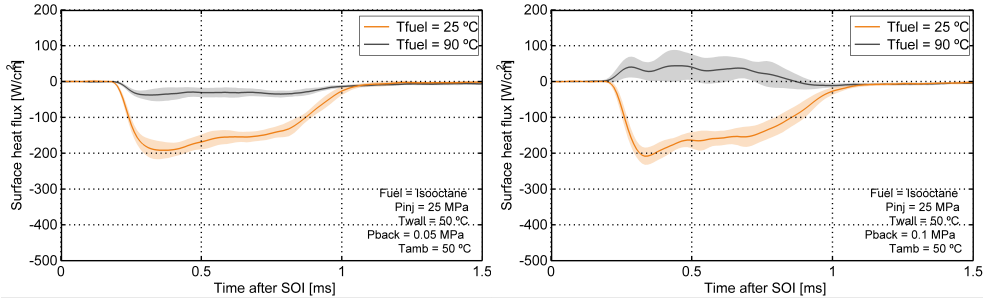

Figure 6.17: Surface heat flux for different ambient back-pressures and fuel temperatures.

Figure 6.18 shows the wall temperature variation effect over the heat flux and ΔT_w. As expected, a higher wall temperature produces a higher temperature variation over the wall surface during the spray-wall interaction. For the presented operation conditions, where the fuel temperature is almost the same as the yellow curve ($T_w = 30\,°C$), the temperature variation is minimal and derives into a small amount of surface heat flux. On the contrary, for a $T_w = 70\,°C$, the temperature variation is considerable, producing an increase of seven times over the surface heat flux magnitude.

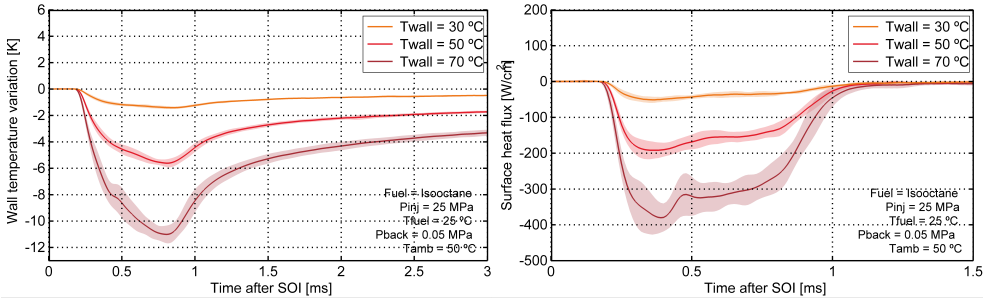

Figure 6.18: Wall temperature variation (left) and surface heat flux (right) for different wall temperatures.

After analyzing the effect of the aforementioned variables, it is clear that the wall and fuel temperature variation produce the most significant changes over the ΔT_w and over the surface heat flux magnitude. The ambient temperature variation also produced changes in the wall surface temperature and surface heat flux but to a lesser extent.

In Figure 6.19, the surface heat flux averaged in the steady zone with wall temperature, and ambient back-pressure is shown. This figure presents the

wall surface cooling behavior, highlighting the order of magnitude obtained. The general trend described before is observed where the injection and ambient back pressures do not produce significant changes in the surface heat flux. It is possible to notice that for the lower wall temperature, the difference between both ambient back pressures is more evident, which could be attributed to differences in the condition represented in the pressure-enthalpy diagram requiring less energy to produce the fuel evaporation.

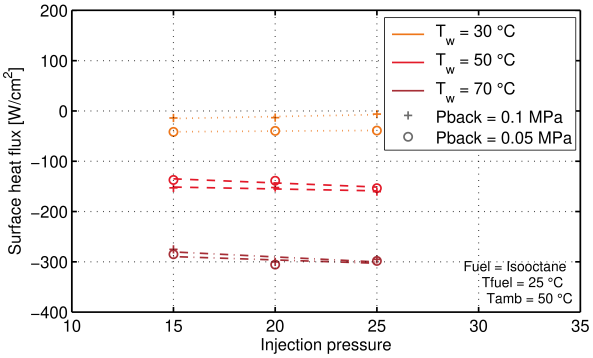

Figure 6.19: Surface heat flux averaged in the steady zone of the curve for different wall temperature and ambient back-pressure.

In Figure 6.20, the surface heat flux averaged in the steady zone with ambient and fuel temperature is depicted. All the trends mentioned previously are shown, and it is possible to see the heating effect of the spray over the wall for the 30 °C and 50 °C wall temperature cases only with the higher fuel temperature and the cooling effect of the spray over the wall for the 70 °C wall temperature case for both fuel temperatures.

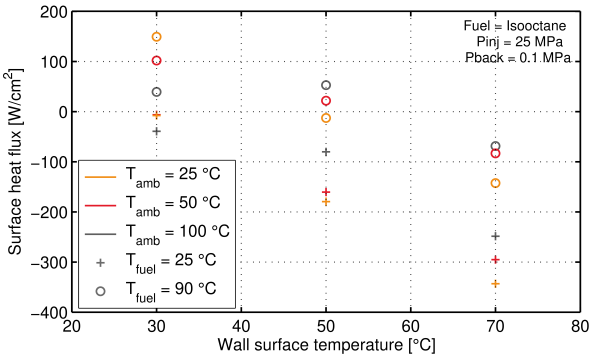

Figure 6.20: Surface heat flux averaged in the steady zone of the curve for different ambient and fuel temperature.

6.4 Convective heat transfer coefficient estimation

This section will present an estimation of the convective heat transfer coefficient h. It is essential to clarify that the methodology followed is made by making several assumptions about the studied phenomena. The aim is to give an order of magnitude for the h coefficient.

The convective coefficient is obtained from Equation 6.1, where T_w corresponds to the wall surface temperature, T_∞ to the temperature measured far from the wall surface and q correspond to the surface wall heat flux. Of the entire test matrix, only were taken into account the points in which the fuel temperature and the ambient temperature were almost the same, corresponding to T_∞. This consideration was done to ensure that the behavior of the presented curves is entirely caused by the process of heating or cooling exerted by the spray during the SWI. The following figures will present the convective heat transfer coefficient by varying several ambient and injection conditions and wall temperature variations.

In Figure 6.21 for a selected test point with a hot fuel temperature and cold ambient temperature, a cooling and heating process is observed. It is very difficult to define a mixture temperature to obtain the convective coefficient for the rest of the cases with different temperatures between the ambient and the spray. For this specific case, a mixture temperature range of 50-80 °C (without considering evaporation) translates into a heating effect over the wall for $T_w = 50\,°C$ (red curve), which is not true. A complex phenomenon related to the spray vapor amount, spray cooled by evaporation, amount of

liquid droplets, and collision and droplet breakup phenomenon governs the obtained heat flux behaviors.

$$q = h \cdot (T_w - T_\infty) \tag{6.1}$$

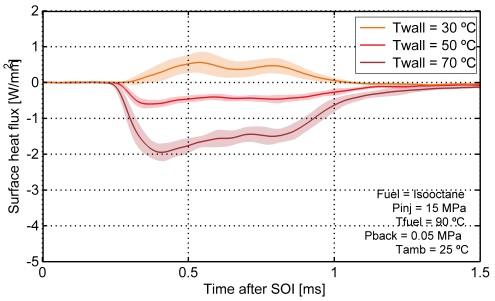

Figure 6.21: Cooling and heating effect of the spray caused by the SWI.

In Figure 6.22, the convective coefficient profiles with time are shown for different injection pressures and ambient back-pressures. The profiles behave equally to the surface heat flux curves in the previous section. No visible variations are obtained by changing the injection pressure and ambient back-pressure conditions. A delay between the curves is obtained, explained by the velocity of the spray at the nozzle exit, where higher injection pressures shorten the impact time of the spray.

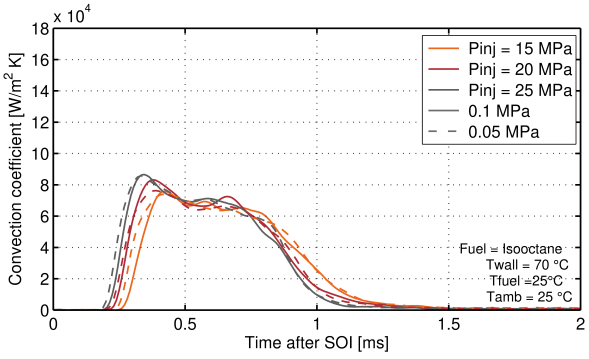

Figure 6.22: Convective coefficient profiles with injection pressure and ambient back-pressure variation.

In Figure 6.23, the effect of the wall temperature over the convective coefficient profiles is depicted. The lower wall temperature produces a higher

convective coefficient caused by a combined effect between the surface heat flux magnitude and the ΔT. Even if the surface heat flux is lower (for the lower wall temperature), the temperature difference between T_∞ and T_w is minor, increasing the h magnitude. The surface heat flux magnitude is higher for the higher wall temperature, but the temperature difference also increases, causing a reduction in the convective coefficient profile.

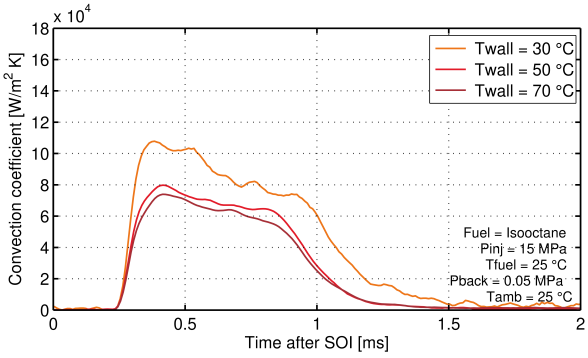

Figure 6.23: Convective coefficient profiles with wall temperature variation.

In Figure 6.24, the average convective coefficient profiles in the nearly constant region are shown with wall temperature and ambient back-pressure variation. It is important to say that the presented methodology to compute the convective coefficient was made to understand the order of magnitude of the studied phenomenon. Considerably high convective coefficient values were obtained in the $2 \cdot 10^4$ and $14 \cdot 10^4$ W/m^{2}K range. The higher convective coefficient was obtained by using the lower wall temperature configuration. Still, almost all the combinations of injection and ambient conditions produced a convective coefficient in the range of $6 \cdot 10^4$ and $9 \cdot 10^4$ W/m^{2}K which agrees with the spray cooling order of magnitude found in literature [9–11].

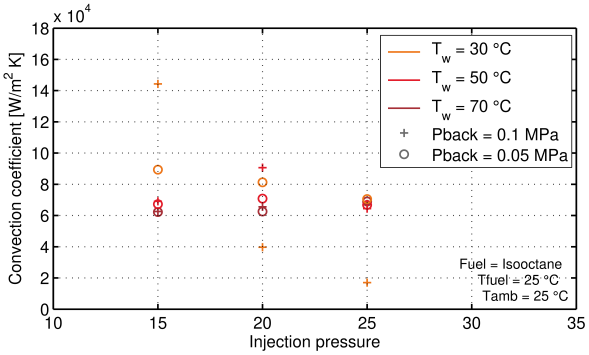

Figure 6.24: Average of the convective coefficient profiles for the nearly constant region.

6.5 Summary and conclusions

This chapter used an instrumented and thermoregulated wall coupled with fast-response thermocouples to analyze the spray-wall interaction at cold-start and other evaporative engine conditions using a GDI injector. One wall-to-tip distance was used to guarantee that the spray hits the sensor surface and to directly analyze the surface temperature variation and heat flux. Different wall temperatures were set by regulating the hot oil flow inside the wall design. The same operating conditions regarding the injection pressure, ambient temperature, back pressure, and fuel temperature used with the isothermal wall were employed, simultaneously performing high-speed imaging visualization of the liquid phase of the spray via DBI and the vapor phase via Schlieren. Finally, the time-resolved surface heat flux prediction using the temperature signals obtained with the thermocouples and the estimation of the convective coefficient were presented.

Regarding the geometrical evolution and development of the spray, the behavior obtained is similar to the one obtained in the previous chapter: Small variations of the spray spreading with the increase of the injection pressure for both phases of the spray and negligible differences by varying the wall temperature. Significant variations between the vapor and liquid phases of the spray were found, remarking the contribution of fuel evaporation caused by the wall temperature increase. For the spray thickness measured at two different points from the "impact point", a remarkable difference between the zth_0 and zth_5 was found, where, for the first case, a steady behavior of the spray width was obtained for the entire SWI duration with slight variations between the liquid and vapor phases. On the contrary, for zth_5, the curves present an

increasing slope with appreciable differences between the liquid and vapor phases with a small effect of the injection pressure. The wall temperature increase showed a decreasing impact over the liquid spray width during the entire SWI.

In the same way, the extinction profile curves in terms of KA were calculated. As in the previous chapter, the ambient temperature and wall temperature highly affect the amount of liquid present in the spray. By increasing both temperatures, a lesser amount of liquid was found.

The isothermal and thermoregulated wall were compared regarding spray-wall spreading, spray thickness, and extinction profiles measured at zth_5. It was found that the heating of the wall surface produced changes in the vapor spray wall spreading. Regarding the spray thickness, the instrumented wall showed a higher vapor width than the isothermal wall caused by fuel evaporation. Finally, the extinction profile comparison showed that increasing the wall surface temperature reduced the spray amount of liquid caused by a higher evaporation rate.

The surface heat flux during the SWI event was calculated with high-temporal resolution using fast-response thermocouples. For the range evaluated in the experimental campaign, the results revealed a significant increase in surface heat flow and wall temperature variance with both wall and fuel temperature and with the ambient temperature but to a lesser extent. By changing the operation condition, a heating or cooling effect was found during the SWI phenomenon. The extinction profiles helped to realize that the amount of liquid colliding with the wall surface has a determining role in the physical phenomenon.

Finally, the heat transfer convective coefficient estimation was performed by using the surface heat flux profiles and the T_∞ (considered as the fuel or ambient temperatures for the cases in which are the same) and T_w temperatures. From this estimation, the profiles behave as the surface heat flux, and important order of magnitude comparables with the spray cooling phenomenon broadly studied in the literature was obtained. A higher heat subtraction due to more liquid droplets colliding with the wall surface produced higher convective coefficients, along with the fact that the ΔT is small for the colder wall and fuel temperature combination cases.

References

[1] Zhao, Zhihao, Zhu, Xiucheng, Zhao, Le, Naber, Jeffrey, and Lee, Seong-Young. "Spray-Wall Dynamics of High-Pressure Impinging Combustion". In: 2019. DOI: 10.4271/2019-01-0067.

[2] Moussou, Julien, Pilla, Guillaume, Rabeau, Fabien, Sotton, Julien, and Bellenoue, Marc. "High-frequency wall heat flux measurement during wall impingement of a diffusion flame". In: *International Journal of Engine Research* (2019).

[3] Mahmud, Rizal et al. "Characteristics of Flat-Wall Impinging Spray Flame and Its Heat Transfer under Small Diesel Engine-Like Condition". In: *SAE Technical Paper 2017-32-0032* (2017).

[4] Kim, Jungho. "Spray cooling heat transfer: The state of the art". In: *International Journal of Heat and Fluid Flow* 28.4 (2007). Including Special Issue of Conference on Modelling Fluid Flow (CMFF'06), Budapest, pp. 753–767. DOI: https://doi.org/10.1016/j.ijheatfluidflow.2006.09.003.

[5] Salman, Azzam S. et al. "Experimental investigation of the impact of geometrical surface modification on spray cooling heat transfer performance in the non-boiling regime". In: *International Journal of Heat and Mass Transfer* 133 (2019), pp. 330–340. DOI: https://doi.org/10.1016/j.ijheatmasstransfer.2018.12.058.

[6] Benther, J.D., Pelaez-Restrepo, J.D., Stanley, C., and Rosengarten, G. "Heat transfer during multiple droplet impingement and spray cooling: Review and prospects for enhanced surfaces". In: *International Journal of Heat and Mass Transfer* 178 (2021), p. 121587. DOI: https://doi.org/10.1016/j.ijheatmasstransfer.2021.121587.

[7] Moreira, A, Moita, Cossali, E, Marengo, M, and Santini, M. "Secondary atomization of water and isooctane drops impinging on tilted heated surfaces". In: *Experiments in Fluids* 200 (2007), p. 117626. DOI: 10.1007/s00348-007-0330-2.

[8] Roque, Anthony, Foucher, F., and Helie, Jerome. "Spray wall interaction: study of preferential vaporization of fuel film as function of injection pressure and wall temperature". In: 2019.

[9] Cebo-Rudnicka, Agnieszka, Malinowski, Zbigniew, and Buczek, Andrzej. "The influence of selected parameters of spray cooling and thermal conductivity on heat transfer coefficient". In: *International Journal of Thermal Sciences* 110 (2016), pp. 52–64. DOI: https://doi.org/10.1016/j.ijthermalsci.2016.06.031.

[10] Freund, S., Pautsch, A.G., Shedd, T.A., and Kabelac, S. "Local heat transfer coefficients in spray cooling systems measured with temperature oscillation IR thermography". In: *International Journal of Heat and Mass Transfer* 50.9 (2007), pp. 1953–1962. DOI: https://doi.org/10.1016/j.ijheatmasstransfer.2006.09.028.

[11] Cheng, Wen-Long, Liu, Qi-Nie, and Fan, Han-lin. "Experimental investigation of parameters effect on heat transfer of spray cooling". In: *Heat and Mass Transfer* 46 (2010). DOI: https://doi.org/10.1007/s00231-010-0631-5.

Chapter 7

Infrared thermography wall heat transfer characterization

7.1 Introduction

This chapter corresponds to the last result chapter. It explains the observations obtained with the infrared thermography technique applied to a heated flat wall using the Joule effect and the well-known Spray G injector. In this chapter, only ambient temperatures and ambient back-pressure were used. Two wall temperatures were defined (100 and 200°C), and two injection pressures (10-20MPa). The results allowed a comparison between the magnitude of the surface heat flux obtained with IR with those obtained with the thermoregulated wall under several injection and ambient conditions variations. All the information regarding the heat model used and its suitability has been explained and shown in section 4.5.

In the first part of this chapter, the results of the "Spray G" injector in terms of heat flux, convective coefficient and impact area as zero-dimensional data (average, maximum and mean absolute deviation) together with an injector angles characterization are first reported and discussed. These data are summarized in Table 7.2, each row of the table corresponds to each pair of pressure and temperature tested in the experimental campaign. In the second part, a comparison between the IR and the heated wall results is presented.

Infrared Thermography (IR) has been already employed to visualize and measure the temperature distribution of impinging sprays [1, 2]. This tech-

nique brings several advantages [3] that make it suitable in such a complex area of investigation: it provides high sensitivity measurements and it is a non-intrusive, two-dimensional technique capable of very low response time. Gibbons and Robinson [4] carried out, for the first time, a study of a single source electrospray using thin foil thermography to investigate the local convective heat transfer. A preliminary study employing IR thermography to study the "Spray G" wall interaction with hot wall was performed by Contino et. al [5]. The latter was focused mainly on the experimental setup and the relative infrared camera calibration procedure. Moreover, the temperature maps presented and discussed are relative to high time delay from the start of injection (up to 20 ms), when the interaction is ended (injection duration 1 ms). By using the same experimental apparatus described in [5], the wall heat transfer interaction was investigated by means of infrared thermography coupled with an inverse heat transfer data reduction.

The details of the operating conditions are summarized in Table 7.1.

Table 7.1: Investigated operating conditions.

Test Conditions		
Injector	Spray G	-
Thin foil temperature (T_w)	373 ± 2, 473 ± 2	[K]
Current through the foil	31.2 ± 0.15 , 53.2 ± 0.27	[A]
Voltage drop through the foil	1.17 ± 0.01, 1.92 ± 0.01	[V]
Injection pressure (p_{inj})	10 ± 0.5, 20 ± 0.5	[MPa]
Nozzle-to-wall distance	11 ± 0.01	[mm]
Fuel	iso-octane (C_8H_{18})	-
Fuel temperature (T_f)	298 ± 2	[K]
Injected fuel mass	10.48 @ $p_{inj} = 10$ MPa 15.44 @ $p_{inj} = 20$ MPa	[mg]
Spray duration	1	[ms]
Ambient temperature	298 ± 0.5	[K]

7.2 Spray impact area, convective heat transfer coefficient and heat flux

The spray impact area for the four investigated cases is depicted in Figure 7.1, and it is possible to see how a larger area of impact is obtained for the lower wall temperature by changing the injection pressure. Also, by increasing the

wall temperature at the same injection pressure (from left to right), an area of impact reduction is obtained.

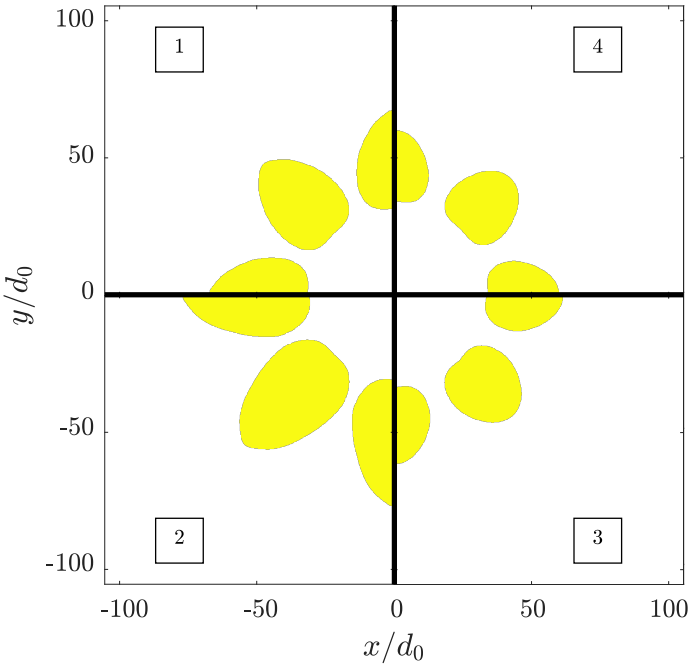

Figure 7.1: Spray impact area. 1) $T_w = 373\,\mathrm{K}, p_{inj} = 10\,\mathrm{MPa}$, 2) $T_w = 373\,\mathrm{K}, p_{inj} = 20\,\mathrm{MPa}$, 3) $T_w = 473\,\mathrm{K}, p_{inj} = 20\,\mathrm{MPa}$, 4) $T_w = 473\,\mathrm{K}, p_{inj} = 10\,\mathrm{MPa}$.

The convective coefficient maps for all the investigated cases are presented in Figure 7.2 by changing the wall temperature and the injection pressure, the heat flux increases as well with a peak in the stagnation point. Also, even the heat flux increase, the convective coefficient is decreased since the wall surface temperature is higher and the fuel temperature remains the same. By changing the injection pressure and maintaining the wall temperature constant, the magnitude of the convective coefficient is slightly higher and it is confirmed by the footprint patterns of the plume shown in Figure 7.2.

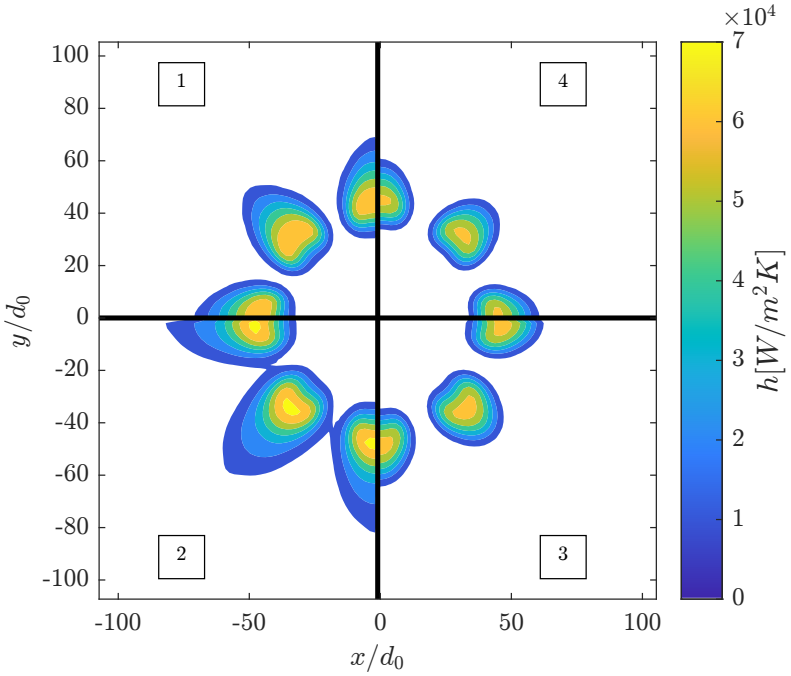

Figure 7.2: Convective coefficient map. 1) $T_w = 373\,\text{K}, p_{inj} = 10\,\text{MPa}$, 2) $T_w = 373\,\text{K}, p_{inj} = 20\,\text{MPa}$, 3) $T_w = 473\,\text{K}, p_{inj} = 20\,\text{MPa}$, 4) $T_w = 473\,\text{K}, p_{inj} = 10\,\text{MPa}$.

The heat flux shows similar maximum values for the two injection pressures as happened in section 6.3 and considerable differences by changing the temperature of the wall, as it can be seen in Figure 7.3. The possible explanation of this phenomenon can be related to the fact that increasing the injection pressure (which increases the jet flow velocity) causes an increase in the appearance of the splashing droplet phenomena over the wall surface, finally causing the droplets to not evaporate onto the wall surface, reducing the total computed heat flux over the wall surface [6]. In the case of the convective coefficient, the higher the wall temperature, the lower is the convective coefficient, reaching its maximum value at the stagnation point of the spray. Also, there is a noticeable difference in the shape of the heat flux and the convective coefficient profiles by changing the wall temperature. For the lower wall temperature the shape is wider and presents variability in the falling edge of the curve after the peak value. This is evidence of the splashing phenomenon and the presence of more liquid fuel on the surface of the wall. With this figure, it is possible to see the concordance with the results obtained for the surface heat flux in the previous chapter, where slight differences were obtained by

increasing the injection pressure. The heat flux variation with the injection pressure begins to appear after the impact when the spray spreads over the wall (depending on the spreading behavior in a region out of the thermocouple sensing surface).

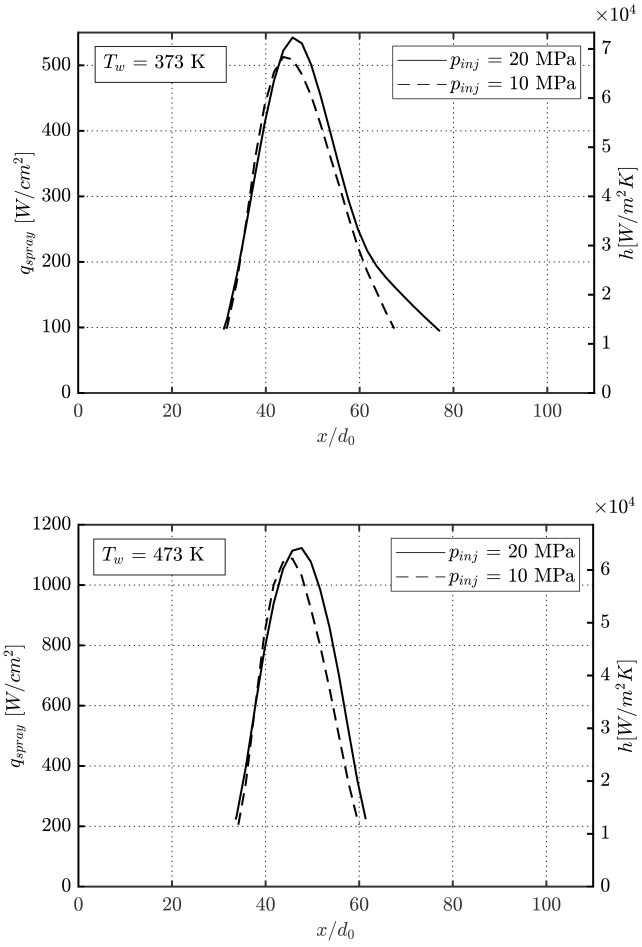

Figure 7.3: Convective coefficient and heat flux spatial distribution along the symmetry axis of a single plume.

7.3 Comparison between experimental campaigns

In Figure 7.4, the maximum convective coefficient values for both experimental campaigns are depicted. The ones carried out at the CMT-Motores Térmicos are surrounded by a dotted square, while the Naples ones are identified with a dotted circle; also, it is important to say that the green cross corresponds to $P_{inj} = 10\,\text{MPa}$. Also, the similarity between the magnitudes obtained in both campaigns is shown, obtaining values around $7{\cdot}10^4$ W/m^{2}K

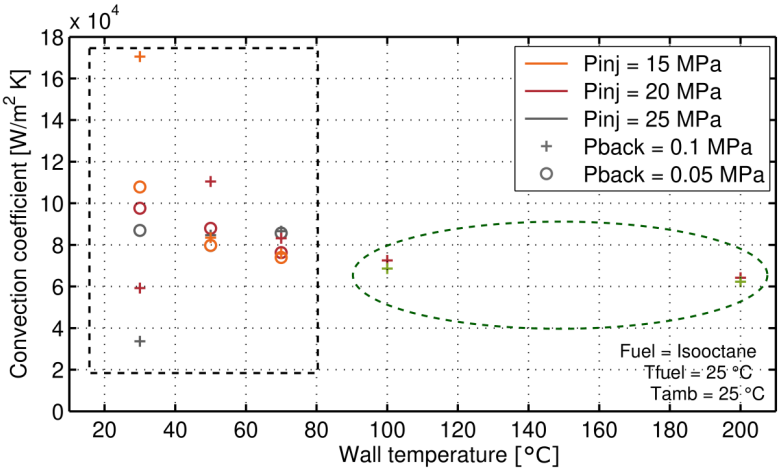

Figure 7.4: Maximum convective coefficient values for both experimental campaigns (CMT and Naples) with injection and ambient back pressure variations.

In Table 7.2 it is possible to notice that the increase in the injection pressure for the lower wall temperature (373 K) produces a change over the area of impact of 33% and a change over the maximum convective coefficient and the maximum heat flux of 5%. On the other hand, for the higher wall temperature (473 K) the increment in the injection pressure produces an 14% increment in the area of impact and a 3% increment for the maximum convective coefficient and the maximum heat flux. Also, when comparing the maximum heat flux results with the obtained in chapter 6, a 6% is obtained for the lower wall temperature and lower injection pressure, and 3% is obtained for the lower wall temperature and the higher injection pressure. Only the lower wall temperature (373 K) was compared due to the high dependence of the heat flux with the surface wall temperature. In the same way, when comparing the maximum convective coefficient h for the lower wall temperature (373 K), it was found that a 9.5% is obtained for the lower wall temperature and lower

injection pressure and 12.7% is obtained for the lower wall temperature and the higher injection pressure.

The increase in the wall temperature for the lower injection pressure (10 MPa) produces a reduction in the area of impact of 31%, and an increase over the maximum heat flux of 52% and 9% over the maximum convective coefficient. For the higher injection pressure (20 MPa), the increase of the wall temperature produces a reduction in the area of impact of 47% and the same increment of 52% over the maximum heat flux and 11% over the maximum convective coefficient . At lower wall temperature the percentage increase of the impact area is higher of the percentage increase of the injected fuel mass (+90% vs +47%), indicating a worsening of the heat exchange mechanism. On the contrary, at higher wall temperature the percentage increase of the impact area is significantly lower of the percentage increase of the injected fuel mass (+18% vs +47%) indicating an improvement of the heat exchange mechanism.

The non-uniformity distribution of the heat flux follows the same trends stated in the previous paragraphs. By keeping the same injection pressure but increasing the wall temperature a higher non-uniformity distribution value is obtained. More, by increasing the injection pressure keeping the wall temperature constant produces an increase in the non-uniformity distribution value. The heat flux mean values are almost the half of the maximum values. As the heat flux peak value is located in the spray impact point, the heat flux in the area of impact has an important variability as the distance with the impact point increases. More heat transfer occurs where the major amount of liquid is in contact with the heated wall.

The plume direction angle shows a slightly dependence form stagnation pressure. The average value of tests at 20 MPa is equal to 32.7° and is in good agreement (about 4% error) with the one reported by Payri et al. [7] numerically computed at same testing condition. About the spray cone angle, was found that it varies from 17.3° to 19.5° as it can be seen in Table 7.2 at the different conditions tested. Numerical results obtained by Payri et al. [8, 9] predicts a spray cone angle about 20° at 20 MPa that is in good agreement with $T_w = 373$ K and 20 MPa present measurement. In the other conditions, the differences can be attributed to the presence of the wall at a small distance from the injector tip and/or the use of spray impact area to estimate this information. The shape of the area of impact for each operating condition are shown in Figure 7.1. It is possible to notice that the impact area of the spray rises by increasing the injection pressure and decreases by increasing the temperature of the plate. This overall behavior and the order

of magnitude are in agreement with the results shown in [10] for toluene as injected fuel. The condition of higher injection pressure (20 MPa) and lower wall temperature ($T_w = 373\,\mathrm{K}$) produces a higher value of major axis of the elliptical like shape spray area of impact, this can be related to the splashing effect of the spray interacting with the wall plus the accumulated amount of non-evaporated liquid which cause a larger footprint.

Conditions	**Results**						
	A_i [cm^2]	q_{max} [W/cm^2]	$\bar{q}$ [W/cm^2]	h_{max} [W/m^{2}K]	δ_q	θ	β
10 MPa 473 K	1.15	1089.9	583.97	$6.23{\cdot}10^4$	73.11	17.3	31.9
10 MPa 373 K	1.67	513.71	270.22	$6.86{\cdot}10^4$	35.26	17.8	31.6
20 MPa 373 K	2.5	542.54	223.41	$7.25{\cdot}10^4$	41.39	19.5	32.5
20 MPa 473 K	1.33	1122.9	620.26	$6.42{\cdot}10^4$	64.91	17.3	32.9

Table 7.2: Summary of zero-dimensional results.

7.4 Summary and conclusions

In this chapter, the IR thermography coupled with an inverse heat transfer data reduction was applied to investigate the spray/wall interaction using the "Spray G" injector and iso-octane as the injected fuel. The effect of the injection pressure and the wall temperature over the convective coefficient, the area of impact and the heat flux of the injector located at 11 mm over a heated thin foil was investigated.

Four cases were taken into account, including two injection pressures (10 and 20 MPa) and two wall temperatures (373 and 473 K). High resolved 2D-heat flux and area of impact maps were evaluated for each condition. The time-history of the wall spray cooling was reconstructed by a single-image acquisition delayed with respect to the start of the injection by making use of 125 repetitions of the injection event.

Results show that for the lower wall temperature ($T_w = 373K$) the injection pressure has a major effect over the spray impact area, and this is in accordance to the literature. Furthermore, an increase in the wall temperature leads to a reduction in the spray area of impact (due to the fluid vaporization)

and a raise in the maximum value of the convective coefficient and the heat flux.

Higher wall temperatures lead to higher fuel vaporization. An increase in the injection pressure enhances the splashing phenomenon which is more evident for the lower wall temperature. The results show that proposed experimental methodology is an interesting technique to investigate the spray/wall interaction and it can measure wall heat flux distributions, the spray area of impact and spray angles. Used in conjunction with more classical optical techniques such as Schlieren and Diffused Background Illumination can contribute to more robust and comparable results.

The data acquired along this chapter will be also useful to focus further investigations in the fuel-rich zones after the spray impingement to achieve a better understanding of soot emissions, fuel film adhesion, and the spray spreading on a hot wall.

It is important to notice that the results presented in this chapter with the infrared thermography technique are comparable in terms of surface heat flux with the ones obtained with the heated wall coupled with fast-response thermocouples. Both works were carried out in different experimental facilities and applied different techniques and different injectors but kept similar injection pressures and wall temperatures. As expected, the cases corresponding to $100°C$ are closer to the results obtained with the $70°C$ wall temperature used in the previous chapter. And the expected trend was obtained in which increasing the wall temperature increases the computed surface heat flux.

References

[1] Akafuah, Nelson K., Salazar, Abraham J., and Saito, Kozo. "Infrared thermography-based visualization of droplet transport in liquid sprays". In: *Infrared Physics and Technology* 53.3 (2010), pp. 218–226. DOI: 10.1016/j.infrared.2009.12.002.

[2] Schulz, Florian, Schmidt, Jurgen, Kufferath, Andreas, and Samenfink, Wolfgang. "Gasoline Wall Films and Spray/Wall Interaction Analyzed by Infrared Thermography". In: *SAE International Journal of Engines* 7.3 (2014), pp. 1165–1177. DOI: 10.4271/2014-01-1446.

[3] Carlomagno, Giovanni Maria and Cardone, Gennaro. "Infrared thermography for convective heat transfer measurements". In: *Experiments in Fluids* 49.6 (2010), pp. 1187–1218. DOI: 10.1007/s00348-010-0912-2.

[4] Gibbons, M.J. and Robinson, A.J. "Heat transfer characteristics of single cone-jet electrosprays". In: *International Journal of Heat and Mass Transfer* 113 (2017), pp. 70–83.

[5] Contino, Mattia, Zaccara, Mirko, Montanaro, Alessandro, Allocca, Luigi, and Cardone, Gennaro. "Dynamic Thermal Behavior of a GDI Spray Impacting on a Heated Thin Foil by Phase-Averaged Infrared Thermography". In: 2020. DOI: https://doi.org/10.4271/2019-24-0036.

[6] Moreira, A, Moita, Cossali, E, Marengo, M, and Santini, M. "Secondary atomization of water and isooctane drops impinging on tilted heated surfaces". In: *Experiments in Fluids* 200 (2007), p. 117626. DOI: 10.1007/s00348-007-0330-2.

[7] Payri, Raúl, Gimeno, Jaime, Martí-Aldaraví, Pedro, and Martínez, María. "Transient nozzle flow analysis and near field characterization of gasoline direct fuel injector using Large Eddy Simulation". In: *International Journal of Multiphase Flow* 148 (2022). DOI: https://doi.org/10.1016/j.ijmultiphaseflow.2021.103920.

[8] Payri, Raul, Hardy, Gilles, Gimeno, Jaime, and Bautista, Abian. "Analysis of counterbore effect in five diesel common rail injectors". In: *Experimental Thermal and Fluid Science* 107 (2019), pp. 69–78. DOI: 10.1016/j.expthermflusci.2019.05.008.

[9] Payri, R., Gimeno, J., Marti-Aldaravi, P., and Martinez, M. "Large Eddy Simulations of the fuel injection and mixing process of the ECN GDi Injector Spray G". In: *ICLASS International Conference on Liquid Atomization and Spray Systems* (2021).

[10] Luo, Hongliang et al. "Effect of temperature on fuel adhesion under spray-wall impingement condition". In: *Fuel* 234 (2018), pp. 56–65. DOI: https://doi.org/10.1016/j.fuel.2018.07.021.

Chapter 8

Conclusions and future works

This chapter aims to synthesize the key findings from the study provided throughout this thesis. Furthermore, future potential investigations and possible upgrades to the current study are highlighted to suggest future advancements on this issue.

8.1 Summary

This study was undertaken with the premise that internal combustion engines (ICEs) will be in use in the near future and the resulting need to decrease fuel consumption and emissions of harmful pollutants in response to upcoming climate challenges. This thesis aims to understand better the processes involved during cold-start and evaporative engine-like injection conditions and the interaction between the spray and a wall. These are relevant for current and future generations of ICEs. The focus was on gasoline conditions, and several optical and sensor-based diagnostic techniques were used in the experiments carried out at the CMT-Motores Térmicos and at the Istituto di Scienze e Tecnologie per l'Energia e la Mobilità Sostenibili (STEMS) and the University of Naples "Federico II" facilities.

Significant resources have been dedicated to creating and applying hardware, experimental methods, and data processing algorithms. These efforts were organized into four experimental campaigns, each with a distinct focus:

- Free-jet visualization conditions.

- Spray-wall interaction using a transparent isothermal wall.
- Spray-wall interaction using an instrumented and thermoregulated wall.
- Infrared thermography of an spray impacting a heated thin wall.

Analyzing the scenarios mentioned above is crucial to comprehend the mechanisms behind the spray-wall interaction phenomenon.

Parametric variations of the conditions were performed to investigate free and impinged spray behaviors for various operating and wall settings. Free penetration and spreading along the wall showed similar behavior. In the case of free-spray penetration, the injection pressure, fuel temperature variation and the flash boiling occurence produced the most remarkable differences. The start of the spray-wall interaction was found to be influenced by the injection pressure, the ambient-back pressure, the wall angle, and the wall-to-tip distance. The spray spreading over the wall, as happens with the free-jet penetration, was influenced by the injection pressure and mainly by the wall angle. As momentum-driven variables, both steady free penetration and wall spreading were proportional to the square root of time. This shows that the *R-parameter* is a helpful parameter to analyze them regardless of temporal reference or beginning state. The flash boiling appearance for the lower ambient back pressure and higher fuel temperature condition changed the spray morphology in terms of the width (spray angle), having significant repercussions over the *R-parameter* (which is reliant on the spray penetration) and in the number of liquid droplets present in the spray affecting both the light extinction profiles and the surface heat flux profiles.

Spray thickness was measured at two different distances from the "impact point", affected by changes in wall-to-tip distance and wall angle but, even more, by the distance from the "impact point" in which it is measured. It was found for the closer measure point (zth_0) a nearly constant spray thickness with a linear decreasing trend over time. Increasing the wall-to-tip distance raises the final measured thickness caused by the air-mixing process in the near nozzle region, which affects the opening of the spray (spray angle) before hitting the wall surface. For zth_5, an increase of the spray width with time was obtained, and the effect of the injection pressure over the spray width became more noticeable, in which a higher injection pressure produces a higher spray width. For the effect of the wall angle over the spray width, it was found that the spray has a favorable spray spreading direction through the inclined wall condition, obtaining higher width values for the bigger wall-to-tip distance for the two measured points.

The extinction profiles in terms of KA were obtained for both free-jet and isothermal wall configuration, the second one measured at zth_5. It was found that even it is not possible to know the droplet diameter or droplet cloud physical behavior with the optical techniques employed in this work, it provides a reliable information about the amount of liquid present in the spray. It was found that the ambient and fuel temperatures increases produce a reduction in the amount of liquid present in the spray.

The semi-circle impact area was calculated as the region between a perpendicular line to the plume direction that passes through the impact point and the furthest contour of the spray in each image frame. The semi-circle impact area is susceptible to wall angles and wall-to-tip distance variations. It is related to the spray-air entrainment in the near nozzle region and to the droplet breakup regime caused by differences in the collision energy obtained by changing geometrical wall parameters.

In general, no remarkable differences were found between the liquid and vapor phases of the spray for either of the free-jet and isothermal wall spray spreading campaigns. However, it is important to highlight the appearance of the flash boiling in one of the conditions studied in this thesis ($T_{fuel} = 90\,°C$ under $P_{back} = 0.05\,MPa$), since under flash boiling interesting trends were obtained for the ambient back pressure and fuel temperature parametric variations.

The thermoregulated wall results emulates the spray-wall interaction phenomenon more realistically, by considering a thermoregulated wall. For this experimental campaign, an instrumented and thermoregulated wall coupled with thermocouples was used to register the temperature variation in the wall surface and compute the surface heat flux using a 1-D model. As in the case of the transparent isothermal wall, a visualization campaign was carried out to obtain macroscopic characteristics of the spray as the spray spreading and the spray thickness at different points over the wall. It was found that the wall temperature variation does not produce any changes in the spray spreading over the wall. Significant variations between the vapor and liquid phases of the spray were found, remarking the contribution of fuel evaporation caused by the wall temperature increase.

For the spray thickness, it was found a nearly constant behavior for the closer measured (zth_0) and a slight distinction between the liquid and vapor phase. The injection pressure does not produce considerable changes in the spray thickness. On the other hand, the wall temperature increasing produced a decreasing in the liquid spray width for zth_5 during the entire SWI. Still,

the trend is clear, where a higher width is obtained for the vapor phase of the spray.

The extinction profiles curves were analyzed, and as in the isothermal wall case, the ambient and wall temperatures highly affect the amount of liquid droplets present in the spray. By increasing both temperatures, a lesser amount of liquid was found.

The temperature of the wall was only altered in the first few millimeters of depth (2mm) under gasoline-like conditions. Surface heat flux measurements were performed using 1-D heat flux assumptions. By using the fast-response thermocouples over the wall surface, the surface wall temperature was obtained. For the range of conditions tested in this thesis, the injection pressure and the ambient back-pressure do not produce considerable changes over the surface heat flux profile, only a clear delay between the curves was obtained as a result of the different spray velocities achieved at the nozzle outlet. The fuel and wall temperatures produce the most important peaks in terms of the ΔT_w and the heat flux caused primarly by the amount of liquid droplets that impacts the wall surface that produce and cooling or warming effect (depending on the condition) as the droplet evaporates when impacting the surface.

The heat transfer convective coefficient estimation was performed by using the surface heat flux profiles and the T_∞ (considered as the fuel or ambient temperatures for the cases in which are the same) and T_w temperatures. From this estimation, the profiles behave as the surface heat flux, and important order of magnitude comparables with the spray cooling phenomenon broadly studied in the literature was obtained ($2 \cdot 10^4$ - $14 \cdot 10^4$ W/m^{2}K range). A higher heat subtraction due to more liquid droplets colliding with the wall surface produced higher convective coefficients, along with the fact that the ΔT is small for the colder wall and fuel temperature combination cases.

The infrared thermography was used to compute the heat transfer of an isooctane spray with a heated thin flat wall. Results show that for the lower wall temperature ($T_w = 373K$) the injection pressure has a major effect over the spray impact area, and this is in accordance to the literature. Furthermore, an increase in the wall temperature leads to a reduction in the spray area of impact (due to the fluid vaporization) and a raise in the maximum value of the spray cooling efficiency and the heat flux. Higher wall temperatures lead to higher fuel vaporization. An increase in the injection pressure enhances the splashing phenomenon which is more evident for the lower wall temperature. The results show that proposed experimental methodology is an interesting technique to investigate the spray/wall interaction and it can measure wall heat flux distributions, the spray area of impact and spray angles. Used in

conjunction with more classical optical techniques such as Schlieren and Diffused Background Illumination can contribute to more robust and comparable results.

A wide range of tests and variables were investigated, yielding illuminating results concerning the behavior of the interaction between gasoline sprays and a flat wall. Experiments have been performed to gather data, gradually progressing from fundamental knowledge under simplified settings to more realistic behavior. The target phenomenon of SWI may be extrapolated to what happens within an internal combustion engine. The data derived from the efforts put into this thesis has been and continues to be used by many researchers from the institutes involved in this inquiry (academy and industry) to create, validate, and enhance their CFD models.

8.2 Future works

The considerable transitoriness of the entire process, the vast number of associated phenomena that significantly depend on operating conditions, and its essentially stochastic nature, the interaction between a fuel spray and a wall in the framework of internal combustion engines is quite complex. Despite the huge amount of data collected in this thesis, it is far from sufficient to have a complete knowledge of the complicated phenomena surrounding spray-wall interaction. There are numerous avenues for continuing the work discussed in this publication, given the importance of this topic in powertrain research. Here is a list of probable future advances that can be undertaken to examine useful conclusions beyond the ones achieved:

- Test different fuels and injectors to analyze the dependance of the studied phenomenom over variables as the L/D, viscocity, density and volatility.
- Investigate the impact of varying the injection duration by considering different energizing times, or exploring multiple-injection schemes in which each injection can alter the initial wall conditions regarding the temperature and deposition accumulation in comparison to the previous injections.
- Conducting droplet-wall and droplet-droplet collision experiments in conjunction with studies involving a tempered wall, using techniques such as PDA measurements or microscopic DBI, would be a suitable enhancement. On the other hand, researchers have discovered that the fuel film formed on the wall after SWI can lead to the formation of

UHCs, therefore, characterizing post-impingement variables like surface wettability, film thickness, and spread under varied conditions would be a significant addition to this investigation.

- Significant hardware modifications could pave the way for more experiments. The next step towards realistic experiments from this thesis would be to incorporate a bowl-shaped wall for both transparent and tempered plates, which presents challenges in terms of both optical access through the wall and cooling, respectively. Also add different wall angles to the instrumented thermoregulated wall to understand the impact of the inclination over the spray-spreading and surface heat transfer.

Appendices

Appendix A

Continental injector hydraulic characterization.

The purpose of this chapter is to present relevant results of the hydraulic characterization of the injector used in this thesis. This information is availabe in Payri et al. [1] where the authors made a complete hydraulic characterization of the Continental Injector identified as C3539. This work was done in the experimental facilities available at CMT-Motores Térmicos .

Various techniques are applied and combined to obtain the complete descriptive behavior of the hardware. The characterization includes the rate of injection and the rate of momentum. Most of the characterization methods and techniques were initially applied to diesel injectors. As discussed in chapter 2, in diesel engines, the spray is essential for mixture formation and correct combustion, in contrast to the pre-GDI gasoline engines era.

A.1 Injection rate (ROI)

The injection rate, known as the rate of injection (ROI), is a critical parameter of an injection system. Because determine how fast and how much fuel is delivered. Accuracy of injection rate was not so crucial in older PFI gasoline engines, but advanced GDI engines demand significant accuracy in ROI measurements [2].

This method was created for diesel injectors and characterized in several previous studies which used diesel as the injected fuel [3–7] and gasoline [8, 9].

An IAV injection rate discharge curve indicator (IRDCI) was used to calculate the mass flow rate. It is based on Bosch Long Tube Method [10], which use the pressure wave propagation theory in liquid tubes. Figure A.1 depicts an IRDCI diagram.

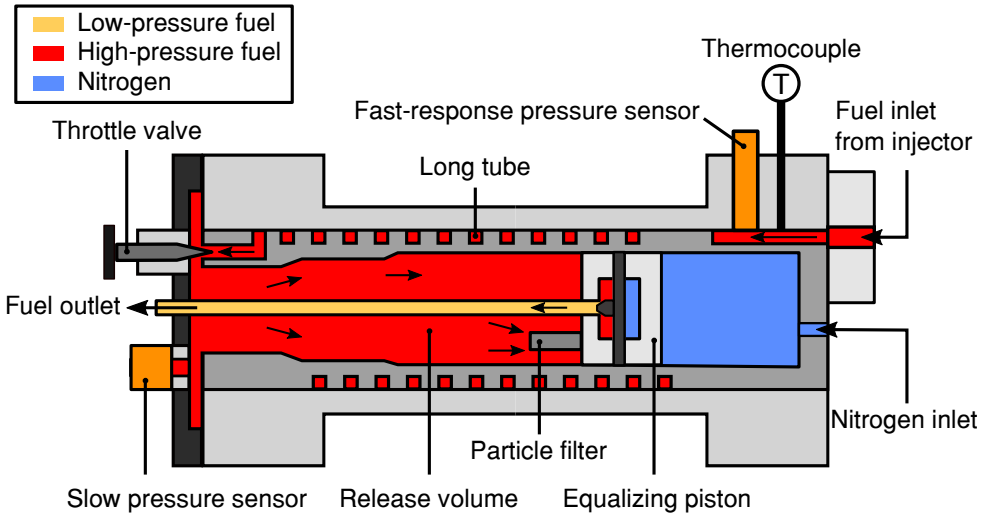

Figure A.1: Scheme of the IRDCI unit [3].

Fuel is injected into the intake, causing a pressure wave to propagate down the previously filled tube. The pulse moves at the speed of sound a certain distance until it reaches the damped discharge volume. The action of nitrogen on the balance piston can adjust the pressure inside the device to the desired outlet pressure. After the piston has been balanced and fuel has entered the piston cavity via the particulate filter, a new injection causes a pressure surge and adds mass. The piston moves and opens the outlet, allowing a small amount of mass equal to the injected mass to exit the IRDCI.

Pressure changes caused by injection events are recorded by the fast response pressure sensor. The electrical signal can be used to calculate the mass flow rate. The momentum conservation equation, ignoring gravity and taking into account a cylindrical control volume where pressure waves propagate across the section area A_c, is as follows:

$$A_c \cdot (p_v + \Delta p) - p_v \cdot A_c = \rho_f \cdot A_c \cdot a_f \cdot \Delta u_f \tag{A.1}$$

where p_v represents the pressure inside the volume, Δ_p represents the pressure difference caused by wave propagation (the injection event), ρ_f represents the

density of the fuel, a_f denotes the fuel speed of sound in the medium, and Δu_f represents fluctuations in fuel flow velocity at the exit section. As shown in Equation A.1 can be simplified to:

$$\Delta p = a_f \cdot \rho_f \cdot \Delta u_f \tag{A.2}$$

A piezoelectric sensor placed close enough to the tip of the injector to avoid signal attenuation due to frictional losses detects the increase in pressure caused by an injection event. When a pressure wave enters the release volume and encounters a cross-sectional change, it generates a reflected wave that propagates upstream. The IRDCI employs two solutions to avoid measurement interference. First, the long tube introduces a time delay between the two signals. Second, a throttle valve at the tube end can alter the flow area, allowing the reflected wave to be adjusted to some extent. Finally, using the continuity equation given in the Equation A.3, the wave-induced pressure difference is related to the mass flow rate.

$$\dot{m}(t) = A_c \cdot \rho_f \cdot \Delta u_f \tag{A.3}$$

Then, by solving Equation A.2 and Equation A.3 for Δu_f, the mass flow rate is obtained using:

$$\dot{m}(t) = \frac{\Delta p \cdot A_c}{a_f} \tag{A.4}$$

A steel injector holder is used to attach the injector to the IRDCI fuel inlet (see Figure A.1). Due to the slightly different geometry, each injector must have its adapter to precisely seal the O-ring. Figure A.2 shows a representation of the injector in the mount. It has a cooling circuit that helps maintain the required operating temperature. In addition, the real assemble implemented during operation is also displayed (A.2b).

On the fuel side, a thermocouple measures fuel temperature, and on the nitrogen side, a pressure sensor detects fuel pressure. These two parameters are critical for correctly calculating the speed of sound in fuel. Figure A.3 shows the measurement setup schematically. First, fuel is provided to the high-pressure pump, which supplies pressurized fuel to the common rail. The rail is then connected to the injector by a fixed high-pressure line. The IRDCI exit has a weight scale that continuously measures the weight of the fuel in the exit. This is done to minimize the uncertainty caused by calculating the speed of sound of the fuel used. This is highly dependent on fuel composition

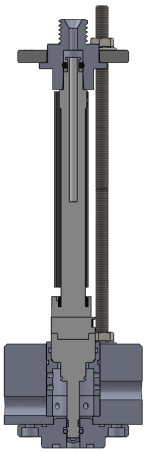

(a)

(b)

Figure A.2: Rate of Injection adaptor for the Continental injector (a) and picture of the system while operation (b).

and system pressure and temperature. The sound velocity data for isooctane (2,2,4 -Trimethylpentane) were also unavailable in the literature. Due to that, the data published in the NIST Webbook [11] were used instead. Once the injection frequency of 10 Hz has been set for the measurement and the injection volume value on the scale has stabilized, data collection is started by saving 50 injections repetitions using a digital oscilloscope. The ROI, rail pressure, and the drive signal data is taken and stored on the lab computer. Finally, the ROI signal is obtained from the IRDCI, whose integrated mean may differ from that measured on the scale. Therefore, the K value is calculated as the ratio between them, as shown in Equation A.5, and it is used to scale the rate of injection signal to make its integral equal to the measured injected mass obtained with the scale.

$$K_{adjust} = \frac{M_{balance}}{M_{int}} \tag{A.5}$$

where $M_{balance}$ is the mass measured with the scale when it reaches stability, and M_{int} is the integral of the rate of injection signal averaged over 50 repetitions. Finally, K_{adjust} corresponds to the used scaling factor. This is a

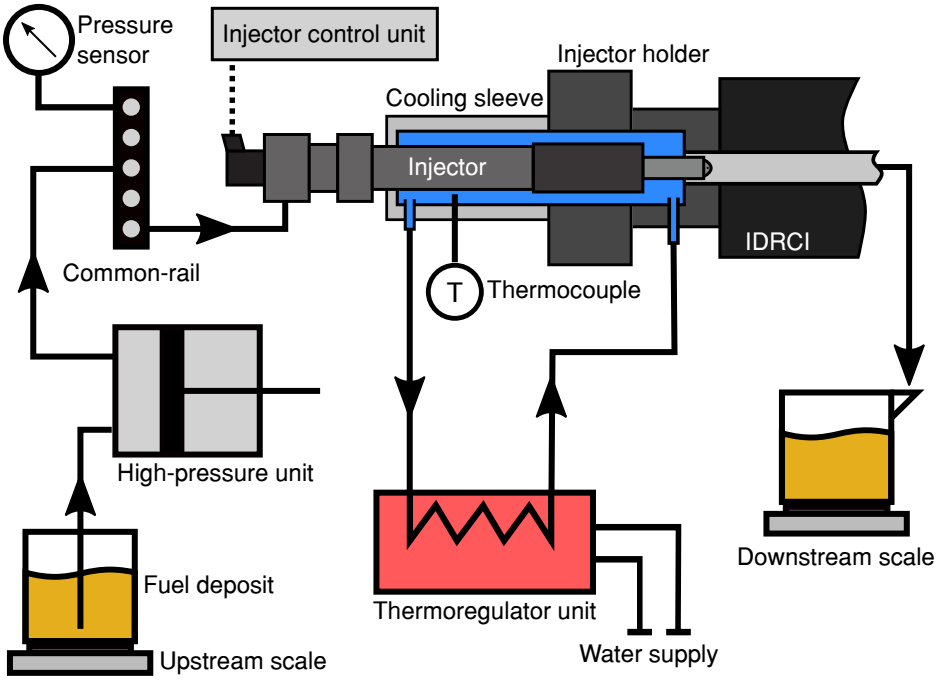

Figure A.3: Schematic set-up used in injection rate (ROI) measurements.

ratio of the previous values which typically ranges from 1.05 to 0.95. There is another aspect to take into account when obtaining the final rate of injection signal which is the accumulation phenomenon that occurs when measuring with IRDCI and is described in detail in Payri et al. [12]. During the injection events, the fuel added increases as measurements are performed, creating a continuous signal increase that must be corrected. The solution implemented to fix the raw signal is published in [12].

A.2 Spray angle measurements

The method used to calculates the spray direction for the Continental injector was derived from the approach of Shahangian et al. [13]. It is well known that the drill angle (geometric angle) at the injector nozzle does not always correspond to the exit spray due to internal or in-orifice flow interactions that deflect the core direction of the plume. Accurate positioning is necessary to minimize possible errors, so it is crucial to know the actual orientation of the plumes before measuring or investigating the injector further. For

example, spray orientation is important to perform the rate of momentum (ROM) measurements (described in subsection A.3.1).

The nozzles of the spray-guided gasoline direct injectors of the latest generation are usually located above the combustion chamber or just below the intake valves. The former are typically created with an even distribution of orifices around the axis of the injector. In contrast, the latter is always atypical due to injector placement and the requirement to deliver fuel to specific zones within the chamber. To achieve that, they have a typical hole distribution. An alternative to this method is to use X-rays to observe the spray and determine jet placement from fuel concentration. However, this is an expensive experiment, and equipment is difficult to access [14].

The technique working principle is to evaluate the jet footprint at a controlled and known distance from the injector tip. Footprint formation is caused by repeated injections that breaks a millimetric paper. With the footprint information and the nozzle tip location, the orientation angle for each orifice was calculated using trigonometry.

The injector is held by a cylinder to facilitate the alignment of the nozzle with the cylinder axis and provides support for the installation. Up to 20 injections were made to break the millimetric paper surface to provide adequate marks to distinguish the footprints. The footprints are then digitized, and a post-processing algorithm is applied to reveal the collision coordinates of the spray plume. This is accomplished by aligning the cylinder base to the circumference to find the central axis and then relating this reference to find the collision location. Finally, the spray orientation angle is determined by trigonometry using the nozzle tip orientation, position information, and impingement coordinates.

A.3 Momentum rate (ROM)

The momentum rate (ROM) is a useful metric for injector characterization. To obtain more specific information regarding the fuel flow at the nozzle exit, data from the ROM is typically combined with data from the ROI. ROM was defined by Payri et al. [15] as the injection rate multiplied by the velocity. If a fluid with a mass flow rate $\dot{m}$, momentum rate $\dot{M}$, and density ρ moves with velocity profiles u through an area A_0, the ROI and ROM are written as Equation A.6 and Equation A.7:

$$\dot{m} = \int_{A_0} u \rho dA \tag{A.6}$$

$$\dot{M} = \int_{A_0} u^2 \rho dA \tag{A.7}$$

Combining the hydraulic injector measurements (ROI and ROM) is possible to obtain useful information that can be used to investigate the flow in greater depth. With the cross-sectional area A_0 used in the previous definition, the flow can be considered as in Figure A.4 (a), where unknown information about the cavitation potential or its composition is available. However, the effective area A_{eff} (Eq. A.8) and the effective velocity u_{eff} (Eq. A.9) serve to characterise the exit flow in a simplified manner as can be seen in Figure A.4 (b).

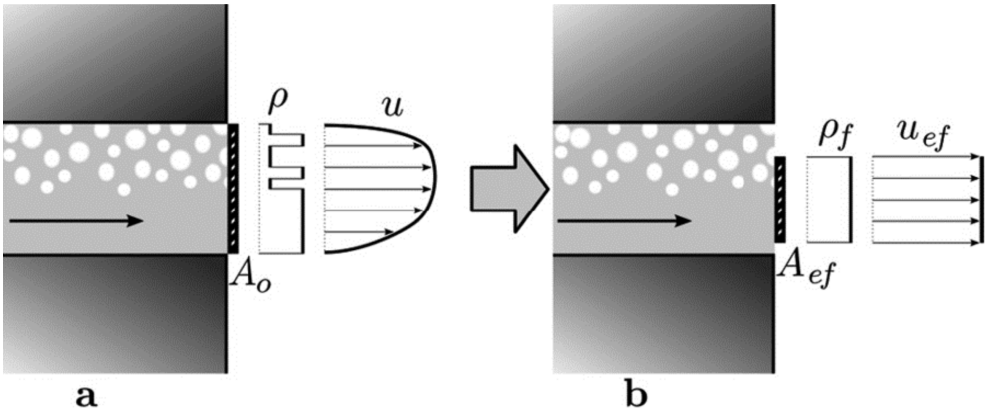

Figure A.4: Representation of the flow in the nozzle exit. In (a) there is a real representation and in (b) a simplification is represented [16].

$$A_{\text{eff}} = \frac{\dot{m}_f^2}{\rho_f M_f} \tag{A.8}$$

$$u_{\text{eff}} = \frac{\dot{M}_f}{\dot{m}_f} \tag{A.9}$$

The momentum rate (ROM) and rate of injection (ROI) are represented by $\dot{M}_f$ and $\dot{m}_f$, respectively, and the fuel density is represented by ρ_f. The theoretical velocity can then be obtained by applying Bernoulli equation to the studied geometry (u_{th}) Equation A.10:

$$u_{\text{th}} = \sqrt{\frac{2\Delta p}{\rho_f}} \tag{A.10}$$

where Δp denotes the pressure difference between the injector nozzle inlet and outlet. The discharge coefficient (Equation A.11) is the ratio of the measured ROI with the theoretical ROI and can be calculated using the mass flow rate of Equation A.6 and substituting for the u_{th} (Equation A.10):

$$C_d = \frac{\dot{m}}{u_{\text{th}} \rho_f A_0} \tag{A.11}$$

The momentum coefficient (C_M) is shown in Equation A.12, which can be expressed as the ratio of the measured momentum to the theoretical momentum obtained by combining Equation A.7 and Equation A.10.

$$C_M = \frac{\dot{M}}{u_{\text{th}}^2 \rho_f A_0} = \frac{\dot{M}}{2 A_0 \Delta p} \tag{A.12}$$

In Payri et al. [15] two additional coefficients were defined to describe the area and velocity losses. These are the effective area and effective velocity, which are displayed in Equation A.13 and Equation A.14, respectively.

$$C_a = \frac{A_{\text{eff}}}{A_0} = \frac{D_{\text{eff}}^2}{D_0^2} \tag{A.13}$$

$$C_{\text{v}} = \frac{u_{\text{eff}}}{u_{\text{th}}} \tag{A.14}$$

Finally, Equation A.15 shows the different coefficients into one equation.

$$C_M = C_d C_{\text{v}} = C_{\text{v}}^2 C_a \tag{A.15}$$

A.3.1 ROM measurement methodology and setup

One of the goals of Gimeno [16] was to develop and design the test rig used for ROM measurements. The vessel is made up of a constant volume reservoir that can simulate internal engine pressures of up to 10 MPa. It was designed to measure diesel injectors, but it could also be used to measure GDI injectors with a few modifications. The idea behind it is to measure the spray plume instantaneous impact force (F) onto a calibrated piezoelectric sensor, as shown in Figure A.5.

Several assumptions were made in Payri et al. [15] and Gimeno [16] for the rate of momentum measurements considering a cylindrical control volume that contains the domain volume between the nozzle orifice and the sensor, as

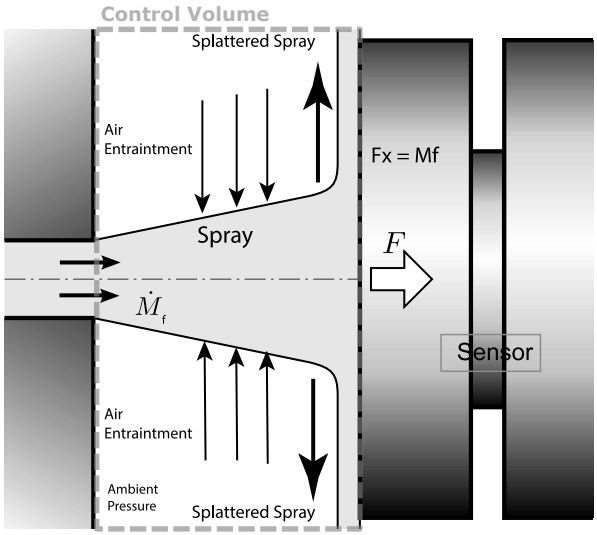

Figure A.5: Assumptions and principle of measure of the rate of momentum technique. [15].

illustrated in Figure A.5: The first is that the volume has a uniform pressure, gravity is ignored, the fuel spray axis is orthogonal to the sensor surface, the airflow that enter the control volume and the fuel leaving it after the impact are orthogonal to the spray axis, and finally, the momentum flux axial component and viscous stresses are equal to 0.

Taking into account the considerations mentioned above the force of the spray impacting the sensor can be written as in Equation A.16:

$$F = \frac{\partial}{\partial t} \int_{\mathrm{CV}} \rho u d\varpi + \dot{M} \tag{A.16}$$

As a result, the spray force is defined in two terms. The first represents changes in the instantaneous momentum flux of the mixture within the control volume, where ρ and u denote the density and velocity of the mixture passing through, respectively, and ϖ denotes the volume contour. The momentum flux at the orifice exit is represented by the second term, $\dot{M}$. However, under steady-state conditions, the Equation A.16 can be reduced to:

$$F = \dot{M} \tag{A.17}$$

This setup is created especially for diesel injectors and is suitable for single orifice injectors (as illustrated in Figure A.6) or diesel multi-orifice injectors

(with a lateral configuration). Therefore, the sensor surface has to be orthogonal to the spray axis. For this purpose, the sensor is located on the bottom of the test rig for frontal configuration or on the lateral for side arrangement.

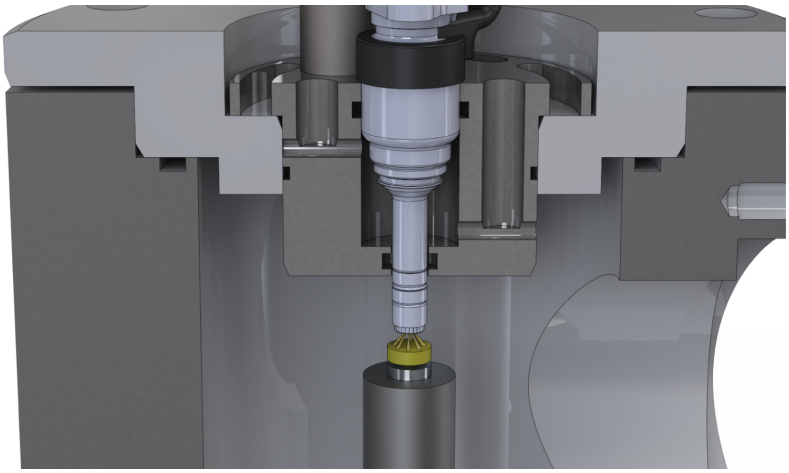

Figure A.6: Scheme of the ROM setup for frontal impact configuration. Adapted from [17].

The technique is fully suitable for GDI injectors, but measurements on the investigated nozzles are more difficult due to the different nozzle geometry. The injectors in this study have much narrower spray cones for spray interaction and flame propagation, and the pressures at which they operate complicate measurements. It is more challenging with GDI injectors since the holes are so close together. GDI, on the other hand, operates at a pressure that is an order of magnitude smaller than diesel. For that, measuring a single orifice introduces significant uncertainty in the sensor range, and the orifice is very difficult to separate has led to the measurement of the entire spray cone. Payri et al. [17] investigated his two Spray G injector configurations, as shown in Figure A.6 and Figure A.7. They reached the conclusion that the frontal configuration produced more consistent measurements.

When measuring the rate of momentum, a compromise between keeping the entire spray close enough to hit the sensor target and far enough away to avoid interaction with adjacent sprays needs to be taken into account. Also, if the distance is too far, aerodynamic effects may take place, affecting the proper amount of momentum transferred to the sensor.

The frontal configuration was used to measure the ROM of the injector in this work. One assumption for ROM measurements, as mentioned in section

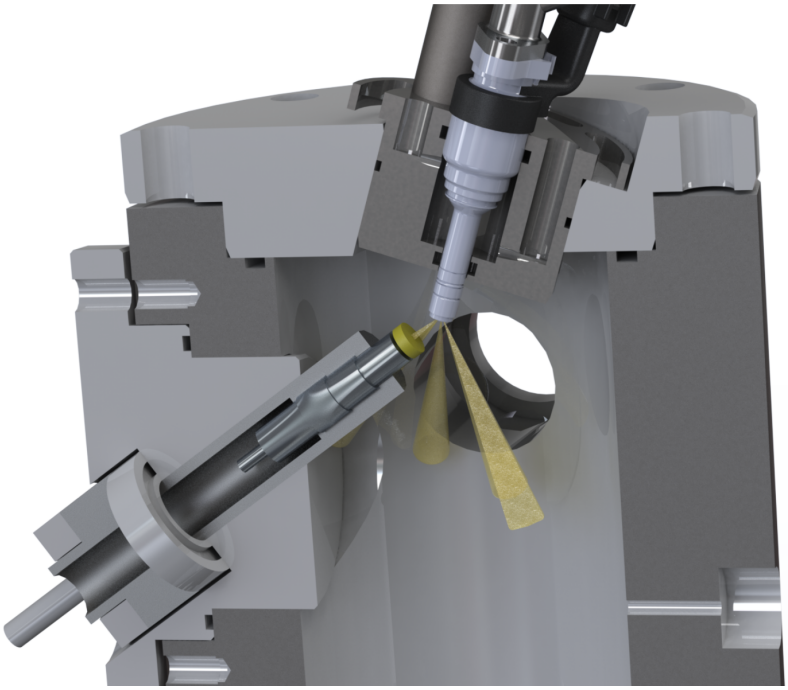

Figure A.7: Scheme of the ROM setup for lateral impact configuration. Adapted from [17].

A.3.1, is that the spray axis is perpendicular to the sensor surface. When all fuel jets are detected at the same time, this is not the case. This implies a more complicated aerodynamic interaction than the simplified problem of Figure A.5. If the detected signal is corrected for each spray angle, measurements can be taken. The spray angle was obtained by considering the spray impact over a millimetric paper (section A.2). Shahangian et al. [13] successfully corrected the ROM measurements for a commercial multi-orifice GDI injector using a similar approach. The momentum correction rate M_c is calculated using Equation A.18:

$$M_c = \sum_{i=1}^{n} \frac{M_m/n}{\cos \alpha_i} \tag{A.18}$$

where M_m is the measured total momentum, n is the number of orifices impinging on the sensor, and α_i is the angle of each fuel jet to the sensor surface.

For each test condition, 50 repetitions were recorded, as in the case of the rate of injection methodology. A digital oscilloscope is used to record ROM

signals, rail pressure signals, and ECU electrical drive signals.

A.4 Rate of injection results

The Continental injector has the same injector body technology as the SprayG of the ECN [18], designed to be installed at the top of the cylinder. From the hydraulic characterization test plan used in [1], the conditions that nearly match with the thesis are summarized in Table A.1.

Table A.1: Test matrix used for the hydraulic characterization.

Parameter	Value/Type	Units
Fuel	Isooctane	
ET	0.8	ms
Rail pressure (P_r)	100/200/300	bar
Back pressure (P_b)	2/6/15	bar
Fuel temperature (T_{fuel})	20/90	°C
Number of repetitions per test	50	

A.4.1 Hydraulic injector characterization

Figure A.8 shows an example of 50 repetitions made for each test condition during the ROI measurement. The overall average signal of all measurements represents the high-fidelity ROI signal, with little shot-to-shot variability. This indicates good injector reproducibility.

Figure A.9 and A.10 show the effect of typical injection parameters such as injection pressure and fuel temperature over the ROI. First, the effect of injection pressure is well-known [16] where, theoretically, a high ROI is primarily caused by an increase in the flow velocity. From the continuity equation, it is possible to extract the proportionality equation that describes the relationship between the two variables given by Equation A.19.

$$\dot{m} \propto \sqrt{p_r - p_b} = \sqrt{\Delta p} \tag{A.19}$$

where p_r and p_b represent the injection and chamber back pressure, respectively, Figure A.9 shows the injection rate for three injection pressures. As expected, increasing injection pressure leads to higher stable ROI. Furthermore, the start of injection (SOI) does not fluctuate with the injection pressure, as opposed to diesel injectors [16]. Changing the injection pressure, on the other

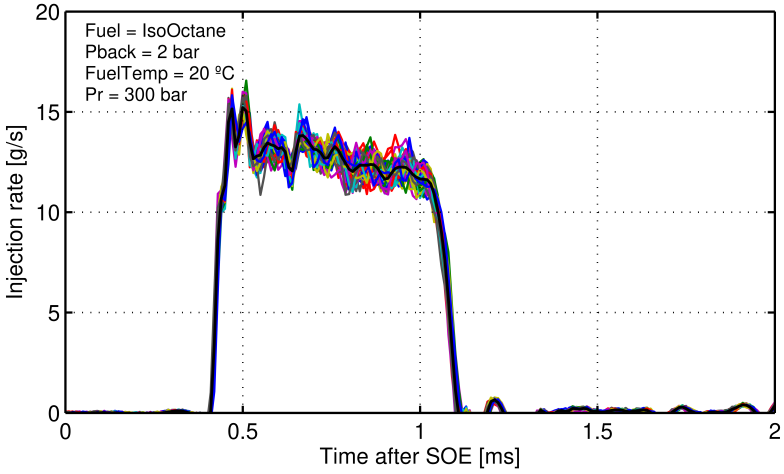

Figure A.8: Rate of injection for the Continental injector.

hand, delays the end of the injection (EOI). The pressure difference across the nozzle explains this behavior. When the electrical signal no longer excites the coil, the pressure from the rail in the injector, together with the spring acting on the needle, contribute with the needle closing.

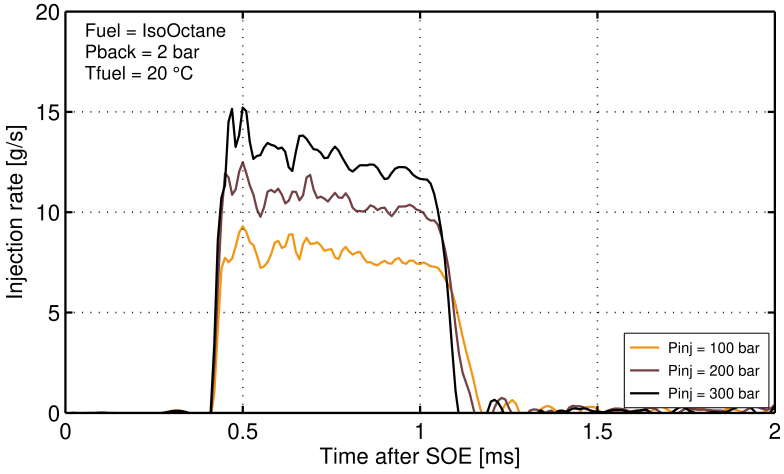

Figure A.9: Effect of rail pressure on the rate of injection signal.

Figure A.10 illustrates the effect of the fuel temperature over the ROI signal. The effect is evident at the end of injection, where a delay is produced when increasing the fuel temperature. This behavior is caused by the changes

in the bulk modulus of the fuel, as explained in [19]. The bulk modulus increases when the fuel temperature decreases, acting directly into the needle dynamics. The fuel at a lower temperature is more difficult to compress due to its high bulk modulus, meaning that the local pressure can increase more substantially, resulting in a faster needle closing.

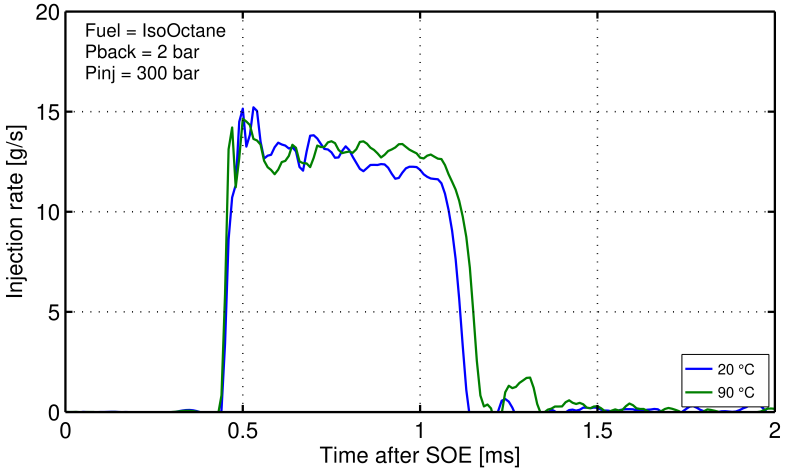

Figure A.10: Effect of the fuel temperature on the rate of injection signal.

Figure A.11 shows the effect of the ambient back-pressure over the ROI signal. The back-pressure do not affect significantly the mass flow rate as has been reported in the literature for GDI [20]

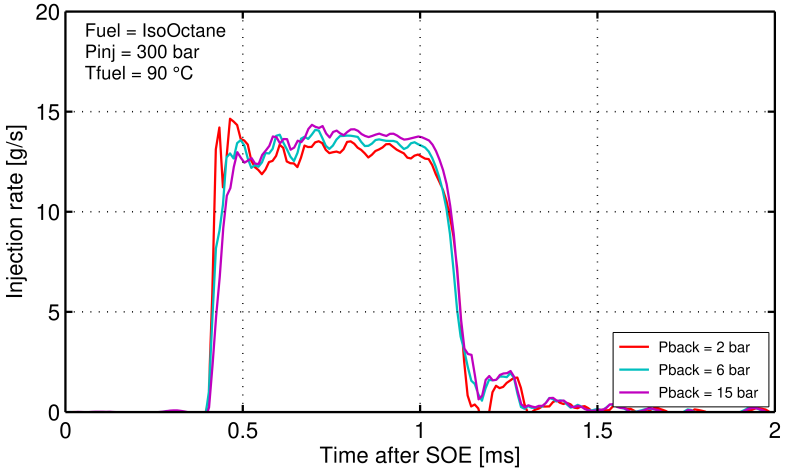

Figure A.11: Effect of the ambient back-pressure on the rate of injection signal.

A.5 Rate of Momentum results

The rate of momentum measurements was carried out by mounting the sensor from the bottom of the vessel with the injector located on the top part. The axis of the injector and the spray axis are aligned for the Continental injector. Because of that, the injector is mounted aligned with the sensor axis to measure the entire spray cloud. The figure A.12 shows a rendered cross-section of the test vessel set up for the Continental Injector. The injector tip was positioned 2.5 mm from the sensor target surface, which was a sufficient distance for all spray plumes to be detected by the sensor. It is important to clarify that the real distance between the injector tip and the sensor surface in the hardware is lesser than the despicted in the scheme.

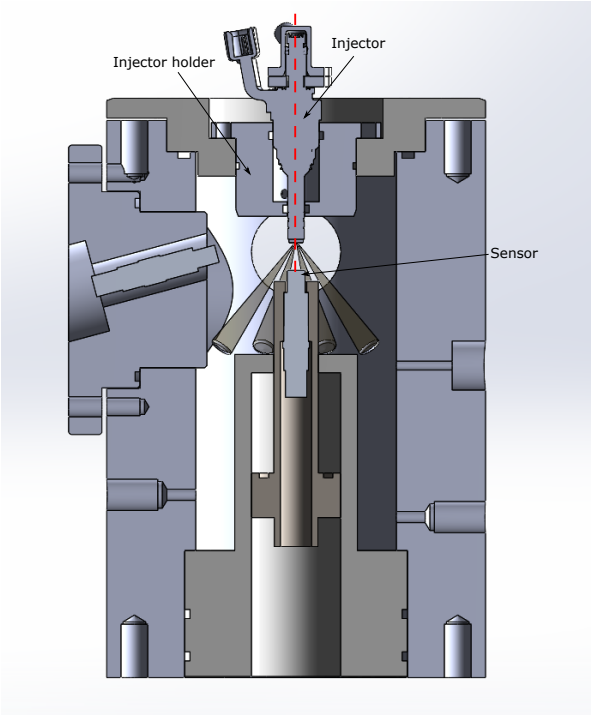

Figure A.12: Position of the injector and the sensor inside the ROM test rig.

Figure A.13 shows the difference between the raw and corrected rate of momentum measurements. Considering each injector spray angle and assuming that all orifices contribute the same amount, the ROM signal is corrected globally using Equation A.18.

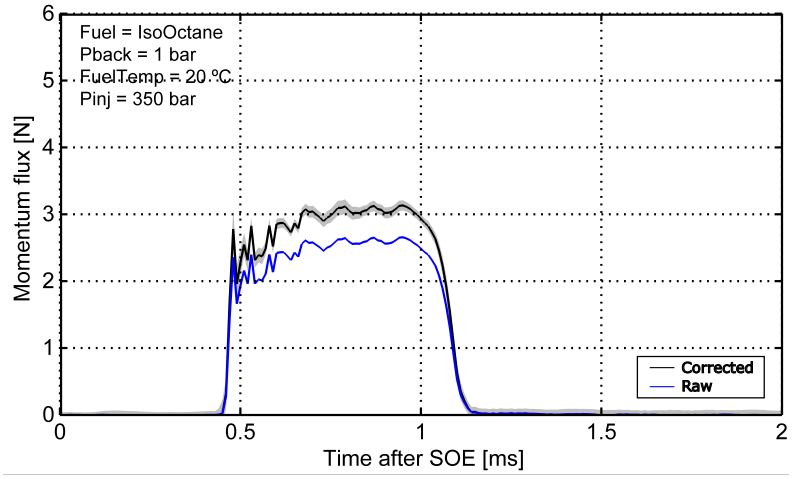

Figure A.13: Corrected and non corrected signal rate of momentum signal. Applying the correction eq. A.18 on the Continental injector.

Figures A.14, A.16 and A.15 show the effect of injection pressure, ambient pressure and fuel temperature on the rate of momentum signal. Figure A.14 shows the expected trend. The behavior is similar to the obtained injection rate for the opening and closing flanks of the signal. On the other hand, Figure A.16 shows that the back-pressure has little effect on the momentum rate. The sensor may not detect some droplets, resulting in a slight decrease in momentum. In Figure A.15 is possible to notice that the fuel temperature has an important effect on the rate of momentum signal.

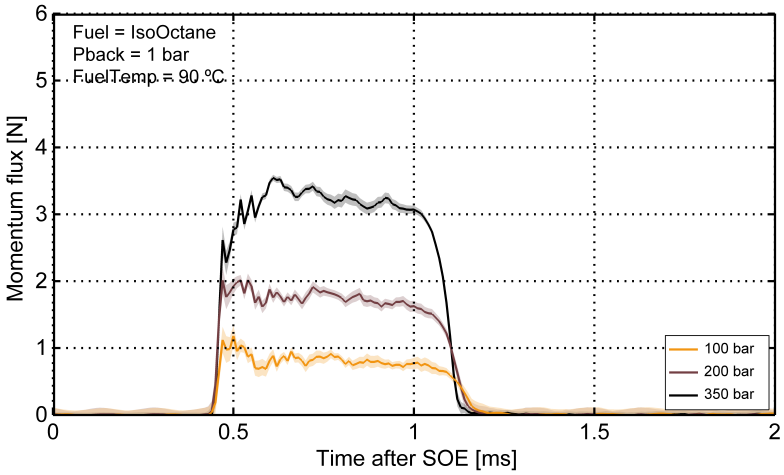

Figure A.14: Rate of momentum with a injection pressure variation.

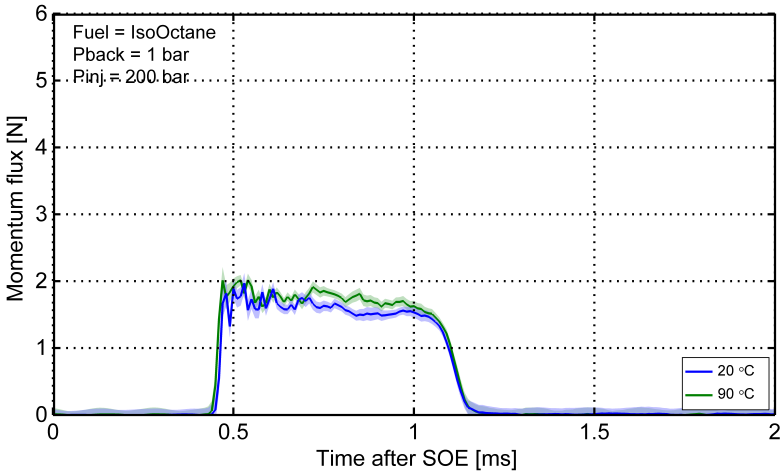

Figure A.15: Rate of momentum with fuel temperature variation.

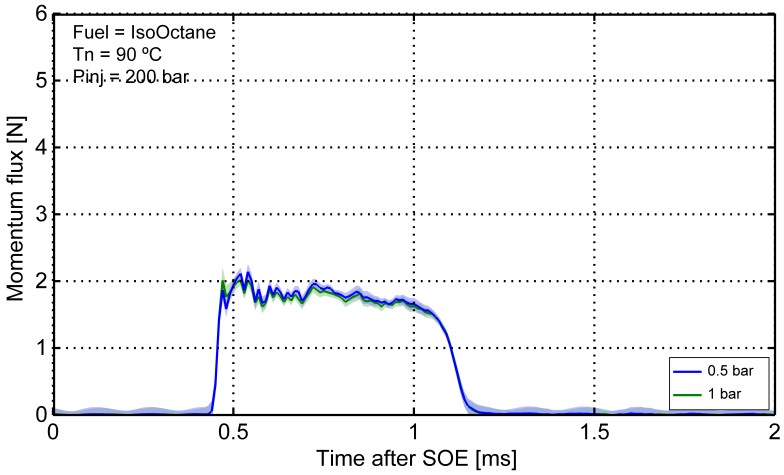

Figure A.16: Rate of momentum with ambient back-pressure variation.

A.6 Hydraulic Analysis

This section describes the hydraulic properties of the injector using flow description coefficients. If the time average from the stable region of the signal (steady injection) is computed, the complete test matrix can be summarized in a single figure for further analysis.

Figure A.17 shows the steady mass flow rate as a function of the square root of the pressure difference across the nozzle. Note that the value increases as rail pressure increases showing a linear relationship. Injector properties and area calculations are shown in Table A.2.

Table A.2: Injector orifice characteristics.

	Continental Injector	Unit
Orifice diameter	170	μm
Orifice area	22698	μm^2
Orifice #	6	-
Total area	136188	μm^2

In Figure A.18 the discharge coefficient is shown for all the conditions tested. The C_d is almost constant over the pressure range and fuel temperature used for the experimental campaign.

As mentioned in chapter 3, the spray rate of momentum is essentially proportional to the pressure drop across the nozzle. The steady-state momentum

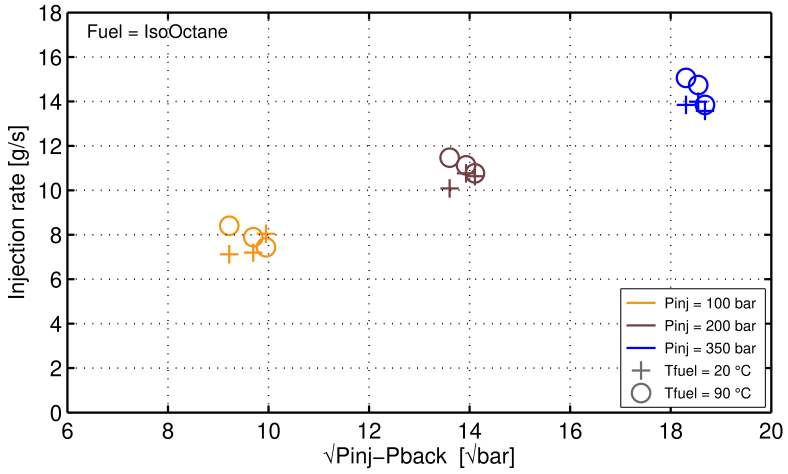

Figure A.17: Averaged steady rate of injection with the square root of the pressure difference. The colors denote different injection pressures and the symbols different fuel temperatures.

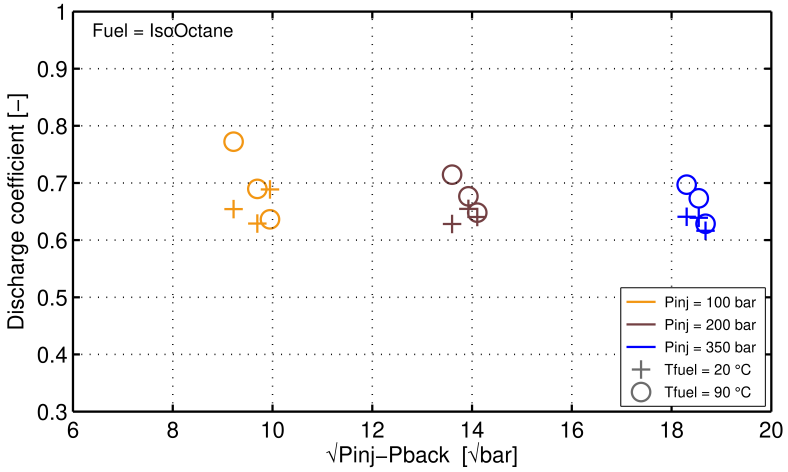

Figure A.18: Discharge coefficient variation with the square root of the pressure difference. The colors denote different injection pressures and the symbols different fuel temperatures.

flux for different injection and ambient pressures is shown in Figure A.19. As predicted, the data follows a straight line trend.

Both the injection rate and the rate of momentum can then be used to calculate the effective velocity and area coefficient at the exit of the nozzle [15]

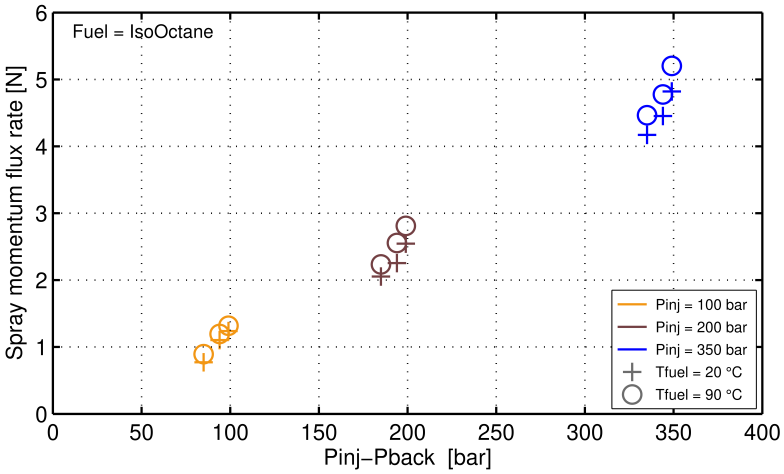

Figure A.19: Stabilized rate of momentum.

as was explained in Appendix A. Figure A.20 shows the estimated effective velocity (u_{eff}) as a function of the square root of the pressure difference across the nozzle. Note that u_{eff} increases with rail pressure. Figure A.21 shows the area coefficient (C_a). It is possible to observe how the C_a is nearly constant over all the conditions tested.

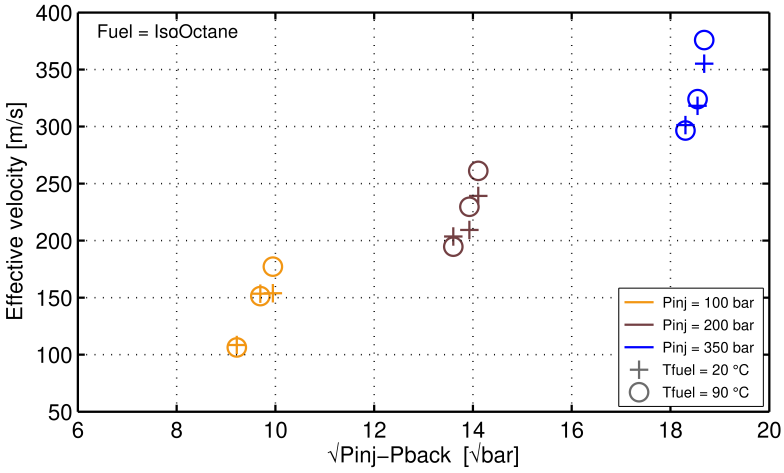

Figure A.20: Effective velocity variation with the square root of the pressure difference. The colors denote different injection pressures and the symbols different fuel temperatures.

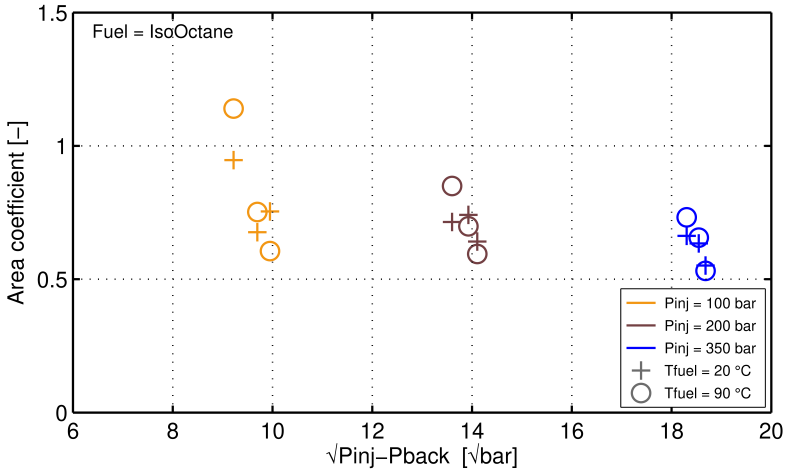

Figure A.21: Area coefficient with the square root of the pressure difference. The colors denote different injection pressures and the symbols different fuel temperatures.

The observed low values of C_d, u_{eff}, and C_a contrast to the typical values found in diesel injectors, the trend being more pronounced, even with cavitation nozzles [6, 16, 21]. The difference between these injectors and diesel injectors is significant. They can be attributed to a different basic nozzle geometry design, the use of more volatile fuels, larger holes, and lower operating pressures. The main reason of this difference is to increase air-fuel mixing and turbulence, promote spray dispersion, and improve plume-to-plume interaction for a convenient flame spread. Sharp inner corners in the orifices cause the reported low coefficients because they cause flow separation and recirculation zones [4, 13, 22–30].

Therefore, the GDI injectors flow phenomenon is much more complex to understand than diesel injectors due to the complex geometry, external plume interactions and more volatile fuels.

A.7 Summary and conclusions

In this appendix, the injector used in the experimental campaign was undergo a complete hydraulic characterization to understand its performance under various conditions commonly encountered in gasoline engines. To this end, the time-resolved injection rate and rate of momentum results were analyzed. The injection pressure was the parameter that most affected the output signal with respect to overall mass and shape.

The injected sprays were very close together that it was impossible to separate them for spray momentum measurements. Therefore, the test was performed by measuring all jets at once. The measurements were adjusted by assuming that all plumes contributed equally and then calculating the corrected spray momentum by using each plume angle. The adjustment formula applied allow to account for each plume contribution.

Regarding the ROI and ROM results, the injector follows the expected trends for p_r and p_b, in which a higher injection rate and momentum flux were obtained by increasing the injection pressure.

From the coefficient analysis, a linear trend for the spray momentum flux, effective velocity, and injection rate were obtained by increasing the square root of the pressure difference across the nozzle.

The results and methods presented help to understand the flow structure of this type of injector. This injector type has low needle lift, relatively large orifices, close together, and a small cone angle. Therefore, reliable experimental data can be obtained and applied to validate simulations with new similar injectors.

References

[1] Payri, Raul, Gimeno, Jaime, Marti-Aldaravi, Pedro, and Mendoza Alvarez, Victor. "Study of the hydraulic characteristics of two injectors fed with different fuels in a GDI system". In: *Fuel* 317 (2022), p. 123196. DOI: https://doi.org/10.1016/j.fuel.2022.123196.

[2] Zhao, Hua. *Advanced direct injection combustion engine technologies and development*. Woodhead Publishing Limited, 2010. DOI: 10.1533/9781845697327.

[3] Viera, Alberto. "Effect of multiple injection strategies on the diesel spray formation and combustion using optical diagnostics". PhD thesis. Universitat Politècnica de València, 2019.

[4] Payri, Raul, Hardy, Gilles, Gimeno, Jaime, and Bautista, Abian. "Analysis of counterbore effect in five diesel common rail injectors". In: *Experimental Thermal and Fluid Science* 107 (2019), pp. 69–78. DOI: 10.1016/j.expthermflusci.2019.05.008.

[5] Payri, Raul, Gimeno, Jaime, Mata, Carmen, and Viera, Alberto. "Rate of injection measurements of a direct-acting piezoelectric injector for different operating temperatures". In: *Energy Conversion and Management* 154.October (2017), pp. 387–393. DOI: 10.1016/j.enconman.2017.11.029.

[6] Viera, Juan Pablo. "Experimental Study of the Effect of Nozzle Geometry on the Performance of Direct-Injection Diesel Sprays for Three Different Fuels". PhD thesis. Universitat Politècnica de València, 2017.

[7] Payri, Raul, Viera, Juan Pablo, Wang, Hua, and Malbec, Louis-Marie. "Velocity field analysis of the high density, high pressure diesel spray". In: *International Journal of Multiphase Flow* 80.24 (2016), pp. 69–78. DOI: 10.1016/j.ijmultiphaseflow.2015.10.012.

[8] Payri, Raul, Gimeno, Jaime, Martí-Aldaraví, Pedro, and Vaquerizo, Daniel. "Internal flow characterization on an ECN GDi injector". In: *Atomization and Sprays* 26.9 (2016), pp. 889–919. DOI: 10.1615/AtomizSpr.2015013930.

[9] Payri, Raul, Bracho, Gabriela, Gimeno, Jaime, and Bautista, Abian. "Rate of injection modelling for gasoline direct injectors". In: *Energy Conversion and Management* 166 (2018), pp. 424–432. DOI: 10.1016/j.enconman.2018.04.041.

[10] Bosch, Wilhelm. "The Fuel Rate Indicator: A New Measuring Instrument For Display of the Characteristics of Individual Injection". In: *SAE Technical Paper 660749*. 1966. DOI: 10.4271/660749.

[11] Lemmon, Eric W., McLinden, M. O., and Friend, D. G. "Thermophysical Properties of Fluid Systems". In: *NIST Chemistry WebBook, NIST Standard Reference Database Number 69*. Ed. by P. J. Linstrom and W. G. Mallard. 2011.

[12] Payri, Raul, Salvador, Francisco Javier, Gimeno, Jaime, and Zapata, Luis Daniel. "Diesel nozzle geometry influence on spray liquid-phase fuel penetration in evaporative conditions". In: *Fuel* 87.7 (2008), pp. 1165–1176. DOI: 10.1016/j.fuel.2007.05.058.

[13] Shahangian, Navid et al. "Spray Orientation Assessment and Correction Method for GDI Momentum Flux Measurements". In: October (2019), pp. 231–241.

[14] Strek, Piotr et al. "X-Ray Radiography and CFD Studies of the Spray G Injector". In: *SAE Technical Papers* 2016-April.April (2016). DOI: 10.4271/2016-01-0858.

[15] Payri, Raul, Garcia-Oliver, Jose Maria, Salvador, Francisco Javier, and Gimeno García, Jaime. "Using spray momentum flux measurements to understand the influence of diesel nozzle geometry on spray characteristics". In: *Fuel* 84.5 (2005), pp. 551–561. DOI: 10.1016/j.fuel.2004.10.009.

[16] Gimeno, Jaime. "Desarrollo y aplicación de la medida de flujo de cantidad de movimiento de un chorro Diesel". PhD thesis. E.T.S. Ingenieros Industriales, Universidad Politécnica de Valencia, 2008.

[17] Payri, Raul, Gimeno, Jaime, Marti-Aldaravi, Pedro, and Vaquerizo, Daniel. "Momentum Flux Measurements on an ECN GDi Injector". In: *SAE Technical Paper 2015-01-1893*. 2015. DOI: 10.4271/2015-01-1893.

[18] ECN. "Engine Combustion Network". In: *https://ecn.sandia.gov/gasoline-spray-combustion/* (2020).

[19] Bae, Gyuhan et al. "Experimental investigation of fuel temperature effects on transient needle motion and injection velocity of solenoid type diesel injector". In: *International Journal of Heat and Mass Transfer* 181 (2021), p. 121838. DOI: https://doi.org/10.1016/j.ijheatmasstransfer.2021.121838.

[20] Payri, Raul, Gimeno, Jaime, Marti-Aldaravi, Pedro, and Vaquerizo, Daniel. "Momentum Flux Measurements on an ECN GDi Injector". In: *SAE* (). DOI: https://doi.org/10.4271/2015-01-1893.

[21] Desantes, Jose Maria, Payri, Raul, Salvador, Francisco Javier, and Gimeno, Jaime. "Measurements of Spray Momentum for the Study of Cavitation in Diesel Injection Nozzles". In: *SAE Technical Paper 2003-01-0703*. Society of Automotive Engineers, Inc., Warrendale, Pennsylvania, USA, 2003. DOI: 10.4271/2003-01-0703.

[22] Shost, Mark A, Lai, Ming-Chia, Befrui, Bizhan, Spiekermann, Peter, and Varble, Daniel L. "GDi Nozzle Parameter Studies Using LES and Spray Imaging Methods". In: *SAE Technical Papers*. Vol. 1. 2014. DOI: 10.4271/2014-01-1434.

[23] Befrui, Bizhan, Corbinelli, Giovanni, Spiekermann, Peter, Shost, Mark, and Lai, Ming-Chia. "Large Eddy Simulation of GDI Single-Hole Flow and Near-Field Spray". In: *SAE International Journal of Fuels and Lubricants* 5.2 (2012), pp. 392–2012. DOI: 10.4271/2012-01-0392.

[24] Moon, Seoksu et al. “Ultrafast X-ray study of multi-hole GDI injector sprays: Effects of nozzle hole length and number on initial spray formation”. In: *Experimental Thermal and Fluid Science* 68 (2015), pp. 68–81. DOI: 10.1016/j.expthermflusci.2015.03.027.

[25] Guo, Hengjie, Li, Yanfei, Wang, Bo, Zhang, Huiqiang, and Xu, Hongming. “Numerical investigation on flashing jet behaviors of single-hole GDI injector”. In: *International Journal of Heat and Mass Transfer* 130 (2019), pp. 50–59. DOI: 10.1016/j.ijheatmasstransfer.2018.10.088.

[26] Cavicchi, Andrea, Postrioti, Lucio, and Scarponi, Edoardo. “Hydraulic analysis of a GDI injector operation with close multi-injection strategies”. In: *Fuel* 235.July 2017 (2019), pp. 1114–1122. DOI: 10.1016/j.fuel.2018.08.089.

[27] Cavicchi, Andrea, Postrioti, Lucio, Berni, Fabio, Fontanesi, Stefano, and Di Gioia, Rita. “Evaluation of hole-specific injection rate based on momentum flux measurement in GDI systems”. In: *Fuel* 263.June 2019 (2020). DOI: 10.1016/j.fuel.2019.116657.

[28] Du, Jianguo, Mohan, Balaji, Sim, Jaeheon, Fang, Tiegang, and Roberts, William L. “Experimental and analytical study on liquid and vapor penetration of high-reactivity gasoline using a high-pressure gasoline multi-hole injector”. In: *Applied Thermal Engineering* 163.July (2019), p. 114187. DOI: 10.1016/j.applthermaleng.2019.114187.

[29] Shahangian, Navid et al. “Transient nozzle flow simulations of gasoline direct fuel injectors”. In: *Applied Thermal Engineering* 175.January (2020). DOI: 10.1016/j.applthermaleng.2020.115356.

[30] Moon, Seoksu, Huang, Weidi, and Wang, Jin. “Spray formation mechanism of diverging-tapered-hole GDI injector and its potentials for GDI engine applications”. In: *Fuel* 270.March (2020), p. 117519. DOI: 10.1016/j.fuel.2020.117519.

Global Bibliography

Akafuah, Nelson K., Salazar, Abraham J., and Saito, Kozo. "Infrared thermography-based visualization of droplet transport in liquid sprays". In: *Infrared Physics and Technology* 53.3 (2010), pp. 218–226. DOI: 10.1016/j.infrared.2009.12.002 (cited on page 161).

Akhtar, S W and Yule, A J. "Droplet impaction on a heated surface at high Weber numbers". In: *ILASS-Europe, Zurich* September 2001 (2001) (cited on page 33).

Akop, Mohd Zaid, Zama, Yoshio, Furuhata, Tomohiko, and Arai, Masataka. "Characteristics Of Adhesion Diesel Fuel On An Impingement Disk Wall Part 1: Effect Of Impingement Area And Inclination Angle Of Disk". In: *Atomization and Sprays* 23.8 (2013), pp. 724–725 (cited on page 35).

Allocca, Luigi, Lazzaro, Maurizio, Meccariello, G, and Montanaro, Alessandro. "Schlieren visualization of a GDI spray impacting on a heated wall: Non-vaporizing and vaporizing evolutions". In: *Energy* 108 (2016), pp. 93–98. DOI: 10.1016/j.energy.2015.09.107 (cited on page 72).

Arai, Masataka, Amagai, Kenji, Nagataki, Tsubasa, and Okita, Hideki. "Ignition Positions of a Diesel Spray Impinging on an Inclined Wall". In: (2005) (cited on page 35).

Araneo, Lucio, Coghe, Aldo, Brunello, G, and Cossali, Gianpietro E. "Experimental Investigation of gas density effects on diesel spray penetration and entrainment". In: *SAE Paper 1999-01-0525* (1999) (cited on page 81).

Astarita, Tommaso and Carlomagno, Giovanni Maria. *Infrared Thermography for Thermo-Fluid-Dynamics*. Springer Berlin Heidelberg, 2013. DOI: 10.1007/978-3-642-29508-9 (cited on pages 90, 91).

Avallone, F., Greco, C. S., Schrijer, F. F. J., and Cardone, G. "A low-computational-cost inverse heat transfer technique for convective heat transfer measurements in hypersonic flows". In: *Experiments in Fluids* 56.4 (2015), p. 86. DOI: 10.1007/s00348-015-1951-5 (cited on page 93).

Bae, Gyuhan et al. "Experimental investigation of fuel temperature effects on transient needle motion and injection velocity of solenoid type diesel injector". In: *International Journal of Heat and Mass Transfer* 181 (2021), p. 121838. DOI: https://doi.org/10.1016/j.ijheatmasstransfer.2021.121838 (cited on page 192).

Bahattin, Mustafa and Ozdaly, Bulent. "Gasoline Direct Injection". In: *Fuel Injection*. Sciyo, 2010. DOI: 10.5772/9693 (cited on pages 14–16, 21).

Bai, Chengxin and Gosman, A. D. "Development of Methodology for Spray Impingement Simulation". In: *SAE Technical Paper 950283* 412 (1995). DOI: 10.4271/950283 (cited on pages 33, 34).

Banerjee, R and Kumar, Santhosh. "Numerical investigation of stratified air/fuel preparation in a GDI engine". In: *Applied Thermal Engineering* 104 (2016), pp. 414–428. DOI: 10.1016/j.applthermaleng.2016.05.050 (cited on page 21).

Bardi, Michele. "Partial needle lift and injection rate shape effect on the formation and combustion of the Diesel spray". PhD thesis. Valencia (Spain): Universitat Politècnica de València, 2014. DOI: 10.4995/Thesis/10251/37374 (cited on pages 55, 79).

Bautista Rodriguez, Abian. "Study of the Gasoline direct injection process under novel operating conditions". PhD thesis. Universitat Politècnica de València, 2021 (cited on pages 4, 5, 55).

Befrui, B, Corbinelli, G, Hoffmann, G, Andrews, R J, and Sankhalpara, S R. "Cavitation and Hydraulic Flip in the Outward-Opening GDi Injector Valve-Group". In: *SAE Technical Papers*. 2009. DOI: 10.4271/2009-01-1483 (cited on page 30).

Befrui, Bizhan, Corbinelli, Giovanni, Spiekermann, Peter, Shost, Mark, and Lai, Ming-Chia. "Large Eddy Simulation of GDI Single-Hole Flow and Near-Field Spray". In: *SAE International Journal of Fuels and Lubricants* 5.2 (2012), pp. 392–2012. DOI: 10.4271/2012-01-0392 (cited on pages 30, 31, 199).

Befrui, Bizhan, Hoffmann, Guy, Kirwan, John, Piock, Walter, and Schilling, Sebastian. "Analytical Optimization of Delphi GDi Fuel Injection Systems". In: *15th Conference "The Working Process of the Internal Combustion Engine"* September 2015 (2015) (cited on pages 27, 29, 31).

Befrui, Bizhan et al. “ECN GDi Spray G : Coupled LES Jet Primary Breakup - Lagrangian Spray Simulation and Comparison with Data”. In: *ILASS Americas 28th* June (2016) (cited on page 31).

Benajes, Jesus, Payri, Raul, Bardi, Michele, and Martí-aldaraví, Pedro. “Experimental characterization of diesel ignition and lift-off length using a single-hole ECN injector”. In: *Applied Thermal Engineering* 58.1-2 (2013), pp. 554–563. DOI: 10.1016/j.applthermaleng.2013.04.044 (cited on page 83).

Benther, J.D., Pelaez-Restrepo, J.D., Stanley, C., and Rosengarten, G. “Heat transfer during multiple droplet impingement and spray cooling: Review and prospects for enhanced surfaces”. In: *International Journal of Heat and Mass Transfer* 178 (2021), p. 121587. DOI: https://doi.org/10.1016/j.ijheatmasstransfer.2021.121587 (cited on page 147).

Bernardin, J D and Mudawar, I. “The Leidenfrost Point: Experimental Study and Assessment of Existing Models”. In: *Journal of Heat Transfer* 121.4 (1999), pp. 894–903. DOI: 10.1115/1.2826080 (cited on page 34).

Berni, Fabio, Breda, Sebastiano, Lugli, Mattia, and Cantore, Giuseppe. “A numerical investigation on the potentials of water injection to increase knock resistance and reduce fuel consumption in highly downsized GDI engines”. In: *Energy Procedia* 81 (2015), pp. 826–835. DOI: 10.1016/j.egypro.2015.12.091 (cited on page 18).

Bornschlegel, Sebastian, Conrad, Chris, Eichhorn, Lisa, and Wensing, Michael. “Flashboiling atomization in nozzles for GDI engines”. In: 2017. DOI: 10.4995/ILASS2017.2017.4750 (cited on page 108).

Bosch, Wilhelm. “The Fuel Rate Indicator: A New Measuring Instrument For Display of the Characteristics of Individual Injection”. In: *SAE Technical Paper 660749*. 1966. DOI: 10.4271/660749 (cited on page 180).

Bruneaux, Gilles. “Mixing Process in High Pressure Diesel Jets by Normalized Laser Induced Exciplex Fluorescence Part II: Wall Impinging Versus Free Jet”. In: *SAE Technical Paper 2005-01-2100* c (2005). DOI: 10.4271/2005-01-2097 (cited on page 36).

Bruneaux, Gilles. “Combustion structure of free and wall-impinging diesel jets by simultaneous laser-induced fluorescence of formaldehyde, poly-aromatic hydrocarbons, and hydroxides”. In: *International Journal of Engine Research* 9.3 (2008), pp. 249–265. DOI: 10.1243/14680874JER00108 (cited on page 35).

Carlomagno, Giovanni Maria and Cardone, Gennaro. “Infrared thermography for convective heat transfer measurements”. In: *Experiments in Fluids* 49.6 (2010), pp. 1187–1218. DOI: 10.1007/s00348-010-0912-2 (cited on pages 68, 162).

Carnahan, Brice, Luther, H A, and Wilkes, James O. *Applied Numerical Methods*. Wiley, 1969 (cited on page 86).

Cavicchi, Andrea and Postrioti, Lucio. “Simultaneous needle lift and injection rate measurement for GDI fuel injectors by laser Doppler vibrometry and Zeuch method”. In: *Fuel* 285.August 2020 (2021), p. 119021. DOI: 10.1016/j.fuel.2020.119021 (cited on page 18).

Cavicchi, Andrea, Postrioti, Lucio, Berni, Fabio, Fontanesi, Stefano, and Di Gioia, Rita. “Evaluation of hole-specific injection rate based on momentum flux measurement in GDI systems”. In: *Fuel* 263.June 2019 (2020). DOI: 10.1016/j.fuel.2019.116657 (cited on pages 18, 199).

Cavicchi, Andrea, Postrioti, Lucio, and Scarponi, Edoardo. “Hydraulic analysis of a GDI injector operation with close multi-injection strategies”. In: *Fuel* 235.July 2017 (2019), pp. 1114–1122. DOI: 10.1016/j.fuel.2018.08.089 (cited on pages 18, 71, 199).

Cavicchi, Andrea et al. “Numerical and experimental analysis of the spray momentum flux measuring on a GDI injector”. In: *Fuel* 206 (2017), pp. 614–627. DOI: 10.1016/j.fuel.2017.06.054 (cited on pages 29, 71).

Cebo-Rudnicka, Agnieszka, Malinowski, Zbigniew, and Buczek, Andrzej. “The influence of selected parameters of spray cooling and thermal conductivity on heat transfer coefficient”. In: *International Journal of Thermal Sciences* 110 (2016), pp. 52–64. DOI: https://doi.org/10.1016/j.ijthermalsci.2016.06.031 (cited on pages 37, 156).

Celata, G P, Cumo, M, Mariani, A, and Zummo, Giuseppe. “Visualization of the impact of water drops on a hot surface: Effect of drop velocity and surface inclination”. In: *Heat and Mass Transfer* 42 (2006), pp. 885–890. DOI: 10.1007/s00231-006-0139-1 (cited on page 34).

Chang, Mengzhao, Yu, Young Soo, Park, Sungwook, and Park, Suhan. “Spray dynamics and atomization characteristics of multi-hole GDI injectors under flash boiling conditions”. In: *Applied Thermal Engineering* 200 (2022), p. 117626. DOI: https://doi.org/10.1016/j.applthermaleng.2021.117626 (cited on page 117).

Chaves, Humberto, Kubitzek, Artur Michael, and Obermeier, Frank. "Dynamic processes occurring during the spreading of thin liquid films produced by drop impact on hot walls". In: *International Journal of Heat and Fluid Flow* 20.5 (1999), pp. 470–476. DOI: https://doi.org/10.1016/S0142-727X(99)00034-X (cited on page 34).

Chehroudi, Bruce. "Laser Ignition For Combustion Engines". In: *Engineering* October (2004), pp. 1–5. DOI: 10.13140/2.1.1845.1206 (cited on page 12).

Chen, Longfei, Liang, Zhirong, Zhang, Xin, and Shuai, Shijin. "Characterizing particulate matter emissions from GDI and PFI vehicles under transient and cold start conditions". In: *Fuel* 189 (2017), pp. 131–140. DOI: 10.1016/j.fuel.2016.10.055 (cited on pages 15, 18).

Cheng, Wen-Long, Liu, Qi-Nie, and Fan, Han-lin. "Experimental investigation of parameters effect on heat transfer of spray cooling". In: *Heat and Mass Transfer* 46 (2010). DOI: https://doi.org/10.1007/s00231-010-0631-5 (cited on pages 37, 156).

Chincholkar, S P and Suryawanshi, J G. "Gasoline Direct Injection: An Efficient Technology". In: *Energy Procedia* 90.December 2015 (2016), pp. 666–672. DOI: 10.1016/j.egypro.2016.11.235 (cited on page 16).

Cho, Jaeho, Kim, Kangjin, Baek, Sungha, Myung, Cha Lee, and Park, Simsoo. "Abatement potential analysis on CO2 and size-resolved particle emissions from a downsized LPG direct injection engine for passenger car". In: *Atmospheric Pollution Research* 10.6 (2019), pp. 1711–1722. DOI: 10.1016/j.apr.2019.07.002 (cited on page 18).

Cho, Jungkeun and Song, Soonho. "Prediction of hydrogen-added combustion process in T-GDI engine using artificial neural network". In: *Applied Thermal Engineering* 181.May (2020), p. 115974. DOI: 10.1016/j.applthermaleng.2020.115974 (cited on page 21).

Coleman, T.F. and Li, Y. "An Interior trust region approach for nonlinear minimization subject to bounds". In: *SIAM* (1996), pp. 418–445. DOI: doi:10.1137/0806023 (cited on page 93).

Contino, Mattia, Zaccara, Mirko, Montanaro, Alessandro, Allocca, Luigi, and Cardone, Gennaro. "Dynamic Thermal Behavior of a GDI Spray Impacting on a Heated Thin Foil by Phase-Averaged Infrared Thermography". In: 2020. DOI: https://doi.org/10.4271/2019-24-0036 (cited on pages 66, 68, 162).

Cossali, G E, Coghe, A, and Marengo, M. "The impact of a single drop on a wetted solid surface". In: *Experiments in Fluids* 22 (1997), pp. 463–472 (cited on page 35).

Costa, M, Catapano, F, Sementa, P, Sorge, U, and Vaglieco, B M. "Mixture preparation and combustion in a GDI engine under stoichiometric or lean charge: an experimental and numerical study on an optically accessible engine". In: *Applied Energy* 180 (2016), pp. 86–103. DOI: 10.1016/j.apenergy.2016.07.089 (cited on page 23).

Costa, M et al. "Split injection in a homogeneous stratified gasoline direct injection engine for high combustion efficiency and low pollutants emission". In: *Energy* 117.2016 (2016), pp. 405–415. DOI: 10.1016/j.energy.2016.03.065 (cited on pages 19, 21, 26).

Dahlander, Petter, Iemmolo, Daniele, and Tong, Yifei. "Measurements of Time-Resolved Mass Injection Rates for a Multi-Hole and an Outward Opening Piezo GDI Injector". In: *SAE Technical Papers*. Vol. 2015-April. April. 2015. DOI: 10.4271/2015-01-0929 (cited on page 25).

Delphi Technologies. "New 500+ bar GDi system cuts particulates by up to 50% without engine changes". In: *News release* (2019) (cited on page 27).

Dempsey, Adam B, Seiler, Patrick, Svensson, Kenth, and Qi, Yongli. "A Comprehensive Evaluation of Diesel Engine CFD Modeling Predictions Using a Semi-Empirical Soot Model over a Broad Range of Combustion Systems". In: *SAE Int. J. Engines* 11 (2018), pp. 1399–1420. DOI: 10.4271/2018-01-0242 (cited on page 35).

Desantes, Jose Maria, Payri, Raul, Salvador, Francisco Javier, and Gil, Antonio. "Development and validation of a theoretical model for diesel spray penetration". In: *Fuel* 85.7-8 (2006), pp. 910–917 (cited on page 81).

Desantes, Jose Maria, Payri, Raul, Salvador, Francisco Javier, and Gimeno, Jaime. "Measurements of Spray Momentum for the Study of Cavitation in Diesel Injection Nozzles". In: *SAE Technical Paper 2003-01-0703*. Society of Automotive Engineers, Inc., Warrendale, Pennsylvania, USA, 2003. DOI: 10.4271/2003-01-0703 (cited on page 199).

Du, Jianguo, Mohan, Balaji, Sim, Jaeheon, Fang, Tiegang, and Roberts, William L. "Experimental and analytical study on liquid and vapor penetration of high-reactivity gasoline using a high-pressure gasoline multi-hole injector". In: *Applied Thermal Engineering* 163.July (2019), p. 114187. DOI: 10.1016/j.applthermaleng.2019.114187 (cited on pages 71, 199).

Duan, Xiongbo et al. “Quantitative investigation the influences of the injection timing under single and double injection strategies on performance, combustion and emissions characteristics of a GDI SI engine fueled with gasoline/ethanol blend”. In: *Fuel* 260.August 2019 (2020), p. 116363. DOI: 10.1016/j.fuel.2019.116363 (cited on page 21).

Duke, Daniel J. et al. “Internal and near nozzle measurements of Engine Combustion Network “Spray G” gasoline direct injectors”. In: *Experimental Thermal and Fluid Science* 88 (2017), pp. 608–621. DOI: https://doi.org/10.1016/j.expthermflusci.2017.07.015 (cited on pages 67, 90).

ECN. “Engine Combustion Network”. In: *https://ecn.sandia.gov/gasoline-spray-combustion/* (2020) (cited on pages 6, 96, 103, 190).

EPA. “Light-Duty Automotive Technology, Carbon Dioxide Emissions, and Fuel Economy Trends: 1975 Through 2016 - Executive Summary (EPA-420-S-16-001, November 2016)”. In: November (2016), pp. 1–11 (cited on page 3).

Erjavec, Jack. *Automotive Technology : A systems approach*. 5th. Cengage Learning, Inc, 2009, p. 1665 (cited on pages 17, 18).

Fansler, Todd D and Parrish, Scott E. “Spray measurement technology: a review”. In: *Measurement Science and Technology* 26.1 (2015), p. 12002. DOI: 10.1088/0957-0233/26/1/012002 (cited on pages 17, 19, 25–27).

Feng, Shuang et al. “Influence of stratified charge organized by double injection strategy on combustion and emissions on an EGR diluted GDI engine”. In: *Applied Thermal Engineering* 158.May (2019), p. 113803. DOI: 10.1016/j.applthermaleng.2019.113803 (cited on page 21).

Fontanesi, Stefano, D’Adamo, Alessandro, and Rutland, Christopher J. “Large-Eddy simulation analysis of spark configuration effect on cycle-to-cycle variability of combustion and knock”. In: *International Journal of Engine Research* (2015). DOI: 10.1177/1468087414566253 (cited on page 3).

Freund, S., Pautsch, A.G., Shedd, T.A., and Kabelac, S. “Local heat transfer coefficients in spray cooling systems measured with temperature oscillation IR thermography”. In: *International Journal of Heat and Mass Transfer* 50.9 (2007), pp. 1953–1962. DOI: https://doi.org/10.1016/j.ijheatmasstransfer.2006.09.028 (cited on pages 37, 156).

García, Antonio, Serrano, Javier Monsalve, Boggio, Santiago Martinez, and Soria Alcaide, Rafael. "Carbon footprint of battery electric vehicles considering average and marginal electricity mix". In: *Energy* 268 (2023), p. 126691. DOI: https://doi.org/10.1016/j.energy.2023.126691 (cited on page 2).

Gawthrop, D. B. "Applications of the Schlieren method of photography". In: *Review of Scientific Instruments* 2.9 (1931), pp. 522–531. DOI: 10.1063/1.1748821 (cited on page 72).

Ghandhi, J B and Heim, D M. "An optimized optical system for backlit imaging". In: *Review of Scientific Instruments* 80 (2009). DOI: 10.1063/1.3128728 (cited on page 74).

Gibbons, M.J. and Robinson, A.J. "Heat transfer characteristics of single cone-jet electrosprays". In: *International Journal of Heat and Mass Transfer* 113 (2017), pp. 70–83 (cited on pages 93, 162).

Gimeno, Jaime. "Desarrollo y aplicación de la medida de flujo de cantidad de movimiento de un chorro Diesel". PhD thesis. E.T.S. Ingenieros Industriales, Universidad Politécnica de Valencia, 2008 (cited on pages 82, 106, 185, 186, 190, 199).

Gimeno, Jaime, Bracho, Gabriela, Martí-Aldaraví, Pedro, and Peraza, Jesús E. "Experimental study of the injection conditions influence over n-dodecane and diesel sprays with two ECN single-hole nozzles. Part I: Inert atmosphere". In: *Energy Conversion and Management* 126 (2016), pp. 1146–1156. DOI: 10.1016/j.enconman.2016.07.077 (cited on pages 74, 82, 83).

Giraldo Valderrama, Jhoan Sebastián. "Macroscopic and microscopic characterization of non-reacting diesel sprays at low and very high injection pressures". In: November (2018) (cited on page 106).

Gladstone, J H and Dale, T P. "Researches on the Refraction, Dispersion, and Sensitiveness of Liquids". In: *Philosophical Transactions of the Royal Society of London* 153 (1863), pp. 317–343. DOI: 10.2307/108799 (cited on page 72).

"Global CO2 emissions from transport by subsector, 2000-2030". In: *IEA* (2021) (cited on pages 10, 11).

Gomot, Dipl Baudouin and Hülser, Holger. "Delphi Technologies Next Generation GDi-System, improved Emissions and Efficiency with higher Pressure". In: *Internationales Wiener Motorensymposium* (2019), pp. 1–21 (cited on pages 2, 24).

Gong, Changming, Yi, Lin, Zhang, Zilei, Sun, Jingzhen, and Liu, Fenghua. "Assessment of ultra-lean burn characteristics for a stratified-charge direct-injection spark-ignition methanol engine under different high compression ratios". In: *Applied Energy* 261.January (2020), p. 114478. DOI: 10.1016/j.apenergy.2019.114478 (cited on pages 21, 23).

González, Uriel. "Efecto del choque de pared en las características del chorro Diesel de inyección directa". PhD thesis. Valencia: E.T.S. Ingenieros Industriales. Universidad Politécnica de Valencia, 1998 (cited on pages 4, 59).

Granqvist, Peter. "High efficient SI-engine with ultra high injection pressure [Research @ Chalmers University]". In: October. Gothenburg, Sweden: Energirelaterad forskning 2017, 2017 (cited on page 24).

Guo, Hengjie, Li, Yanfei, Wang, Bo, Zhang, Huiqiang, and Xu, Hongming. "Numerical investigation on flashing jet behaviors of single-hole GDI injector". In: *International Journal of Heat and Mass Transfer* 130 (2019), pp. 50–59. DOI: 10.1016/j.ijheatmasstransfer.2018.10.088 (cited on pages 71, 199).

Halderman, James D. *Automotive Fuel and Emissions control systems*. 2012 (cited on page 14).

Hamzah, A et al. "A comparison of diffuse back-illumination (DBI) and Mie-scattering technique for measuring the liquid length of severely flashing spray". In: *20th Australasian Fluid Mechanics Conference*. December. Perth, Australia, 2016 (cited on page 75).

Harada, Jun, Tomita, Tsutomu, Mizuno, Hiroyuki, Mashiki, Zenichiro, and Ito, Yasushi. "Development of direct injection gasoline engine". In: *SAE Technical Papers* 412 (1997). DOI: 10.4271/970540 (cited on page 17).

He, Lv, Jingyuan, Li, Xiumin, Yu, Mengliang, Li, and Tian, Yang. "Numerical study on combustion and emission characteristics of a PFI gasoline engine with hydrogen direct-injection". In: *Energy Procedia* 158 (2019), pp. 1449–1454. DOI: 10.1016/j.egypro.2019.01.348 (cited on page 15).

Hentschel, W et al. "Optical Diagnostics and CFD-Simulations to Support the Combustion Process Development of the Volkswagen FSI®Direct-Injection Gasoline Engine". In: *SAE Technical Papers*. 724. 2001. DOI: 10.4271/2001-01-3648 (cited on page 20).

Hentschel, Werner. "Optical Diagnostics Combustion Process Development DI Gasoline Engines". In: 28 (2000), pp. 1119–1135 (cited on page 20).

Hoffmann, Guy, Befrui, Bizhan, Berndorfer, Axel, Piock, Walter F, and Varble, Daniel L. "Fuel System Pressure Increase for Enhanced Performance of GDi Multi-Hole Injection Systems". In: *SAE International Journal of Engines* 7.1 (2014), pp. 1209–2014. DOI: 10.4271/2014-01-1209 (cited on pages 24, 27).

Husted, Harry, Spegar, Timothy D, and Spakowski, Joseph. "The Effects of GDi Fuel Pressure on Fuel Economy". In: *SAE Technical Papers*. Vol. 1. 2014. DOI: 10.4271/2014-01-1438 (cited on page 24).

IEA. *A technology roadmap: Electric and plug-in hybrid electric vehicles*. Tech. rep. June. International Energy Agency, 2011, pp. 3471–3473 (cited on page 10).

Ingraham, Joseph C. *Automobiles: Races; Everybody Manages to Win Something At the Daytona Beach Contests*. 1957 (cited on page 15).

Iwamoto, Y, Noma, K, Nakayama, O, Yamauchi, T, and Ando, H. "Development of Gasoline Direct Injection Engine". In: *SAE Technical Papers*. 412. 1997. DOI: 10.4271/970541 (cited on page 17).

Jeon, J, Bock, N, and Northrop, W F. "In-cylinder flame luminosity measured from a stratified lean gasoline direct injection engine". In: *Results in Engineering* 1.January (2019), p. 100005. DOI: 10.1016/j.rineng.2019.100005 (cited on pages 21, 23).

Jeon, Joonho. "Spatiotemporal flame propagations, combustion and solid particle emissions from lean and stoichiometric gasoline direct injection engine operation". In: *Energy* 210 (2020), p. 118652. DOI: 10.1016/j.energy.2020.118652 (cited on page 23).

Johansson, Anders N, Hemdal, Stina, and Dahlander, Petter. "Reduction of Soot Formation in an Optical Single-Cylinder Gasoline Direct-Injected Engine Operated in Stratified Mode Using 350 Bar Fuel Injection Pressure, Dual-Coil and High-Frequency Ignition Systems". In: *SAE International Journal of Engines* 10.3 (2017), pp. 2017–9278. DOI: 10.4271/2017-01-9278 (cited on pages 23, 27).

Johnson, Timothy. "Vehicular Emissions in Review". In: *SAE International Journal of Engines* 7.3 (2014), pp. 1491–2014. DOI: 10.4271/2014-01-1491 (cited on page 3).

Jung, Yongjin, Manin, Julien, Skeen, Scott A, and Pickett, Lyle M. "Measurement of Liquid and Vapor Penetration of Diesel Sprays with a Variation in Spreading Angle". In: *SAE Technical Paper 2015-01-0946* (2015). DOI: 10.4271/2015-01-0946 (cited on pages 72, 74).

Kanda, Mutsumi et al. “Application of a New Combustion Concept to Direct Injection Gasoline Engine”. In: *SAE Technical Papers*. Vol. 2000. 724. 2000. DOI: 10.4271/2000-01-0531 (cited on page 25).

Khalifa, Abdul-Jabbar N. “Natural convective heat transfer coefficient a review: I. Isolated vertical and horizontal surfaces”. In: *Energy Conversion and Management* 42.4 (2001), pp. 491–504. DOI: https://doi.org/10.1016/S0196-8904(00)00042-X (cited on page 92).

Kim, Jungho. “Spray cooling heat transfer: The state of the art”. In: *International Journal of Heat and Fluid Flow* 28.4 (2007). Including Special Issue of Conference on Modelling Fluid Flow (CMFF’06), Budapest, pp. 753–767. DOI: https://doi.org/10.1016/j.ijheatfluidflow.2006.09.003 (cited on page 147).

Köpple, Fabian et al. “Experimental Investigation of Fuel Impingement and Spray-Cooling on the Piston of a GDI Engine via Instantaneous Surface Temperature Measurements”. In: *SAE International Journal of Enginesngines* 7.3 (2014), pp. 2014–01–1447. DOI: 10.4271/2014-01-1447 (cited on page 59).

Kuo, Kenneth K and Zarchan, Paul. *Recent Advances in Spray Combustion: Spray Atomization and Drop Burning Phenomena*. 1996. DOI: 10.2514/4.866418 (cited on page 2).

Kwak, H C et al. “The New V6 3.5L Turbo GDI Engine from Hyundai-Kia”. In: *27th Aachen Colloquium Automobile and Engine Technology*. Aachen, 2018 (cited on page 27).

Labeish, V.G. “Thermohydrodynamic study of a drop impact against a heated surface”. In: *Experimental Thermal and Fluid Science* 8.3 (1994), pp. 181–194. DOI: 10.1016/0894-1777(94)90047-7 (cited on page 34).

Lee, Sang Yong and Ryu, Sung Uk. “Recent progress of spray-wall interaction research”. In: *Journal of Mechanical Science and Technology* 20.8 (2006), pp. 1101–1117. DOI: 10.1007/BF02916010 (cited on page 33).

Lee, Ziyoung, Kim, Taehoon, Park, Sungwook, and Park, Suhan. “Review on spray, combustion, and emission characteristics of recent developed direct-injection spark ignition (DISI) engine system with multi-hole type injector”. In: *Fuel* 259.July 2019 (2020), p. 116209. DOI: 10.1016/j.fuel.2019.116209 (cited on page 21).

Lefeuvre, T., Myers, P. S., and Uyehara, O. A. “Experimental Instantaneous Heat Fluxes in a Diesel Engine and Their Correlation”. In: (1969). DOI: 10.4271/690464 (cited on page 65).

Lemmon, Eric W., McLinden, M. O., and Friend, D. G. "Thermophysical Properties of Fluid Systems". In: *NIST Chemistry WebBook, NIST Standard Reference Database Number 69*. Ed. by P. J. Linstrom and W. G. Mallard. 2011 (cited on pages 105, 182).

Li, Chao, Wu, Guanjie, Li, Mengzhe, Hu, Chunbo, and Wei, Jinjia. "A heat transfer model for aluminum droplet/wall impact". In: *Aerospace Science and Technology* 97 (2020), p. 105639. DOI: https://doi.org/10.1016/j.ast.2019.105639 (cited on page 34).

Li, Yaoting et al. "A comprehensive experimental investigation on the PFI spray impingement: Effect of impingement geometry, cross-flow and wall temperature". In: *Applied Thermal Engineering* 159.May (2019), p. 113848. DOI: 10.1016/j.applthermaleng.2019.113848 (cited on page 15).

Lillo, Peter M, Pickett, Lyle M, Persson, Helena, Andersson, Öivind, and Kook, Sanghoon. "Diesel Spray Ignition Detection and Spatial/Temporal Correction". In: *SAE Technical Paper 2012-01-1239* (2012). DOI: 10.4271/2012-01-1239 (cited on page 72).

Luca, L. de, Cardone, G., Aymer de la Chevalerie, D., and Fonteneau, A. "Goertler instability of a hypersonic boundary layer". In: *Experiments in Fluids* 16.1 (1993), pp. 10–16. DOI: 10.1007/BF00188500 (cited on page 93).

Luo, Hongliang et al. "Effect of temperature on fuel adhesion under spray-wall impingement condition". In: *Fuel* 234 (2018), pp. 56–65. DOI: https://doi.org/10.1016/j.fuel.2018.07.021 (cited on page 168).

Ma, Dong Shuo and Sun, Z Y. "Progress on the studies about NOx emission in PFI-H2ICE". In: *International Journal of Hydrogen Energy* 45.17 (2020), pp. 10580–10591. DOI: 10.1016/j.ijhydene.2019.11.065 (cited on page 15).

Macian, Vicente, Bermudez, V, Payri, Raul, and Gimeno, Jaime. "New technique for determination of internal geometry of a diesel nozzle with the use of silicone methodology". In: *Experimental Techniques* 27.2 (2003), pp. 39–43. DOI: 10.1111/j.1747-1567.2003.tb00107.x (cited on page 32).

Magneti Marelli. "Gasoline Direct Injection Technology advancements". In: *2015 SAE-China Congress & Exhibition*. Shanghai, China: Society of Automotive Engineers, 2015 (cited on pages 24, 27).

Mahmud, Rizal et al. "Characteristics of Flat-Wall Impinging Spray Flame and Its Heat Transfer under Small Diesel Engine-Like Condition". In: *SAE Technical Paper 2017-32-0032* (2017) (cited on page 147).

Maliha, Malki et al. “Optical investigation on the interaction between a fuel-spray and an oil wetted wall with the focus on secondary droplets”. In: *International Journal of Engine Research* 0.0 (0000), p. 14680874221095235. DOI: 10.1177/14680874221095235 (cited on page 36).

Manin, Julien, Bardi, Michele, and Pickett, Lyle M. “Evaluation of the liquid length via diffused back-illumination imaging in vaporizing diesel sprays”. In: *Comodia*. Fukuoka, 2012 (cited on page 73).

Manin, Julien et al. “Experimental Characterization of DI Gasoline Injection Processes”. In: *SAE Technical Paper Series*. SAE International, 2015. DOI: 10.4271/2015-01-1894 (cited on pages 32, 67).

Marchi, A, Nouri, J, Yan, Y, and Arcoumanis, C. “Spray stability of outwards opening pintle injectors for stratified direct injection spark ignition engine operation”. In: *International Journal of Engine Research* 11.6 (2010). Ed. by Dinos Arcoumanis, pp. 413–437. DOI: 10.1243/14680874JER605 (cited on page 26).

Martí-Aldaraví, Pedro. “Development of a computational model for a simultaneous simulation of internal flow and spray break-up of the Diesel injection process”. PhD thesis. Valencia: Universitat Politècnica de València, 2014. DOI: 10.4995/Thesis/10251/43719 (cited on page 82).

Matusik, Katarzyna E, Duke, Daniel J, Swantek, Andrew B, Powell, Christopher F, and Kastengren, Alan L. “High Resolution X-Ray Tomography of Injection Nozzles”. In: *ILASS Americas 28th Annual Conference on Liquid Atomization and Spray Systems, Dearborn, MI, May 2016*. May. 2016 (cited on pages 32, 33).

Matusik, Katarzyna E et al. “A study on the relationship between internal nozzle geometry and injected mass distribution of eight ECN Spray G nozzles.” In: *Proceedings ILASS–Europe 2017. 28th Conference on Liquid Atomization and Spray Systems*. September. Valencia: Universitat Politècnica València, 2017, pp. 6–8. DOI: 10.4995/ILASS2017.2017.4766 (cited on page 32).

McCaffery, Cavan, Durbin, Thomas D, Johnson, Kent C, and Karavalakis, Georgios. “The effect of ethanol and iso-butanol blends on polycyclic aromatic hydrocarbon (PAH) emissions from PFI and GDI vehicles”. In: *Atmospheric Pollution Research* August (2020), p. 1. DOI: 10.1016/j.apr.2020.08.024 (cited on pages 15, 18).

Meingast, Ulrich, Staudt, Michael, Reichelt, Lars, and Renz, Ulrich. "Analysis of Spray / Wall Interaction Under Diesel Engine Conditions". In: *SAE Technical Paper 2000-01-0272* 724 (2000), pp. 1–15 (cited on pages 35, 36, 59, 85).

Mitroglou, N, Nouri, J M, Yan, Y, Gavaises, M, and Arcoumanis, C. "Spray structure generated by multi-hole injectors for gasoline direct-injection engines". In: *SAE Technical Papers* 724 (2007), pp. 776–790. DOI: 10.4271/2007-01-1417 (cited on page 72).

Montanaro, Alessandro, Allocca, Luigi, Meccariello, Giovanni, and Lazzaro, Maurizio. "Schlieren and Mie Scattering Imaging System to Evaluate Liquid and Vapor Contours of a Gasoline Spray Impacting on a Heated Wall". In: *SAE Technical Papers* 2015 (2015). DOI: 10.4271/2015-24-2473 (cited on page 35).

Montanaro, Alessandro et al. "Schlieren and Mie Scattering Visualization for Single- Hole Diesel Injector under Vaporizing Conditions with Numerical Validation". In: *SAE Technical Paper* (2014). DOI: 10.4271/2014-01-1406 (cited on page 72).

Montorsi, Luca, Magnusson, Alf, and Andersson, Sven. "A Numerical and Experimental Study of Diesel Fuel Sprays Impinging on a Temperature Controlled Wall". In: *SAE Technical Paper 2006-01-3333* 724 (2006), pp. 776–790. DOI: 10.4271/2006-01-3333 (cited on page 35).

Moon, Seoksu, Huang, Weidi, and Wang, Jin. "Spray formation mechanism of diverging-tapered-hole GDI injector and its potentials for GDI engine applications". In: *Fuel* 270.March (2020), p. 117519. DOI: 10.1016/j.fuel.2020.117519 (cited on pages 21, 199).

Moon, Seoksu et al. "Ultrafast X-ray study of multi-hole GDI injector sprays: Effects of nozzle hole length and number on initial spray formation". In: *Experimental Thermal and Fluid Science* 68 (2015), pp. 68–81. DOI: 10.1016/j.expthermflusci.2015.03.027 (cited on pages 29, 30, 72, 199).

Moreira, A, Moita, Cossali, E, Marengo, M, and Santini, M. "Secondary atomization of water and isooctane drops impinging on tilted heated surfaces". In: *Experiments in Fluids* 200 (2007), p. 117626. DOI: 10.1007/s00348-007-0330-2 (cited on pages 114, 148, 164).

Moreira, A L N and Moita, A.s. "Droplet-Wall Interactions". In: 2011, pp. 183–197 (cited on page 34).

Moulai, Maryam, Grover, Ronald, Parrish, Scott, and Schmidt, David. "Internal and Near-Nozzle Flow in a Multi-Hole Gasoline Injector Under Flashing and Non-Flashing Conditions". In: *SAE Technical Paper Series*. SAE International, 2015. DOI: 10.4271/2015-01-0944 (cited on pages 67, 104).

Moussou, Julien, Pilla, Guillaume, Rabeau, Fabien, Sotton, Julien, and Bellenoue, Marc. "High-frequency wall heat flux measurement during wall impingement of a diffusion flame". In: *International Journal of Engine Research* (2019) (cited on pages 85, 147).

Naber, Jeffrey D and Siebers, Dennis L. "Effects of Gas Density and Vaporization on Penetration and Dispersion of Diesel Sprays". In: *SAE Paper 960034* (1996). DOI: 10.4271/960034 (cited on pages 81, 82).

Nakamura, Joyce. *Applied Numerical Methods with Software*. 1st. Upper Saddle River, NJ, USA: Prentice Hall PTR, 1990 (cited on page 86).

NIST. *National Institute of Standards and Technology standard reference data*. Online (cited on page 65).

Otsu, Noboyuki. "A Threshold Selection Method from Gray-Level Histograms". In: *IEEE Transactions on system, Man, and Cybernetics* (1979). DOI: 0018-9472/79/0100-006200.75 (cited on page 95).

Panão, M R O and Moreira, A L N. "Thermo- and fluid dynamics characterization of spray cooling with pulsed sprays". In: *Experimental Thermal and Fluid Science* 30 (2005), pp. 79–96. DOI: 10.1016/j.expthermflusci.2005.03.020 (cited on page 34).

Papoulias, D, Giannadakis, E, Mitroglou, N, Gavaises, M, and Theodorakakos, A. "Cavitation in fuel injection systems for spray-guided direct injection gasoline engines". In: *SAE Technical Papers* 724 (2007), pp. 776–790. DOI: 10.4271/2007-01-1418 (cited on page 72).

Parotto, Marco, Sgatti, Stefano, and Sensi, Fabio. "Advanced GDI Injector Control with Extended Dynamic Range". In: *SAE Technical Papers*. Vol. 2. 2013. DOI: 10.4271/2013-01-0258 (cited on page 23).

Pastor, Jose Vicente, Payri, Raul, Garcia-Oliver, Jose Maria, and Briceño, Francisco Javier. "Schlieren Methodology for the Analysis of Transient Diesel Flame Evolution". In: *SAE International Journal of Engines* 6.3 (2013), pp. 1661–1676. DOI: 10.4271/2013-24-0041 (cited on page 72).

Pastor, Jose Vicente, Payri, Raul, Garcia-Oliver, Jose Maria, and Nerva, Jean-Guillaume. "Schlieren Measurements of the ECN-Spray A Penetration under Inert and Reacting Conditions". In: *SAE Technical Paper 2012-01-0456* (2012). DOI: 10.4271/2012-01-0456 (cited on page 79).

Pauer, Thomas, Yilmaz, Hakan, Zumbrägel, Joachim, and Schünemann, Erik. "New Generation Bosch Gasoline Direct-injection Systems". In: *MTZ worldwide* 78.7-8 (2017), pp. 16–23. DOI: 10.1007/s38313-017-0053-6 (cited on pages 24, 26, 27, 31).

Pavel, Nicolaie et al. "Laser ignition - Spark plug development and application in reciprocating engines". In: *Progress in Quantum Electronics* 58.April (2018), pp. 1–32. DOI: 10.1016/j.pquantelec.2018.04.001 (cited on page 12).

Payri, F, Payri, Raul, Salvador, F J, and Martínez-López, Jorge. "A contribution to the understanding of cavitation effects in Diesel injector nozzles through a combined experimental and computational investigation". In: *Computers & Fluids* 58 (2012), pp. 88–101. DOI: 10.1016/j.compfluid.2012.01.005 (cited on page 31).

Payri, Francisco and Desantes, Jose Maria. *Motores de combustion interna alternativos*. Editorial Universitat Politecnica de Valencia, 2011 (cited on pages 12–14, 16).

Payri, R., Gimeno, J., Marti-Aldaravi, P., and Martinez, M. "Large Eddy Simulations of the fuel injection and mixing process of the ECN GDi Injector Spray G". In: *ICLASS International Conference on Liquid Atomization and Spray Systems* (2021) (cited on page 167).

Payri, Raul, Bracho, Gabriela, Gimeno, Jaime, and Bautista, Abian. "Rate of injection modelling for gasoline direct injectors". In: *Energy Conversion and Management* 166 (2018), pp. 424–432. DOI: 10.1016/j.enconman.2018.04.041 (cited on pages 23, 27, 55, 179).

Payri, Raul, Garcia-Oliver, Jose Maria, Salvador, Francisco Javier, and Gimeno García, Jaime. "Using spray momentum flux measurements to understand the influence of diesel nozzle geometry on spray characteristics". In: *Fuel* 84.5 (2005), pp. 551–561. DOI: 10.1016/j.fuel.2004.10.009 (cited on pages 184, 186, 187, 197).

Payri, Raul, Gimeno, Jaime, Marti-Aldaravi, Pedro, and Mendoza Alvarez, Victor. "Study of the hydraulic characteristics of two injectors fed with different fuels in a GDI system". In: *Fuel* 317 (2022), p. 123196. DOI: https://doi.org/10.1016/j.fuel.2022.123196 (cited on pages 5, 179, 190).

Payri, Raul, Gimeno, Jaime, Marti-Aldaravi, Pedro, and Vaquerizo, Daniel. "Momentum Flux Measurements on an ECN GDi Injector". In: *SAE Technical Paper 2015-01-1893*. 2015. DOI: 10.4271/2015-01-1893 (cited on pages 23, 32, 188, 189).

Payri, Raul, Gimeno, Jaime, Marti-Aldaravi, Pedro, and Vaquerizo, Daniel. "Momentum Flux Measurements on an ECN GDi Injector". In: *SAE* (). DOI: https://doi.org/10.4271/2015-01-1893 (cited on page 192).

Payri, Raul, Gimeno, Jaime, Martí-Aldaraví, Pedro, and Vaquerizo, Daniel. "Internal flow characterization on an ECN GDi injector". In: *Atomization and Sprays* 26.9 (2016), pp. 889–919. DOI: 10.1615/AtomizSpr.2015013930 (cited on pages 23, 27, 179).

Payri, Raul, Gimeno, Jaime, Mata, Carmen, and Viera, Alberto. "Rate of injection measurements of a direct-acting piezoelectric injector for different operating temperatures". In: *Energy Conversion and Management* 154.October (2017), pp. 387–393. DOI: 10.1016/j.enconman.2017.11.029 (cited on pages 26, 179).

Payri, Raul, Gimeno, Jaime, Peraza, Jesús E, and Bazyn, Tim. "Spray / wall interaction analysis on an ECN single-hole injector at diesel-like conditions through Schlieren visualization". In: *Proc. 28th ILASS-Europe, Valencia* September (2017) (cited on pages 35, 79, 82).

Payri, Raul, Hardy, Gilles, Gimeno, Jaime, and Bautista, Abian. "Analysis of counterbore effect in five diesel common rail injectors". In: *Experimental Thermal and Fluid Science* 107 (2019), pp. 69–78. DOI: 10.1016/j.expthermflusci.2019.05.008 (cited on pages 31, 79, 167, 179, 199).

Payri, Raul, Salvador, Francisco Javier, Bracho, Gabriela, and Viera, Alberto. "Differences between single and double-pass schlieren imaging on diesel vapor spray characteristics". In: *Applied Thermal Engineering* 125 (2017), pp. 220–231. DOI: 10.1016/j.applthermaleng.2017.06.140 (cited on pages 79, 84).

Payri, Raul, Salvador, Francisco Javier, Gimeno, Jaime, and Peraza, Jesús E. "Experimental study of the injection conditions influence over n-dodecane and diesel sprays with two ECN single-hole nozzles. Part II: Reactive atmosphere". In: *Energy Conversion and Management* 126 (2016), pp. 1157–1167. DOI: 10.1016/j.enconman.2016.07.079 (cited on page 82).

Payri, Raul, Salvador, Francisco Javier, Gimeno, Jaime, and Viera, Juan Pablo. "Experimental analysis on the influence of nozzle geometry over the dispersion of liquid n-dodecane sprays". In: *Frontiers in Mechanical Engineering* 1 (2015), pp. 1–10. DOI: 10.3389/fmech.2015.00013 (cited on pages 83, 84).

Payri, Raul, Salvador, Francisco Javier, Gimeno, Jaime, and Zapata, Luis Daniel. "Diesel nozzle geometry influence on spray liquid-phase fuel penetration in evaporative conditions". In: *Fuel* 87.7 (2008), pp. 1165–1176. DOI: 10.1016/j.fuel.2007.05.058 (cited on page 183).

Payri, Raul, Salvador, Francisco Javier, Manin, Julien, and Viera, Alberto. "Diesel ignition delay and lift-off length through different methodologies using a multi-hole injector". In: *Applied Energy* 162 (2016), pp. 541–550. DOI: 10.1016/j.apenergy.2015.10.118 (cited on page 72).

Payri, Raul, Salvador, Francisco Javier, Marti-Aldaravi, Pedro, and Vaquerizo, Daniel. "ECN Spray G external spray visualization and spray collapse description through penetration and morphology analysis". In: *Applied Thermal Engineering* 112 (2017), pp. 304–316. DOI: 10.1016/j.applthermaleng.2016.10.023 (cited on pages 74, 79).

Payri, Raul, Viera, Juan Pablo, Gopalakrishnan, Venkatesh, and Szymkowicz, Patrick G. "The effect of nozzle geometry over the evaporative spray formation for three different fuels". In: *Fuel* 188 (2017), pp. 645–660. DOI: 10.1016/j.fuel.2016.06.041 (cited on pages 79, 84, 105).

Payri, Raul, Viera, Juan Pablo, Wang, Hua, and Malbec, Louis-Marie. "Velocity field analysis of the high density, high pressure diesel spray". In: *International Journal of Multiphase Flow* 80.24 (2016), pp. 69–78. DOI: 10.1016/j.ijmultiphaseflow.2015.10.012 (cited on page 179).

Payri, Raúl, Gimeno, Jaime, Martí-Aldaraví, Pedro, and Martínez, María. "Transient nozzle flow analysis and near field characterization of gasoline direct fuel injector using Large Eddy Simulation". In: *International Journal of Multiphase Flow* 148 (2022). DOI: https://doi.org/10.1016/j.ijmultiphaseflow.2021.103920 (cited on page 167).

Peraza Avila, Jesus Enrique. "Experimental study of the diesel spray behavior during the jet-wall interaction at high pressure and high temperature conditions". PhD thesis. Universitat Politècnica de València, 2020 (cited on page 4).

Pham, P X, Vo, D Q, and Jazar, R N. "Development of fuel metering techniques for spark ignition engines". In: *Fuel* 206 (2017), pp. 701–715. DOI: 10.1016/j.fuel.2017.06.043 (cited on pages 14, 15, 19, 20, 22).

Pickett, Lyle M, Genzale, Caroline L, and Manin, Julien. "Uncertainty quantification for liquid penetration of evaporating sprays at diesel-like conditions". In: *Atomization and Sprays* 25.5 (2015), pp. 425–452. DOI: 10.1615/AtomizSpr.2015010618 (cited on page 105).

Pickett, Lyle M, Genzale, Caroline L, Manin, Julien, Malbec, Louis-Marie, and Hermant, Laurent. "Measurement Uncertainty of Liquid Penetration in Evaporating Diesel Sprays". In: *ILASS Americas 23rd Annual Conference on Liquid Atomization and Spray Systems*. Ventura, CA (USA): ILASS-Americas, 2011 (cited on page 74).

Postrioti, Lucio et al. "Momentum Flux Measurement on Single-Hole GDI Injector under Flash-Boiling Condition". In: *SAE Technical Papers*. Vol. 24. 2480. 2015. DOI: 10.4271/2015-24-2480 (cited on page 29).

Raghu, O. and Philip, J. "Thermal properties of paint coatings on different backings using a scanning photo acoustic technique". In: *Measure. Sci. Technol* (2006) (cited on page 92).

Konrad Reif, ed. *Gasoline Engine Management*. Wiesbaden: Springer Fachmedien Wiesbaden, 2015. DOI: 10.1007/978-3-658-03964-6 (cited on pages 15, 23, 27–29).

Rivera, Edwin A, Mastro, Noreen, Zizelman, James, Kirwan, John, and Ooyama, Robert. "Development of Injector for the Direct Injection Homogeneous Market using Design for Six Sigma". In: *SAE Technical Papers*. 2010. DOI: 10.4271/2010-01-0594 (cited on pages 27, 29).

Roque, Anthony, Foucher, F., and Helie, Jerome. "Spray wall interaction: study of preferential vaporization of fuel film as function of injection pressure and wall temperature". In: 2019 (cited on pages 36, 148).

Roque, Anthony et al. "Impact of gasoline direct injection fuel films on exhaust soot production in a model experiment". In: *International Journal of Engine Research* 21.2 (2020), pp. 367–390. DOI: 10.1177/1468087419879851 (cited on page 36).

Saliba, Georges et al. "Comparison of Gasoline Direct-Injection (GDI) and Port Fuel Injection (PFI) Vehicle Emissions: Emission Certification Standards, Cold-Start, Secondary Organic Aerosol Formation Potential, and Potential Climate Impacts". In: *Environmental Science and Technology* (2017). DOI: 10.1021/acs.est.6b06509 (cited on pages 3, 15).

Salman, Azzam S. et al. "Experimental investigation of the impact of geometrical surface modification on spray cooling heat transfer performance in the non-boiling regime". In: *International Journal of Heat and Mass Transfer* 133 (2019), pp. 330–340. DOI: https://doi.org/10.1016/j.ijheatmasstransfer.2018.12.058 (cited on page 147).

Savitzky, Abraham. and Golay, M J E. "Smoothing and Differentiation of Data by Simplified Least Squares Procedures." In: *Analytical Chemistry* 36.8 (1964), pp. 1627–1639. DOI: 10.1021/ac60214a047 (cited on page 87).

Schulz, Florian, Schmidt, Jurgen, Kufferath, Andreas, and Samenfink, Wolfgang. “Gasoline Wall Films and Spray/Wall Interaction Analyzed by Infrared Thermography”. In: *SAE International Journal of Engines* 7.3 (2014), pp. 1165–1177. DOI: 10.4271/2014-01-1446 (cited on page 161).

Settles, G. S. *Schlieren and Shadowgraph Techniques*. 2001. DOI: 10.1007/978-3-642-56640-0 (cited on page 72).

Shahangian, Navid et al. “Spray Orientation Assessment and Correction Method for GDI Momentum Flux Measurements”. In: October (2019), pp. 231–241 (cited on pages 183, 189, 199).

Shahangian, Navid et al. “Transient nozzle flow simulations of gasoline direct fuel injectors”. In: *Applied Thermal Engineering* 175.January (2020). DOI: 10.1016/j.applthermaleng.2020.115356 (cited on page 199).

Shi, Hao et al. “Study of spray/wall interaction in transition zones from HCCI via PPC to CI combustion modes”. In: *Fuel* 268 (2020), p. 117341. DOI: https://doi.org/10.1016/j.fuel.2020.117341 (cited on page 36).

Shi, M H, Bai, T C, and Yu, J. “Dynamic behavior and heat transfer of a liquid droplet impinging on a solid surface”. In: *Experimental Thermal and Fluid Science* 6.2 (1993), pp. 202–207. DOI: https://doi.org/10.1016/0894-1777(93)90030-M (cited on page 34).

Shost, Mark A, Lai, Ming-Chia, Befrui, Bizhan, Spiekermann, Peter, and Varble, Daniel L. “GDi Nozzle Parameter Studies Using LES and Spray Imaging Methods”. In: *SAE Technical Papers*. Vol. 1. 2014. DOI: 10.4271/2014-01-1434 (cited on pages 30, 72, 199).

Shost, Mark Anthony. “Evaluation of nozzle geometry on high pressure Gasoline Direct Injection spray atomization”. PhD thesis. Wayne State University, 2014, p. 295 (cited on pages 30, 31).

Shuai, Shijin, Ma, Xiao, Li, Yanfei, Qi, Yunliang, and Xu, Hongming. “Recent Progress in Automotive Gasoline Direct Injection Engine Technology”. In: *Automotive Innovation* 1.2 (2018), pp. 95–113. DOI: 10.1007/s42154-018-0020-1 (cited on page 16).

Shway, Kamal, Jüngst, Niklas, Bardi, Michele, Bruneaux, Gilles, and Kaiser, Sebastian A. “A multispectral UV–vis absorption technique for quantitative high-speed field-sequential imaging of fuel films and soot in combustion”. In: *Proceedings of the Combustion Institute* (2022). DOI: https://doi.org/10.1016/j.proci.2022.08.099 (cited on page 36).

Smith, James, Szekely Jr, Gerald, Solomon, Arun, and Parrish, Scott. "A Comparison of Spray-Guided Stratified-Charge Combustion Performance with Outwardly-Opening Piezo and Multi-Hole Solenoid Injectors". In: *SAE International Journal of Engines* 4.1 (2011), pp. 1217–2011. DOI: 10.4271/2011-01-1217 (cited on page 26).

Spicher, U, Reissing, J, Kech, J M, and Gindele, J. "Gasoline Direct Injection (GDI) Engines - Development Potentialities". In: *SAE Technical Papers*. 724. 1999. DOI: 10.4271/1999-01-2938 (cited on page 13).

Stanton, Donald W. and Rutland, Christopher J. "Multi-dimensional modeling of thin liquid films and spray-wall interactions resulting from impinging sprays". In: *International Journal of Heat and Mass Transfer* 41.20 (1998), pp. 3037–3054. DOI: 10.1016/S0017-9310(98)00054-4 (cited on page 35).

Starikovskiy, Andrey and Aleksandrov, Nickolay. "Plasma-assisted ignition and combustion". In: *Progress in Energy and Combustion Science* 39.1 (2013), pp. 61–110. DOI: 10.1016/j.pecs.2012.05.003 (cited on page 12).

Steinberg, Christoph, Liu, Menqgi, and Hung, David L.S. "A combined experimental numerical study towards the elucidation of spray wall interaction on step geometries". In: *Engineering Applications of Computational Fluid Mechanics* 16.1 (2022), pp. 1866–1882. DOI: 10.1080/19942060.2022.2098828 (cited on page 36).

Strek, Piotr et al. "X-Ray Radiography and CFD Studies of the Spray G Injector". In: *SAE Technical Papers* 2016-April.April (2016). DOI: 10.4271/2016-01-0858 (cited on pages 32, 184).

Su, Yu Hsuan and Kuo, Ting Fu. "CFD-assisted analysis of the characteristics of stratified-charge combustion inside a wall-guided gasoline direct injection engine". In: *Energy* 175.x (2019), pp. 151–164. DOI: 10.1016/j.energy.2019.03.031 (cited on page 21).

Tang, Qinglong et al. "Experimental Study on the Effects of Spray Wall Interaction on Partially Premixed Combustion and Engine Emissions". In: *Energy & Fuels* 33.6 (2019), pp. 5673–5681. DOI: 10.1021/acs.energyfuels.9b00602 (cited on page 36).

Toda, Saburo. "A Study of Mist Cooling : 1st Report, Experimental Investigations on Mist Cooling by Mist Flow Sprayed Vertically on Small and Flat Plates Heated at High Temperatures". In: *Transactions of the Japan Society of Mechanical Engineers* 38.307 (1972), pp. 581–588. DOI: 10.1299/kikai1938.38.581 (cited on page 34).

Tu, Po-Wen et al. “Numerical Investigation of GDI Injector Nozzle Geometry on Spray Characteristics”. In: *SAE Technical Papers*. Vol. 2015-Septe. September. 2015. DOI: 10.4271/2015-01-1906 (cited on page 30).

Van Basshuysen, Richard and Spicher, Ulrich. *Gasoline engine with direct injection : processes, systems, development, potential*. Ed. by Richard Van Basshuysen and Ulrich Spicher. Wiesbaden, 2009 (cited on page 16).

Vaquerizo, Daniel. “Study on Advanced Spray-Guided Gasoline Direct Injection Systems”. PhD thesis. Universitat Politècnica de València, 2017 (cited on pages 4, 5, 16, 23, 28, 55, 56, 71).

Vende, Trinque, Lacour, Delahaye, and Fournaison. “Efficiency of water spraying on a heat exchanger: Local characterization with the impacted surface”. In: *Applied Thermal Engineering* 128 (2017), pp. 684–695. DOI: http://dx.doi.org/10.1016/j.applthermaleng.2017.09.031 (cited on page 95).

Vent, Guido and Enderle, Christian. “The new 2.0 l turbo engine from the Mercedes-Benz 4-cylinder engine family”. In: *2nd Aachen Colloquium China* (2012) (cited on page 26).

Viera, Alberto. “Effect of multiple injection strategies on the diesel spray formation and combustion using optical diagnostics”. PhD thesis. Universitat Politècnica de València, 2019 (cited on pages 55, 179, 180).

Viera, Juan Pablo. “Experimental Study of the Effect of Nozzle Geometry on the Performance of Direct-Injection Diesel Sprays for Three Different Fuels”. PhD thesis. Universitat Politècnica de València, 2017 (cited on pages 55, 179, 199).

Walker, D. Greg and Scott, Elaine P. “Evaluation of Estimation Methods for High Unsteady Heat Fluxes from Surface Measurements”. In: *Journal of Thermophysics and Heat Transfer* 12.4 (1998), pp. 543–551. DOI: 10.2514/2.6374 (cited on page 91).

Wang, Zhongli et al. “Experimental Study of Influence on Microwave Plasma Ignition Combustion Performance of Pulse Microwave Signals”. In: *IEEE Access* 7 (2019), pp. 23951–23958. DOI: 10.1109/ACCESS.2019.2899911 (cited on page 12).

Watson, T. W. and Robinson, H. E. “Thermal Conductivity of Some Commercial Iron-Nickel Alloys”. In: *Journal of Heat Transfer* 83.4 (1961), pp. 403–407. DOI: 10.1115/1.3683651 (cited on page 91).

Westlye, Fredrik R et al. “Diffuse back-illumination setup for high temporally resolved extinction imaging”. In: *Applied Optics* 56.17 (2017). DOI: 10.1364/AO.56.005028 (cited on page 74).

Wigley, G, Pitcher, G, Nuglisch, H, Helie, J, and Ladommatos, N. "Fuel Spray Formation and Gasoline Direct Injection". In: *8th AVL international symposium on combustion diagnostics*. 2008 (cited on page 27).

Wood, Andrew. "Optical investigations of the sprays generated by gasoline multi-hole injectors under novel operating conditions". PhD thesis. Loughborough University, 2014 (cited on pages 25, 27).

Wu, Zengyang, Wang, Libing, Badra, Jihad A, Roberts, William L, and Fang, Tiegang. "GDI fuel sprays of light naphtha, PRF95 and gasoline using a piezoelectric injector under different ambient pressures". In: *Fuel* 223.December 2017 (2018), pp. 294–311. DOI: 10.1016/j.fuel.2018.03.009 (cited on page 25).

Wu, Zhenkuo, Deng, Peng, and Han, Zhiyu. "A numerical study on fuel film and emissions formations during cold start in a diesel engine using an improved spray-wall impingement model". In: *Fuel* 320 (2022), p. 123898. DOI: https://doi.org/10.1016/j.fuel.2022.123898 (cited on page 36).

Xu, Min, Cui, Yi, and Deng, Kangyao. "One-dimensional model on liquid-phase fuel penetration in diesel sprays". In: *Journal of the Energy Institute* 89.1 (2016), pp. 138–149. DOI: 10.1016/j.joei.2015.01.002 (cited on page 105).

Yang, Zhengjun et al. "Real driving particle number (PN) emissions from China-6 compliant PFI and GDI hybrid electrical vehicles". In: *Atmospheric Environment* 199.September 2018 (2019), pp. 70–79. DOI: 10.1016/j.atmosenv.2018.11.037 (cited on pages 15, 18).

Yao, Shi-Chune and Cai, Kang Yuan. "The dynamics and leidenfrost temperature of drops impacting on a hot surface at small angles". In: *Experimental Thermal and Fluid Science* 1.4 (1988), pp. 363–371. DOI: 10.1016/0894-1777(88)90016-7 (cited on page 34).

Yi, Jianwen et al. "Development and Optimization of the Ford 3.5L V6 EcoBoost Combustion System". In: *SAE International Journal of Engines* 2.1 (2009), pp. 1494–2009. DOI: 10.4271/2009-01-1494 (cited on pages 27, 29).

Yu, Hanzhengnan, Liang, Xingyu, Shu, Gequn, Sun, Xiuxiu, and Zhang, Hongsheng. "Experimental investigation on wall film ratio of diesel, butanol/diesel, DME/diesel and gasoline/diesel blended fuels during the spray wall impingement process". In: *Fuel Processing Technology* 156 (2017), pp. 9–18. DOI: https://doi.org/10.1016/j.fuproc.2016.09.029 (cited on page 35).

Yu, Hanzhengnan, Liang, Xingyu, Shu, Gequn, Wang, Yuesen, and Zhang, Hongsheng. "Experimental investigation on spray-wall impingement characteristics of n-butanol/diesel blended fuels". In: *Fuel* 182 (2016), pp. 248–258. DOI: https://doi.org/10.1016/j.fuel.2016.05.115 (cited on page 35).

Yu, Xiumin et al. "Investigation of combustion and emissions of an SI engine with ethanol port injection and gasoline direct injection under lean burn conditions". In: *Energy* 189 (2019), p. 116231. DOI: 10.1016/j.energy.2019.116231 (cited on page 23).

Zeng, Wei and Sjöberg, Magnus. "Utilizing boost and double injections for enhanced stratified-charge direct-injection spark-ignition engine operation with gasoline and E30 fuels". In: *International Journal of Engine Research* 18.1-2 (2017), pp. 131–142. DOI: 10.1177/1468087416685512 (cited on page 21).

Zeng, Wei, Sjöberg, Magnus, Reuss, David L, and Hu, Zongjie. "The role of spray-enhanced swirl flow for combustion stabilization in a stratified-charge DISI engine". In: *Combustion and Flame* 168.x (2016), pp. 166–185. DOI: 10.1016/j.combustflame.2016.03.015 (cited on page 21).

Zhang, Fan, Ma, T Y, Zhang, F, Liu, H F, and Yao, M F. "Modeling of droplet / wall interaction based on SPH method". In: *International Journal of Heat and Mass Transfer* 105.February (2017), pp. 296–304. DOI: 10.1016/j.ijheatmasstransfer.2016.09.103 (cited on page 34).

Zhang, Yanzhi et al. *Development of anew spray/wall interaction model for diesel spray under PCCI-engine relevant conditions*. Vol. 24. 1. 2014, pp. 41–80. DOI: 10.1615/AtomizSpr.2013008287 (cited on page 35).

Zhao, F, Lai, M.-C, and Harrington, D L. "Automotive spark-ignited direct-injection gasoline engines". In: *Progress in Energy and Combustion Science* 25.5 (1999), pp. 437–562. DOI: 10.1016/S0360-1285(99)00004-0 (cited on pages 13, 19, 25, 26).

Zhao, Hua. *Advanced direct injection combustion engine technologies and development*. Woodhead Publishing Limited, 2010. DOI: 10.1533/9781845697327 (cited on pages 17, 19, 22, 23, 25, 27, 179).

Zhao, Le et al. "Evaluation of Diesel Spray-Wall Interaction and Morphology around Impingement Location". In: 2018. DOI: 10.4271/2018-01-0276 (cited on page 36).

Zhao, Zhihao, Zhu, Xiucheng, Zhao, Le, Naber, Jeffrey, and Lee, Seong-Young. "Spray-Wall Dynamics of High-Pressure Impinging Combustion". In: 2019. DOI: 10.4271/2019-01-0067 (cited on page 147).

Zheng, Zhaolei, Tian, Xuefeng, and Zhang, Xiaoyu. "Effects of split injection proportion and the second injection time on the mixture formation in a GDI engine under catalyst heating mode using stratified charge strategy". In: *Applied Thermal Engineering* 84 (2015), pp. 237–245. DOI: 10.1016/j.applthermaleng.2015.03.041 (cited on page 21).

Zhou, Jianwei et al. "Characteristics of near-nozzle spray development from a fouled GDI injector". In: *Fuel* 219.92 (2018), pp. 17–29. DOI: 10.1016/j.fuel.2018.01.070 (cited on page 21).

Zhu, Rencheng et al. "Tailpipe emissions from gasoline direct injection (GDI) and port fuel injection (PFI) vehicles at both low and high ambient temperatures". In: *Environmental Pollution* 216 (2016), pp. 223–234. DOI: 10.1016/j.envpol.2016.05.066 (cited on pages 15, 18).

Zhu, Xiucheng et al. "An Experimental Study of Diesel Spray Impingement on a Flat Plate: Effects of Injection Conditions". In: September (2017). DOI: 10.4995/ilass2017.2017.4733 (cited on page 36).

Zhuang, Yuan et al. "Investigation of water injection benefits on downsized boosted direct injection spark ignition engine". In: *Fuel* 264.October 2019 (2020). DOI: 10.1016/j.fuel.2019.116765 (cited on page 18).

Zigan, L, Schmitz, I, Flügel, A, Wensing, M, and Leipertz, A. "Structure of evaporating single- and multicomponent fuel sprays for 2nd generation gasoline direct injection". In: *Fuel* 90.1 (2011), pp. 348–363. DOI: 10.1016/j.fuel.2010.08.001 (cited on page 26).

Zimmerman, Naomi, Wang, Jonathan M, Jeong, Cheol Heon, Wallace, James S, and Evans, Greg J. "Assessing the Climate Trade-Offs of Gasoline Direct Injection Engines". In: *Environmental Science and Technology* (2016). DOI: 10.1021/acs.est.6b01800 (cited on page 3).